Fermilab

FERMILAB-THESIS-2003-16

Measuring the Jet Response and the Search for the Higgs Boson in the Channel $ZH \to e^+e^-b\overline{b}$ with the DØ Detector

M. Petteni

Imperial College of Science Technology and Medicine

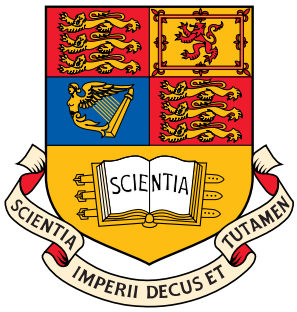

A thesis submitted for the degree of
Doctor of Philosophy
of the University of London
and the Diploma of Imperial College

February, 2003

Measuring the Jet Response and the Search for the Higgs Boson in the Channel $ZH \to e^+e^-b\overline{b}$ with the DØ Detector

Michele Petteni
Imperial College of Science Technology and Medicine.

Submitted for the degree of Doctor of Philosophy
the University of London.
February 2003

ABSTRACT

The DØ detector is an all purpose detector at the 1.96 TeV proton-antiproton Tevatron collider at Fermilab. One of the significant upgrades to the DØ detector for Run II was the addition of a silicon tracker. The procedures for the testing and production of the F-Disk sub-module of the silicon tracker are described in detail.

The largest contribution to the jet energy scale at DØ is the calorimeter response to jets. The jet response is calculated using the Missing E_T Projection Fraction method for the p10 version of the DØ reconstruction software using a Monte Carlo Z+jet sample. A comparison to the certified jet energy scale is made. The results derived from these two independent samples are found to be consistent.

A Monte Carlo sequential cuts analysis in the $ZH \to e^+e^-b\overline{b}$ channel is performed using the p10 DØ reconstruction software. The sensitivity in this channel, for an integrated luminosity of 2 fb^{-1}, is found to be 0.15 for a Higgs mass of 115 GeV/c^2. This is a factor of two lower than the previous estimate derived as part of the SUSY Higgs Workshop. The major factor limiting the sensitivity is the preliminary b-tagging technique used in the analysis. An improved mass resolution of 10% increases the sensitivity by 20%. An optimised cuts analysis is also performed and this method gives a sensitivity of 0.16 for the same mass. Events from the ICHEP02 data sample are compared to Z+di-jet Monte Carlo events. Although the results are limited by the integrated luminosity of the data sample, the data and Monte Carlo are found to be consistent.

Acknowledgements

First and foremost I wish to thank my parents; for always encouraging me to pursue my interests in this field and for all their support throughout my undergraduate and postgraduate degrees.

Throughout my PhD I have had the pleasure of working with many people whom I profoundly respect. In particular I would like to thank Prof P. Dornan for introducing me to particle physics research, the members of the Imperial College DØ group for all their assistance and Dr T. Bacon for proof reading my thesis. At Fermilab I am indebted to many; to all the technicians I worked with at SiDet, to Dr R. Lipton, Dr M. Demarteau, Dr I. Iashvili and Dr A. Bean on the SMT project and to Dr J. Hobbs and Dr A. Kharchilava, the conveners of the Higgs group. I would especially like to thank Dr A. Goussiou, my acting supervisor while at Fermilab, for all her help and advice.

On a more personal note; Kahae and Dan thank you for being such good friends over the course of these years. Jay, John, Greg thank you for showing me the better side of the States. Rick, thank you for your friendship and for being there for me. Aside from single-handedly keeping me sane you even made me enjoy baseball... what else is there to say?

I know that my PhD experience would have been lacking in many respects if it hadn't been for my supervisor, Dr Gavin Davies. Thank you for always listening to my rants, not only when I was right but more importantly when I was wrong. I don't think that I could have wished for a better supervisor or for better advice throughout my PhD.

Contents

List of Figures

List of Tables

Preface

This thesis describes work performed as a member of the DØ Collaboration from 1999-2002. The main focus of the work was on three distinct topics: the production and testing of the new DØ silicon tracker, the calibration of the measured jet energy and the search for the Higgs boson.

As part of the silicon tracker group at Fermilab I was extensively involved in the testing of the F-Disk sub-detector modules and subsequently oversaw and managed the F-Disk production and testing. As a member of the Jet Energy Scale group I derived the calorimeter energy response for jets, a part of the jets energy scale, using a Z+jet sample. The Z+jet sample can be used as an independent check of the jet response and, more generally, the jet energy scale derived using the default γ+jet sample. Lastly as part of the Higgs group I worked on the search for a light mass Standard Model Higgs boson, developing an analysis of the channel $ZH \to e^+e^-b\bar{b}$.

The thesis is structured as follows:

- Chapter 1 is a review of Electroweak theory and of the Higgs mechanism. The need for the Higgs mechanism and how it gives rise to the Higgs particle is outlined. The constraints on the Standard Model Higgs boson mass from theory are mentioned and the current limits on the Standard Model Higgs boson mass from indirect and direct searches are described.

- Chapter 2 is a brief description of the Fermilab accelerator and of the DØ detector. Sample plots of the current DØ detector performance are shown.

- Chapter 3 is an in-depth description of the testing and production of the F-Disk modules. A brief introduction of the silicon tracker and the F-Disks is given. The testing procedure actually used and the problems encountered are highlighted.

- Chapter 4 describes the measurement of the jet response using a Z+jet sample. The method used to calculate the jet energy scale at DØ is outlined and the various corrections which compose it are briefly mentioned. The derivation of the jet response is described in detail, as is the method used to calculate the jet response using a Z+jet sample. The response for this sample using Monte Carlo events is derived and a comparison is made to the Monte Carlo response derived using a γ+jet sample. The jet response from γ+jet data collected for the ICHEP 2002 conference is shown.

- Chapter 5 focuses on the search for a light mass Standard Model Higgs boson in the channel $ZH \rightarrow e^+e^-b\overline{b}$. It summarises the important aspects of the search strategy for a Standard Model Higgs boson at the Tevatron. Issues relevant to the $ZH \rightarrow e^+e^-b\overline{b}$ channel are addressed and the tools required to detect the signal in this channel are described. The Monte Carlo efficiency for the objects relevant to the search is calculated for the signal and main background channels. The sensitivity in this channel using a sequential cuts approach is calculated, as is the sensitivity when using an optimisation of these cuts. Results using the data sample reconstructed using the p10 version of the DØ reconstruction code are shown and are compared to Z+di-jet events in Monte Carlo.

- Chapter 6 provides a brief summary of the thesis and an outlook of the immediate future for DØ .

Chapter 1

The Standard Model

The $SU(3)_C \times SU(2)_I \times U(1)_Y$ description of fundamental particle interactions, commonly known as the Standard Model, is one of the most successful and most precisely tested theories to date. The Standard Model is based on the underlying principle of symmetry which, in physical terms, translates to the unification of forces which are seemingly different in nature. The least experimentally verified aspect of the theory is the Higgs sector, needed to unify the observed weak and electromagnetic forces. The presence of the Higgs field allows other particles to acquire a mass term without breaking the gauge invariance of the Lagrangian. The focus of this chapter will be on the electroweak sector and the Higgs mechanism.

1.1 Symmetry Principles and Gauge Invariance

The principle of symmetry and its application to modern particle physics theory is both powerful and far-reaching. The requirement that the Standard Model Lagrangian should conserve its properties under symmetry transformations is at the heart of all aspects of the Standard Model and to many of the proposed extensions. This is what makes the electroweak sector of the Standard Model so attractive; starting from a very basic principle one can build the Lagrangian of the Standard Model. This is also why there is such a focus on finding the Higgs (or a Higgs-like particle). Without the Higgs the Standard Model would be incomplete as it would not be able to explain the difference in mass between the photon and the vector bosons or indeed the presence of massive particles.

To understand the electroweak sector of the Standard Model one needs to understand the basic principles on which it is based and how the Standard Model stems naturally from them. The Lagrangian for a free Dirac field under U(1) and

SU(2) gauge transformations is studied in order to see how imposing the invariance of the Lagrangian under gauge transformations affects particle content and particle interactions.

1.1.1 Abelian Gauge Transformations

Global Gauge Transformations

The Lagrangian Density, $\mathcal{L}_{Dirac}$, for a free Dirac field, Ψ, is given in Equation 1.1

$$\mathcal{L}_{Dirac} = \overline{\Psi}(x)(i\gamma^{\mu}\partial_{\mu} - m)\Psi(x). \tag{1.1}$$

$\overline{\Psi}(x)$ is the conjugate field defined as $\Psi^{\dagger}(x)\gamma^{0}$. The γ^{μ} are the 4×4 gamma-matrices. It is common to denote $\gamma^{\mu}\partial_{\mu}$ as $\not{\partial}$.

Equation 1.1 is manifestly invariant under the following global gauge transformation:

$$\Psi(x) \rightarrow \Psi'(x) = e^{iq\theta}\Psi(x), \tag{1.2}$$

where the conjugate field transforms in an equivalent way but with the opposite sign in the exponential. θ is a real, continuous parameter and q is the charge of the field. The transformation in Equation 1.2 is that for an Abelian U(1) group and is global because the transformation is the same for all space-time points. The invariance of the Lagrangian under global, continuous transformations can be directly linked with a conserved current via Noether's Theorem. In this example the conserved current is that of electric charge.

Local Gauge Transformations

A more interesting case is that in which the transformation is not global but has a space-time dependency i.e. θ in Equation 1.2 is replaced by $\theta(x)$. Under the new transformation the Dirac Lagrangian density is no longer invariant as the partial derivative in Equation 1.1 will now contribute a non-zero term from its action on the exponential. In order to impose local gauge invariance the extra $q\overline{\Psi}(x)\Psi(x)\not{\partial}\theta(x)$ term from the action of the partial derivative has to be compensated for. A real gauge field, $A_{\mu}(x)$, is introduced with the following gauge transformation property:

$$A_{\mu} \rightarrow A'_{\mu}(x) = A_{\mu}(x) - \frac{1}{g}\partial_{\mu}\theta(x), \tag{1.3}$$

where g is a real number. The Lagrangian density is modified to that in Equation 1.4:

$$\begin{aligned}\mathcal{L} &= \overline{\Psi}(x)(i\not{\partial} - gq\not{A}(x) - m)\Psi(x) \\ &= -m\overline{\Psi}(x)\Psi(x) + i\overline{\Psi}(x)\gamma^{\mu}(\partial_{\mu} + igqA_{\mu}(x))\Psi(x),\end{aligned} \tag{1.4}$$

where the mass term is manifestly invariant as before. The gauge transformation of $A_{\mu}(x)$ gives rise to a term -$q\overline{\Psi}(x)\Psi(x)\not{\partial}\theta(x)$ which cancels the extra term from the action of the partial derivative and restores gauge invariance. The last term in Equation 1.4 describes the interaction of the Dirac field with the gauge field with a strength given by a coupling constant, g and the field charge, q. In QED this is the interaction between the electron and the photon fields where the coupling is simply e, the magnitude of the electron charge.

Equation 1.4 can be re-written in terms of a "covariant derivative", D_{μ}. A covariant derivative has the property given in Equation 1.5 i.e. when replacing the partial derivative by the covariant derivative the gauge invariance of the Lagrangian density follows as in the global case.

$$D_{\mu}\Psi(x) \rightarrow D'_{\mu}\Psi'(x) = e^{iq\theta(x)}D_{\mu}\Psi(x), \tag{1.5}$$

For QED the covariant derivative is

$$D_{\mu} \equiv \partial_{\mu} + ieqA_{\mu}(x) \tag{1.6}$$

In order for $A_{\mu}(x)$ to represent the photon field the Lagrangian density needs to include a kinetic energy term and, in the most general case, a mass term. As the Lagrangian density is now invariant under local gauge transformations these additional terms also have to be locally gauge invariant. A kinetic term can be constructed from the antisymmetric "field strength tensor" $F_{\mu\nu}$ defined as:

$$F_{\mu\nu} = \partial_{\mu}A_{\nu}(x) - \partial_{\nu}A_{\mu}(x). \tag{1.7}$$

This is invariant under the gauge transformation in Equation 1.3. The kinetic term appears as:

$$\mathcal{L}_{\gamma}^{K.E.} = -\frac{1}{4}F_{\mu\nu}F^{\mu\nu}, \tag{1.8}$$

where the factor of -1/4 is an equivalence factor with respect to Maxwell's Equations. A mass term for the field $A_{\mu}(x)$ would be of the form:

$$-\frac{1}{2}m_{\gamma}^{2}A_{\mu}(x)A^{\mu}(x). \tag{1.9}$$

This is clearly not gauge invariant unless $m_{\gamma} = 0$, which is perfectly consistent with observations.

1.1.2 Non-Abelian Gauge Transformations

The gauge transformation in Equation 1.2 can be extended trivially to non-Abelian local gauge transformations. It will be seen that local non-Abelian gauge transformations can be directly linked to the presence of the vector gauge bosons. The SU(2) isospin group can be used as an example without any loss of generality as the procedure is equivalent for an arbitrary group of N dimensions. The Lagrangian density given in Equation 1.1 has to be modified to account for the different group structure. The Lagrangian density for a free isodoublet is:

$$\mathcal{L} = \overline{\psi}^i(x)(i\not{\partial} - m)\psi_i(x), \tag{1.10}$$

where the index i is summed over 1 and 2. SU(2) is a dimension 3 group and hence has three generators. In the 2×2 matrix representation the generators $\mathbf{T}^a (a = 1, 2, 3)$ are given by 1/2 times the Pauli spin matrices:

$$\mathbf{T}^1 = \frac{1}{2}\begin{pmatrix} 0 & 1 \\ 1 & 0 \end{pmatrix}, \quad \mathbf{T}^2 = \frac{1}{2}\begin{pmatrix} 0 & -i \\ i & 0 \end{pmatrix}, \quad \mathbf{T}^3 = \frac{1}{2}\begin{pmatrix} 1 & 0 \\ 0 & -1 \end{pmatrix}, \tag{1.11}$$

and obey the following commutation relations:

$$[\mathbf{T}^a, \mathbf{T}^b] = i\epsilon_{abc}\mathbf{T}^c. \tag{1.12}$$

Hence the gauge transformation for a field $\psi_i(x)$ is

$$\psi_i(x) \rightarrow \psi_i'(x) = (e^{i\mathbf{T}\cdot\boldsymbol{\omega}(\mathbf{x})})_i^j \psi_j(x), \tag{1.13}$$

where $\omega^a(x)(a = 1, .., 3)$ are analogous to the real space-time fields $\theta(x)$ in the Abelian case. It is useful to consider only the infinitesimal transformations $\delta\psi_i(x)$ and $\delta\overline{\psi}^i(x)$ where

$$\begin{aligned} \delta\psi_i(x) &= i\omega^a(x)(\mathbf{T}^a)_i^j\psi_j(x) \\ \delta\overline{\psi}^i(x) &= -i\omega^a(x)\overline{\psi}^j(x)(\mathbf{T}^a)_j^i \end{aligned} \tag{1.14}$$

Substituting the field transformations given in Equation 1.14 into Equation 1.10 and dropping $O(\omega^2)$ terms, the change in the Lagrangian density, $\delta\mathcal{L}$, is

$$\delta\mathcal{L} = -\overline{\psi}^i(x)(\mathbf{T}^a)_i^j(\not{\partial}\omega^a(x))\psi_j(x). \tag{1.15}$$

Similarly to the Abelian case, 3 gauge fields, $W_\mu^a(x)$, with the infinitesimal transformation properties given in Equation 1.16 are introduced and again a covariant derivative as in Equation 1.17 can be defined.

$$\delta W_\mu^a(x) = \epsilon_{abc} W_\mu^b(x)\omega^c(x) - \frac{1}{g}\partial_\mu \omega^a(x) \tag{1.16}$$

$$D_\mu \equiv \partial_\mu \mathbf{I} + ig\mathbf{T}^a W_\mu^a(x) \tag{1.17}$$

The new Lagrangian density is therefore modified to that in Equation 1.18.

$$\mathcal{L} = \overline{\psi}^i(x)(i\not{D} - m\mathbf{I})_i^j \psi_j(x), \tag{1.18}$$

As the mass term is again invariant only the change to the covariant derivative term needs to be calculated. By considering $\delta(\overline{\psi}^i(x)(i\not{D})_i^j\psi_j(x))$ to first order in $\omega^a(x)$, the second term in the Equation 1.16 acts to cancel that introduced by demanding that the field be local. The first term in Equation 1.16 acts to compensate for the non-Abelian nature of the field which results in a commutation relation from $(\delta\overline{\psi}^i(x))(i\not{D})_i^j\psi_j(x) + \overline{\psi}^i(x)(i\not{D})_i^j(\delta\psi_j(x))$. Hence, with the addition of the three gauge fields, the Lagrangian density in Equation 1.18 is invariant under local SU(2) gauge transformations.

In the interaction term, which couples the Dirac fields to the gauge fields via the covariant derivative, the $W_\mu^1(x)$ and $W_\mu^2(x)$ fields mix the isodoublet Dirac fields whereas the $W_\mu^3(x)$ field does not. This is similar to what is observed for the Weak force; the W^+ and W^- couple lepton and neutrino states while the Z does not.

Again kinetic and mass terms for the gauge fields need to be added to the Lagrangian density. In the case of the non-Abelian gauge transformations a field strength of the form in Equation 1.7 is no longer gauge invariant due to the first term in Equation 1.16. A field strength tensor, $G_{\mu\nu}^a$, can be defined, as in Equation 1.19, such that the combination $-\frac{1}{4}G_{\mu\nu}^a G^{a,\mu\nu}$ is invariant under the gauge transformations.

$$G_{\mu\nu}^a = \partial_\mu W_\nu^a(x) - \partial_\nu W_\mu^a(x) - g\epsilon_{abc} W_\mu^b(x) W_\nu^c(x) \tag{1.19}$$

Again a mass term cannot be added in a gauge invariant way. The Lagrangian density invariant under SU(2) local gauge transformations is given in Equation 1.20.

$$\mathcal{L} = -\frac{1}{4}G_{\mu\nu}^a G^{a,\mu\nu} + \overline{\psi}^i(x)(i\not{D} - m\mathbf{I})_i^j\psi_j(x) \tag{1.20}$$

There are significant differences with respect to the U(1) case. There are three fields with kinetic terms and hence three distinct gauge bosons after second quantisation. Also the gauge boson kinetic term in Equation 1.20 now contains self-interaction terms which correspond to 3 and 4 point interactions. Again this is what is observed for the Weak sector in which, for example, the W^+, W^- and Z can couple.

Particle Type	Fields	T	T_3	Y
Leptons	$l_L = \begin{pmatrix} \nu_L^e \\ e_L^- \end{pmatrix}$	1/2 1/2	1/2 −1/2	−1 −1
	e_R	0	0	-2
Quarks	$q_L = \begin{pmatrix} u_L \\ d_L \end{pmatrix}$	1/2 1/2	1/2 −1/2	1/3 1/3
	u_R d_R	0 0	0 0	4/3 -2/3

Table 1.1: Charges and fields for the first generation of fermions in the Standard Model

1.2 Electroweak Theory

The Standard Model neatly groups the experimentally observed elementary particles of the Universe [1]. The electroweak sector describes the interactions of the photon and the W and Z bosons with quarks and leptons in a unified model [2]. Electroweak unification was developed before the existence of the W and Z bosons, or indeed the presence of an additional neutral current besides the photon, had been established. It aimed to explain the Fermi point interactions for processes such as $\beta-$decay in the framework of field theory.

With hindsight the $SU(2) \times U(1)$ structure seems natural for the unification of the Weak and the Electromagnetic force, as QED (a U(1) theory) already describes the Electromagnetic force to a high degree of accuracy and the invariance of the Lagrangian under SU(2) gauge transformations gives rise to 3 gauge fields of which one is neutral. The electroweak $SU(2)_I \times U(1)_Y$ group structure however does not directly describe the physical photon and vector boson fields; some manipulation is needed to recover the physical fields. In fact the $U(1)_Y$ field charge is not the electric charge, q, but the hypercharge Y. The SU(2) weak-isospin generators are those in Equation 1.11 and the fermion fields have a total weak-isospin T and a third component of weak-isospin T^3, which corresponds to the eigenvalue of the third weak-isospin generator. The gauge bosons are thus $B_\mu(x)$ (equivalent to $A_\mu(x)$ in Section 1.1.1) and the three vector bosons $W_\mu^a(x)$.

The particle properties, using as an example the first generation of fermions, are given in Table 1.1. The structure is dictated by the observation of parity violation in the Weak sector, hence the presence of left-handed weak-isospin doublet fields and singlet right-handed fields. As one can note, there is no right handed neutrino. Extensions to the Standard Model in which neutrinos have a mass, as recent observations indicate [4] [5] [6], can add a sterile right handed neutrino singlet field with weak-isospin and hypercharge both zero.

The unified electroweak Lagrangian can be obtained by adding the kinetic terms for the $U(1)$ gauge boson given in Equation 1.8 to the Lagrangian density given in Equation 1.20. The covariant derivative is modified to a combination of the ones defined in Sections 1.1.1 and 1.1.2 i.e.

$$D_\mu \equiv \partial_\mu \mathbf{I} + ig\mathbf{T}^a W_\mu^a(x) + ig'\frac{\mathbf{Y}}{2}B_\mu(x), \tag{1.21}$$

where $\mathbf{Y}$ is the hypercharge eigenvalue Y times the identity matrix. The full covariant derivative only acts on the left handed weak-isospin doublet as the singlet fields have 0 weak-isospin. Similarly their gauge transformation properties are different: the doublets transform under both SU(2) and U(1) gauge transformations, the singlet fields only under U(1). The transformations are equivalent to those described in the previous sections except for the different coupling (g') and generator ($\mathbf{Y}$) for the U(1) transformation, i.e for the left handed lepton field:

$$l_L \rightarrow l'_L = \exp i(g\mathbf{T}^a\omega^a(x) + ig'\frac{\mathbf{Y}}{2}\lambda(x))l_L. \tag{1.22}$$

In order to identify the physical gauge fields one needs to perform a rotation of the fields. The following definitions can be used:

$$\begin{aligned} \mathbf{T}^\pm &= \frac{1}{\sqrt{2}}(\mathbf{T}^1 \mp i\mathbf{T}^2) \\ \Rightarrow W_\mu^\pm(x) &= \frac{1}{\sqrt{2}}(W_\mu^1(x) \pm iW_\mu^2(x)). \end{aligned} \tag{1.23}$$

and

$$\begin{pmatrix} B_\mu(x) \\ W_\mu^3(x) \end{pmatrix} = \begin{pmatrix} \cos\theta_w & -\sin\theta_w \\ \sin\theta_w & \cos\theta_w \end{pmatrix} \begin{pmatrix} A_\mu(x) \\ Z_\mu(x) \end{pmatrix} \tag{1.24}$$

where θ_w is the Weinberg angle. Substituting these definitions changes the covariant derivative to:

$$\begin{aligned} D_\mu \equiv \partial_\mu &+ ig(\mathbf{T}^+ W_\mu^+(x) + \mathbf{T}^- W_\mu^-(x)) \\ &+ i(g\mathbf{T}^3\sin\theta_w + g'\frac{\mathbf{Y}}{2}\cos\theta_w)A_\mu(x) \\ &+ i(g\mathbf{T}^3\cos\theta_w - g'\frac{\mathbf{Y}}{2}\sin\theta_w)Z_\mu(x) \end{aligned} \tag{1.25}$$

Substituting Equation 1.25 into the electroweak Lagrangian density the interaction terms for the lepton field are of the form:

$$\begin{aligned}\mathcal{L}_{int} =& \bar{l}_L\gamma^\mu(g\mathbf{T}^+W_\mu^+(x) + \mathbf{T}^-W_\mu^-(x))l_L \\ &+\bar{l}_L\gamma^\mu(g\mathbf{T}^3\sin\theta_w + g'\frac{\mathbf{Y}}{2}\cos\theta_w)A_\mu(x)l_L + \overline{e}_R\gamma^\mu(g'\frac{\mathbf{Y}}{2}\cos\theta_w)A_\mu(x)e_R \\ &+\bar{l}_L\gamma^\mu(g\mathbf{T}^3\cos\theta_w - g'\frac{\mathbf{Y}}{2}\sin\theta_w)Z_\mu(x)l_L - \overline{e}_R\gamma^\mu(g'\frac{\mathbf{Y}}{2}\sin\theta_w)Z_\mu(x)e_R\end{aligned} \tag{1.26}$$

Equation 1.26 involves three distinct, physical, interactions. The first violates parity maximally and couples electrons to neutrinos (via the $\mathbf{T}^\pm$ generators). This can clearly be identified with the charged weak interactions. The second term can be identified with the QED interactions between the photon and charged particles if

$$g\sin\theta_w = g'\cos\theta_w = e \tag{1.27}$$

and if the generator of the $U(1)_{em}$ electromagnetic charge, Q is

$$\mathbf{Q} = \mathbf{T}^3 + \frac{\mathbf{Y}}{2}. \tag{1.28}$$

By substituting the appropriate eigenvalues T^3 and Y from Table 1.1 into this term, it is apparent that $A_\mu(x)$ couples only to electrons, not to neutrinos. Furthermore the strength of the interaction is the same for left handed and right handed electron fields i.e. the $A_\mu(x)$ interaction does not violate parity. The last term, using the relations in Equations 1.27 and 1.28, describes the V-A structure needed for the weak neutral current which couples to electrons and neutrinos. Hence using the field transformations in Equations 1.2 and 1.24 the physical gauge fields can be clearly identified.

There is one major problem with the structure of the theory as developed so far and that is the absence of mass terms. As seen previously mass terms for the gauge bosons are not gauge invariant. This is problematic as the Weak interactions, due to their short range, have to be mediated by massive vector bosons which has been verified experimentally. Furthermore as the mass terms for fermions are of the form:

$$M\overline{\Psi}\Psi = M(\overline{\Psi}_L\Psi_R + \overline{\Psi}_R\Psi_L) \tag{1.29}$$

they are no longer gauge invariant due to the different gauge transformations of the left and right handed fields.

Experimentally the electroweak couplings and interactions have been measured to a high degree of accuracy and are all consistent with those described by the electroweak Lagrangian. However fermion and gauge bosons are known to have a

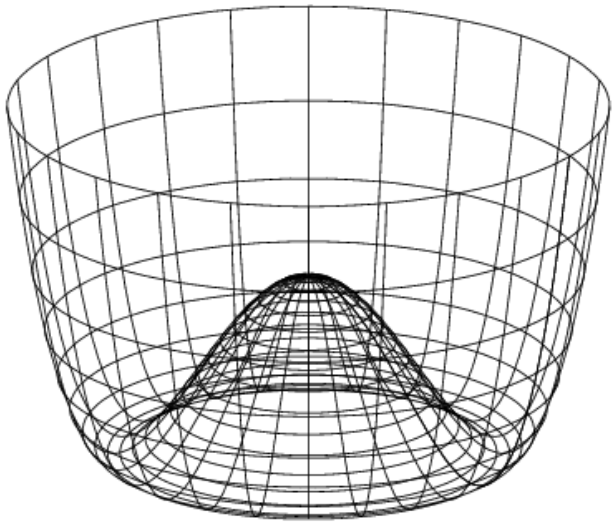

Figure 1.1: Higgs potential, $V(\Phi(x))$ for the case in which $\mu^2 < 0$ [13]

mass. Theoretically a mechanism exists which enables mass terms to be introduced in a gauge invariant way [7]-[10]. This mechanism was originally incorporated into the Standard Model in order to break the $SU(2)_I \times U(1)_Y$ symmetry [11].

1.2.1 The Higgs Mechanism

To illustrate the principle of the Higgs mechanism consider the Lagrangian density for a complex scalar field obeying a U(1) local gauge symmetry. The Lagrangian density can be written in an analogous way to that in Section 1.1.1:

$$\mathcal{L}_{scalar} = (D_\mu \Phi(x))(D^\mu \Phi(x))^* - V(\Phi) - \frac{1}{4} F^{\mu\nu} F_{\mu\nu}. \tag{1.30}$$

The V(Φ) potential term has to be of the form $\Phi(x)\Phi^*(x)$ to some power in order to preserve gauge invariance. The first possible form of interest is:

$$V(\Phi) = \mu^2(\Phi(x)\Phi^*(x)) + \lambda(\Phi(x)\Phi^*(x))^2 \tag{1.31}$$

For $\mu^2 > 0$ the potential minimum is at $\Phi(x) = 0$ or more precisely the vacuum expectation value of the field $\Phi(x)$ is 0. For $\mu^2 < 0$ the potential acquires a local maximum at $\Phi(x) = 0$. The global minimum is now at $\Phi = \nu/\sqrt{2}$ where ν is the vacuum expectation value $\sqrt{\mu^2/\lambda}$. This potential is shown in Fig. 1.1 [13], the minimum can take on an infinite number of values along an annulus of radius ν i.e. the vacuum is degenerate. There is freedom to choose a particular value to represent the physical vacuum; one choice is so that the physical vacuum is aligned along the real axis of the field $\Phi(x)$. By making such a choice $U(1)$ is said to be "spontaneously

broken"; the Lagrangian is still invariant however the physical vacuum is not. This is the essence of the Higgs mechanism.

The field $\Phi(x)$ can be expressed by expanding around the physical vacuum:

$$\Phi(x) = \frac{1}{\sqrt{2}}(\nu + \chi_1(x) + i\chi_2(x)), \tag{1.32}$$

however, one can make a $U(1)$ gauge transformation in order to remove the $\chi_2(x)$ field so that $\Phi(x)$ is always real. This choice is known as the Unitary gauge and translates to:

$$\Phi(x) = \frac{1}{\sqrt{2}}(\nu + \chi(x)). \tag{1.33}$$

Substituting $\Phi(x)$ into the Lagrangian density and using $-\mu^2 = \nu^2\lambda$ the following terms are obtained:

$$V(\Phi) = \lambda\nu^2\chi^2(x) + \lambda\chi^3(x)\nu + \frac{\lambda\chi^4(x)}{4} + const. \tag{1.34}$$

$$\begin{aligned}(D_\mu\Phi(x))(D^\mu\Phi(x))^* = \frac{1}{2}(\partial_\mu\chi(x))(\partial^\mu\chi(x)) + \frac{g^2\nu^2}{2}A_\mu(x)A^\mu(x) \\ + g^2\nu A_\mu(x)A^\mu(x)\chi(x) + \frac{g^2}{2}A_\mu(x)A^\mu(x)\chi^2(x).\end{aligned} \tag{1.35}$$

The Lagrangian now describes a massive scalar field, $\chi(x)$, interaction terms between the fields $\chi(x)$ and $A_\mu(x)$, self interaction terms for $\chi(x)$ and most notably, as there is now a quadratic term in $A_\mu(x)$, a massive gauge field. Via the Higgs mechanism, the gauge field has acquired a mass $\propto gv$ in a gauge invariant manner.

1.2.2 Electroweak Symmetry Breaking

In an analogous way the same mechanism can be applied to generate mass terms for the vector gauge bosons in the electroweak Lagrangian. In this case a complex scalar doublet is needed to which is assigned a hypercharge 1 and weak-isospin 1/2:

$$\mathbf{\Phi}(x) = \begin{pmatrix}\Phi^+(x) \\ \Phi^\circ(x)\end{pmatrix} \tag{1.36}$$

The new scalar doublet interactions in the Lagrangian are the following:

$$\mathcal{L}_{scalar} = (D_\mu\mathbf{\Phi}(x))(D^\mu\mathbf{\Phi}(x))^\dagger - \mu^2\mathbf{\Phi}^\dagger(x)\mathbf{\Phi}(x) - \lambda(\mathbf{\Phi}^\dagger(x)\mathbf{\Phi}(x))^2, \tag{1.37}$$

where all terms are invariant under gauge transformations. Again there is a choice of physical vacuum: in this case the choice is made that the physical vacuum be in the $T^3 = -\frac{1}{2}$ direction and real:

$$\mathbf{\Phi}_{vac} = \begin{pmatrix} 0 \\ \frac{\nu}{\sqrt{2}} \end{pmatrix} \tag{1.38}$$

Again expanding around the vacuum expectation value and working in the unitary gauge:

$$\mathbf{\Phi}(x) = \frac{1}{\sqrt{2}} \begin{pmatrix} 0 \\ \nu + h(x) \end{pmatrix}, \tag{1.39}$$

where $h(x)$ is the Higgs field. The action of the covariant derivative, defined in Equation 1.21, on the field $\mathbf{\Phi}(x)$, defined as above, gives rise to the following terms:

$$\begin{aligned} D_\mu \mathbf{\Phi}(x) = \frac{1}{\sqrt{2}} (\partial_\mu \mathbf{I} + ig(\mathbf{T}^+ W_\mu^+(x) + \mathbf{T}^- W_\mu^-(x) \\ + \mathbf{T}^3 W_\mu^3(x)) + ig' \frac{\mathbf{Y}}{2} B_\mu(x)) \begin{pmatrix} 0 \\ \nu + h(x) \end{pmatrix} \end{aligned} \tag{1.40}$$

Thus,

$$\begin{aligned} |D_\mu \mathbf{\Phi}(x)|^2 = \frac{1}{2} \partial^\mu h(x) \partial_\mu h(x) + \frac{g^2}{4} (v + h(x))^2 W^{+,\mu}(x) W_\mu^-(x) \\ + \frac{1}{8} (v + h(x))^2 (g' B_\mu(x) - g W_\mu^3(x))^2. \end{aligned} \tag{1.41}$$

The first term is just the kinetic term for the Higgs field, whereas the second contains three and four point interactions of the W with the Higgs and a mass term for the W boson:

$$\begin{aligned} M_W^2 W^{\mu +}(x) W_\mu^-(x) = \frac{(gv)^2}{4} W^{+,\mu}(x) W_\mu^-(x) \\ \Rightarrow M_W = \frac{gv}{2} \end{aligned} \tag{1.42}$$

The last term in Equation 1.41 can be better interpreted as follows:

$$(g W_\mu^3(x) - g' B_\mu(x))^2 \equiv (g^2 + g'^2)(\cos\theta_w W_\mu^3(x) - \sin\theta_w B_\mu(x))^2, \tag{1.43}$$

where $g'/g = \tan\theta_w$. This is the same rotation of the $W_\mu^3(x)$ and $B_\mu(x)$ gauge fields needed in order to relate them to the physical Z boson field for the weak neutral current. Hence this is simply a mass term for the Z boson:

$$\frac{1}{2}M_Z^2 Z^\mu(x)Z_\mu(x) = \frac{(gv)^2}{8\cos\theta_w}Z^\mu(x)Z_\mu(x) \qquad (1.44)$$
$$\Rightarrow M_Z = \frac{gv}{2\cos\theta_w}$$

For both the Z and the W the coupling to the Higgs is proportional to the mass squared. The mass term for the Higgs field is as in Equation 1.34 i.e. $M_{Higgs} = \sqrt{2\lambda}\nu$. There is no mass term for the photon, as observed. However there are still no mass terms for the fermions. This is remedied by introducing Yukawa terms of the form (suppressing the space-time dependence of the lepton fields):

$$\mathcal{L}_{Yukawa} = -G_e \bar{l}_L \mathbf{\Phi}(x) e_R + h.c. \qquad (1.45)$$

for the leptons, where $\mathbf{\Phi}(x)$ can be decomposed as before in order to obtain the value for the mass. This term has zero hypercharge and therefore is invariant under $U(1)_Y$. The different transformation of e_R and l_L under the $SU(2)_I$ gauge transformations is now compensated for by $\mathbf{\Phi}(x)$ which transforms with an opposite sign to $\bar{l}_L$ (e_R has zero isospin and therefore does not transform under $SU(2)_I$). Hence the Yukawa term is gauge invariant. A slightly more complicated form is needed to generate a mass for both the "up" and "down" type quarks:

$$\mathcal{L}_{Yukawa} = -G_d\ \overline{q}_L^i \mathbf{\Phi}(x)_i d_R - G_u\ \epsilon_{ij}\overline{q}_L^i \mathbf{\Phi}(x)^{\dagger,j} u_R + h.c., \qquad (1.46)$$

where ϵ_{ij} is the two-dimensional anti-symmetric tensor. For fermions the coupling is only proportional to the mass of the fermion and not to its square.

When considering three generations it is possible to have mass mixing terms between different generations. One can re-write the mass term for, for example, the down type quarks in Equation 1.46 in the form:

$$-(M_d)_{ij}\overline{d}_L^i d_R^j \equiv -(M_d)_{ij}\overline{d'}_L^m (\mathbf{V}_d^*)_m^i (\mathbf{V}_d)_k^j d_R'^k = -(M_d)_{ii}\overline{d}_L'^i d_R'^i. \qquad (1.47)$$

where $\mathbf{V}_d$ is a 3×3 unitary matrix and the indices run over the three generations. The effect of $\mathbf{V_d}$ is to transform the down type quark weak eigenstates to a basis (denoted by the prime) where the mass terms are diagonal and therefore represent the physical quarks. There is an equivalent matrix for the up type quarks. The consequence of this rotation is apparent once we substitute the physical (or mass) eigenstates into the interaction terms in Equation 1.26, which are diagonal in the weak eigenbasis. As $\mathbf{V}_{d,u}$ are unitary the change of eigenstates has no effect on the neutral current, indeed there are no flavour changing neutral currents. This is

not the case for the charged current as $\mathbf{V}_u^\dagger \mathbf{V}_d \neq \mathbf{I}$. Hence there is mixing between generations for charged current interactions. A unitary 3×3 complex matrix has nine independent parameters and there are five relative phases between the quarks. Therefore there are four free independent parameters, of which one can be complex. Hence there is the possibility of CP violation, which has been experimentally established.

As seen, the addition of the complex scalar doublet, which spontaneously breaks the gauge symmetry, allows for mass terms which preserve the symmetry of the electroweak Lagrangian. It also explains the origin of CP violation. However it adds an extra scalar particle, the Higgs, which has not been detected experimentally and which needs to be discovered before the topic of electroweak unification can be closed.

1.3 Current Limits on the Higgs Mass

The only free parameter in the Higgs sector is the mass of the Higgs. All other parameters, the width, branching ratios, production cross-section, etc. can be determined from the mass of the Higgs. Although the Higgs mass is unknown, and more significantly its actual existence is conjectural, there are various constraints on its possible mass from theory, indirect measurements and direct searches.

1.3.1 Limits from Theory

Theory places a upper bound on the Higgs mass of 1 TeV/c^2 from unitarity requirements in W_L scattering. This is a hard limit and applies not only to the Standard Model but to all extensions which involve a Higgs or a Higgs-like particle. Much more stringent limits are derived when considering the value of λ, the quartic coupling of the Higgs field in Equation 1.31, as a function of the energy scale, Λ, at which new physics appears. The running of the self-interaction coupling as a function of Λ is shown in Fig 1.2 [14] and the limits are shown in Fig. 1.3 [15]. The upper limit is set by the requirement that $\lambda(\Lambda) < \infty$, as Higgs boson loops modify the coupling this requirement can be translated to a constraint on the Higgs mass. The lower limit is set by requiring vacuum stability. If λ is too small the effect of top quark loops to the self-interaction of the Higgs field can be such that λ is driven to negative values and the Higgs potential loses its minimum. It is interesting to note that Fig. 1.3 does not rule out the possibility that the Standard Model is valid up to the Planck scale. If that were the case the Higgs mass would have to be between 130 GeV/c^2 and 190 GeV/c^2.

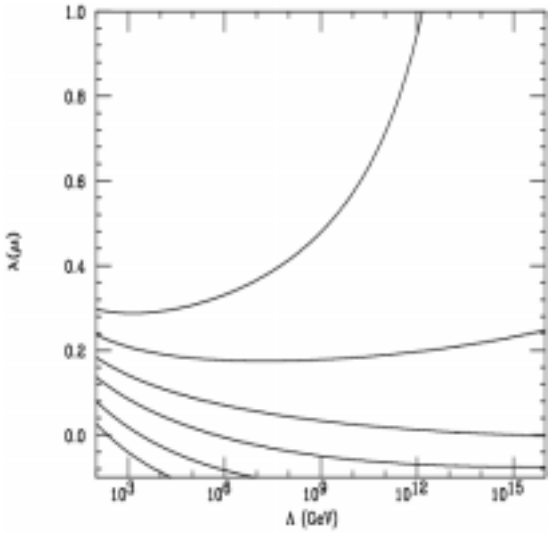

Figure 1.2: Scaling of the self-coupling of the Higgs field, λ, with the energy scale Λ [14]

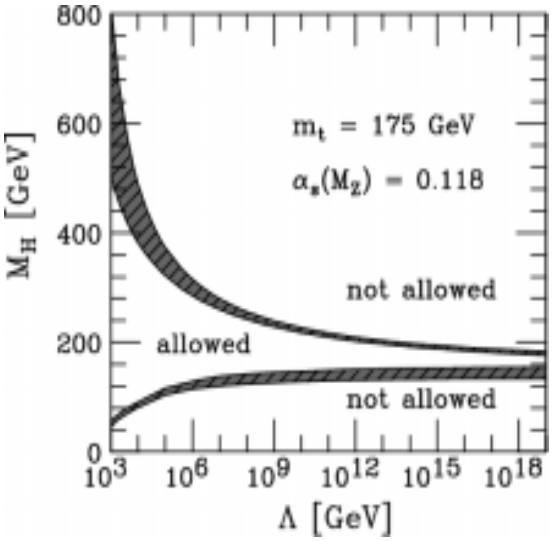

Figure 1.3: Theoretical bounds on the Higgs mass as a function of the energy scale Λ [15]

1.3.2 Indirect Experimental Limits

The existence of the Higgs has an impact on the value of most electroweak parameters via higher order loop corrections. Indeed the theory is only renormalisable in the presence of the Higgs. One way to place a limit on the Higgs mass is to measure the effect of loop corrections to e.g. the W mass which is logarithmic in the Higgs boson mass. The W mass also has a noticeable correction due to top quark loops which is quadratic in the mass of the top quark. Hence, by accurate measurements of the masses of the top quark and W, one can infer the Higgs mass, if it exists. Other electroweak parameters have a similar dependence on the Higgs and top quark mass and can be combined to perform an overall fit for the Higgs mass.

The results are shown in Fig. 1.4 [16]. The contours correspond to the measured mass values at a 68% confidence level. It is significant to note that the different measurements seem compatible with each other and that they point to a light Higgs. The electroweak fits place an upper limit on the Higgs mass of 193 GeV/c^2 at 95% confidence level.

1.3.3 Direct Searches

The most stringent limit on the Standard Model Higgs mass comes from the direct searches at LEP. The CDF collaboration at the Tevatron also performed a direct search for the Higgs during Run I. The limits derived from this search are much weaker than those from LEP but are included for completeness.

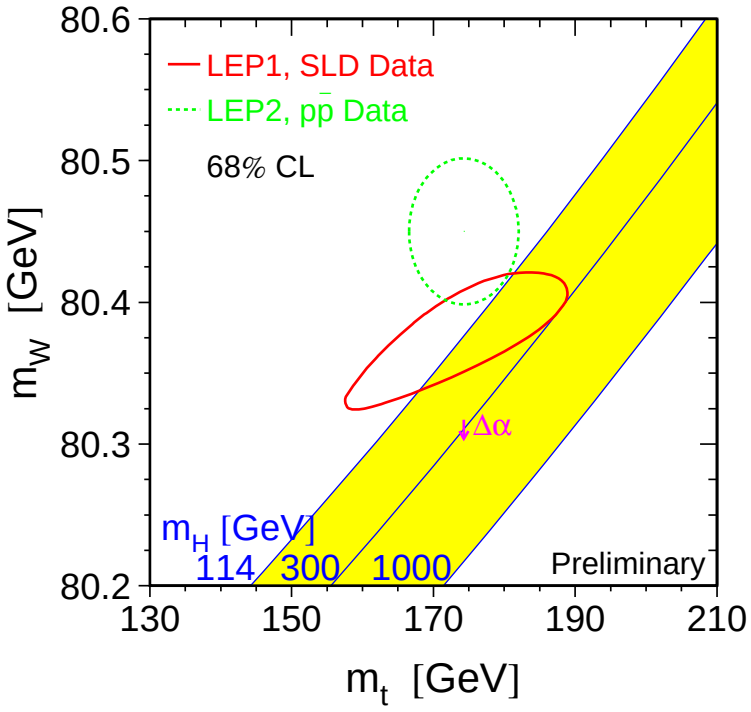

Figure 1.4: Limit on the Higgs boson mass from electroweak measurements [16]

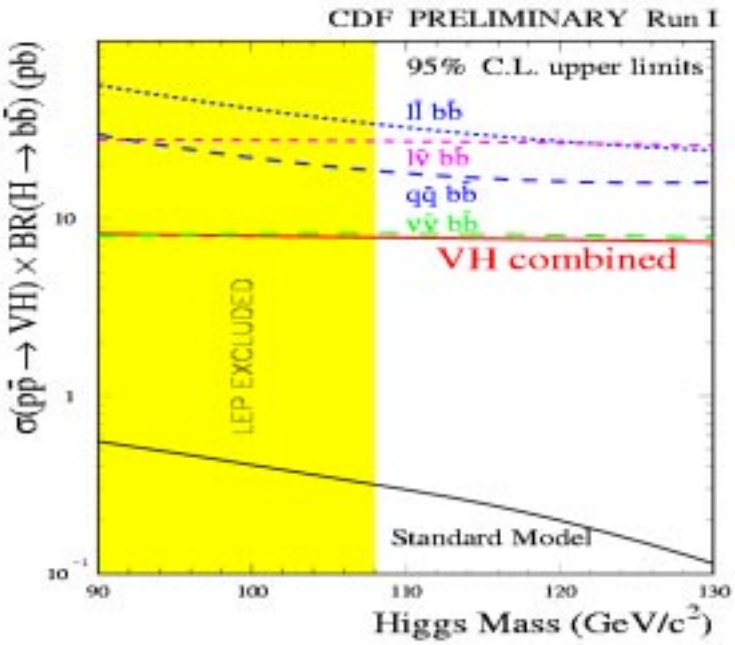

Figure 1.5: CDF limits for Standard Model Higgs production cross-sections from Run I data [17]

Searches at the Tevatron During Run I

Searches for the Higgs were performed by the CDF collaboration at the Tevatron during Run I [17]. The data sample was ~ 110 pb^{-1} at a centre of mass energy of 1.8 TeV. The channels considered were $p\overline{p} \rightarrow HV \rightarrow b\overline{b} + X$, where V was either Z or W and X includes the majority of the possible Z and W boson decays. The results were expressed as 95% exclusion curves for the HV cross-sections in the various decay channels. The results are shown in Fig 1.5 and are an order of magnitude above the Standard Model predictions.

Searches at LEP

The LEP experiments performed a direct search for the Higgs boson using 2461 pb^{-1} of data at centre of mass energies between 189 and 209 GeV [18]. At LEP the main production process was $e^+e^- \rightarrow HZ$, with $H \rightarrow b\overline{b}$ and all possible decays of the Z. Also the τ decays of the Higgs with the Z decaying to quarks was used. The data from the four experiments were subjected to a likelihood test based on the background-only or background + signal hypothesis. The following likelihood ratio was used to rank the data between the background-only and the signal+background hypotheses:

$$Q(m_H) = \mathcal{L}_{s+b}/\mathcal{L}_b = \frac{e^{-(s(m_H)+b)}}{e^{-b}} \prod_{j=1}^{N_{obs}} \frac{xs(m_H)S(m_H,[m_j^{rec},\mathcal{G}]) + bB([m_j^{rec},\mathcal{G}])}{bB([m_j^{rec},\mathcal{G}])} \tag{1.48}$$

where N_{obs}, $s(m_H)$ and b are number of observed total, signal and background events. $S(m_H, m_J^{rec})$ and $B(m_j^{rec})$ are the expected distributions for signal and background for a reconstructed mass m_j^{rec} and for the set of discriminating variables $\mathcal{G}$. The likelihood ratio was then combined for all channels, all experiments and all sets of energies to give a final value. The curve for $-2ln(Q(m_H))$ is shown in Fig. 1.6. The solid line shows the observed curve, the dashed that expected in the background-only hypothesis and the dash-dotted line that expected in the background + signal case. The observed distribution has a broad minimum at a mass of ~ 116 GeV/c^2, showing that the data favour the signal + background hypothesis over the background only hypothesis. The expectation for the signal + background hypothesis crosses the observed curve close to this minimum value which indicates that this is the favoured mass value.

The expected distributions of $-2ln(Q(m_H))$ for background-only and signal + background can be normalised into Probability Density Functions (PDF). From the

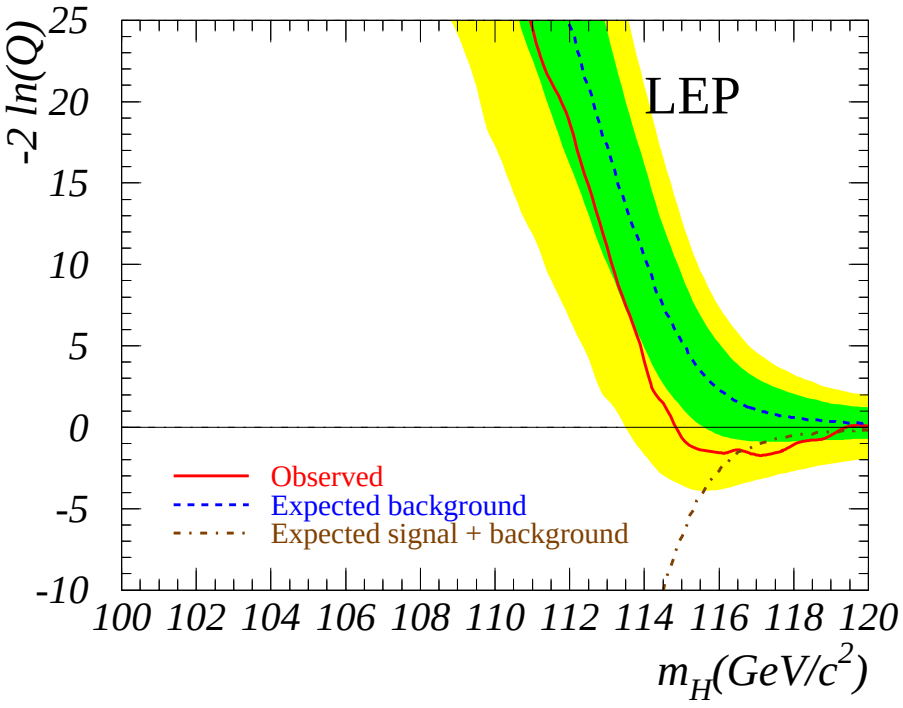

Figure 1.6: Observed and expected behaviour of $-2ln(Q(m_H))$ as a function of the test-mass m_H. Bands correspond to the 68% and 95% probability bands compatible with a background-only hypothesis [18]

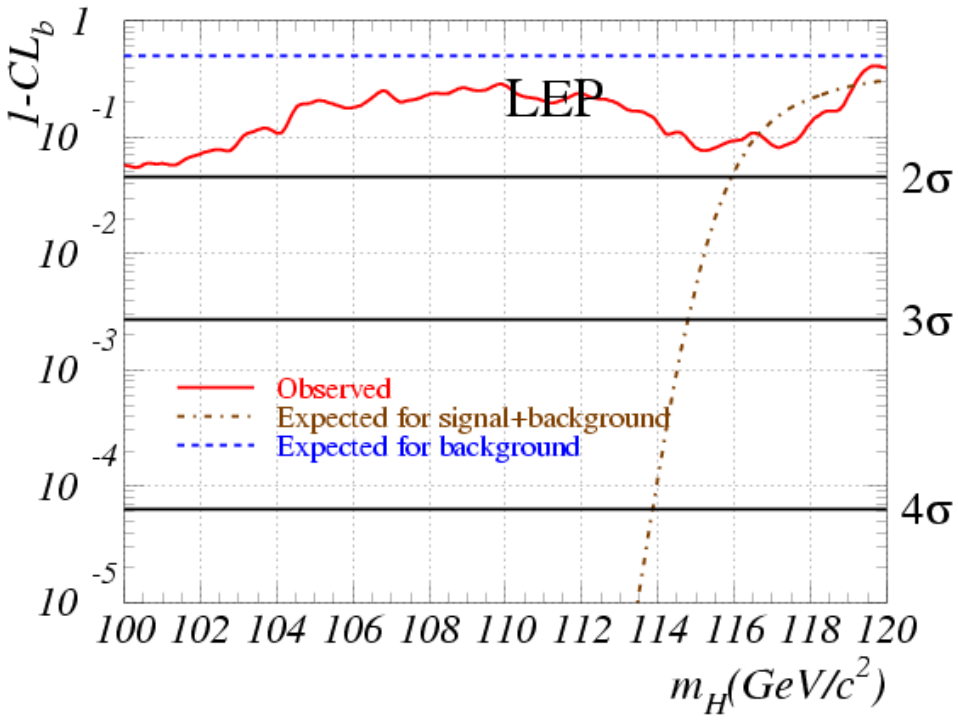

Figure 1.7: Confidence level of background-only incompatibility $1 - CL_b$ as a function of test mass m_H. CL_b is the confidence level for the background-only hypothesis [18]

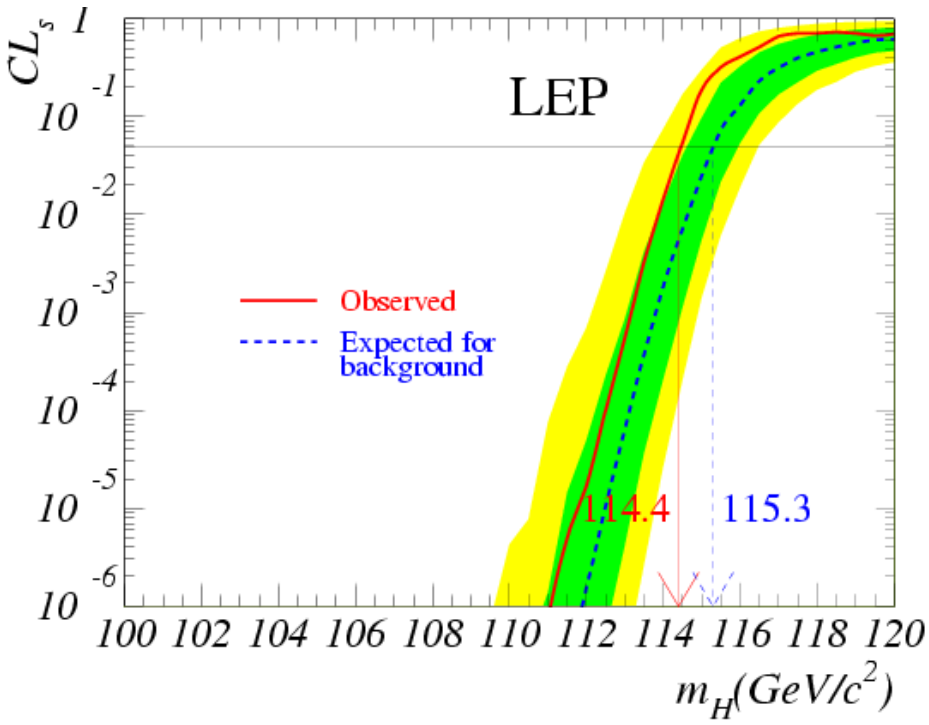

Figure 1.8: Confidence level of the signal + background hypothesis CL_s as a function of test mass m_H. Bands correspond to the 68% and 95% probability bands compatible with the signal + background hypothesis. The horizontal line corresponds to $CL_s = 0.05$ [18]

PDF and the observed value of $-2ln(Q(m_H))$ a confidence level can be calculated for the background-only (CL_b) and the signal+background hypothesis (CL_{s+b}). The distribution for $1 - CL_b$ as a function of the test mass m_H is shown in Fig. 1.7. A true hypothesis is expected to have a confidence level of 0.5. Thus for an excess of events with respect to the background-only hypothesis at a given mass, CL_b will be greater than 0.5 and $1 - CL_b$ will show a dip at that mass value. A general excess of events is visible throughout the mass range in Fig. 1.7, there is also a more pronounced dip close to the mass value favoured by Fig. 1.6. The significance of the excess is given on right-hand scale. For a Higgs test mass of ~ 116 GeV/c^2 this translates to a deviation of 1.7σ from the background-only hypothesis. Conversely one can plot the confidence level for CL_s, defined as CL_{s+b}/CL_b; this is shown in Fig. 1.8. The observed value intersects $CL_s = 0.05$ at a test mass 114.4 GeV/c^2 , this corresponds to the lower bound at 95% confidence level on the mass of the Standard Model Higgs. The excess seen in Fig. 1.7, combined with the electroweak fits, gives reason to believe that the Higgs is light and could have a mass under 130 GeV/c^2.

Chapter 2

The DØ Detector and the Tevatron Upgrades

Run I at the Tevatron (1992-1996) produced many results worthy of note, most significantly the discovery of the top quark [19][20][21]. Although Run I was a real success its physics capability was limited by the statistics available due to the limited integrated luminosity and the low production cross-sections of some of the processes under study. The Run II physics programme is more ambitious than that of Run I and includes precise measurements of the properties of the top quark and W boson, in addition to B physics and QCD studies, measurements of CP violation, Higgs searches and searches for physics beyond the Standard Model. In order to meet the Run II physics goals substantial modifications and upgrades to the Fermilab accelerator and to the DØ detector were necessary [22][23]. The changes to the accelerator were motivated by the desire to increase the centre of mass energy and to increase the data sample. These changes made significant upgrades to the DØ detector necessary. The DØ detector was also upgraded in order to improve its physics capability.

Run II has been subdivided into two parts: Run IIa and Run IIb. Run IIa is defined to last until the first $\sim$2 - 4 fb^{-1} of integrated luminosity have been delivered by the Tevatron. At this point various detector components will need replacing due to radiation damage. Run IIb is defined to start once this subsequent detector upgrade has taken place.

2.1 The Fermilab Accelerator Upgrade

A schematic of the Fermilab accelerator is shown in Fig. 2.1.

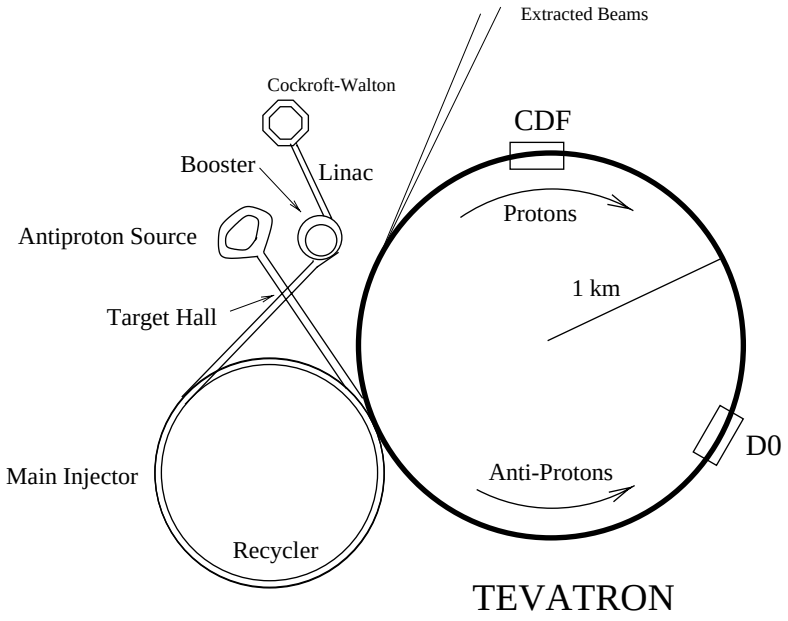

Figure 2.1: Fermilab Run II accelerator complex

2.1.1 Proton and Antiproton Production

Protons are obtained by stripping the electrons from gaseous hydrogen ions. This is done by accelerating the ions to 750 keV by a Cockcroft-Walton accelerator and subsequently to 400 MeV via the Linac. The ions are then focused onto a thin graphite sheet where they are stripped of their electrons. The protons are then accelerated to 8 GeV by the Booster (a small synchrotron accelerator) and collected into bunches before their insertion into the Main Injector.

The Main Injector is a 3 km synchrotron which pre-accelerates protons and antiprotons to an energy of 150 GeV before injecting them into the Tevatron. Protons from the Main Injector are also extracted to produce the antiprotons. Antiprotons are obtained by dumping a 120 GeV proton bunch onto a nickel target. A lithium lens is used to collect antiprotons produced with an energy close to 8 GeV. The antiprotons are produced in bunches because the protons are extracted in bunches. In order to cool the antiprotons they are transformed into a continuous beam in the Debuncher Ring, stochastically cooled and then fed into the Accumulator Ring. Here they are further cooled and stored.

When enough antiprotons have accumulated they are cooled into a bunch and passed into the Recycler Ring. The Recycler Ring is a fixed energy ring located in the same tunnel as the Main Injector. It acts as an extra storage ring for antiprotons originating from the Accumulator Ring and for the remaining antiprotons left at the end of stores from the Tevatron and the Main Injector. The antiprotons from the

Recycler Ring are then injected into the Main Injector in order to accelerate them up to 150 GeV.

2.1.2 The Tevatron

The Tevatron is a 6 km circular $p - \overline{p}$ collider with the two beams travelling in opposite directions within the same beam pipe. The beams are accelerated to their final energy before they are crossed and collided. The Tevatron operating parameters are given in Table 2.1.

	Run I	Run IIa	Run IIb
Energy p,$\overline{p}$ (GeV)	900	980	980
Proton bunches	6	36	140
Antiproton bunches	6	36	103
Protons/ bunch	2.3×10^{11}	2.7×10^{11}	2.7×10^{11}
Antiprotons/ bunch	5.5×10^{10}	3.0×10^{10}	0.94×10^{10}
Bunch Spacing (ns)	3500	396	132
Peak Luminosity ($cm^{-2}s^{-1}$)	0.16×10^{32}	0.86×10^{32}	5.2×10^{32}
Luminosity (pb^{-1}/week)	3.2	17.3	105
Interactions per Crossing	2.5	2.3	4.8
Crossing Angle (μrad)	-	-	280 - 354

Table 2.1: Tevatron operating parameters for Run I and Run II

The switch from 396 ns to 132 ns bunch spacing has recently been at the centre of discussions at Fermilab [25]. The original plan was to switch to 132 ns as a default in order to reduce the number of interactions per crossing at a given instantaneous luminosity. From recent discussions the new baseline solution is to remain at 396 ns spacing and adopt luminosity levelling to half the peak luminosity while keeping $\sim$85% of the total store luminosity. The principle of luminosity levelling is to dynamically modify the focusing at the interaction point. This maintains the luminosity profile flat and fixed to a peak luminosity for a considerable period of time before falling once the maximum focusing is reached. Luminosity levelling effectively would reduce the number of interactions per crossing compared to running at 396 ns as is, without having to face the problems associated with the smaller bunch spacing. The Tevatron parameters corresponding to this solution are the same for Run IIa (36×36) with a peak luminosity of 4×10^{32} $cm^{-2}s^{-1}$ before luminosity levelling. As luminosity levelling has never been tested at the Tevatron the option for the Tevatron to move to 132 ns will also be kept.

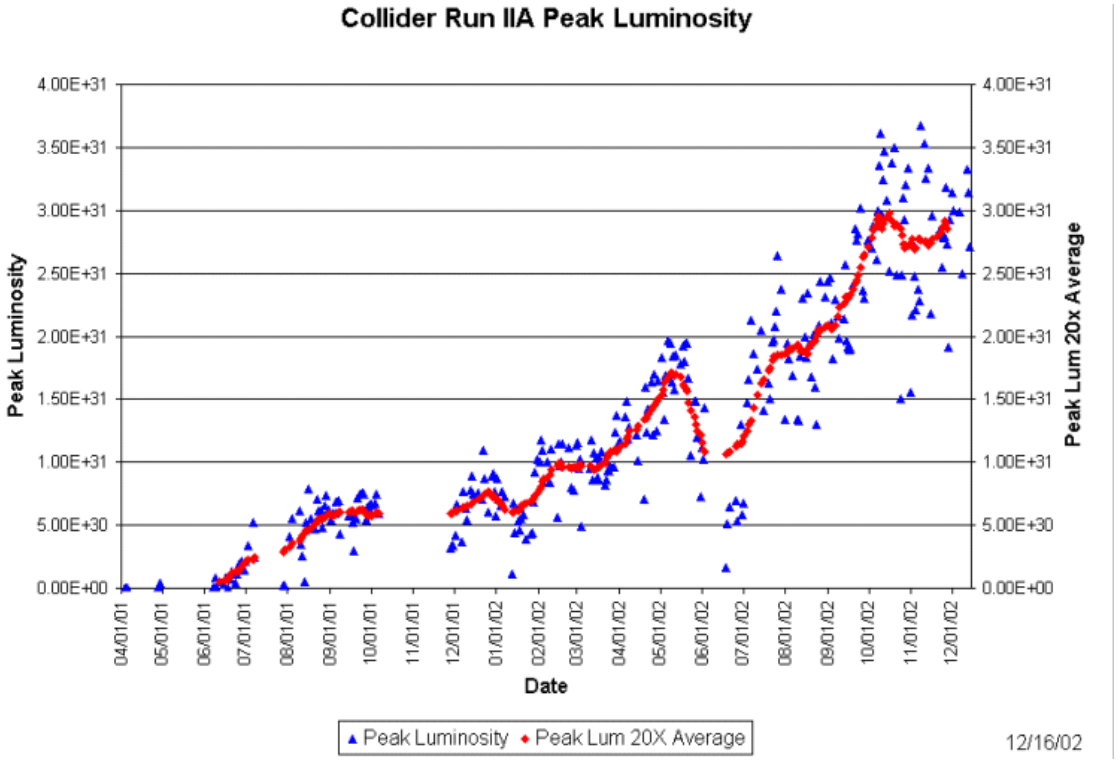

Figure 2.2: Tevatron peak luminosity

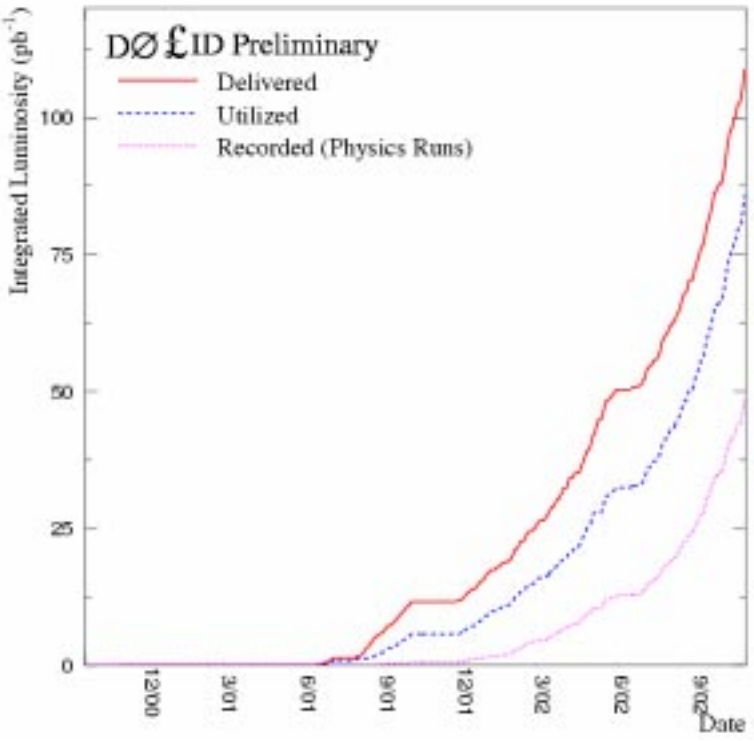

Figure 2.3: Integrated luminosity at DØ

2.1.3 Current Status

The peak luminosity profile for Run II is shown in Fig. 2.2. The Tevatron has been colliding beams since 2001 although the peak luminosity has been significantly lower than expectations. However, as seen in Fig. 2.2, there has been a steady rise in peak luminosity as a function of time, up to 3.7 $\times 10^{31}$ cm^{-2}s^{-1} at the end of 2002. This is still a factor of 2-3 lower than the expected running conditions. The reasons for the low peak luminosity are linked to a variety of factors, rather than one major problem. Various steps such as improvements in the beam injection into the Tevatron and upgrades in the core cooling have contributed to the steady increase in peak luminosity. The Tevatron has also had three shutdown periods which can be clearly seen in Fig. 2.2. The total integrated luminosity delivered by the Tevatron and the recorded by DØ is shown in Fig. 2.3, the effect of the increase in peak luminosity can be seen in the integrated luminosity profile. Much of the initial data taking period was used to commission the detector and to complete the installation of some of the new electronics. The current emphasis is to improve the live-time of the detector. Currently the DØ detector is running at $\sim$75% live-time.

2.2 The DØ Detector

The DØ detector [22][26] is a multi purpose detector, with a similar layout to other modern large scale collider physics detectors. The DØ detector is shown in Fig. 2.4. As the beams collide in the centre of mass frame the detector is as symmetric as possible with respect to the centre. The DØ detector consists of an inner region for tracking charged particles and identifying vertices, a detector to measure energy deposits from electrons, photons and jets and an outer region for the detection of muons.

The focus of the Run II upgrade was to complement the already excellent calorimetry and the large angular coverage of the muon system with an improved, more complete tracking system. There was also a substantial upgrade of the electronics and the trigger system in order to handle the shorter bunch spacing.

The co-ordinate system used at DØ (hence the co-ordinate system used throughout unless otherwise stated) is centred on the centre of the detector i.e. the nominal interaction point. The z-axis is aligned along the direction of the proton beam, with the x-axis pointing outward from the centre of the ring and with the y-axis pointing upward. The common spherical co-ordinate system (r, ϕ, θ) is replaced with (r, ϕ, η), where the pseudo-rapidity η is defined as:

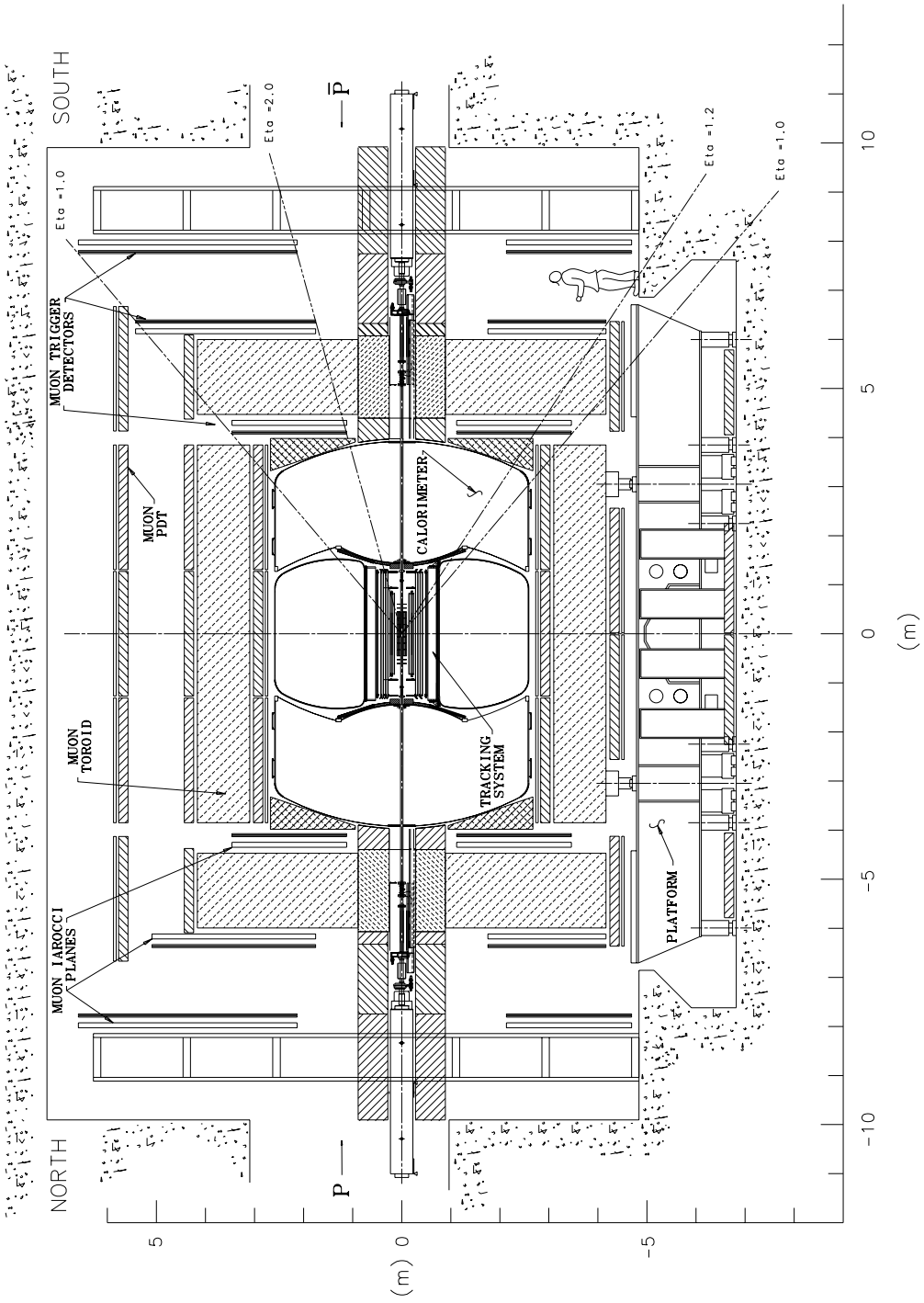

Figure 2.4: Side view of the DØ Run II detector

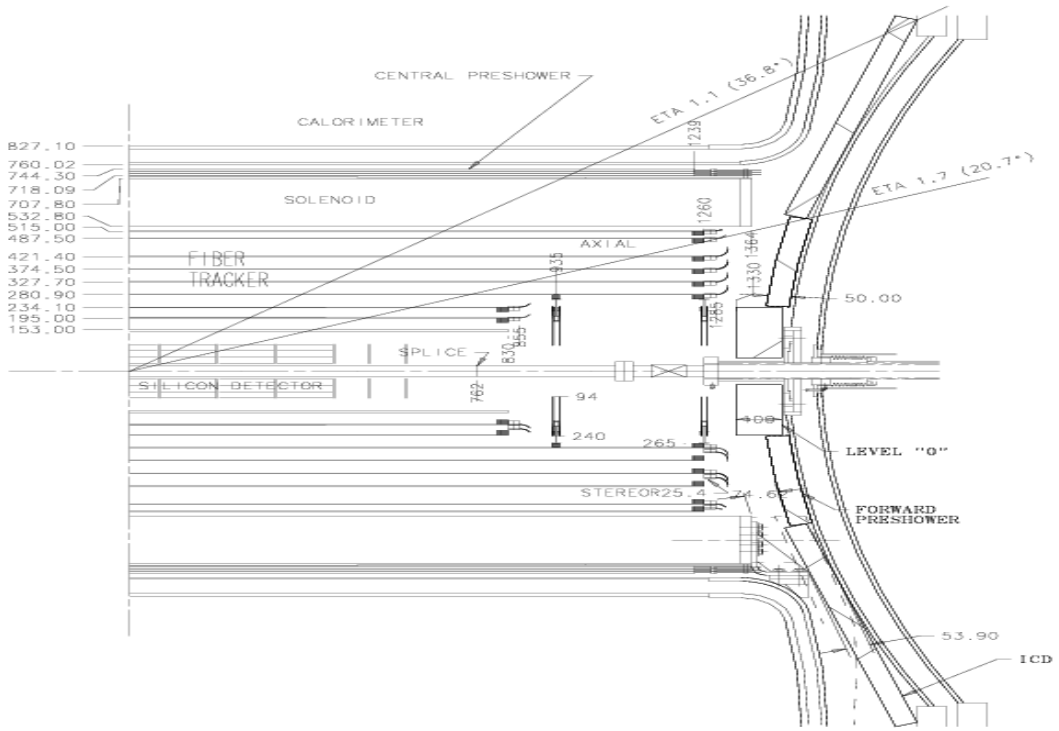

Figure 2.5: One-half side view of the DØ tracking system

$$\eta = -ln \tan \frac{\theta}{2}. \tag{2.1}$$

2.2.1 Tracking System

The tracking system consists of an inner silicon detector and an outer scintillating fibre tracker which are placed within a 2 Tesla superconducting solenoid[27]. The one-half side view of the new tracking system is shown in Fig. 2.5, taken from the Technical Design Report [22]. The tracking system is designed to provide tracking out to large pseudo-rapidities ($|\eta| < 3$), measurement of charged particle momenta, e/π separation, electron identification and the detection of secondary vertices for heavy flavour tagging. The combined tracking system is expected to have a momentum resolution of $\Delta p_T/p_T = 0.002$ [22].

Silicon Microstrip Tracker (SMT)

The Silicon Microstrip Tracker (SMT) is composed of 3 sub-detectors: the central barrels, the F-Disks and the H-Disks. The central barrels consist of six cylindrical barrels, three on either side of the nominal interaction point. The barrels have a length of 12.4 cm and extend out to a radius of $\sim$ 10 cm. The barrels consist

of 4 double layers of rectangular shaped silicon detectors (ladders) mounted on a beryllium support structure. The F-Disks are 12 disks of 12 double-sided, wedge-shaped detectors. Six disks are interspersed between the barrels; one attached to the end of each barrel segment. The other six disks form two triplets of disks located a small distance from either end of the outermost barrels. About one metre from the interaction point are the H-Disks which have an active region between 9.6 cm $< r <$ 23.6 cm (Fig. 3.1). The design and the commissioning of the SMT will be described in more detail in Chapter 3.

Central Fibre Tracker

Outside the silicon is the Central Fibre Tracker (CFT) [28]. The CFT is designed to provided full coverage out to $|\eta| < 1.6$. The CFT is composed of 32 concentric cylindrical layers of scintillating fibres. The 32 layers span a radius of 19.5 cm to 51.4 cm and are arranged into 8 super-layers, each of which consists of two doublet layers. The inner doublet in each super-layer has axial fibres while the fibres in the outer doublet alternate from super-layer to super-layer between a stereo angle of $\pm 2^{\circ}$. The fibres in each doublet layer are offset by a fibre radius in order to minimise any gaps between the fibres and to provide complete coverage. The total CFT system consists of 76 800 fibres. The axial layers of the CFT provide a track trigger for the first level of the DØ trigger system.

The scintillating fibres have a diameter of 835 μm and are composed of a polystyrene core doped with p-terphenyl and with 3-hydroxyflavone. The purpose of the dopants is to increase the light yield and to act as a wavelength shifter to match the light transmission properties of the core. The core is enveloped in a thin acrylic layer and a thin layer of fluoroacrylate. This is to increase the light trapping and to provide extra mechanical strength.

The fibres are connected to photo-detectors via 7-11 m long optical waveguides. The photo-detectors are visible light photon counters (VLPCs) which are basically solid state photo-multiplier tubes. The VLPCs have an operating temperature of $\sim$10 K, a high gain of 50 thousand electrons per converted photon and a quantum efficiency of $\sim$85%.

Solenoid Magnet

The 2.8 m long superconducting solenoid surrounds the SMT and the CFT. The magnet has a mean radius of 60 cm, provides a 2 Tesla field and has a stored energy of 5 MJ. There is no designed flux return; however, most of the flux returns between

the cryostat and the muon system. The effect on the muon system was found to be negligible. Inside the tracking volume the field is designed to be uniform to within 0.5% [29]. A total of approximately 1.1 radiation lengths are added by the solenoid and its cryostat.

2.2.2 Preshower and Calorimeter

The DØ calorimeter measures the energy of electrons, photons and jets. The design has been basically left untouched from Run I [26] although preshower detectors have been added to enhance electron identification, aid triggering and to compensate for the energy losses in the central region due to the addition of the new tracking system [30]. The front-end electronics for the calorimeter have been completely replaced to meet the challenge of the lower bunch crossing times in Run II.

Preshowers

There are two sets of preshower (PS) detectors: the central and the forward. The central preshower detectors are located at a radius of 72 cm, in the 51 mm gap between the solenoid and the central calorimeter, and cover the region $|\eta| < 1.2$. A lead absorber has been placed before the preshower, tapered in such a way that the total radiation length of the lead and the solenoid is two radiation lengths throughout. The central preshower consists of 3 layers of triangular-shaped scintillating strips. The inner layer is axial, whereas the other two are stereo layers with a stereo angle of approximately $\pm 23^\circ$. The strips have a base width of 7.1 mm and a 1 mm hole in the centre for a wavelength-shifting fibre used to read out the preshower. The wavelength-shifting fibres connect to clear waveguides which lead to VLPCs under the detector platform.

The forward preshower detectors are mounted on the inner surfaces of the end calorimeters and span $1.4 < |\eta| < 2.5$. The forward preshower has a similar design to the central preshower with two layers of $\sim \pm 23^\circ$ stereo strips. In order to initiate a shower and hence measure the energy in this region the two layers are separated by a 11 mm thick lead plate (which corresponds to about two radiation lengths). Hence the inner layer is present to detect minimum ionizing particles. The lead plate and the inner layer are not needed in the range $1.4 < |\eta| < 1.6$ as particles with this pseudo-rapidity have to traverse part of the solenoid. Consequently they shower upstream of the forward preshower.

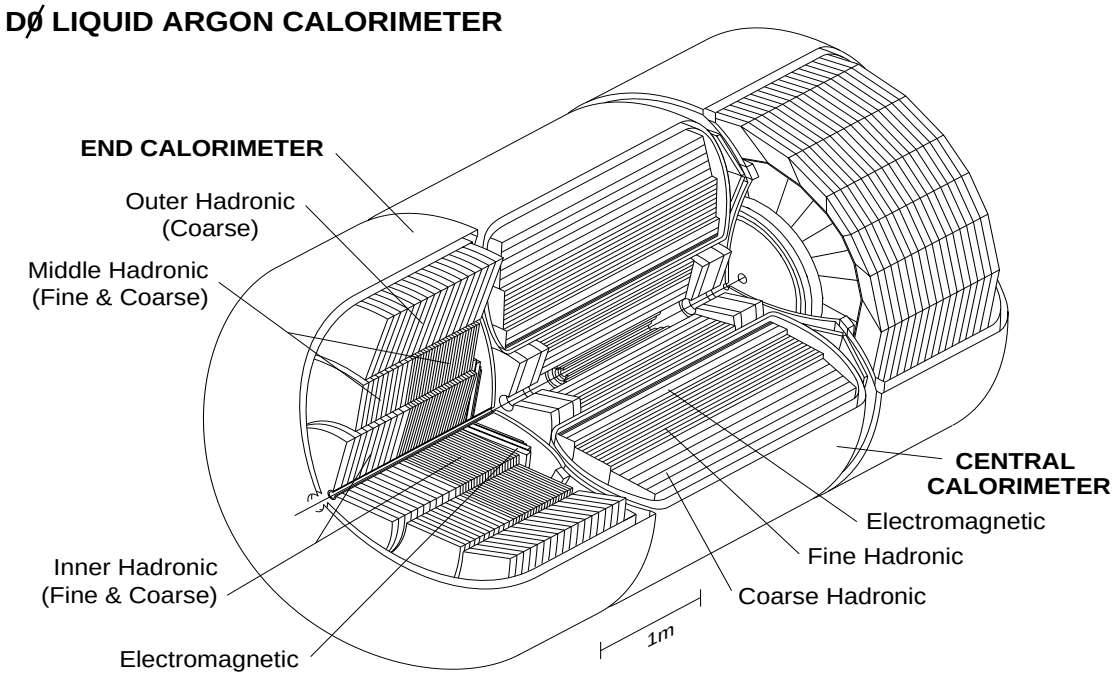

Figure 2.6: 3-D view of the DØ calorimeter

Central and Forward Calorimeter

The DØ calorimeter is shown in Fig. 2.6 and consists of a central and two end calorimeters covering $|\eta| < 4$. The DØ calorimeter is a hermetic sampling calorimeter with liquid argon as the ionizing medium and an absorber composed, for the most part, of depleted uranium. In the outer regions of the end calorimeters the uranium is replaced with copper or with stainless steel. Since the calorimeter uses liquid argon it has to be contained within a cryostat to keep the argon cold. The two end calorimeters and the central calorimeter are each enclosed in their own cryostat.

The central calorimeter covers $|\eta| < 1.2$ and consists of three concentric regions: the electromagnetic, the fine hadronic and the coarse hadronic. Each region is segmented into layers, which are further segmented into cells approximately 0.1×0.1 in $\Delta\eta \times \Delta\phi$. The electromagnetic section is subdivided into four layers and is 20.5 radiation lengths thick, which is sufficient to contain most electromagnetic showers. The third layer of the electromagnetic section is more finely segmented into 0.05×0.05 cells as this is where the maximum energy deposition of the electromagnetic showers is most likely to occur. The fine hadronic section has three layers and measures the majority of the energy from showering hadronic particles. The coarse hadronic region has only one layer and its purpose is to measure any leakage out of

the fine hadronic region and to reduce leakage out of the back of the calorimeter. The total thickness of the central calorimeter is approximately 7 absorption lengths.

The end calorimeters similarly have four regions: the electromagnetic, inner hadronic, middle hadronic and outer hadronic. The middle and inner hadronic regions are further split into fine and coarse sections. The calorimeter cell segmentation is the same as for the central calorimeter, except that the finer cell segmentation for the third layer of the electromagnetic calorimeter is only present up to $|\eta| < 2.6$. Beyond $|\eta| > 3.2$ the overall cell segmentation has $\Delta\phi = 0.2$ and the $\Delta\eta$ segmentation is also greater.

The DØ calorimeter is almost compensating, which signifies that the response to electromagnetic particles and non-electromagnetic particles is almost equal. The calorimeter response for electrons and pions was measured from test beam data to be [31]:

$$\begin{aligned} \sigma_E/E &= 15\%/\sqrt{E} + 0.3\% \ (EM) \\ \sigma_E/E &= 45\%/\sqrt{E} + 4\% \ (\pi^{\pm}) \end{aligned} \tag{2.2}$$

Intercryostat Detector

The intercryostat detector is located in the region where there is an overlap between the central and the end calorimeter, between $0.7 < |\eta| < 1.4$. The overlap region of the calorimeter is particularly problematic as there is a large amount of uninstrumented material such as the cryostat walls, support structures, etc. The intercryostat detector corrects for the energy lost in these regions in order to have an energy measurement which is as accurate as possible and to have a correct missing transverse energy distribution. The intercryostat detector consists of a single layer array of 384 scintillating tiles mounted on the face of the end cryostats. The signal from the detector is picked up by wavelength-shifting fibres and transported via optical fibres to phototubes located outside the magnetic field region.

2.2.3 Muon System

The muon system has been upgraded to provide efficient triggering on muons out to $|\eta| < 2.0$ [32]. The muon system consists of the Wide Angle Muon System (WAMUS), the Forward Muon System (FAMUS) and a 1.9 T toroid magnet used for tracking and momentum measurement.

Wide Angle Muon System

The WAMUS region covers $|\eta| < 1.0$ and consists of three layers of proportional drift tubes (PDTs), one of which is located inside the toroid magnet and the other two outside. The PDT chambers are constructed from extruded aluminium of rectangular cross-section and the anode wires are made of gold-plated tungsten. As the PDT's drift time of 750 ns is longer than the bunch spacing in Run II there are extra layers of scintillation counters in order to provide a trigger output. The two layers of counters are located between the calorimeter and the first layer of PDTs and mounted on the outside of the third PDT layer. Due to the DØ support structure on the underside of the detector some scintillation counters are located on the outside of the second layer of PDTs.

Forward Muon System

The FAMUS has three layers of drift tubes and also three layers of scintillation counters. Due to the more severe radiation level in the forward region than that in Run I the PDTs have been replaced with radiation hard Mini Drift Tubes (MDTs). The MDTs are composed of 8 cells of extruded aluminium combs. The cells have a 10×10 mm^2 internal cross-section and have 50 μm anode wires in the centre. The cathode is formed by a coating of stainless steel foil on the internal walls. Although the drift time of the MDTs is of 60 ns, considerably less than the bunch spacing, scintillating counters are also used by the trigger in order to reject sources of backgrounds (such as cosmic rays).

2.2.4 Trigger System

The DØ trigger has been completely upgraded for Run II [33][34]. The need for a highly efficient trigger at the Tevatron is driven by the hadronic environment. The majority of $p\overline{p}$ crossings will result in a "minimum bias" QCD scattering of the quarks composing the protons. In order to select physically interesting events, and so reduce the number of background events written to tape, the event is compared to a trigger list which consists of a list of basic properties associated with interesting events. In order to trigger on events the information from various sub-detectors is used at each level of the trigger and a decision is made as to whether it meets the requirements of the trigger list. The event is then discarded or passed to the next, more refined, level of the trigger system. The DØ trigger consists of four levels of trigger (L0 - L3). The expected trigger rates and latency are listed in Table 2.2.

Trigger	Accept Rate	Latency
Collision Rate	7.6 MHz	-
Level 1	10 kHz	4.2 μs
Level 2	1 kHz	100 μs
Level 3	20-50 Hz	100-150 ms

Table 2.2: Trigger rates for Run II

The parameters in Table 2.2 are the design specifications of the trigger with the Run II design luminosity. For the current trigger list, running at an instantaneous luminosity of 2×10^{31} cm^{-2}s^{-1}, with a bunch spacing of 396 ns (equivalent to an event rate of 2.5 MHz) the L1 trigger rate is 350 Hz, the L2 rate is 190 Hz and the L3 rate is 50 Hz. As the instantaneous luminosity increases, the L1 and L2 rates will change significantly due to the higher number of interactions. In order to keep the L3 rate to tape constant the rejection of the L2 and L3 triggers will have to increase.

Level 0 Trigger

The L0 system has two separate functions: to trigger on inelastic $p\overline{p}$ collisions and to function as a luminosity monitor. The L0 system is composed of luminosity monitors which are two arrays of plastic scintillation counters mounted, symmetrically around the beam pipe, on the inside of the end calorimeters.

Level 1 and Level 2 Trigger

The L1 and L2 triggers are hardware triggers. A schematic of the L1 and L2 triggers is shown in Fig. 2.7. The L1 trigger uses a reduced set of the data from the calorimeter (CAL), preshowers (PS), CFT and muon systems. The L1 system tests, via Field Programmable Gate Arrays (FPGAs), if any of the 128 Level 1 trigger bits are set. If any have been, the data are digitized and stored in a buffer 16 events deep pending a L2 decision. The basic elements of the L1 trigger from the calorimeter are the E_T of trigger towers (a collection of calorimeter cells) and total E_T sums. The CFT matches $r-\phi$ hit patterns in 4.5° sectors with predefined sets of tracks. The CFT system allows discrimination of four different momentum thresholds. The muon system outputs hits in the muon system consistent with tracks from the CFT.

The L2 trigger uses the information from the L1 output, combines the information from different sub-detectors and bases its decision on these global objects. The data are processed in a similar way to L1 using FPGAs and microprocessor cards

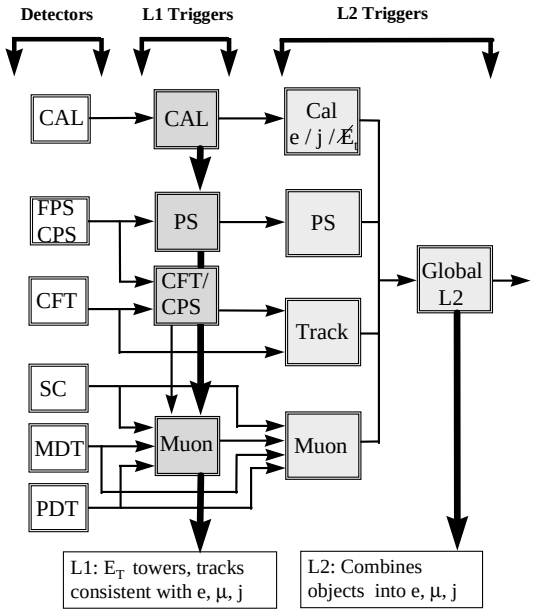

Figure 2.7: Schematic of the Level 1 and Level 2 trigger system [33]

and there is a one-to-one correspondence between the L1 trigger bits and the L2 trigger bits. A L2 silicon track trigger is currently being commissioned which will allow triggering on tracks consistent with long-lived particles e.g. b quarks. In case of a L2 accept, the full detector is read out and the data passed to the L3 trigger.

Level 3 Trigger

The L3 trigger is purely software based. It takes as an input the global objects from the L2 output and refines them. A limited reconstruction of the event is performed in order to do this. The L3 trigger software runs on a farm of PCs running the Linux operating system. Each event is analysed by a different processor which runs an independent instance of the L3 filtering software. To trigger on an event the filtering software compares the properties of the physics objects against a fixed set of constraints defined in a filter script. Each set of constraints corresponds to a L3 trigger filter bit which is associated to a particular L2 trigger bit. If a L2 trigger bit fires the associated filters in the L3 filter script are processed. There is no limit to the number of L3 trigger filter bits which can be associated to a L2 trigger bit. If the event passes a L3 filter the event is transmitted from the farm node to the datalogger and then to tape.

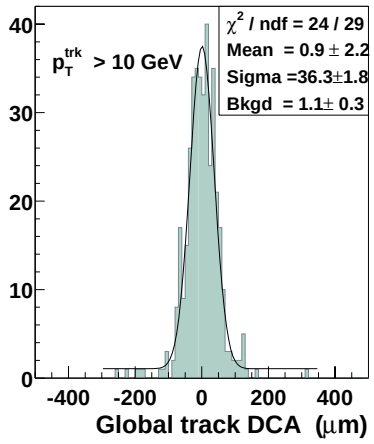

Figure 2.8: Plots of the distance of closest approach in data for tracks with $p_T > 10$ GeV/c [35]

2.3 Current Performance of the DØ Detector

2.3.1 Performance of the Tracking System

The DØ tracking system and its readout are fully installed and functioning. The status of the SMT will be described in Section 3.4.1. The CFT currently has a hit efficiency greater than 98% with less than 1.5% of dead channels. The distance of closest approach to the primary vertex of tracks with a $p_T > 10$ GeV/c is shown in Fig. 2.8 [35]; the combined resolution of the CFT and the SMT is of 36 μm. Taking into account the 30 μm beam spot this corresponds to a resolution of $\sim$20 μm. This is close to the expected value of $\sim$15 μm.

Fig. 2.9 [35] shows a reconstructed J/ψ peak where the J/ψ decays to muons. These events are collected by combining the tracking information from the SMT and the CFT with that from the muon system: the correct mass value and the good resolution demonstrates that the tracking system is well calibrated and that both systems are working well. Fig. 2.10 [35] instead displays the reconstructed K°_S mass in the $\pi^+\pi^-$ channel, using a first pass alignment of the SMT and CFT.

2.3.2 Calorimeter Performance

The calorimeter is functioning well, out of the 55 thousand channels in the calorimeter the fraction of dead and noisy channels is approximately 0.1%. Fig 2.11 [36] shows $Z \to e^+e^-$ events in data; again the calibration is, to first order, understood. The width of the reconstructed Z mass in data is a factor of < 1.3 greater then that in Monte Carlo [37]. Initially there were problems with the calorimeter from "hot" cells i.e. isolated cells with a high occupancy due to noise. In order to keep these

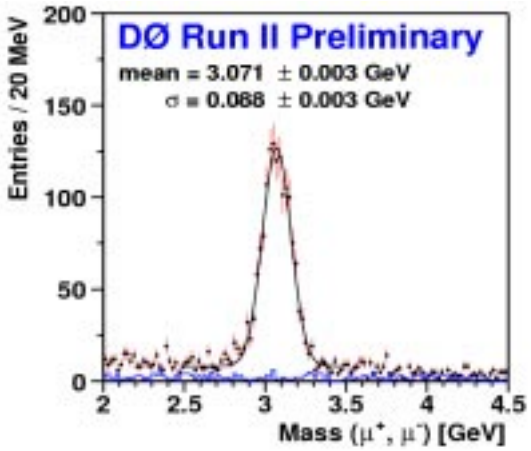

Figure 2.9: Reconstructed J/ψ mass from di-muon events in data [35]

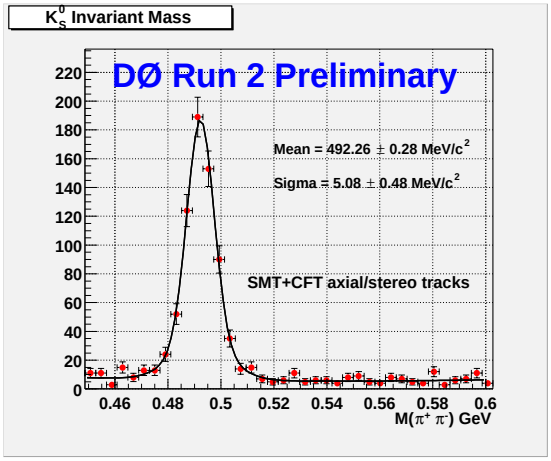

Figure 2.10: Reconstructed K°_{S} mass in the $\pi^{+}\pi^{-}$ channel in data using global CFT and SMT tracks [35]

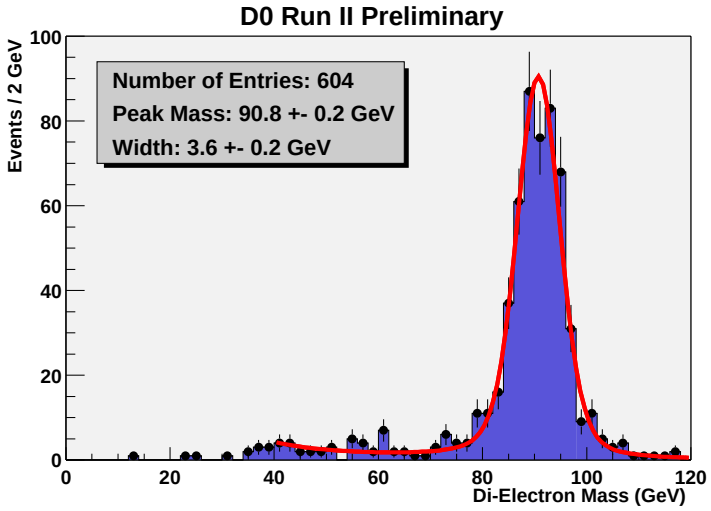

Figure 2.11: Reconstructed Z boson mass in the electron channel in data [36]

cells from having an impact on the physics, a hot cell killer (reference NADA) was implemented for use on-line and off-line. The implementation of this was successful; however there are still "warm" regions in the calorimeter which need to be taken into account.

Chapter 3

The Production and Testing of the DØ SMT F-Disks

The SMT detector production and testing was a major effort at DØ especially considering the short timescale available and the importance of the silicon detector for the achievement of the goals of the Run II physics programme. The SMT system is of an intermediate size between the previous generation of silicon vertex detectors and the future detectors to be constructed for the LHC. The total SMT detector consists of 3 sub-detectors, 5 different module designs (in terms of shape, number of chips, readout circuits and silicon sensors) and 912 modules giving a total of 792 576 readout channels, making it the silicon strip detector with the most readout channels to be constructed so far. This section describes the production and testing procedures for the F-Disk sub-detector. The procedures for the sub-detectors were similar [38] but were overseen by different groups due to the different properties and distinct problems associated with each sub-system.

I was initially involved in the debugging of the F-wedges and gained experience in all the other stages of the testing at Fermilab. For a period of time I was subsequently responsible for the production of the modules and the testing of the F-wedges and F-Disks.

3.1 The DØ Silicon Microstrip Tracker (SMT) Design

The SMT was designed primarily to maintain track and vertex reconstruction over a wide η range i.e. out to $|\eta| = 3$. This choice, together with an extended interaction region ($\sigma_z = 25$ cm), led to the hybrid design of barrels and disks [22]. The detector

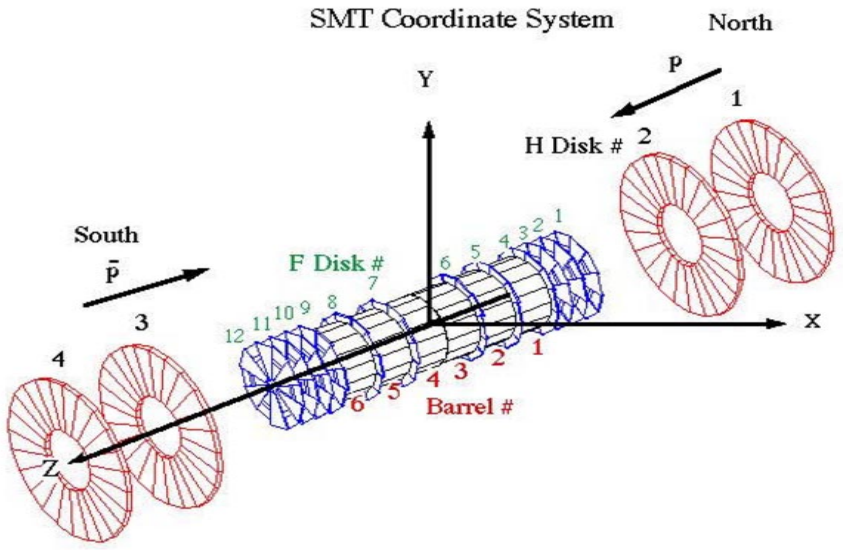

Figure 3.1: Detail of the SMT tracker and of the reference co-ordinate system used

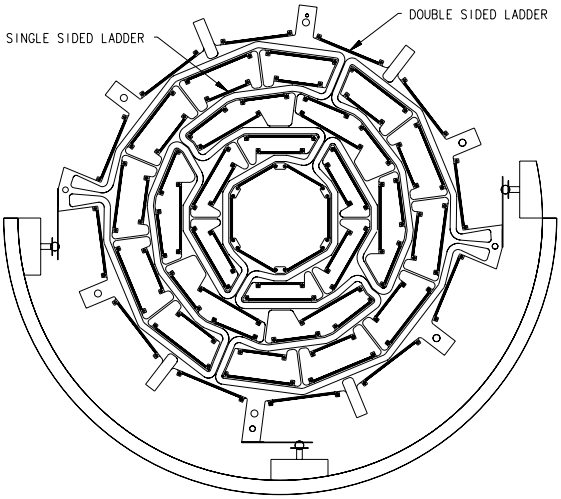

Figure 3.2: $r - \phi$ view of a Barrel

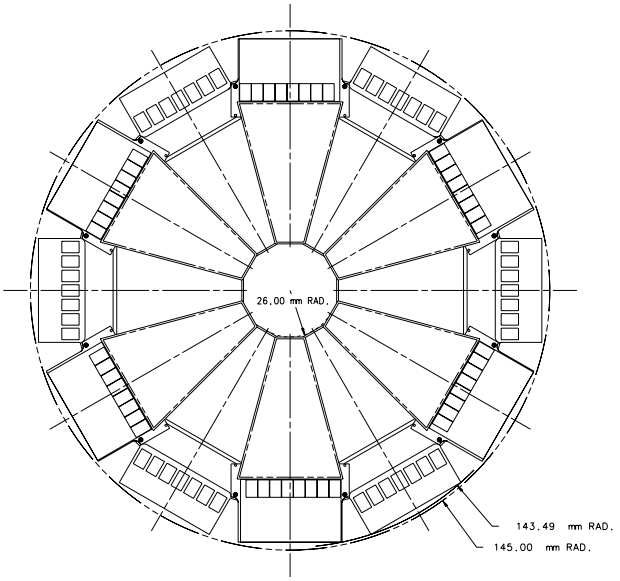

Figure 3.3: $r-\phi$ view of a F-Disk

design is shown in Fig. 3.1, together with the SMT co-ordinate system and the numbering of the SMT sub-detector components.

The extended interaction region and the presence of a magnetic field means that it is impossible to have all tracks perpendicular to the layers of the detector for all η. The hybrid design permits DØ to use the disks to reconstruct high η tracks in both $r-\phi$ and $r-z$, with the barrels primarily measuring $r-\phi$ for more central tracks. When using a hybrid design there is a conflict between keeping extrapolation errors low in the reconstruction of tracks passing through the disks, thus minimizing the distance between disks, and the introduction of dead regions between the barrels, thus lowering the overall efficiency of the detector. This conflict can be seen as keeping a high tracking efficiency in the central region while trying to maintain a good vertex resolution at large η. It was decided to compromise between the two factors and introduce one disk attached to each barrel at $|z|$ = 12.5 cm, 25.3 cm and 38.1 cm and then a triplet of tightly spaced disks at $|z|$ = 43.3 - 53.6 cm. This combined system of disks is known as the F-disks. The inclusion of disks between the barrels introduces a separation of about 8 mm. This gap was minimized by placing the readout electronics on top of the active detector surfaces and by routing the barrel readout to the outer radius as opposed to the end of the barrel. The H-disks are located even further from the interaction region at $|z|$ $\simeq$110 cm and $\simeq$120 cm.

The barrel geometry in $r-\phi$ is shown in Fig. 3.2, it consists of 4 doublet layers spanning a radius of 2.7 - 9.43 cm. The inner two layers of each barrel hold 12

ladders whereas the outer two hold 24. Layers 2 and 4 are double-sided detectors with 50 μm pitch axial strips and 62.5 μm, 2° stereo strips and have 9 readout chips. Layers 1 and 3 have different detectors for different barrels: barrels 1 and 6 have single-sided 3-chip ladders with 50 μm, axial strips. Barrels 2-5 instead have double-sided 6-chip ladders with axial, 50 μm pitch strips and 90°, 153.5 μm strips. Each chip has a total of 128 readout channels and the barrels have a total of 432 modules which account for approximately 39 K channels. The H-Disks are composed of 24 back to back pairs of single-sided silicon detectors with a pitch of 80μm and $\pm$7.5° stereo angle. The 12 F-Disks consist of 12 double-sided F-wedges with an inner radius of 2.6 cm and an outer radius of 10.5 cm. The F-wedges will be described in more detail in Section 3.1.1.

The F-disk geometry is shown in Fig. 3.3. The 12 F-wedges per disk are mounted on either side of a beryllium support structure (which also functions as a cooling ring). The F-wedge sensors use a variety of depletion voltages as they were produced by two different companies: Micron and Eurisys. The Micron sensors included high and medium depletion devices (around 70 and 40 V respectively) and the Eurisys sensors had only low depletion voltages (around 25 V). In order to keep the SMT detector isotropic and to simplify the voltage settings of the wedges on the disks it was decided to group the high, medium and low devices separately.

The choice of positioning of the different sensor types was made in view of radiation damage of the sensors and the physics impact of the hypothetical loss of disks before the end of Run IIa. As lower depletion devices will be type inverted earlier than the higher depletion sensors they will be more susceptible to higher noise and higher leakage currents, affecting their efficiency and performance. The positioning was symmetric around z =0. The outer disks (1, 2, 11, 12) and the outermost of the barrel disks (4, 9) were populated with Micron high depletion devices, the innermost disks (6, 7) with the Micron medium and the remaining (3, 5, 8, 10) with the Eurisys. The decision made reflects the need for good resolution at high η and the need to maintain the vertex resolution for these tracks over the course of time. Another motivation for placing the high depletion disks at high $|z|$ is that this region is not covered by the barrels or by the CFT and therefore an inferior performance cannot be compensated for by other detector elements.

3.1.1 The F-Disk Detector Modules

The F-wedges, as are the other modules, are composed of three main parts: the SVX-IIe chips, the High Density Interconnect and the silicon sensor. The SVX-IIe readout chip [40] is a 128 channel custom made silicon chip.

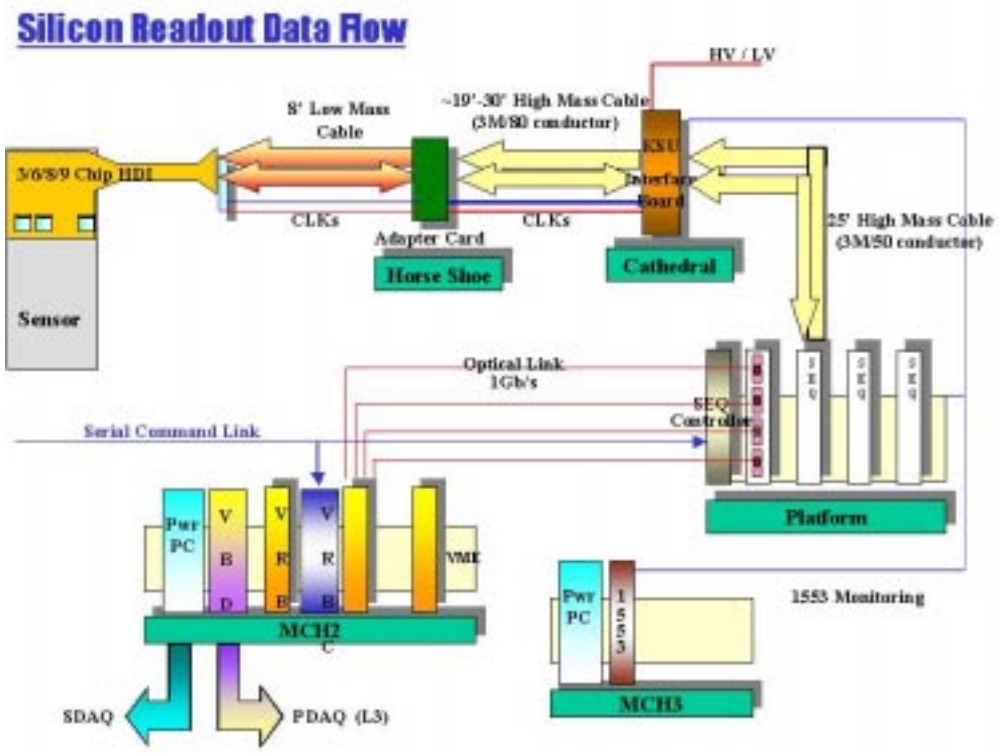

Figure 3.4: Schematic of the SMT data acquisition system

The F-wedge silicon sensors are double-sided, AC coupled, 300 μm thick with 15° strips on the p-side and $-15°$ strips on the n-side. The wedge shape of the silicon sensor has the consequence that the silicon strips are not all of equal length but vary depending on the chip and strip number. The F-wedges have a total of 14 chips, 8 on the p-side and 6 on the n-side. This amounts to 1792 channels per F-wedge. The total F-Disk system has 144 F-wedges which corresponds to a total of 258 thousand channels, about a third of the total SMT.

The chips and associated readout electronics are mounted on a flexible kapton circuit commonly referred to as the High Density Interconnect (HDI). Unlike the other modules the F-wedges have separate readout tails for the n and the p-sides due to the high number of chips. The extra readout electronics, the high number of chips and the double-sided sensor render the F-wedges the most complex detector module in the SMT.

3.2 The SMT Readout System

The readout chain for the SMT detector is shown in Fig. 3.4. Data passes from the SMT detector via adaptor cards to the Interface Boards. The adaptor cards are

passive components which allow the low mass readout cables to be switched for high mass 80/3M cables.

The Interface Boards are the first active interface to the SMT. The Interface Boards have the following functions:

- Act as an interface to the low voltage and high voltage supplies used to power the SVX-IIe chips and to bias the detectors.
- Interface to the monitoring system via 1553 cables. The system monitors the temperature of the detectors and the various voltages and currents.
- Handle the refreshing of the signal and timing adjustments i.e. clock pulse shaping.
- Act as a stage for the next set of cables.

The data are then passed via 50/3M cables to the Sequencer Boards which control the SVX-IIe chips i.e. the downloading, readout, digitisation and data acquisition. The boards also modify the data structure so that it can interfaced to the next stage of the readout chain. The Sequencers are controlled by a Sequencer Controller which transmits the trigger and clock signals. The data are then passed to the VME Readout Buffers where they are stored pending a Level 2 trigger decision.

3.3 F-Wedge Production and Testing

The general procedure for the construction and testing of the modules was similar for ladders and for wedges. A schematic of the construction and testing procedure is shown in Fig. 3.5. The testing of components initially followed two paths; one associated with the silicon sensor and the other with the readout electronics and SVX-IIe chips.

Before arrival at Fermilab the sensor was tested by the manufacturer by probing DC pads on the silicon. This test determined a rough depletion voltage, leakage current and a micro-discharge breakdown voltage which was then verified at Fermilab/ Boston University (BU) [39]. The tests at Fermilab/ BU also tested the integrity of each strip, the capacitance, leakage current and resistance. This information was used when wire bonding the strips to the readout channels in order to skip strips with problems.

The readout electronics were mounted on the HDIs. The bare HDIs were visually inspected upon arrival at Fermilab and were then laminated. Lamination consisted

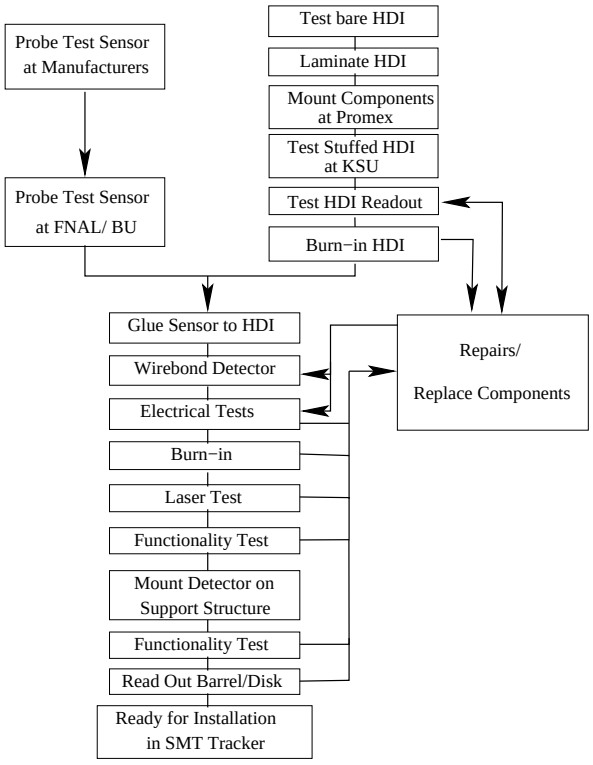

Figure 3.5: General testing procedure flow chart

of mounting the 6-chip and the 8-chip HDIs back to back on a 300 μm thick beryllium plate. The beryllium plate was used to provide a thermal connection between the readout heat sources and the coolant channel on the F-Disks. During lamination layers of kapton and other small components were also added to the HDIs.

A further part of lamination was the addition of a jumper to the 6-chip side HDI. The jumper was a flexible rectangular circuit with 6 sets of 128 copper traces for connection to the silicon and the SVX-IIe chips. In addition there were 5 traces which were used to supply the bias voltage to the sensor. The jumper was primarily used as a pitch adaptor in order to compensate for the different pitch of the silicon strips (62.5 μm) and the SVX-IIe chips (50 μm). The jumper also doubled as the mounting point for the F-wedges onto the beryllium F-Disk ring, hence the jumper needed to be flat and a thermal conductor.

The complete F-wedge HDI was then sent to Promex for "stuffing", in which resistors and the SVX-II-e chips were mounted on the HDI surface and then micro bonded to it. The readout and proper functioning of the chips was then verified at Kansas State University (KSU) and subsequently at Fermilab. If the HDI passed the initial test at Fermilab it was "burned in", i.e. read out continuously for 24-48 hours.

If both sensor and HDI were functioning correctly they were glued together and the silicon strips were wire bonded to the chips (or via the jumper in the case of the n-side). The modules were then electronically tested (or debugged).

Once the module was drawing a moderate leakage current (around 20 μA at a voltage of 20 V above the measured depletion voltage) and had no other problems it was sent to burn-in where it was read out under controlled conditions. If the module passed this test i.e. if the electronics were read out correctly and the leakage current was stable it was sent to a laser test. If it failed then it was sent back up the chain: in the case of readout failures it was sent to chip verification and HDI readout testing. If the problem was associated with high leakage currents or problems with the bias voltage it was sent back to debugging.

The laser test was performed to measure the depletion voltage, the operational voltage and the number of dead channels. Once the laser test had been completed the module was electronically graded, based on the results from the laser and the burn-in tests.

3.3.1 Test Stands

The preliminary electrical verification of the HDI, and of the completed modules, before burn-in was performed on stand-alone test stands. It was decided early on in the SMT production that the testing of the modules during production would not be connected to the testing of the full readout chain. This was to allow both efforts to continue in parallel and to ensure that the production and testing of the detector modules would not be slowed down by an incomplete readout system. The stand-alone test stand consisted of low and high voltage power supplies which were interfaced directly to the modules via a passive board. In order to interface to the SVX-IIe a Stand Alone Sequencer Board (SASeq) was used. This board was in many ways analogous to the Sequencer Boards used in the full readout chain. In order to control the SASeq the board was housed in a VME crate containing a bit-3 controller card. An Excel spreadsheet running on a commercial PC was used to control all the settings except for the low voltage, which was set manually. Most of the testing, aside from burn-in, was performed using these test stands.

The test stand used for burn-in was somewhat different and incorporated a few more elements of the full readout chain. A schematic of the burn-in test stand is shown in Fig. 3.6. The main difference between the stand-alone test stand and the burn-in test stand was the use of KSU Interface Boards to supply, among other things, the low voltage to the SVX-IIe chips. These Interface Boards were analogous to those subsequently used in the full readout chain and served the same purpose.

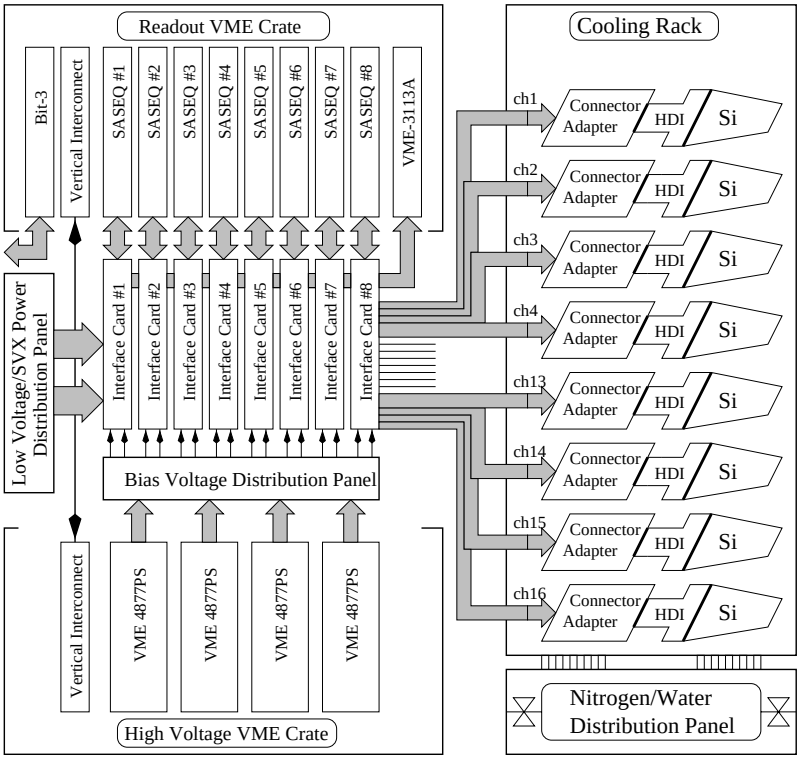

Figure 3.6: Schematic of the burn-in test stand

The burn-in test stand could hold up to eight F-wedges at a time (or 16 ladders). The burn-in stations were outfitted with a chiller so that the modules could be operated at low temperatures. In order to keep the modules in a controlled environment the modules were placed on an aluminium plate with a pipe for cool water and with holes in order to supply a constant nitrogen flow and maintain the modules in a dry environment. When using either type of test-stand the operator made sure that they were grounded to avoid applying a static charge to a module thus potentially damaging it.

3.3.2 High Density Interconnect Testing

The HDI testing was conducted in various steps. A visual inspection of the wire-bonds from the HDI to the SVX-IIe chips was performed using a microscope. This step was performed in order to identify missing or crushed bonds. Also chips with obvious defects could be identified together with any debris from previous handling. A preliminary verification and diagnosis of the readout was performed via the chip pedestals and injection of charge. Due to the nature of the design of the F-wedge HDI tails, it was more likely that a bad connection to the board connector was made

than for the ladders. Therefore the currents had to be monitored carefully when powering up the SVX-IIe chips.

After burn-in a further verification of the HDI data was performed. This further test was required as the SVX-IIe chips were encapsulated at this point to avoid damaging the chips in the subsequent production stages. The encapsulation made any subsequent repairs and diagnosis of the HDI difficult. Subsequent electrical verification was performed after the encapsulation to ensure that none of the wire bonds had "popped" (lost adhesion to the bond pad) during the encapsulation. At this point the HDI was glued to the silicon sensor and the chips were wire bonded to the sensor.

Common Problems During HDI Testing

The vast majority of the general problems were linked with faults in the HDI manufacture or problems resulting from chip replacements. Early on it was discovered that there was a fold-over on the HDI which connected one of the SVX-IIe chip low voltage power lines on the p and n-sides. It was concluded that this extra connection was redundant and could cause problems as the voltage could be set differently on either side, resulting in a potentially damaging current flow. Consequently it was decided to sever this connection on all the HDIs.

A common problem encountered was that of shorts appearing between the HDI traces in the tail to either the ground mesh or to adjacent traces. In the case of the low voltage traces the HDIs would draw very high currents when powering up. These high currents were also linked to an improper insertion of the HDI tails and to chip failures. It was unclear whether the two effects were linked, i.e. whether the improper insertion of the tail or actual shorts between the traces could cause a failure in chips. In order to minimize this effect, especially in the later stages of production, the resistance between the low voltage supplies and ground was measured before powering the SVX-IIe chips.

Defects and failures in the chips and their subsequent replacement could cause further complications. Bonding on the same bond pads could be problematic especially after several iterations as bonds would not stick or would pop after a short period of time. Furthermore in replacing a chip the procedure would be to bond the chip to HDI bonds first and then test the functioning of the HDI. Subsequently the chip would be then bonded to the sensor (via the jumper for the n-side). In this case there was the chance that the wedge would go through debugging with a chip not connected. The general symptoms would be low noise (about 1 ADC count) in a extended number of consecutive channels together with a very flat pedestal.

The n-side of the HDI had a further problem linked with the jumper. In various HDIs the jumper traces would be damaged or disconnected over a number of nearby channels. This showed up either as low noise or else as regions of variable noise together with a different pedestal from the rest of the chip. The jumper traces could be easily verified by visual inspection. These channels could be connected by bump bonding on the traces themselves. However this was not possible if the trace was broken close to the bond pad. For the jumper traces which could not be fixed in this way the channels were disconnected.

3.3.3 Detector Module Debugging

The debugging of detector modules was the first attempt to read out and bias a completed module after assembly. Even though the chips were encapsulated the chances of damaging the modules during assembly were substantial; about 25% of all the assembled modules failed to download or readout all the SVX-IIe chips. Furthermore the leakage current was found to be unacceptably high for virtually all the assembled modules. The aim of debugging was to restore the functionality of the modules and verify that the functioning was within the accepted parameters.

The preliminary step of debugging was a visual verification of all the wire bonds and the sensor to ensure that there had been no damage during gluing or wire bonding. Then the resistance between the active beryllium pieces and the HDI ground was measured. If this was more than 10Ω then the grounding was improved directly using silver epoxy.

The next test was a verification of the readout with no bias applied to the sensors. If this test was successful then the module was biased separately on the p and n-sides. The leakage current for the first test was typically on the order of 100 μA at a bias voltage of 10 V in positive bias (voltage applied to the n-side) and slightly less in negative bias (voltage applied to the p-side). The reason for such high leakage currents was generally due to "pinholes" (broken AC coupling capacitors) which caused the leakage current to pass directly through the readout electronics connected to the strip in question. In order to reduce the leakage current the broken capacitor had to be identified and the strip disconnected from the chip by removing the wire bond between the chip and the sensor.

It is important to stress that if the modules were to develop a pinhole while installed in the SMT the whole module would become inoperable simply due to the current trip limit on the high voltage supplies (2 mA). This limit would easily be surpassed by such a module under full bias and furthermore there would be

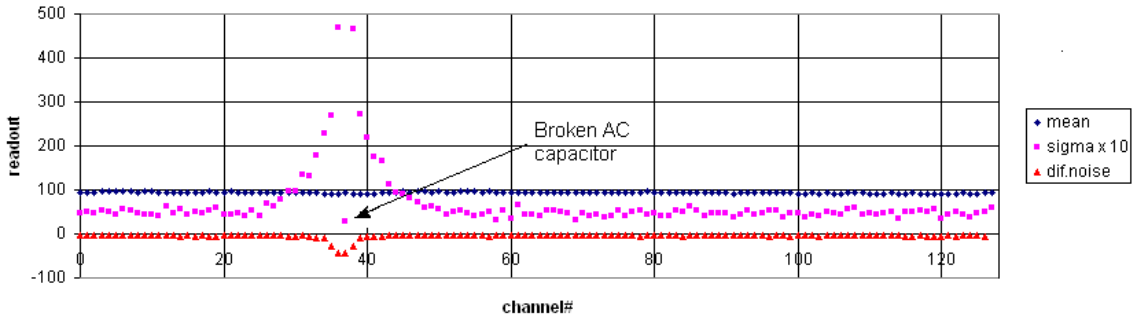

Figure 3.7: Example of a typical signature of a pinhole

no possibility of disconnecting the problematic strip. Hence the main priority of debugging was to check the stability of the AC coupling capacitors under high bias voltages.

The typical signature for a pinhole is shown in Fig. 3.7. As the DC component of the current dominates the input to the chip preamplifier, the output would be virtually constant and hence exhibit a low noise. The neighbouring strips on the other hand would show a much higher noise. After pulling all the bonds corresponding to strips with broken AC coupling capacitors the voltage applied to the p-side was raised to a value of 100 V or the voltage at which a discharge region was reached, whichever was lower. At the time of testing the design of the Run IIb silicon tracker was uncertain; hence there was the possibility that the wedges would be used in RunIIb. This uncertainty, combined with an uncertainty in the time needed for the F-wedges to undergo type inversion meant that there was the possibility that the F-wedges would have to be operated at a higher bias voltage. Therefore the maximum bias voltage applied during debugging was generally higher compared to that applied to the other modules.

A typical I-V profile for a SMT module after debugging is shown in Fig. 3.8. The voltage which could be applied in negative bias was severely limited by micro-discharge effects [41]. In the absence of broken capacitors the maximum negative voltage which could be safely applied was defined to be that just before the current would increase exponentially. In the absence of such a rise it was defined to be half of the voltage applied in positive bias. There were a number of F-wedges that had high, stable leakage currents even though there were no broken capacitors evident. It was concluded that these sensors had defects in the bulk of the silicon and hence the leakage current could not be reduced.

A further problem encountered was the voltage supply tripping due to high currents even when applying as low as one volt in negative bias. This would be

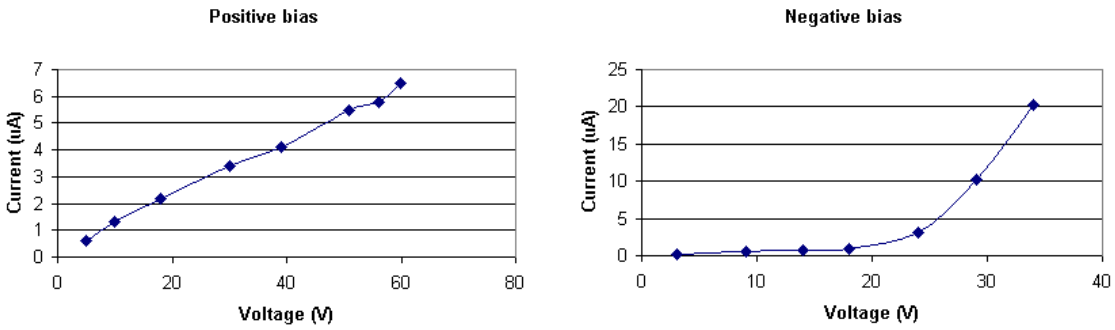

Figure 3.8: Typical current - voltage curve of a SMT module

Sensor Type	n-side	p-side
Micron High	5.5	3.3
Micron Medium	5.5	2.8
Eurisys Low	4.3	12.0

Table 3.1: Average number of bonds pulled for the various sensor types in debugging

linked with a physical short on the HDI tail between the secondary bias line and ground. These type of shorts were often solved by finely sanding the tail or by cropping the very end of the tail. Table 3.3.3 shows the average number of bonds pulled for each sensor type.

The F-wedges had many problems which were distinct from those of the other SMT detector elements. The problems were generally specific to the sensors from a particular manufacturer.

Micron Sensor Related Problems

The Micron sensors were found to have two main problems: regions in which pinholes would seemingly propagate to adjacent strips and problems related to the stability of the leakage current when biased. The first problem had a very distinctive signature: the wedge in positive bias would exhibit a high current and the diagnosis would clearly locate a pinhole. This channel would therefore be disconnected and the pinhole would seemingly propagate to the next strip. This area could extend to 10-15 consecutive strips or even more in the worst cases. When examined under a high power microscope, p-stop implantation faults could be seen in the areas affected; however this correlation wasn't complete as some affected wedges didn't exhibit visible faults. The general impression was that this problem was linked to faults in the masking procedure of the silicon. In order to limit the number of iterations

required for each wedge an extra bond than needed was pulled when a faulty region started to develop.

The second problem was the lack of reproducibility and stability over time of the bias currents. The stability was an issue in negative bias as the currents seemed to increase over time. As a result the definition of a safe operating voltage in negative bias would be modified to a lower voltage which seemed to reduce the drift. The problem in the definition of a safe voltage in secondary bias was linked to the Micron sensor characteristics. The I-V curve in negative bias would not exhibit a clear junction breakdown, although above a certain voltage the measured current would tend to increase more rapidly with time with an increase in voltage. Once this point had been reached the currents measured previously at a lower voltage would be higher as well. As a result the decision as to the voltage at which the junction breakdown occurred was somewhat arbitrary. Consequently, the definition was based on the voltage at which the current wouldn't drift significantly (less than 5 - 10 μA) over the total period biased, combined with a decrease in the rate at which the current would increase with time. This effect was seen also in some Eurisys wedges, but the effect was not as pronounced and furthermore the I-V curve always exhibited a clear junction breakdown.

The problem observed with the reproducibility was that the currents (especially in positive bias) would sometimes suddenly jump by a factor of 4-5 without showing any indication of pinholes or other signs for such a large discontinuity. The currents would be stable but much higher. This variation would not always be permanent and sometimes, after leaving the F-wedge in a dry box for a couple of weeks, the wedge would have an I-V curve similar to that before the effect was observed. However in a limited number of cases (about 4) the currents remained high and stable. In total the number of wedges which exhibited this were less than 15. After exhibiting this discontinuity the measured current under positive bias was more stable and had little tendency to drift even at high voltages (90-100V). This behaviour was not understood, however it was decided to use these wedges if they passed all subsequent tests.

Eurisys Sensor Related Problems

The Eurisys sensors generally exhibited less problems than the Micron sensors. While the Micron sensors generally had problems on the n-side, the Eurisys sensors exhibited a larger number of pinholes on the p-side. This was correlated with the fact that the wrong set of bond pads had been used to probe the sensors, thus the

chips were bonded to the pads which had probe marks. As the pads which should have been probed were covered when glued to the HDI there was no alternative.

The I-V characteristics were well defined as a clear junction breakdown was visible when applying negative bias. The only real problem encountered was that the wedges would generally exhibit discharges at around 70 V in positive bias, which signified that the wedges could not be biased to as high a voltage as would have been ideal. As the Eurisys sensors are low depletion devices this will only become an issue when the F-wedges become type inverted and the depletion voltage increases past the discharge voltage.

3.3.4 F-Wedge Burn-In

There were various data integrity tests performed during burn-in and various parameters not related directly with the readout were also monitored. The most important of these were the temperature, the chip low voltages and their associated currents, the bias voltage and leakage current, the pedestals, total noise, gain, random noise and the occupancy of the detector in sparsification ("sparse") mode. In sparse mode only the channels with a response above a given threshold and the neighbouring strips are read out, as opposed to the whole chip. The sparse performance check was important as the SMT operates in sparse mode during data taking due to the excessive time needed to read out all the channels of the SMT. In fact only 3-5% of the SMT channels can be read out in the allotted time. In order to test the performance of the detector modules in this mode every eighth channel was pulsed and the frequency of false readouts in the channels not being pulsed was studied.

In the initial stages of production, the burn-in test stand had many problems in trying to download the SVX-IIe chips of the F-wedges. The reason for this difficulty was probably a consequence of various factors and was not well understood, especially as the other detector types did not have the same problems. Initially when trying to download the F-wedges at least 20% would trip the low voltage supplies or not download. This did not create problems for the modules. However, this would blow the low voltage fuses on the KSU boards as they had a lower current limit than the trip on the power supplies. Furthermore the F-wedges, having two HDI tails, provided a direct connection between the two channels on the KSU Interface Boards. Theoretically there should be no coupling between the two sides of an F-wedge (except for a common ground) and also the two KSU Interface Board chains should be decoupled. The extent of this decoupling, however, was not clear.

Another issue was that the spreadsheet used to download the F-wedges in burn-in was different to that used in electrical debugging and probably some of the bad

	FW-6	FW-8	FA-6	FA-8
Pedestal (ADC counts)	100	100	100	100
σ_{ped}	2	2	1	0.75
Charge Inject (ADC counts)	110	100	100	100
σ_{cal}	2	2	1	1
Gain (ADC / fc)	$8 \rightarrow 12$	$9 \rightarrow 12$	$12 \rightarrow 14$	13
σ_{gain}	0.5	0.25	0.25	0.25
AVDD Current (mA)	330	400	340	350
AVDD2 Current (mA)	140	180	140	180
DVDD Current (mA)	40	60	40	60

Table 3.2: Typical values of some parameters monitored during burn-in, for F-wedges (FW) and HDIs (FA)

downloads seen in burn-in and not during the subsequent debugging were linked to this difference. With time, modifications to the KSU boards (such as a larger fuse for the low voltage supplies) and to the spreadsheet meant that the downloads problems ceased to be a major issue, although they still sporadically occurred.

Table 3.2 lists typical values for a selection of parameters monitored during burn-in. The label W refers to F-wedges and A to HDIs. The numbers 6 and 8 refer to the number of SVX-IIe chips on the HDI tail being readout. A range is given for the gain as the gain profile had a slope starting at the lowest channel and rising linearly with channel number to the final value. AVDD, AVDD2 and DVD are the three low voltages supplied to the SVX-IIe chips.

There were other distinct readout characteristics of F-wedges during burn-in; these would not necessarily be problems per se but were particular to the F-wedges. Figs. 3.9 and 3.10 show the average chip gain for complete F-wedges and for the HDIs for the n-side and the p-side during burn-in. What can be seen is a gradual increase in gain in the F-wedge distribution with chip number. This is due to the shorter strip length with increasing chip number.

Probably the most important test for the grading of the detector modules was the noise test. The results for the mean random noise per chip are shown in Figs. 3.11 and 3.12. Again there is a strong dependence of the noise on the chip number which is again linked with the shorter strips. A reason for this is that longer strips have a larger capacitance which can lead to a higher noise. A channel was considered to be noisy if the σ on the pedestal was greater than 3 ADC counts. For the wedges installed on the F-Disks the total number of noisy channels on the p-side was determined to be 419 channels (0.28%) and 416 (0.32%) for the n-side.

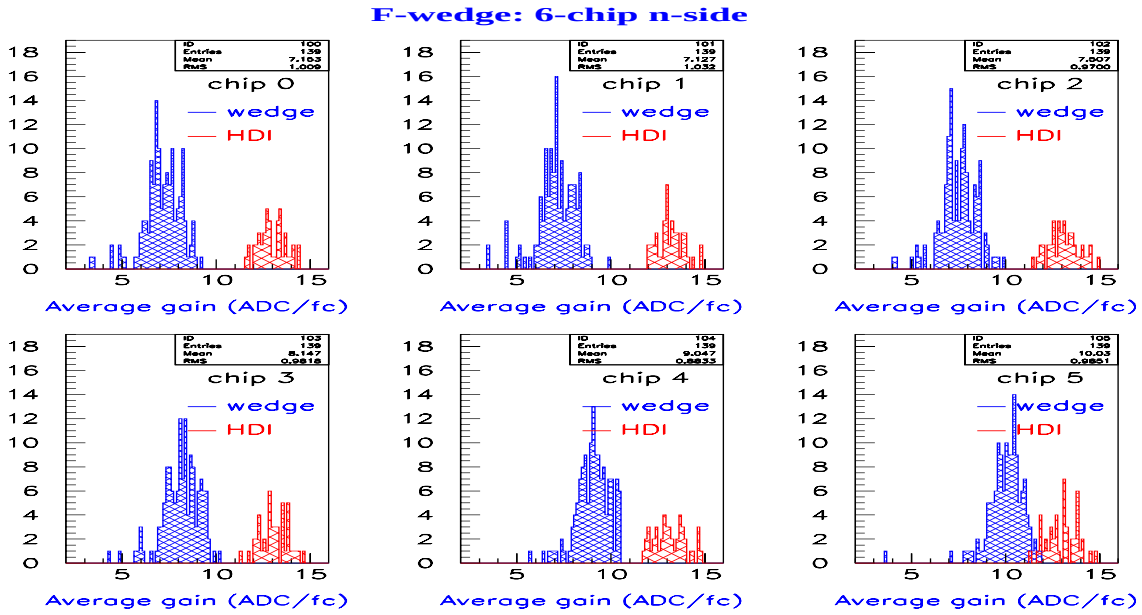

Figure 3.9: Average chip gain of a F-wedge and an HDI, n-side

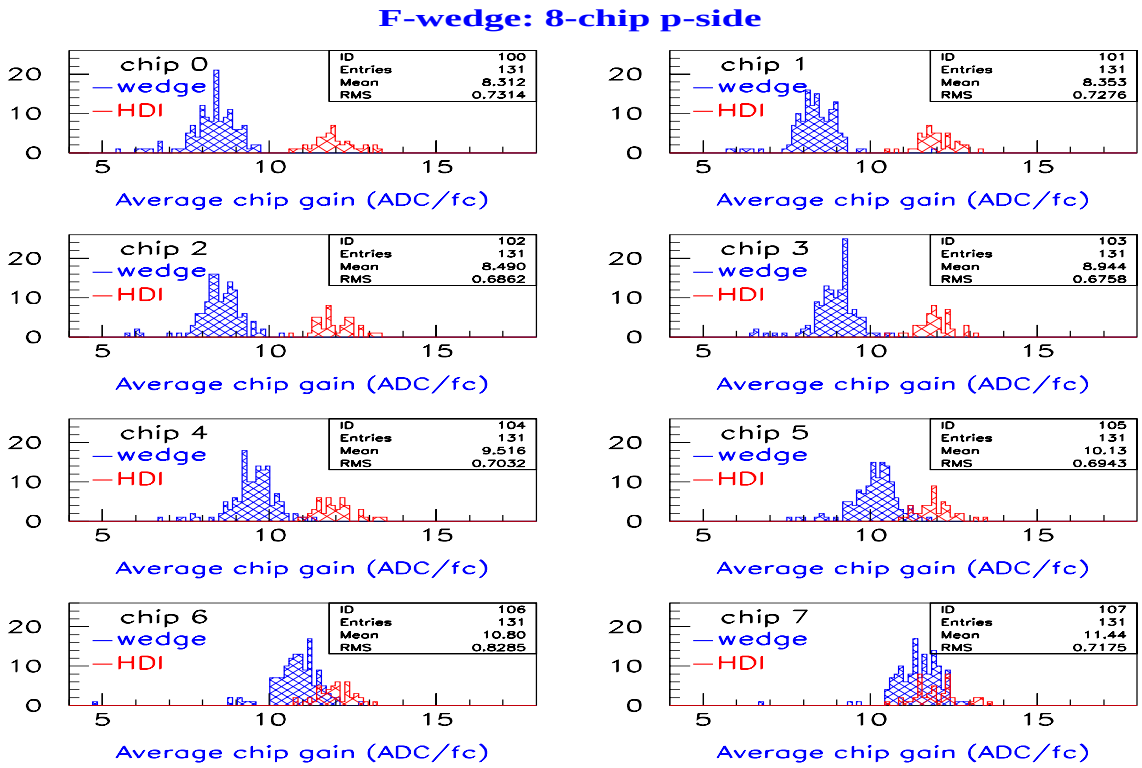

Figure 3.10: Average chip gain of a F-wedge and an HDI, p-side

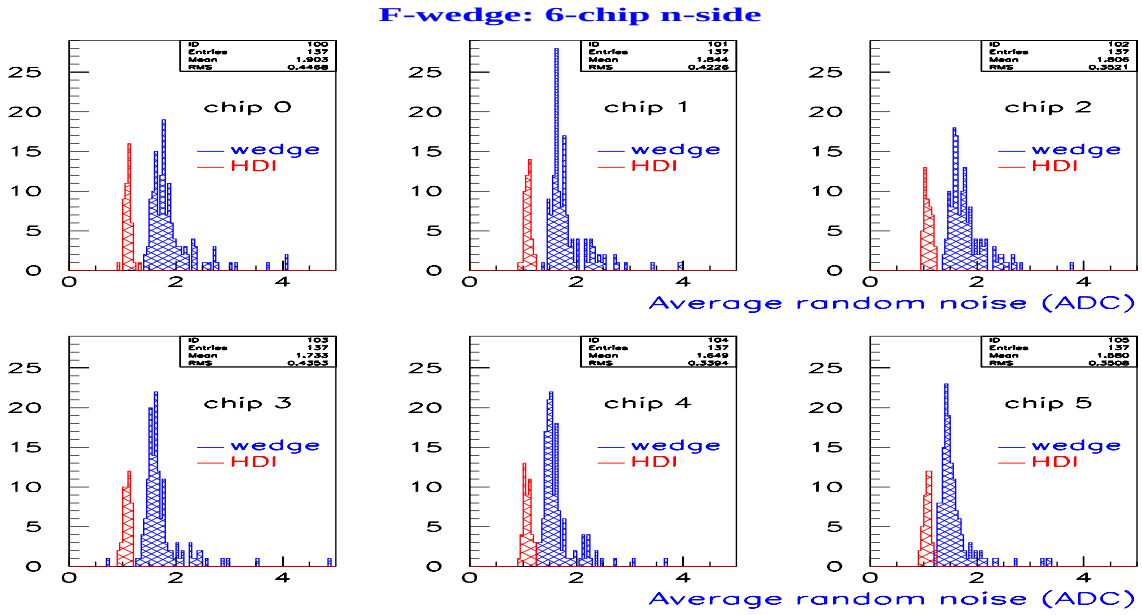

Figure 3.11: Mean random noise distribution for a F-wedge and an HDI, n-side

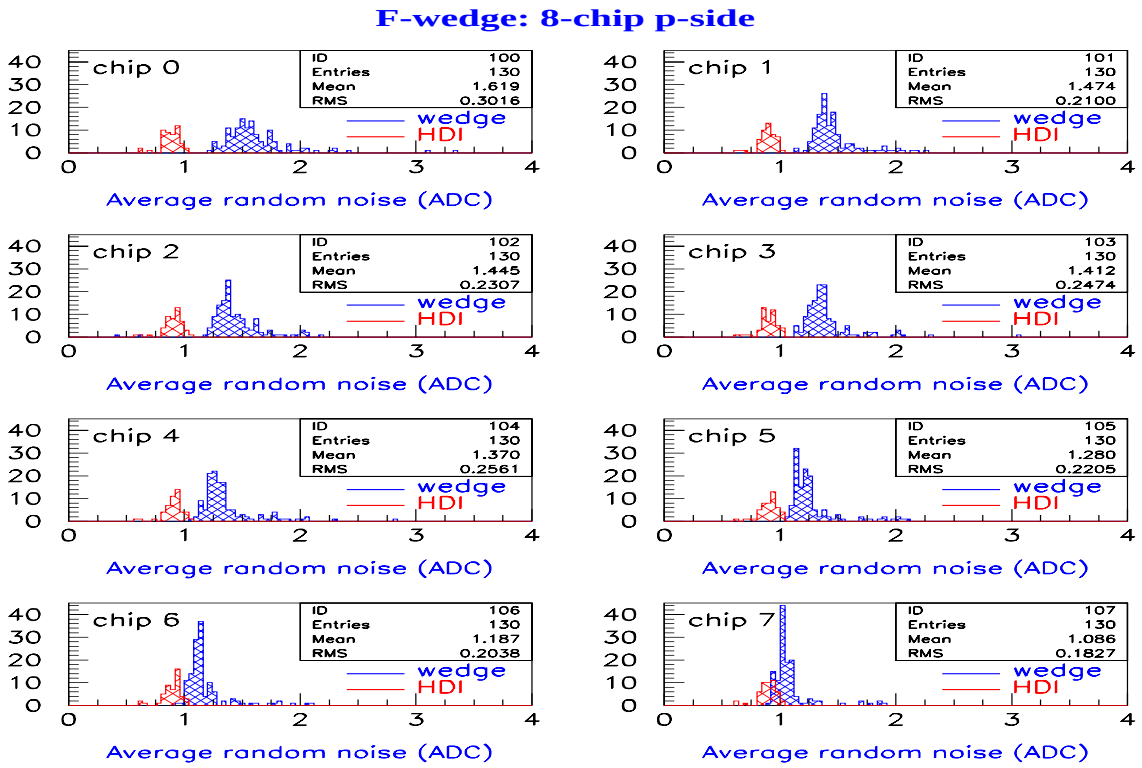

Figure 3.12: Mean random noise distribution for a F-wedge and an HDI, p-side

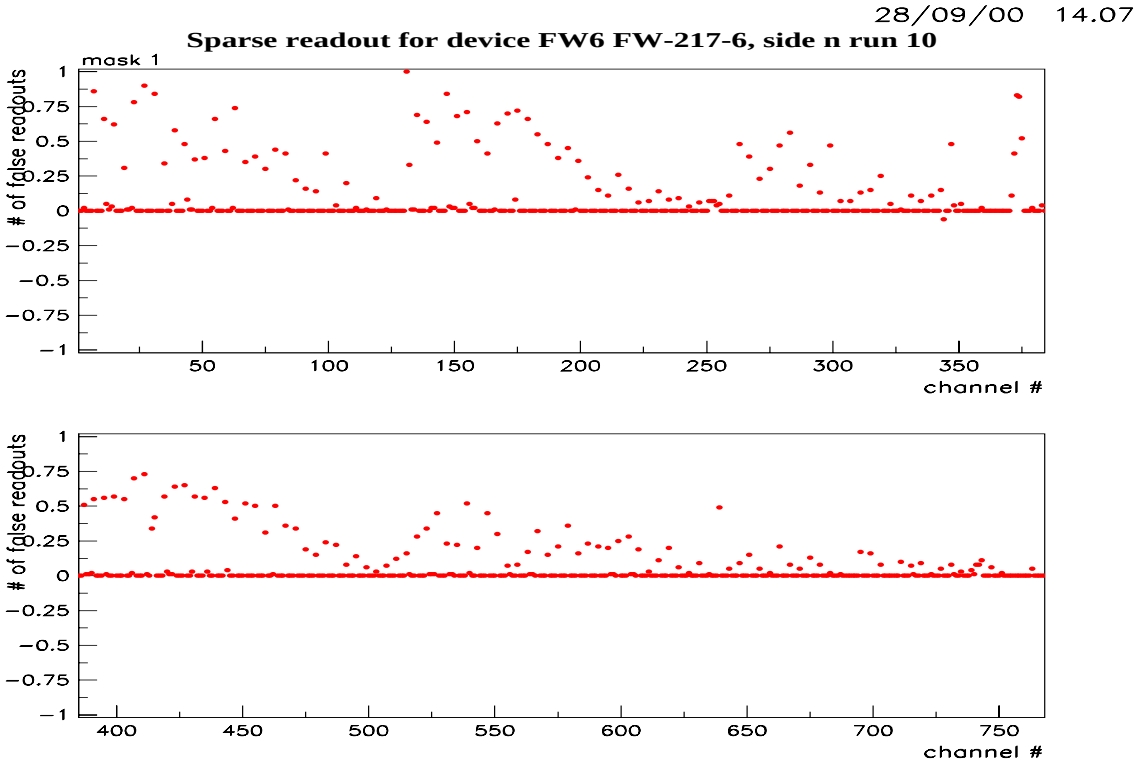

Figure 3.13: Typical F-wedge n-side sparse readout during burn-in

There were problems at burn-in which were present throughout the whole period of testing. These can be classified into two broad categories, readout problems and high voltage problems.

Readout Problems

The main issues with the readout were, for the most, problems with the KSU boards. Various errors were observed on a regular basis; the primary one was that the sparse readout was often irregular for the 6-chip side, with periodic variations on a chip-to-chip basis. An example of this is shown in Fig. 3.13. This feature would not be seen for the HDI burn-in. The reason for this was linked with the fact that at burn-in the low voltages were optimised for the first chip on the 8-chip side and not for the 6-chip side as there was only one low voltage power source for both chains. Whereas this would not have an impact for an HDI, the presence of the silicon sensor would amplify this difference and cause an erroneous sparse readout. A check was performed on another test-stand using the same spreadsheet as that in burn-in but optimising the low voltages for the 6-chip side. The results showed the sparse readout to be acceptable.

There were other features often seen and linked to problems with the KSU boards used at burn-in. For example the gain for chips was sometimes monitored to be zero

although the chips would respond correctly to an injection of charge. Also the noise pedestal would be displayed as 20 ADC counts for certain chips but the chips which displayed this and the total number of such noisy chips would change from run to run. A similar effect was seen with the pedestals under charge injection, although in this case the pedestals would fluctuate from their normal value to 0 ADC counts on a run-to-run basis. The last two problems would often be seen on the same wedge during burn-in.

High Voltage Problems

There were various problems seen at burn-in related to bias currents. There would be a tendency for the wedges to develop pinholes and trip the high voltage supplies even though the debugging procedure would test the wedges under a higher voltage. This would usually occur during the first run of the burn-in; however this could occur also while applying the voltage to the sensor (even at 5 V). This led to the belief that occasionally the power supplies would have a surge in voltage, when turning them on, which could blow the capacitors. This would not be worrying in itself as one of the functions of burn-in was to make sure that the wedges were in a stable state. However only one capacitor would fail at a time, making some wedges go through the burn-in procedure multiple times. The F-wedges with Micron sensor were especially problematic in this respect. In order to limit the failure rate at burn-in, the wedges were left fully biased for 30 minutes during debugging and the currents were monitored. If they passed this further test they were then sent to burn-in.

The leakage currents also had a tendency to increase over the course of the burn-in cycle as shown in Fig. 3.14. This was similar to what was seen during debugging. The increase was found, from subsequent tests, to be temperature dependent. As the temperature at burn-in was higher than the theoretical operating temperature value of 5° C it was expected that for most of these F-wedges the currents would stabilize when operating at the correct temperature.

3.3.5 Laser Test

The laser test was the only test which verified the response of individual channels to charge. The schematic of the laser test is shown in Fig. 3.15. The wavelength of the laser was 1064 nm, for which the attenuation length of the laser light through the silicon was 206 μm; long enough to allow the whole silicon to be tested, as opposed to just the surface layer. The objective of the laser test was two-fold: to determine

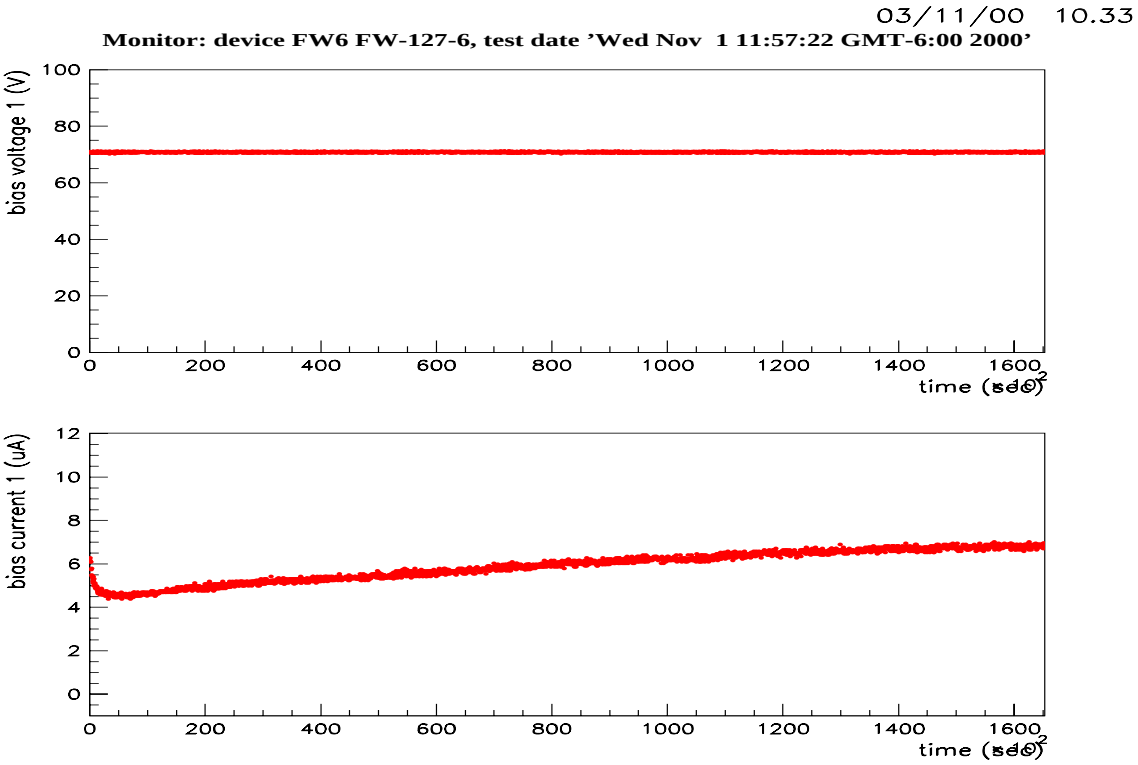

Figure 3.14: Bias voltage (top) and bias current (bottom) for a Micron sensor during burn-in

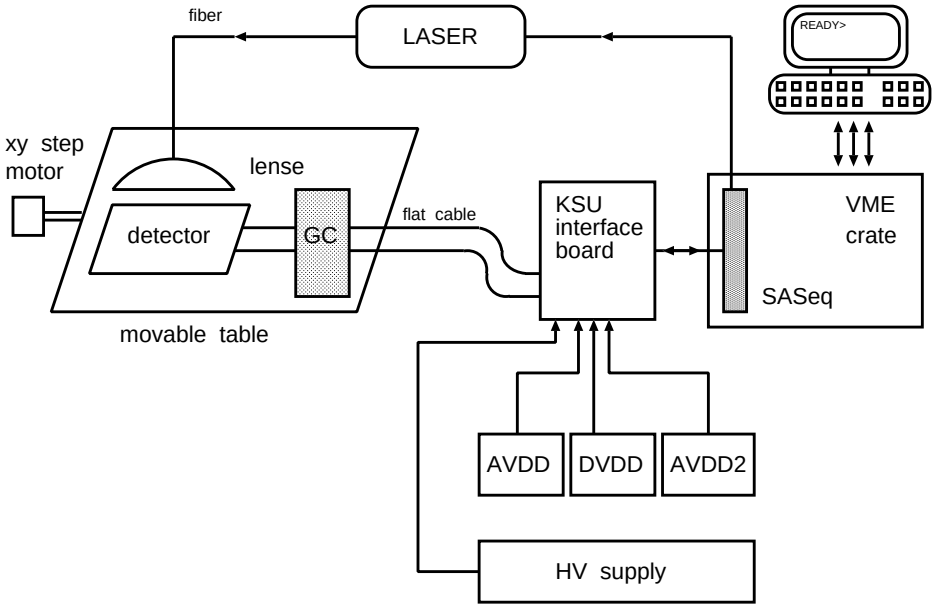

Figure 3.15: Schematic of the laser test stand

the number of dead/disconnected channels by scanning all the channels with the laser and to determine the depletion and operating voltages of the module.

The interface to the module was similar to the stand-alone test stand although the low voltage and the bias voltage were interfaced via the KSU boards as in the burn-in test. The module was mounted on a movable table which could be positioned such that the laser light was focused on one particular point. The table could also be moved across the laser beam to scan all channels.

The depletion and operating voltages of the module were determined in the course of the same test. The laser was focused on a fixed point on the sensor far from the sensor boundary. The positive bias voltage was scanned in 5 V steps from 0 V to the maximum voltage determined during debugging while the negative bias voltage was fixed to its maximum value. After each step in voltage the amplitude of the laser light in ADC counts was recorded. The profile versus voltage is characterised by two features: a linear increase in the number of ADC counts as the bulk is cleared of free charge carriers and a plateau beyond which there is no increase in collected charge. The operational voltage was defined to be 5 V above the voltage at which the ADC counts plateau. The depletion voltage was defined as the intersection point between straight line fits to the two regions. The depletion voltage was in good agreement with that measured during the preliminary sensor tests.

The number of dead channels was determined by scanning all the strips with the laser. The sensor high voltage bias was set to the operational bias voltage determined in the previous test. The laser intensity was adjusted so that amplitude was 90-120 ADC counts. The table was positioned and then moved so that all the strips would pass under the laser. Every channel was read out 10 times while the maximum of the laser spot was located on that strip and from this the mean amplitude and standard deviation of the channel was calculated. A strip was determined to be dead if the mean was less than 40 ADC counts.

3.3.6 F-Disk Assembly

Once the laser test had been performed, the F-wedges were graded according to the following four criteria:

- Number of dead channels as determined by the laser test.
- Number of noisy channels as determined by burn-in.
- Leakage current and I-V characteristics.

- Mechanical grade.

A F-wedge module was classified as "A" if the number of dead and noisy channels was less than 2.6% of the number of channels for the n and the p-side independently, "B" grade if either side had more than 2.6% but less than 5.2% and "C" grade for the case in which the total number for either side was greater than 5.2%. The grade could be lowered if the F-wedge had particularly high or unstable leakage currents.

The mechanical grade was a measure of the flatness of the beryllium plate used and on the general physical properties of the detector module. The mechanical grade would lower the overall grade of the module if less than "A". Only "A" and "B" grade modules were installed on the F-Disks.

Before mounting on the rings the bonds providing the bias voltage to the sensor were encapsulated to protect them during the alignment. Initially also the chip to sensor bonds were encapsulated using the same encapsulant as that used for the HDIs. This however was seen to have problems. The weight of the encapsulant could squash some of the bonds so that bonds from adjacent channels would touch resulting in crosstalk and in a high current. Furthermore leakage current tests indicated that there was an additional problem due to interaction of the encapsulant and the double-sided sensor, which tended to result in higher, more unstable currents. Hence this process was discontinued and only a few modules which had these bonds encapsulated and which did not exhibit problems were mounted on the first F-Disk produced.

The F-wedges were again electrically tested prior to mounting. One side of the ring was populated at a time and once a few wedges had been installed and aligned the installed F-wedges were tested again to ensure that there had been no damage during the installation and alignment process. Although most wedges were installed without incident, the procedure was inherently risky which led to some of the wedges being damaged after installation. These had to be removed, repaired and passed through debugging again. Working F-Disks were removed from the mounting fixture and stored in a static-free dry-box before mating with a Barrel or with other F-Disks. Before mating, the F-Disk would be tested again in its entirety. In order to minimize heat transfer from the chips in the Barrel modules to the F-Disk a 1 mil kapton diaphragm was mounted between the two. It had been previously verified that the presence of the kapton did not modify the I-V characteristics of the F-wedge modules.

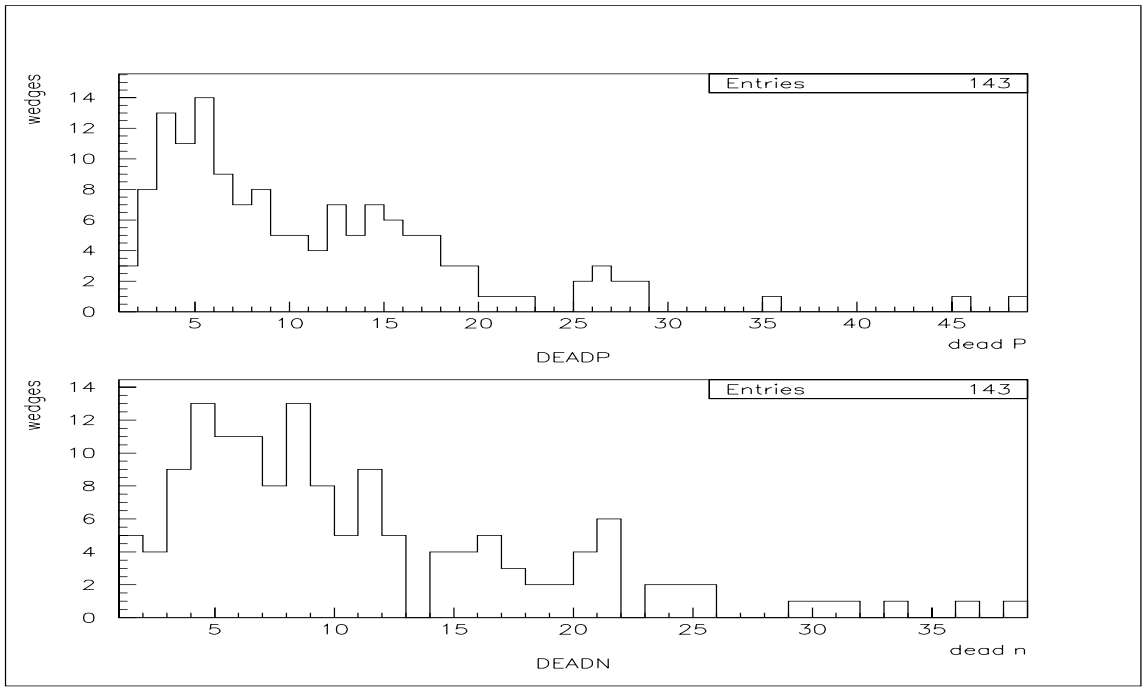

Figure 3.16: Number of dead channels per wedge for the p-side (top) and the n-side (bottom)

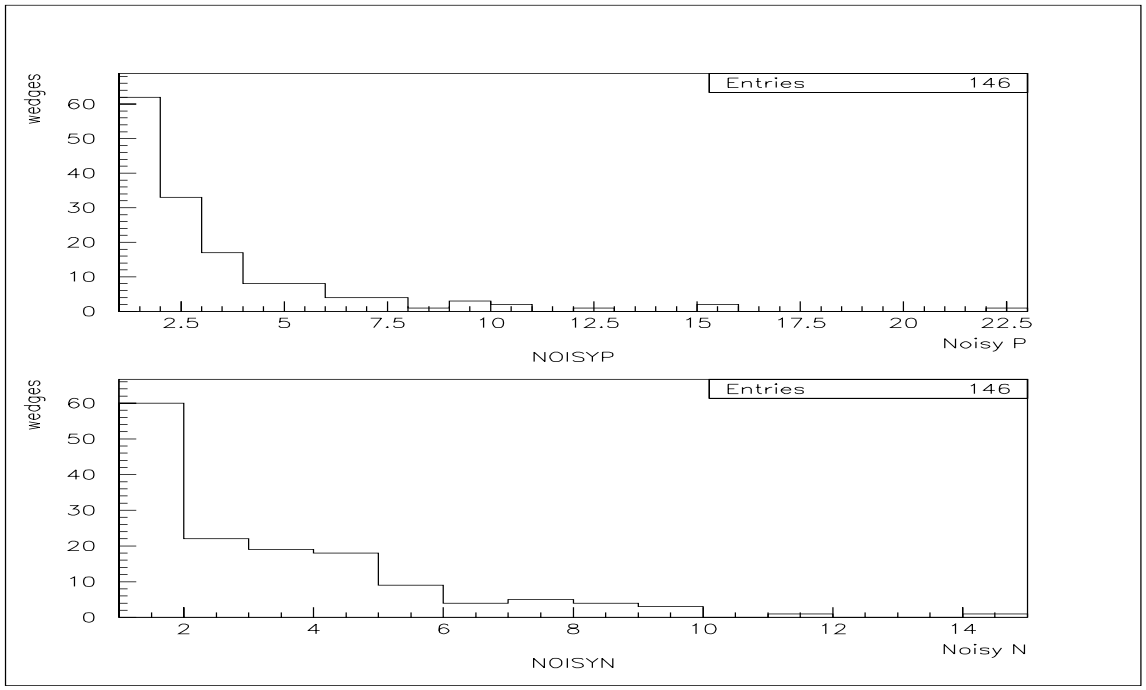

Figure 3.17: Number of noisy channels per wedge for the p-side (top) and the n-side (bottom)

Disk No.	Dead (%)	Noisy (%)
1	0.92	0.23
2	1.00	0.21
3	1.75	0.05
4	1.00	0.32
5	1.65	0.05
6	1.02	0.25
7	1.25	0.33
8	1.40	0.13
9	1.22	0.45
10	1.32	0.15
11	1.15	0.45
12	1.25	0.35

Table 3.3: Percentage of dead and noisy channels in the F-Disks

3.4 F-Disk Performance

After disk assembly there were a total of 1521 dead channels on the p-side (1.03%) and 1486 dead channels on the n-side (1.15%). Fig. 3.16 shows the distribution of dead channels on the p and n sides for all of the wedges. The highest percentage of dead channels per side for a wedge was 4.9%.

The total number of noisy channels was determined to be 419 on the p-side (0.28%) and 416 on the n-side (0.32%). The noisiest p-side has 22 channels, while the noisiest n-side has 14 channels. Fig. 3.17 shows the distribution of noisy channels. A summary of the percentage of dead and noisy channels per disk is given in Table 3.3

The disks were assembled so that each disk had wedges with similar bias voltage requirements. Each disk has three distinct high voltage supplies because every high voltage power supply provides the voltage to four modules. Hence the wedges are biased in three groups of four wedges. The voltage is applied as a split bias voltage so that there is a maximum negative voltage and a positive operating voltage determined as described in the previous sections. Table 3.4 lists the negative and positive voltage for each of the three high voltage groupings for each disks. The operating voltage for each F-wedge is displayed in Fig. 3.18.

Fig. 3.19 shows the distribution of leakage current at operational voltage for the F-wedges mounted on the F-Disks. Most of the wedges operate with a leakage current of less than 20μA although a couple of F-wedges have a leakage current over 100 μA.

Disk No.	Wedge type	Group 1		Group 2		Group 3	
		V^-	V^+	V^-	V^+	V^-	V^+
1	MH	20	50	20	60	10	80
2	MH	10	70	5	80	25	65
3	E	20	25	15	30	20	35
4	MH	30	50	20	55	5	75
5	E	20	25	20	35	15	40
6	MM	15	35	20	30	10	45
7	MM	10	55	15	35	10	40
8	E	15	45	25	25	20	30
9	MH	10	75	15	65	30	50
10	E	20	25	15	35	20	30
11	MH	20	60	20	70	15	60
12	MH	5	75	30	50	20	60

Table 3.4: F-Disk operating voltages in Volts. The wedge types are: MH - Micron High Depletion, MM - Micron Medium Depletion, E - Eurisys

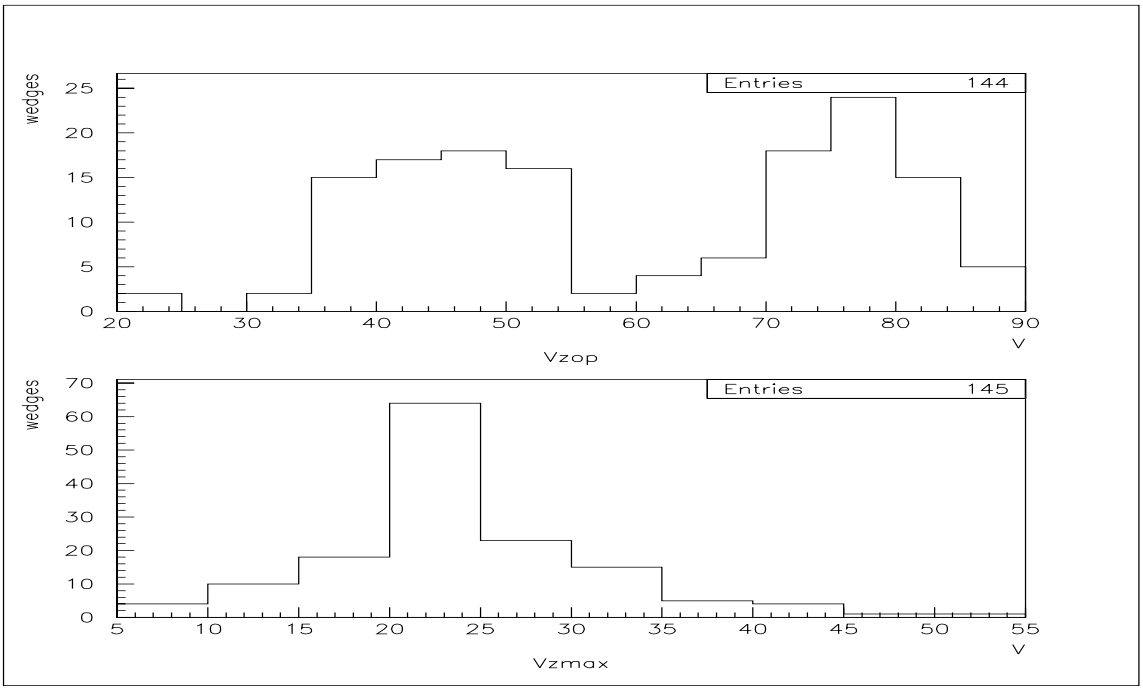

Figure 3.18: Positive bias voltage (top) and the maximum negative bias voltage (bottom) for F-wedges mounted on the F-Disks

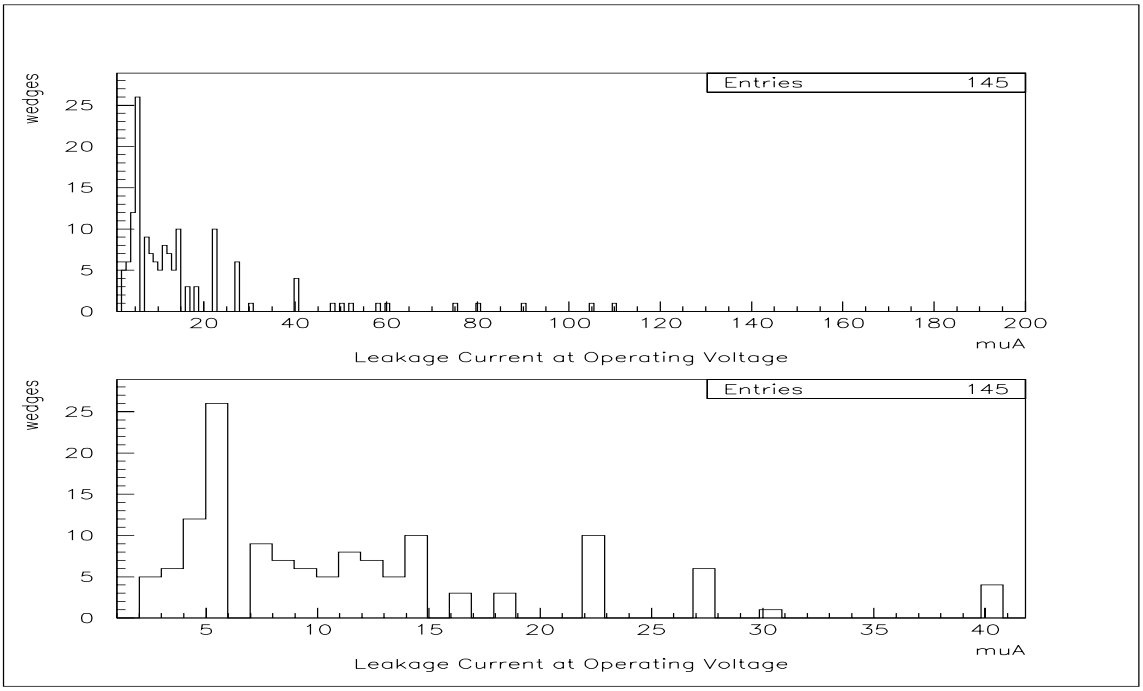

Figure 3.19: Leakage current for each F-wedge in μA. The bottom plot shows an expanded scale of the region of lower leakage current

3.4.1 Current Performance

The SMT was completed on schedule and installed on time. The SMT, despite its complexity, was the first major Run II upgrade detector to be fully operational both mechanically and in terms of the read-out system. First alignment results show that the SMT was constructed and installed to within expectations. Currently 89% of the barrel modules, 94% of the F-disk modules and 84% of the H-disk modules are enabled and operational. The modules which are not currently operational are not necessarily disabled due to problems with the actual HDI or the chips but could be linked to problems with the interface boards or the sequencer boards. During the next shutdown it is envisioned that a subset of the disabled modules will be recovered.

Since its installation the SMT system has had various problems; such as the failure of various low voltage power supplies. These were fixed and are now working reliably. There were also problems with some of the high voltage fan-out boxes. The fan-out boxes branch each co-axial cable from the high voltage power supplies into four ribbon cables such that each high voltage pod can bias four modules. It was discovered that problems with the design and construction of these boxes led to unstable bias currents, hence they were re-designed and requisitioned. The bias currents generally show a large spread in values and in stability, ranging from 2-3 μA

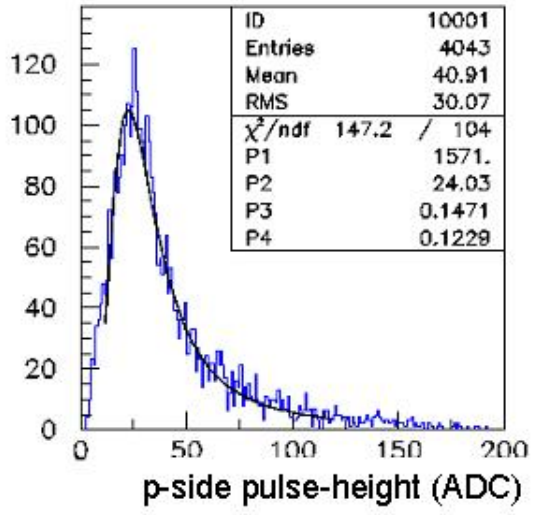

Figure 3.20: Cluster charge distribution in an SMT module [42]

and stable to 450 μA and wildly fluctuating. This does not seem to be bulk current i.e. it does not originate from the sensor. This is being investigated together with the dependence of the bias currents on radiation.

There have also been some problems connected with the readout. One of the most noticeable is linked with the number of noisy channels for some F-Disk modules. There are 40 modules with more than 10% of noisy channels (noise greater than 3 ADC counts) for the p-side , of which 16 have more than 30% of noisy channels. There are about half the number of modules with the same percentage of noisy channels on the n-side. Such high noise levels were never seen during the production stage. The noise seems to be generally linked to F-wedges with Micron sensors and does not seem to have any bias or temperature dependence. Furthermore it only affects a limited number of chips on each detector and the modules affected are distributed throughout the F-Disks. The source of the noise is currently under investigation, as is a way to limit the impact on the physics.

Despite these problems the SMT is fully functioning and, as seen by the p-side pulse height distribution shown in Fig. 3.20, is successfully detecting charge particles. The signal for a minimum-ionising particle is of $\sim$25 ADC counts and the noise level is on the order of 2 ADC counts, giving a signal to noise > 12. Hence Fig. 3.20 clearly displays the signal due to a minimum-ionising particle, this is consistent with the theoretical distribution [42][43].

Overall the SMT is working well, is fully commissioned and, as demonstrated by the physics results, is to first order understood. There are various features which still need to be addressed before the SMT can be considered to be fully understood.

Chapter 4

Jet Response Using a Z + Jet Sample

The jet response is a component of what is commonly referred to as the jet energy scale. The purpose of the jet energy scale is to derive a correction factor for jets such that, on average, the energy measured in the calorimeter can be related to the particle level energy of the same jet. In Run I the jet response at DØ was primarily derived using a γ + jet sample [44][45]. A complementary sample which can feasibly be used in Run II is one in which the photon is replaced by a Z boson, subsequently decaying to either muons or to an electron-positron pair. This sample is topologically similar to the photon sample, hence a similar method can be used. In Run I its use was limited due to its lower cross-section and consequent lack of statistics [20][46]. In Run II, due to the higher integrated luminosity, this method can be used as a verification of the response from the photon sample both via a direct derivation of the response and via a closure test of the overall jet energy scale.

4.1 Basic Objects

4.1.1 Jet Reconstruction

Jets at DØ are reconstructed using either a modified cone or the K_T algorithm [47]. The default algorithm at DØ is the cone algorithm and the jet energy scale using the photon + jets sample is calculated for this algorithm. K_T jets will not be discussed in detail here. A complete description of the K_T algorithm can be found in the literature [48][49][50]. The cone jet algorithm used at DØ is based on the joint theoretical and experimental recommendations for the reconstruction of jets at hadron colliders [51].

All the jet variables are defined using a 4-vector recombination scheme in which the energy and the momentum is calculated as a vector sum from the components of the individual towers within the jet. From the energy and the components of the momentum, the p_T is defined as the magnitude of the momentum component in the $x-y$ plane, while the ϕ and rapidity are defined as in Equations 4.1 and 4.2:

$$\phi = \tan^{-1}\frac{p_y}{p_x}, \tag{4.1}$$

$$y = \frac{1}{2} ln \frac{E+p_z}{E-p_z}. \tag{4.2}$$

The rapidity defined in Equation 4.2 in the case of massless particles/ towers/ partons is equivalent to the pseudo-rapidity η defined in Equation 2.1. As the energy deposits in the towers are treated as massless i.e. $E_{tower} = |\mathbf{p}_{tower}|$ the p_T, for objects encompassing more than one tower, is equivalent to the vector sum of the transverse components of the energy of each tower. Historically, at DØ E_T is equivalent to p_T for this reason, as opposed to it being the scalar sum of the transverse energy of each tower. The term E_T, unless otherwise stated, will refer to the vector sum and for consistency the units GeV/c will be used in this chapter.

The reconstruction of jets starts from an E_T ordered list of seed towers above a threshold of 500 MeV/c. Using these seed towers all towers, i, within a cone size R centred on the seed tower i.e.

$$\sqrt{(y^i - y^{seed})^2 + (\phi^i - \phi^{seed})^2} \leq R, \tag{4.3}$$

are added to create proto-jets and are used to calculate the p_T weighted centroid. If the new centroid is still within the seed tower the calculation of the centroid is re-iterated until the centroid either falls outside the boundary of the original seed tower or the shift in position of the centroid is less than a distance ϵ. The latter proto-jets are kept. The default value of ϵ for the Run II DØ algorithm is 0.001.

Also added to the list of proto-jets are proto-jets calculated from the position of the mid-points between all combinations of the original proto-jets. The mid-points are identified from the vector sum of the momentum of the proto-jets. Proto-jets from the mid-points are only included in the final list if all the proto-jets from which the mid-point is defined lie within a distance $\Delta R \leq 2 \cdot R_{cone}$. The inclusion of mid-points is to eliminate the dependency of seed based jet algorithms on infra-red radiation.

The proto-jets are then passed through a split-merge algorithm to determine the final list of jets. In this algorithm the highest p_T proto-jet in the proto-jet

list is selected. If this proto-jet does not share calorimeter towers with any other proto-jet it is added to the final jet list and removed from the proto-jet list. If it does share towers with other proto-jets the highest p_T neighbour is selected and if $E_T^{shared}/E_T^{neighbour} \geq f$ (typically 0.5) the proto-jets are merged, the proto-jet is recalculated and the neighbour is dropped from the proto-jet list. If this equality is not satisfied the proto-jets are split, the shared towers are assigned to the closest proto-jet and both proto-jets are recalculated. This procedure is iterated until there are no more proto-jets remaining.

The main variables associated with a jet are the following:

- Hot fraction, defined as the scalar E_T ratio of the tower with the highest E_T deposit to the tower with the second highest.
- n90, defined as the number of towers which comprise at least 90% of the jet energy.
- Coarse hadronic fraction, defined as the ratio of energy deposited in the coarse hadronic layers to the total jet energy.
- Electromagnetic fraction, defined as the ratio of the energy deposited in the electromagnetic section of the calorimeter to the total energy of the jet.

The hot fraction and n90 concern primarily real data as they are used to eliminate non-physical jets which are the result of hot cells in the calorimeter.

4.1.2 Electromagnetic Objects

Electromagnetic objects are constructed using a simple cone of radius, $R = 0.2$ in $\eta - \phi$ space centred on p_T ordered seed towers exceeding 1.5 GeV/c . The basic variables associated with the electromagnetic object are isolation, electromagnetic fraction and H-matrix. Isolation is calculated as in Equation 4.4, where R_{cone} refers to the cone size used.

$$iso = \frac{E(R_{cone} = 0.4) - E(R_{cone} = 0.2)}{E(R_{cone} = 0.2)}. \tag{4.4}$$

The electromagnetic fraction is defined in a similar manner to that for jets. The H-matrix is a χ^2 likelihood parameter based on an 8×8 matrix [52]. The parameters used in the H-matrix are the four fractional energy deposits in the different layers of the electromagnetic calorimeter, the logarithm of the total energy deposit in the calorimeter, the transverse size of the cluster in the 3rd electromagnetic layer $\sigma(\phi)$

and $\sigma(r/z)$ and the position of the vertex along the z-axis divided by the vertex resolution.

If the electromagnetic object has a track match the ϕ and θ values are taken from the track. The object's momentum vectors p_x, p_y and p_z are defined respectively as $E\cos\phi\sin\theta$, $E\sin\phi\sin\theta$ and $E\cos\theta$ where E is the energy deposited in the electromagnetic calorimeter. If there is no track match all the variables are calculated with respect to the reconstructed primary vertex using the position of the 3rd electromagnetic layer.

4.2 The Jet Energy Scale

The three main factors at DØ which contribute to the discrepancy between the measured jet energy and the particle level jet energy are the following: the jet cone size, the collider environment and the inherent nature of a sampling calorimeter which does not detect all the energy deposited in it. The collider environment can add additional energy deposits in the calorimeter whereas the nature of the calorimeter can distort the measured jet energy due to resolution and reconstruction effects. The limited jet cone size implies that there can be a net energy flow out of the jet boundary due to showering in the calorimeter. A correction for showering effects is only applicable to jets reconstructed using the cone algorithm and henceforth jets can be understood to be cone jets unless otherwise stated. A similar energy scale method to the one presented here was used in Run I to correct jets found using the K_T algorithm [53][54]. All three factors contribute in different ways, at different energies and need compensation via different methods. The relation between the measured energy and the particle level energy of a jet is given in Equation 4.5.

$$E_{jet}^{particle} = \frac{E_{jet}^{calor} - E_{offset}(R, \eta_{phys}, L)}{R_{jet}(R, \eta_{det}, E)F_S(R, \eta_{phys}, E)} \tag{4.5}$$

Where E_{offset} is the offset correction, R_{jet} is the jet response and F_S is the showering correction.

4.2.1 Offset Correction

The offset correction, E_{offset}, in Equation 4.5 is the contribution to the measured energy from factors which are not directly related to the physics process of interest. This correction is assumed to be independent of the physics process being analysed, hence it is simply an offset term to the measured energy. This term arises from various contributions:

- From the underlying physics event, i.e. from the spectator partons which do not take part in the hard-scatter.
- From additional minimum bias $p\overline{p}$ interactions per crossing.
- From pile-up in the calorimeter, due to residual signals present in the calorimeter from the previous bunch crossing. This arises as the calorimeter electronics have a longer shaping time than the spacing of the bunches.
- From noise due to radioactive decay of the uranium absorber.

The offset correction depends on the radius of the cone R (as a larger cone size will include more energy), on the instantaneous luminosity L (due to an increase in the number of interactions per crossing with luminosity) and on the physics pseudo-rapidity, η_{phys}, the pseudo-rapidity with respect to the interaction vertex. The dependence on the last term is present due to the different topologies of the processes which contribute to the offset energy. Whereas the noise can be assumed to be uniform throughout the calorimeter, the contribution of minimum bias events and the underlying physics event is mostly in the forward direction, i.e. at large η_{phys}.

The offset term can be written in the form given in Equation 4.6 [46]:

$$E_{offset} = (1+ < N_{ZB} >)E_{ue} + E_{noise} + E_{pile}. \tag{4.6}$$

E_{ue} is the energy from the underlying physics event, E_{noise} is the contribution of the noise from uranium decays and E_{pile} is the energy due to pile-up. The underlying physics event has a contribution from the spectator quarks in the hard scatter but also from additional hard core interactions from other $p\overline{p}$ pairs. Hence the form of Equation 4.6, $< N_{ZB} >$ is the average number of hard core interactions events in addition to the hard scatter at a given luminosity. The subscript ZB refers to a Zero Bias sample, i.e. events for which there is no trigger requirement other than a $p\overline{p}$ crossing. This is opposed to a minimum bias data sample for which there is a trigger requirement of a hard core interaction. The $< N_{ZB} >$ distribution is Poissonian.

The contribution of the underlying physics event purely from the spectator quarks of the hard scatter can be determined by taking the difference in energy density between minimum bias events and events in which there are no hard core interactions. The other terms are simply determined by the energy density from a sample of zero bias events.

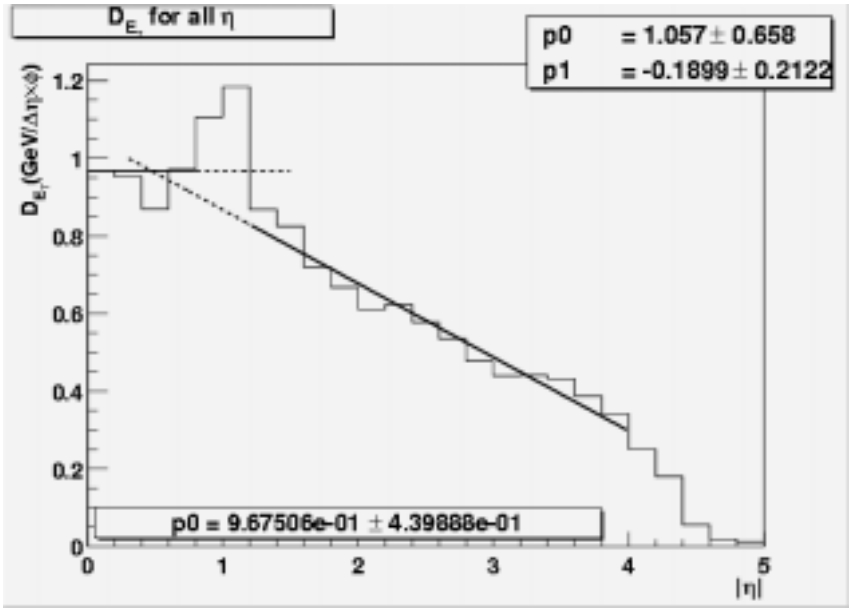

Figure 4.1: E_T density in $\eta \times \phi$ space in minimum bias data [55]

As the contributions from pile-up and multiple interactions are a function of instantaneous luminosity they need to be determined at a variety of luminosities. The underlying physics event from the spectator quarks instead does not, as it is the energy associated with the interaction of a single $p\overline{p}$ collision and hence does not scale with luminosity.

At present the instantaneous luminosity of the Tevatron is low enough for pile-up and multiple interactions to have a negligible effect. As a consequence the offset correction is simply defined as the energy density in minimum bias events. This is shown in Fig. 4.1 for the ICHEP02 data sample [55].

4.2.2 Jet Response

The jet response, R_{jet} is the largest correction to the energy of the jet. R_{jet} is generally less than one due to dead material in the calorimeter, uninstrumented regions, module-to-module differences and an e/π response ratio greater than one. The response is a function of the detector pseudo-rapidity, η, i.e. the pseudo-rapidity with respect to the centre of the detector. This dependence is due to module to module differences and uninstrumented regions which are not homogeneous throughout the detector. The response is parametrised as a function of the jet energy which introduces a further dependency on the cone size as different cone sizes will have varying amounts of energy in the cone. The response is obtained using the Missing E_T Projection Fraction (MPF) method which will be described in detail in Section 4.3

4.2.3 Showering Correction

The showering correction uses the results of the previous corrections hence it is the final correction to be applied to complete the jet energy scale. The showering correction compensates for the net energy flow out of the cone due to particles interacting with the detector. This interaction with the detector subsequently forms a shower of other particles which may deposit energy outside of the original cone boundary. It is important to stress that not all of the energy deposited outside of the cone can be attributed to this process as there are physics processes, such as final state gluon radiation and out of cone fragmentation, which produce significant energy deposits from the original quark jet outside the cone boundary. When correcting to the "particle level" this type of contribution should not be taken into account as it would result in an over-correction to the jet energy.

The showering correction is calculated by constructing concentric cones centred around the original jet centroid with $\Delta r = 0.1$ in $\eta \times \phi$ space up to a radius of 2.0. The energy density in each cone is calculated by summing up all the calorimeter towers in the cone and is plotted as a function of radius. The energy offset, as well as an extra baseline term due to particles produced far from the jet, is subtracted from this. From this the fraction of energy deposited in the cone size of interest with respect to the "real jet limit" is calculated.

The real jet limit is defined to be the radius at which all of the energy of the jet is contained in the cone. The real jet limit changes with η_{phys} as pseudo-rapidity space shrinks toward higher values whereas real space does not, therefore the jet limit is larger at high pseudo-rapidities. If the same jet limit were to be used for all pseudo-rapidities the effect of the showering correction would be artificially low at high η_{phys} as less of the showering would be included within this limit.

The out-of-cone physics which should not be included in the correction can be compensated for via Monte Carlo simulations which keep track of the connection between the energy deposits in the calorimeter and the individual particles. These Monte Carlo simulations can subsequently be used to subtract the extra energy density due to out-of-cone physics from the correction.

The showering correction is parametrised in term of jet energy after the offset and response corrections and is binned in terms of η_{phys}. The showering profile, after offset and baseline energy subtraction, for 0.7 cone jets in the central calorimeter region for the ICHEP02 data sample is shown in Fig. 4.2 [55]. The profile in Fig. 4.2 does not include the correction for out-of-cone physics effects.

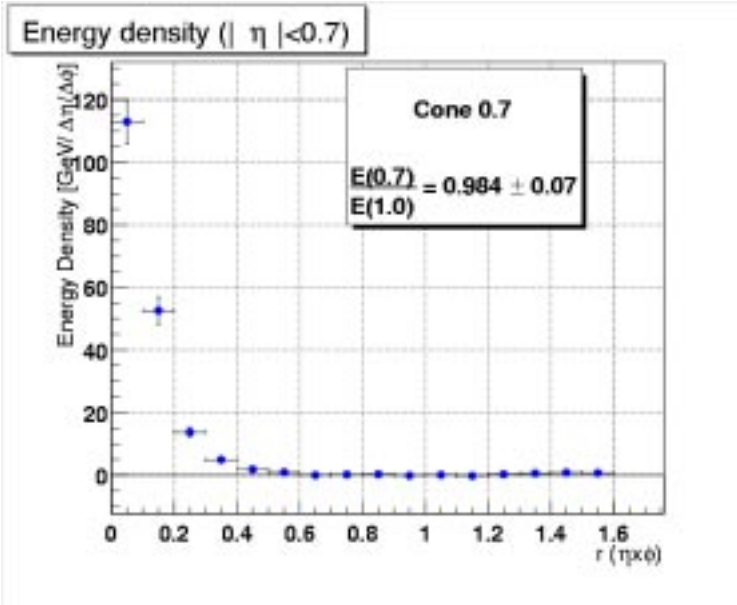

Figure 4.2: Showering profile for $R = 0.7$ cone jets in the central calorimeter region after offset and baseline energy subtraction [55]

4.3 The Missing E_T Projection Fraction Method

4.3.1 Principle of the Method

The MPF method is based on the fact that, for jets in the GeV energy range, the intrinsic transverse momentum of the partons in the $p\overline{p}$ collision is negligible. Therefore momentum in the transverse plane $(r - \phi)$ can be considered conserved. Hence if the jet recoils against an object, whose energy can be measured accurately, transverse momentum conservation can be used to calibrate the jet energy. Fig. 4.3 shows the two leading order processes in which a jet recoils against a Z boson. In principle both the muon and the electron decays of the Z can be used but henceforth the focus will be on the decay to electrons.

Although the electromagnetic particles are detected in the same calorimeter as

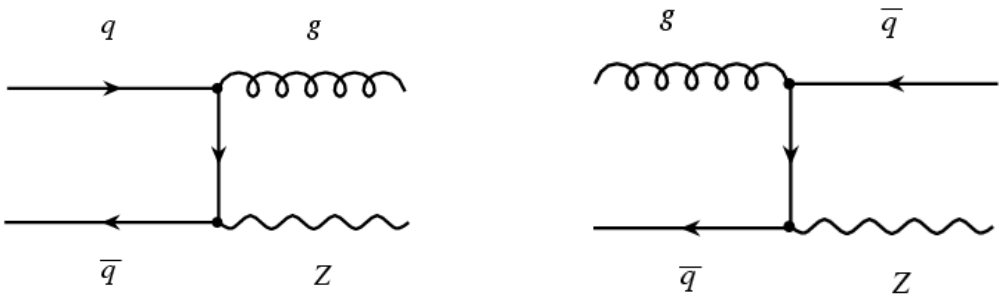

Figure 4.3: Leading order Feynman diagrams for Z + jet production

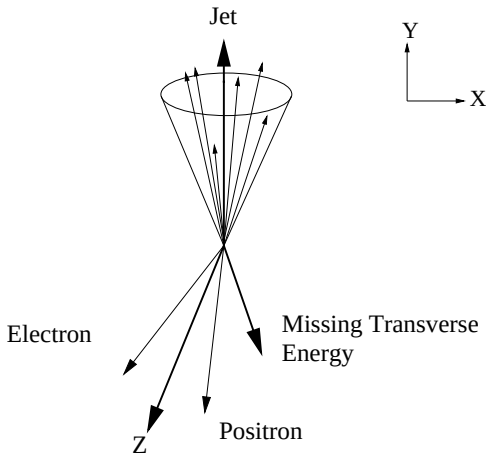

Figure 4.4: Schematic of a Z + jet event in the transverse plane

the jets their energy can be measured and calibrated more accurately than that of the jets, for a variety of reasons. Electromagnetic showers are contained, for the most part, within the electromagnetic section of the calorimeter which is more finely segmented than the hadronic section. Furthermore the electromagnetic energy scale, R_{em} can be accurately calibrated using well known resonances such as the Z boson. The MPF method is described in detail from its use in Run I [44][45].

4.3.2 Basic Definitions

Fig. 4.4 shows a schematic of a typical event which can be used to measure the jet response. The missing transverse energy, $\not\!\!E_T$, is defined as in Equation 4.7. The transverse momentum of the Z boson is defined as the vector sum of the transverse energy of the electron and the positron.

$$\not\!\!E_T = -\left(\sum_i E_{x_i},\ \sum_i E_{y_i}\right). \tag{4.7}$$

Thus the missing transverse energy in an event, treating the energy in the towers as if deposited by a zero mass particle, is the vector sum over all calorimeter towers of their transverse momenta. For a perfect calorimeter a non-zero missing transverse energy would indicate the presence of particles which do not deposit all their energy within the calorimeter, such as muons or neutrinos. For a real calorimeter and in the case of the schematic event shown in Fig. 4.4, $\not\!\!E_T$ is a direct consequence of the difference in response of the calorimeter to the electromagnetic particles and to the jet. By invoking the conservation of transverse momentum the $\not\!\!E_T$ in an event can be used to measure the response of the calorimeter to the jet. At a particle level,

ignoring detector effects, the conservation of momentum in the transverse plane reduces to the following vector sum:

$$\mathbf{p}_{T_Z} + \mathbf{E}_{T_{recoil}} = 0, \tag{4.8}$$

where the label *recoil* refers to the collection of particles deriving from the fragmentation of the parton. Taking into account the detector, the measured energies correspond to the particle level energies multiplied by a response factor. The relationship then changes to:

$$R_{em}\ \mathbf{p}_{T_Z} + R_{recoil}\ \mathbf{E}_{T_{recoil}} = -\not\mathbf{E}_T. \tag{4.9}$$

Assuming that R_{em} is determined from known resonances, the energy deposited by the electrons can be corrected back to the particle level. Multiplying Equation 4.9 by the unit vector $\hat{\mathbf{n}}_{T_Z}$ defined as $\mathbf{p}_{T_Z}/|\mathbf{p}_{T_Z}|$ the relations in Equations 4.10 and 4.11 are obtained.

$$p^{cor}_{T_Z} + R_{recoil}\ \hat{\mathbf{n}}_{T_Z} \cdot \mathbf{E}_{T_{recoil}} = -\hat{\mathbf{n}}_{T_Z} \cdot \not\mathbf{E}_T, \tag{4.10}$$

$$1 + R_{recoil}\frac{\hat{\mathbf{n}}_{T_Z} \cdot \mathbf{E}_{T_{recoil}}}{p^{cor}_{T_Z}} = -\frac{\hat{\mathbf{n}}_{T_Z} \cdot \not\mathbf{E}_T}{p^{cor}_{T_Z}}. \tag{4.11}$$

Finally substituting $-p^{cor}_{T_Z}$ for $\hat{\mathbf{n}}_{T_Z} \cdot \mathbf{E}_{T_{recoil}}$ from Equation 4.8, Equation 4.12 is obtained:

$$R_{recoil} = 1 + \frac{\hat{\mathbf{n}}_{T_Z} \cdot \not\mathbf{E}_T}{p^{cor}_{T_Z}}. \tag{4.12}$$

When including the offset and showering correction, Equation 4.12 no longer represents the correction for the total recoil but becomes the energy response to jets, i.e. R_{jet}. Furthermore Equation 4.12 is exact only for a perfect 2-body process (Z + one jet) which is generally not the case once higher order diagrams and final state radiation are taken into account. Hence the relation in Equation 4.12 is only approximate. Event cuts have to be applied to select events for which the topology of the event renders this a good approximation.

4.3.3 Event Selection

The event selection for the calculation of the jet response has to be such that an unbiased jet sample is obtained, in which the missing energy can be accurately related to the dynamics of the event and in which the electron and positron electromagnetic

energy deposits can be accurately calibrated. The event selection can be roughly divided into two parts; the basic object selection to identify Z+jet events and subsequent requirements to identify events which are suitable for the calibration.

Object Selection

At least one jet is required which satisfies the following cuts:

- Hot fraction < 10.
- Coarse hadronic fraction < 0.5.
- Electromagnetic fraction between 0.05 and 0.95.
- A minimum of three or more calorimeter towers contained within the jet cone have to account for 90% of the jet energy.

Two valid electromagnetic candidates are selected with the following cuts:

- H-matrix8 < 20.
- Electromagnetic fraction > 0.9.
- Isolation < 0.15.

After applying the energy correction using the certified electromagnetic energy scale v2.0 [56], a p_T cut of 15 GeV/c is made on the electromagnetic candidates. The two leading electromagnetic objects passing the cuts are selected, combined and a Z boson mass window cut of ± 20 GeV/c^2 around a central mass value of 90 GeV/c^2 is applied. Furthermore the electromagnetic candidates are required to be well contained in the electromagnetic section of the calorimeter ($|\eta| < 2.5$), away from ϕ cracks between the calorimeter modules and not located in the Inter-Cryostat Region (ICR) where there are areas with no electromagnetic calorimeter coverage. The last two requirements are imposed in order to minimise the effect of particles whose energy is not sampled in the calorimeter. Their energy would not be corrected for when correcting the energy of the electromagnetic objects and hence could distort the $\not\!\!E_T$. For a similar reason events which have jets passing the selection cuts which are located in the ICR are rejected. A jet response for the ICR can be, and indeed is, calculated using the photon+jet method: however it is not necessary for the verification of the photon+jet response using the Z+jet method.

In order to obtain a response consistent with the overall jet energy scale, the offset energy is subtracted from the energy of the leading jet. Finally, if the leading jet is in the forward region it is required to have a $p_T > 25$ GeV/c in order to avoid the effect of the low E_T bias which will be described in detail in Section 4.4.1.

Vertex quality cuts are also applied to ensure the quality of the calculation of the various energy components and of the $\not\!\!E_T$. At least one primary vertex has to have been identified and, in the case of several primary vertices, the vertex with the hardest sum of the p_T of the particles associated with it is selected. There also have to be at least three tracks pointing to this vertex and the z-position of the primary vertex is required to be within two σ of the beam interaction region with respect to (0,0,0) i.e. $\pm$50 cm.

Topology Cuts

In order for the MPF formula to be accurate the leading jet in the event is selected and is required to be back-to-back in the plane transverse to the Z boson direction. A cut $\Delta\phi > 2.8$ is placed on the separation in ϕ between the jet direction and the Z boson direction. The effect of doing this is two-fold: it eliminates events in which there is a significant contribution from either final state radiation or additional hard jets from fragmentation and also events in which the jet direction is biased due to additional energy deposits in the calorimeter not associated with the jet. This cut is a trade-off between statistics and preserving the accuracy of Equation 4.12. The value of the cut used was determined from studies of the MPF calculation in Run I. The effect of the residual topology bias will need to be re-derived for Run II. This was of the order of a few percent for Run I.

4.3.4 Method

Response Binning

The objective of the response calculation is to obtain an overall jet response for the whole calorimeter as a function of jet energy. As mentioned previously, for the purpose of this analysis, only the response for the central calorimeter, CC ($0. < |\eta| \leq 0.7$), and the end cap calorimeter, EC ($1.8 < |\eta| \leq 2.5$), are considered. There are various problems associated with calculating the response, via Equation 4.12, directly in terms of jet energy. The intrinsic energy resolution of the calorimeter, the dependence of the cross-section on energy and the trigger and reconstruction thresholds all add additional biases when binning directly in energy. In order to avoid these the response is binned in terms of E' defined as:

$$E' = p_{T_Z}^{cor} \cdot cosh(\eta_{jet}). \tag{4.13}$$

This variable is highly correlated to the particle jet energy and has the advantage that both $p_{T_Z}^{corr}$ and η_{jet} can be measured to a high degree of accuracy [44][45].

Missing Transverse Energy Correction

As the definition of the missing transverse energy in Equation 4.7 has no connection with the reconstructed physics objects, any correction to the energy of the objects must be compensated for by a change in the missing transverse energy. The missing transverse energy cannot be recalculated as in Equation 4.7 as the energy of each calorimeter cell is not stored in the files for data analysis. Hence an effective missing transverse energy has to be formulated which uses the variation in energy of the physics objects:

$$\not\!\!E_T^{eff} = \not\!\!E_T + \sum_{obj} (\mathbf{p}_{T_{obj}}^{meas} - \mathbf{p}_{T_{obj}}^{cor}). \tag{4.14}$$

Consequently the missing transverse energy now depends on the physics objects and hence on the way that their energy components are calculated. This is of limited significance for electrons as all their energy is generally contained in a few towers.

Response Calculation

After correcting for the electromagnetic energy scale as per Equation 4.14, the response can then be calculated for the EC and CC separately. The response is binned as a function of E' and the histogram is fitted using a Gaussian, as shown in Figs. 4.7 and 4.8. From the results of the fits, the response can be mapped to jet energy using a separate mapping for the CC and EC. This "average" response is fitted using the following function:

$$R(E_{jet}) = a + b \cdot ln(E_{jet}) + c \cdot ln(E_{jet})^2. \tag{4.15}$$

The functional form in Equation 4.15 was that used in Run I and is motivated by the composition of jets at different energies. As the calorimeter is "almost compensating" and assuming that the actual response of the calorimeter to electrons and to charged pions does not vary significantly with energy, the only factor which determines the jet response would be the ratio of hadronic to electromagnetic objects in the jet. The fraction of the jet which fragments into π° and η increases, to first approximation, logarithmically with jet energy. As π° and η decay mainly to electromagnetic objects this justifies the above functional form [44][57].

Cryostat Factor

Due to the separate cryostats used for the CC and the EC, there is potentially a difference in response between the two sections as there are differing amounts of material in front of the two calorimeters. However the EC and CC are identical in composition and in segmentation and hence should have the same intrinsic response. In order to constrain the response fit and increase statistics for high energy jets the response of the EC is corrected to that of the CC. This is done by taking the ratio of the points in the overlap region as a function of E' and fitting the ratio with a straight line. The response calculation is then repeated in its entirety correcting the momentum of the jets in the forward region by the cryostat factor; hence correcting the $\not\!\!E_T$ via Equation 4.14. The response is then fitted using both EC and CC points while keeping an independent E' - E mapping. The cryostat factor effectively allows the energy range of the response fit to be extended, as for the same E_T value, forward jets generally have a higher energy.

4.4 Response from Monte Carlo

The response using the MPF method was calculated from a sample of 450000 $Z(\rightarrow e^+e^-)$ + multijet events produced using the Pythia Monte Carlo generator v6.155 [58] and reconstructed with version p10.15.03 of the DØ reconstruction code. Pythia generates an inclusive sample of Z + multijets, with a primary jet produced as in Fig. 4.3 and any additional jets via DGLAP evolution. This sample was also used for the measurement of the low E_T bias in Section 4.4.1. The selection criteria and the method outlined in Section 4.3 were used in order to calculate the response.

Fig. 4.5a) shows the difference in angle, ϕ, between the selected Z boson and the leading jet. The back-to-back structure can be clearly seen. Fig. 4.5b) instead shows the difference in ϕ between the Z boson and the missing transverse energy after the selection cuts. As one expects, the majority of events have the $\not\!\!E_T$ aligned with the jet i.e. events for which the response is less than one. However there are also a number of events in which the $\not\!\!E_T$ is aligned in the Z boson direction. These events correspond to the case in which the jet E_T fluctuates above that of the Z and hence the response is greater than 1. This is more likely for low energy jets, for which the energy resolution is worse and for which the inclusion of low energy towers has a greater effect. Furthermore any variation in the $\not\!\!E_T$, due to e.g. a large noise contribution, will have a considerable effect on the response, simply due to the low energy. Fig. 4.6 displays the $\not\!\!E_T$ distributions for events in which the jet is back-to-back with the Z.

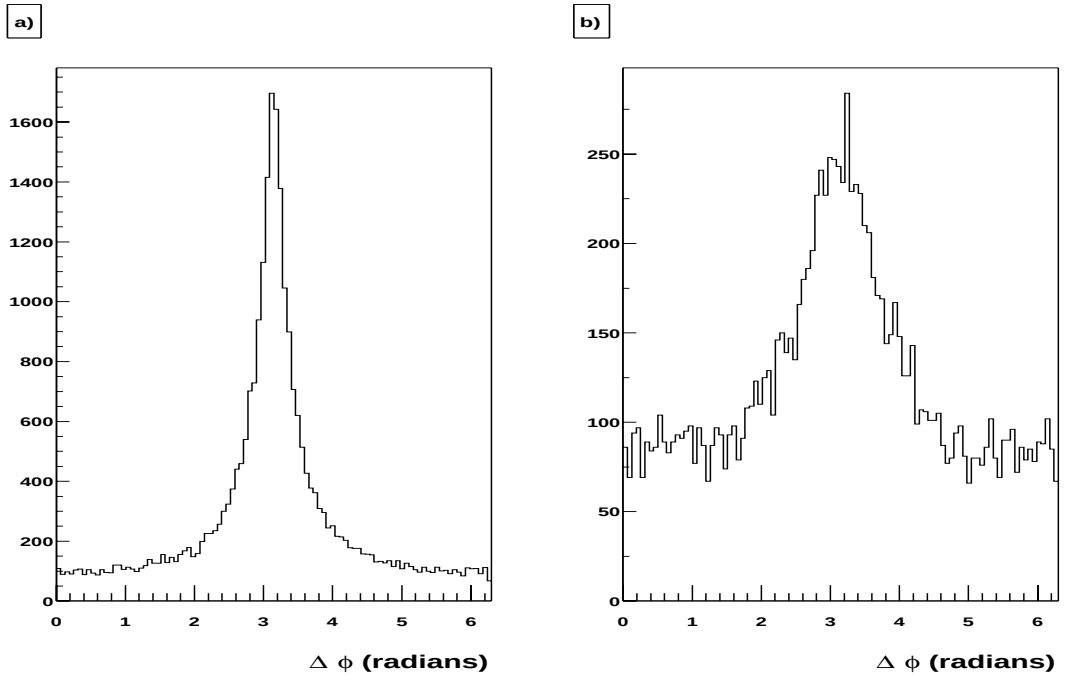

Figure 4.5: Difference in azimuthal angle in radians between Z boson and a) leading jet b) $\not\!\!E_T$

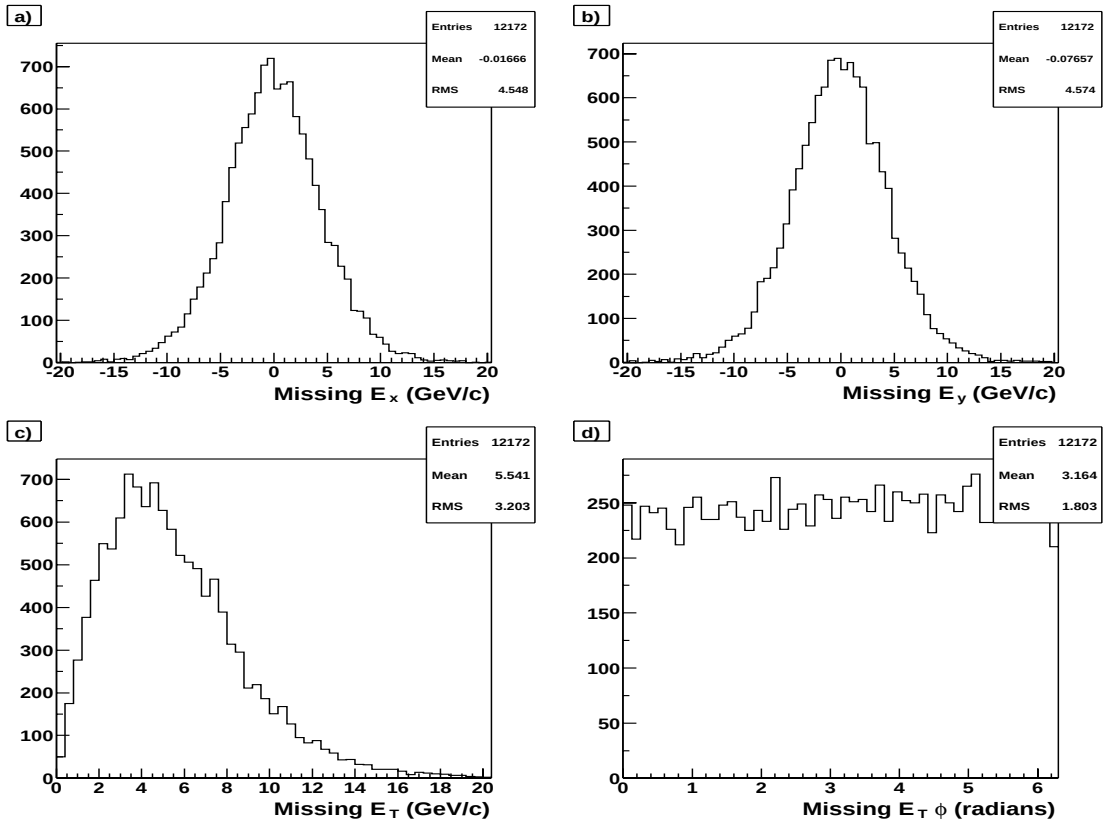

Figure 4.6: $\not\!\!E_T$ distributions for Z+jet events passing selection cuts
a) $\not\!\!E_{T_x}$, b) $\not\!\!E_{T_y}$, c) $\not\!\!E_T$ and d) ϕ (radians)

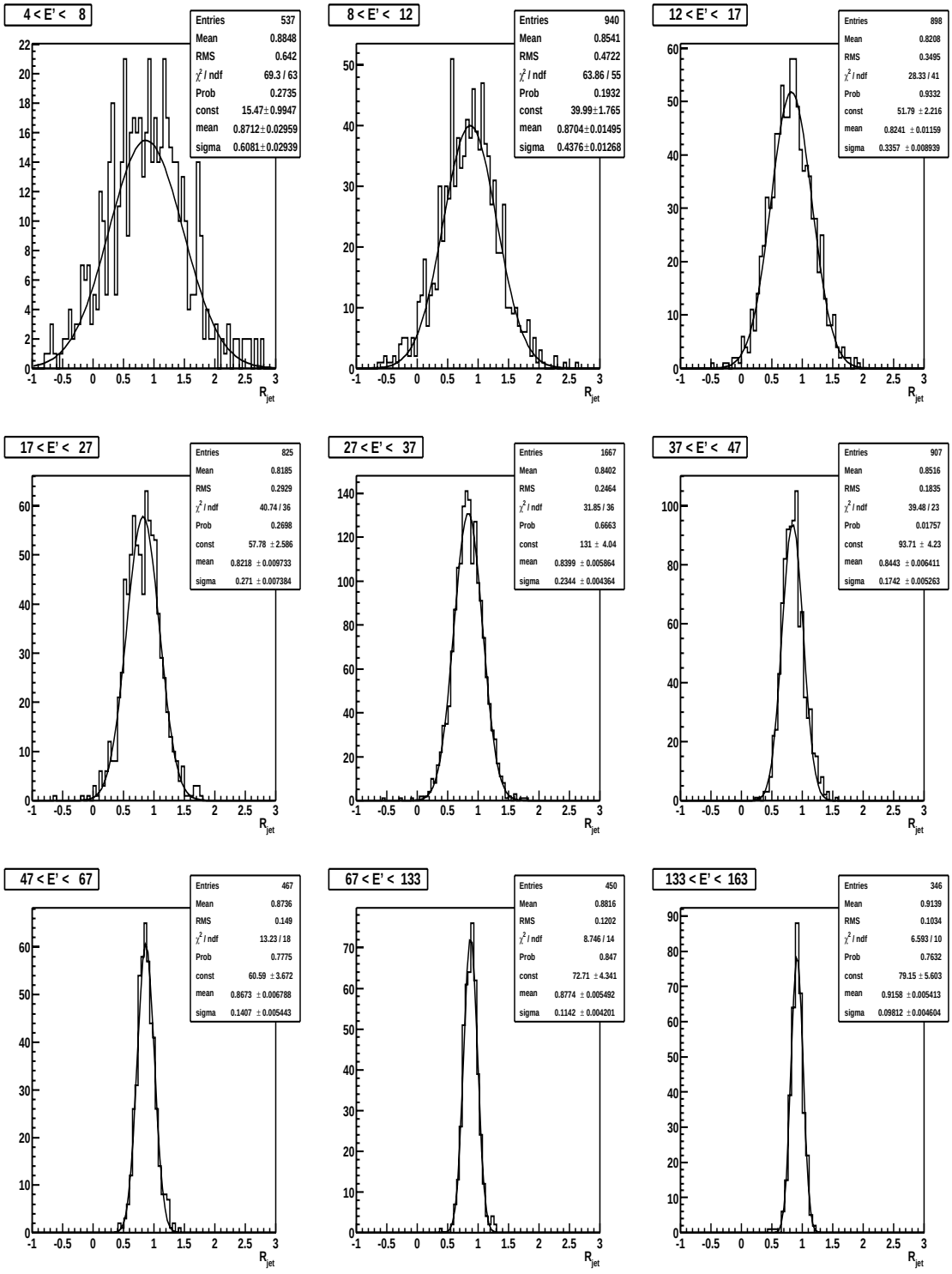

Figure 4.7: Response, R_{jet}, in E' (GeV) bins for the CC

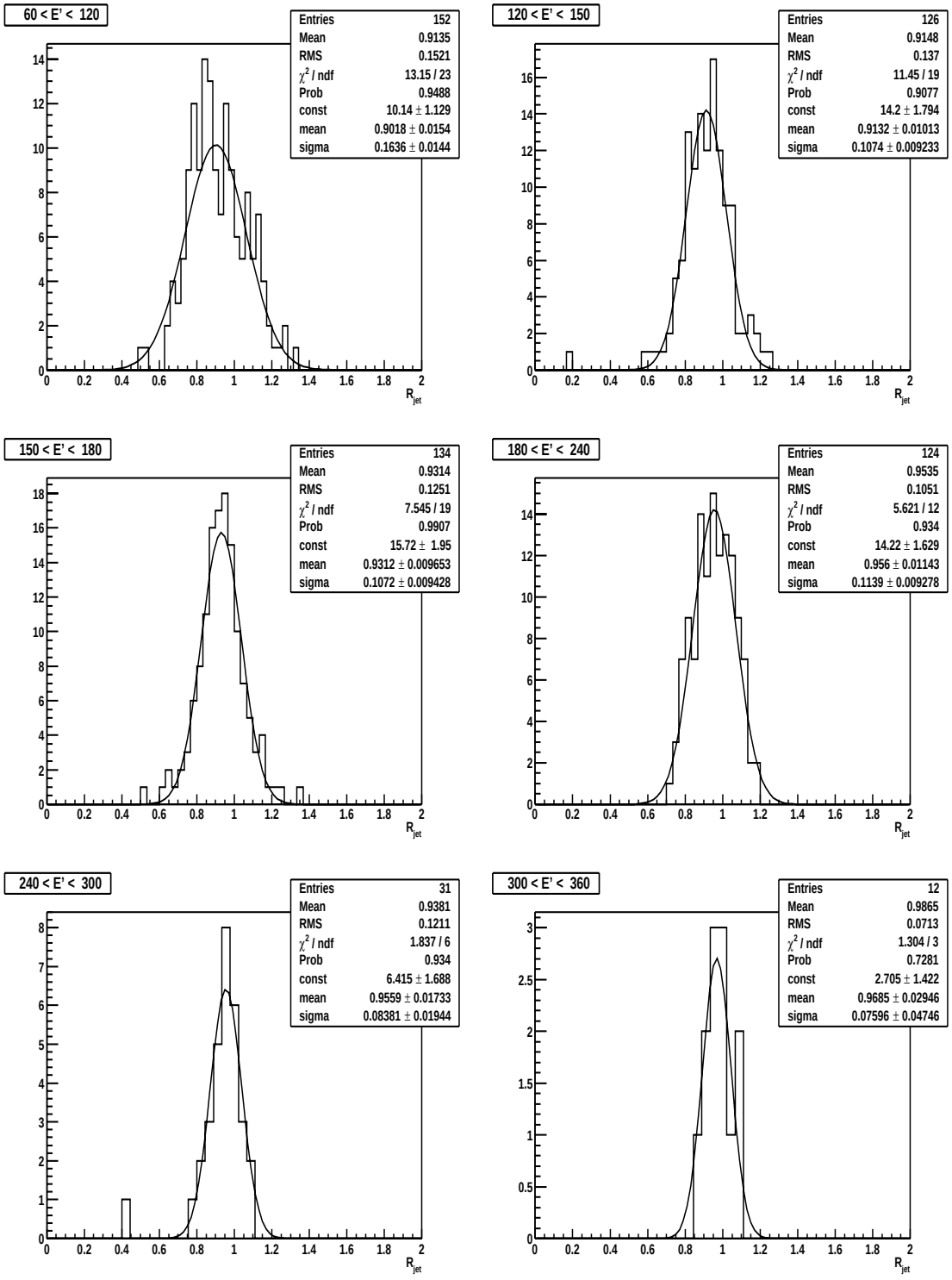

Figure 4.8: Response, R_{jet}, in E' (GeV) bins for the EC

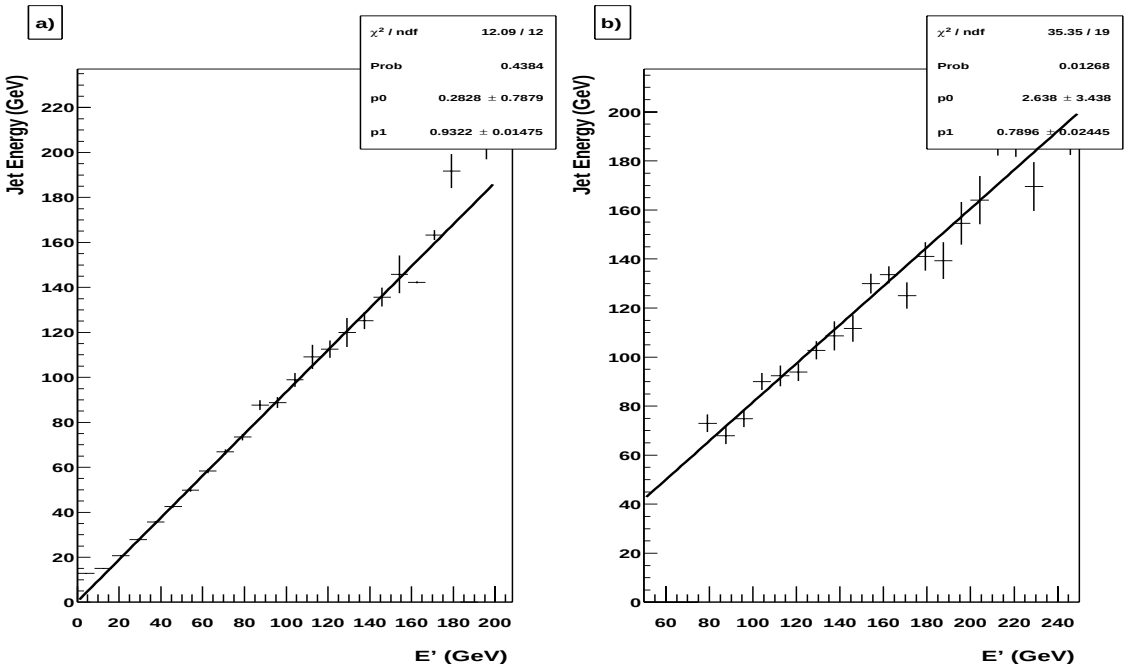

Figure 4.9: E' - E mapping for a) CC and b) EC

The response distributions, as calculated via Equation 4.12, for the CC and EC per E' bin, together with the Gaussian fit to the response are shown in Figs. 4.7 and 4.8. The improvement in the jet energy resolution is apparent in the decreasing width of the distributions with E'. Overall the distributions are described well by the Gaussian fit. Using the results from the Gaussian fits in Figs. 4.7 and 4.8 the response as a function of E' is obtained. This is shown in Fig. 4.10a). The response changes rapidly as E' decreases, first decreasing and then seemingly increasing again. The decrease is due to the rapidly degrading jet resolution toward lower energies, whereas the subsequent increase is due to the low E_T bias which will be described in Section 4.4.1.

The separate mapping from E' to E for the EC and the CC is shown in Figs. 4.9a) and 4.9b). Using the independent mapping for the CC and EC from Fig. 4.9, the response can be expressed in terms of jet energy (Fig. 4.10b)). The response profile in Fig. 4.10b) develops a plateau around 75 GeV which can be related to the jet resolution.

The way the $\not\!\!E_T$ is calculated has a noticeable effect on the response. The $\not\!\!E_T$ used so far uses all the calorimeter towers, however the $\not\!\!E_T$ is also calculated using only calorimeter towers which have an energy greater than 200 MeV. A reason for doing this is to eliminate towers with large negative energy due to the pedestal subtraction and to reduce the impact of noisy cells in towers. Fig. 4.11 displays the

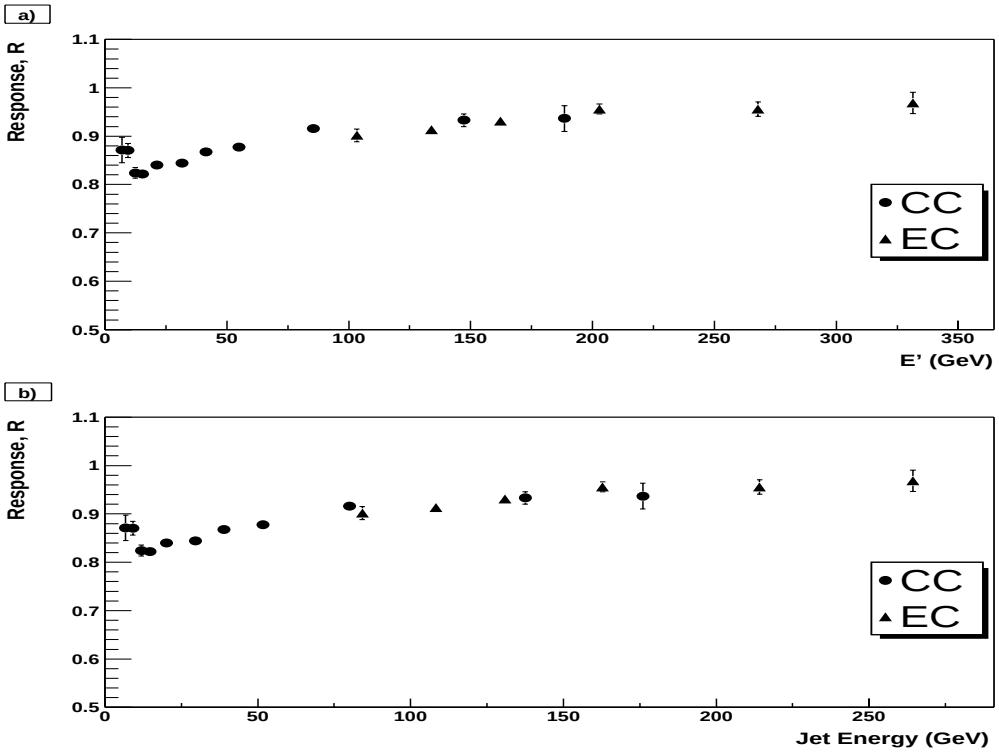

Figure 4.10: Jet response as a function of a) E' and b) jet energy

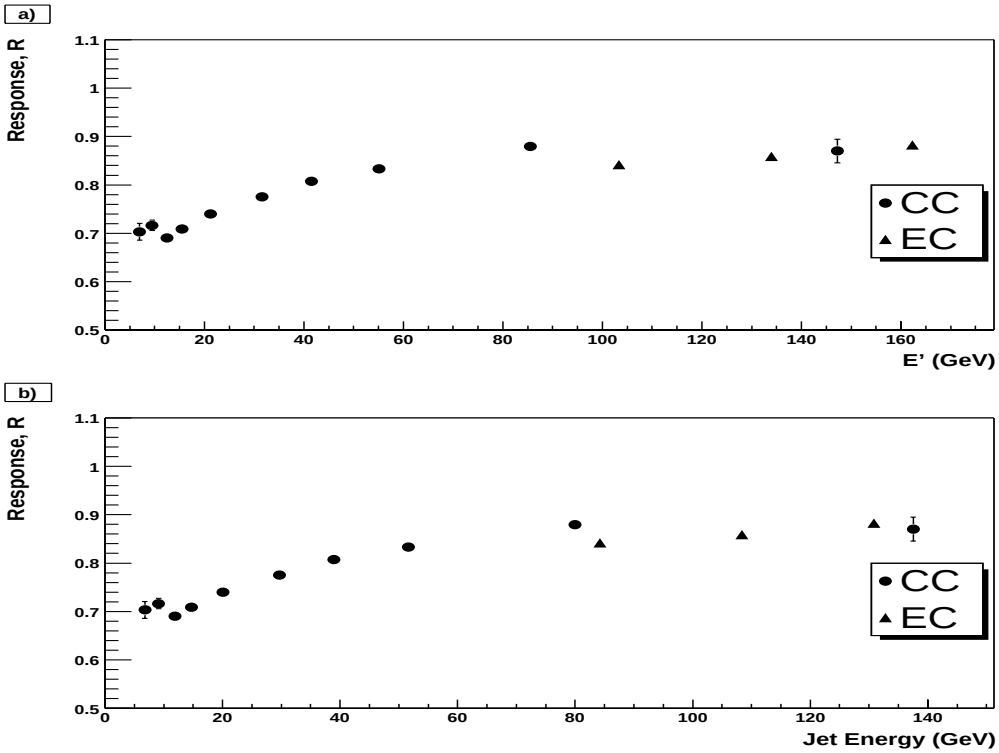

Figure 4.11: Jet response using towers with an energy > 200 MeV for the calculation of the $\not\!\!E_T$ as a function of a) E' and b) jet energy

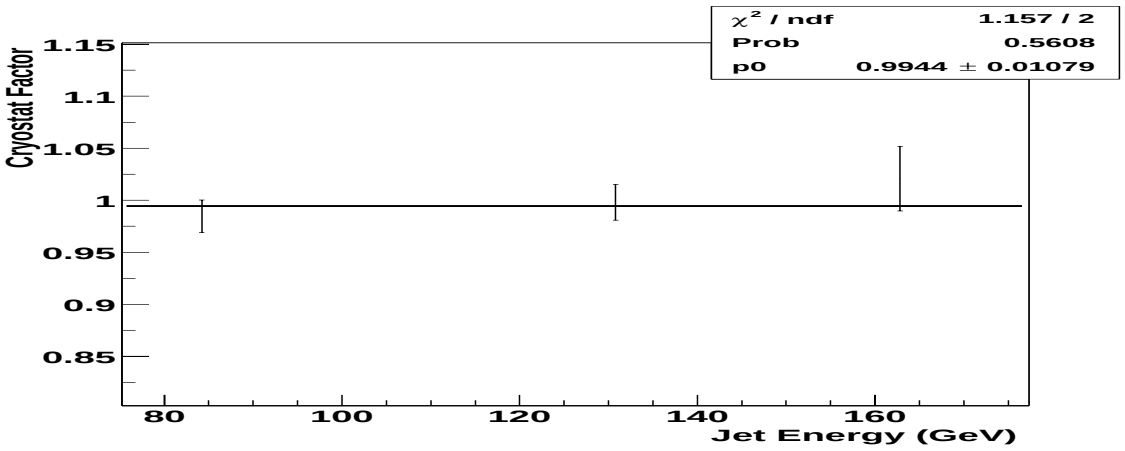

Figure 4.12: Cryostat factor

response using the latter method for calculating the $\not\!\!E_T$. Compared to Fig. 4.10 the response is significantly lower, especially for a jet energy less than 60 GeV.

The cryostat factor is shown in Fig. 4.12. The cryostat factor was derived to be 0.99 ± 0.01 which is consistent with 1 and with the cryostat factor from γ+jet Monte Carlo [55] of 1.022 ± 0.003. Fig. 4.13a) displays the modified response using the cryostat factor as a function of E', that as a function of jet energy is shown in Fig. 4.13b). For Fig. 4.13b) an equivalent independent E' - E mapping as for Fig. 4.10b) is used, however modified due to the inclusion of the cryostat factor. The difference between the mapping with and without the cryostat factor was found to be small and within the errors of the fit. The function used for the fit to the response in Fig. 4.13b) is that of Equation 4.15 and is of the same form as that used for the γ+jet sample.

The response derived using the Z+jet and γ+jet sample are consistent. The differences in the actual fit are mainly due to a lack of points to constrain the fit at high energy for the Z+jet sample, although the response seems slightly lower than the γ+jet response fit between 25 and 50 GeV. Again this could be due to the fact that the γ+jet response is highly constrained at high jet energy.

4.4.1 Low E_T bias

Origin

The low E_T bias is a reconstruction bias arising from the finite resolution of the calorimeter. It arises as there is an artificial jet E_T reconstruction threshold of 8 GeV/c below which jets are not reconstructed. Therefore the lower end of the energy resolution distribution for jets with low real energy (up to ~20 GeV) will not

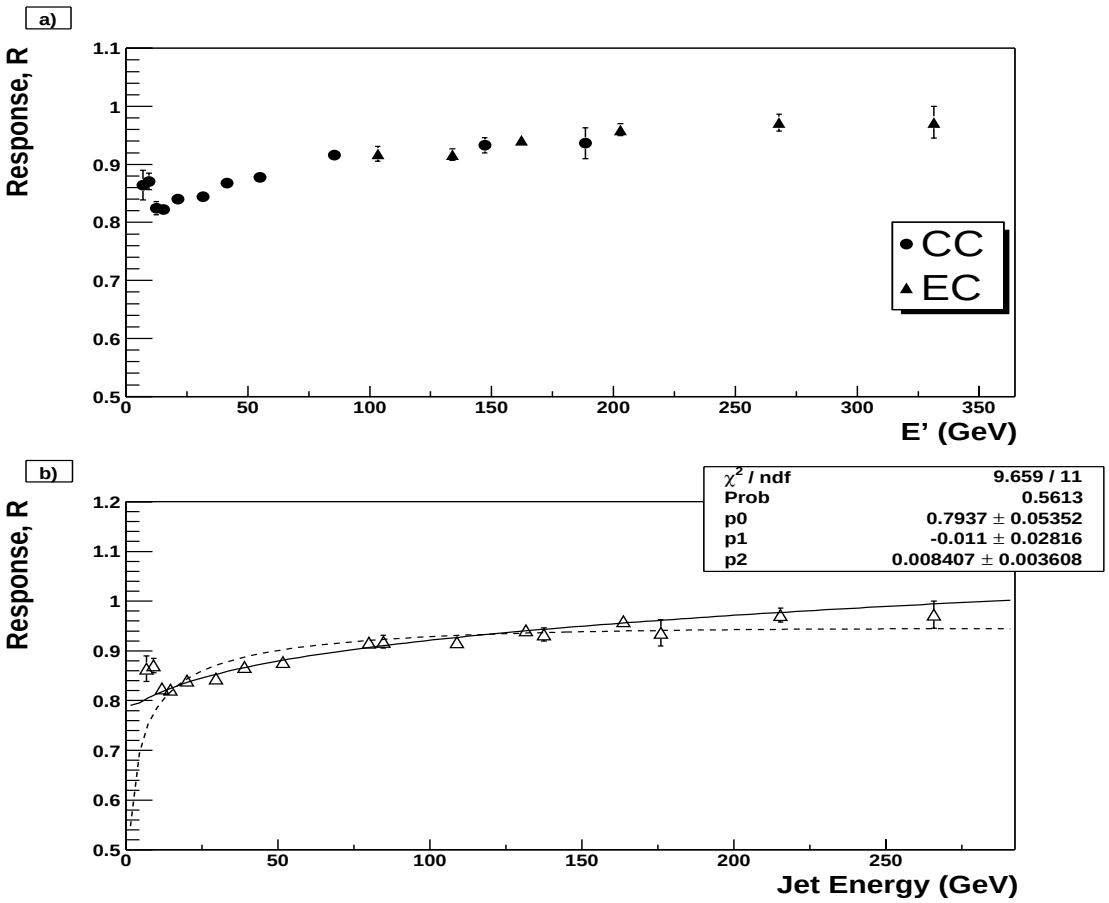

Figure 4.13: Jet response after cryostat factor correction as a function of a) E' b) jet energy. The dotted line shows the response fit derived from γ+jet Monte Carlo [55]

be included. Hence the average measured E_T for a jet with a fixed generated E_T will be biased high. The upper E_T limit for which this bias has an effect is determined largely by the energy resolution, as expected, but also by the jet reconstruction efficiency which is a function of E_T. The low E_T bias is obviously a problem for the response as a bias in the E_T measured in the calorimeter will result in a distortion of the missing transverse energy. In this case by biasing the E_T high, the missing transverse energy is lowered and hence, from Equation 4.12, the observed response is greater then the real response.

This is what is observed in the low energy region in e.g. Fig. 4.13b). Also the effect of the low E_T bias is apparent in the E' - E mapping in Fig. 4.9, in which the corresponding energy for the lowest E' bins clearly lies above the straight line fit.

Low E_T Bias Correction

The method used in Run I [44][45] is based on the fact that a jet does not have to be detected in order to calculate the response using Equation 4.12. Naturally the response measured without the detection of a jet is no longer a measure of the jet response but becomes the overall calorimeter response to energy deposits. The response measured in this way has the benefit of not being susceptible to the low E_T bias as there is no jet requirement. Therefore events in which the jet E_T fluctuates below 8 GeV/c are not rejected and are included in the response binning. A measure of the low E_T bias is consequently the ratio of the response with a jet requirement to that without:

$$R_{bias} = \frac{R_{jet}}{R_{nojet}}. \tag{4.16}$$

In an analogous way to the jet response calculation, in order to avoid further bias by binning directly in E_T, the low E_T bias is binned in terms of p_{T_Z} and then mapped to $E_{T_{jet}}$ using the mapping from the numerator. Furthermore the jet selected in the numerator is restricted to be in the CC.

Figs. 4.14 and 4.15 show the response distributions per p_{T_Z} bin with and without a jet requirement. The results of the fits in Figs. 4.14 and 4.15 as a function of p_{T_Z} with and without a jet requirement are shown in Figs. 4.16a) and 4.16b). The presence of the low E_T bias is evident. In Fig. 4.16a) the response increases at low p_T, whereas the response falls smoothly in Fig. 4.16b). Fig. 4.16c) shows R_{bias} as a function of Z p_T. R_{bias} is fitted using the following functional form:

$$f(x) = p0 + e^{(p1+p2\cdot x)}. \tag{4.17}$$

The comparison to Run I data in Fig. 4.16c) highlights the fact that the distributions agree well (aside from an overall offset) down to a p_T of ~12 GeV/c and then R_{bias} increases very rapidly for the Z+jet sample. Due to the different environment and the presence of more material in front of the calorimeter there is no reason to expect that the distributions should be exactly the same. From the difference between the two distributions there seems to be a deterioration of the energy resolution at low energy compared to Run I.

The mapping from the p_T of the Z boson to jet E_T is shown in Fig. 4.17a). The effect of the low E_T bias is manifest in Fig. 4.17a) from the levelling off of the jet E_T at low Z p_T. Due to the significant departure from a straight line, instead of the mapping in Fig. 4.17a) the average jet E_T per Z p_T bin is used.

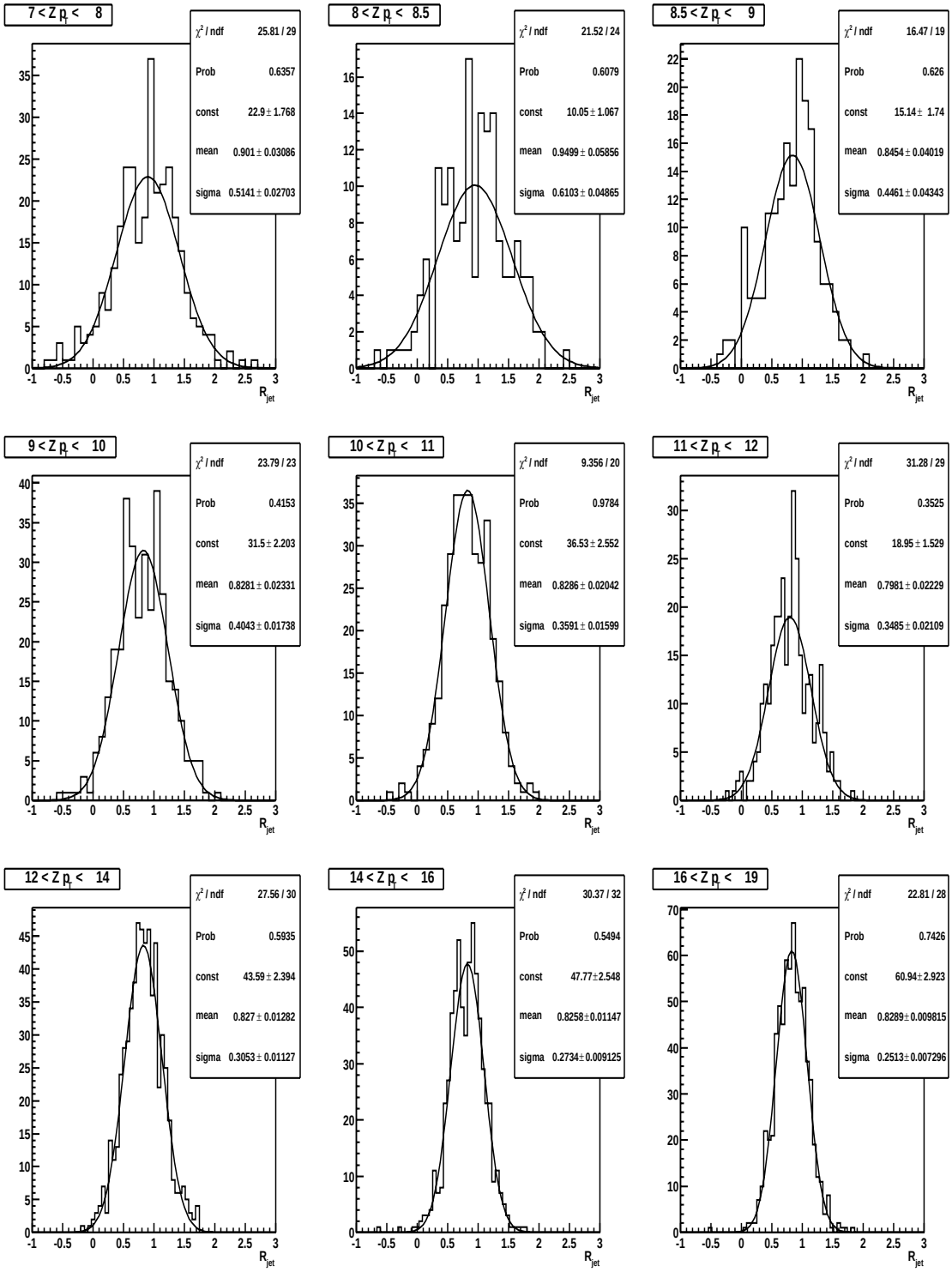

Figure 4.14: Response, R_{jet}, in p_{T_Z} (GeV/c) bins for events with a jet requirement

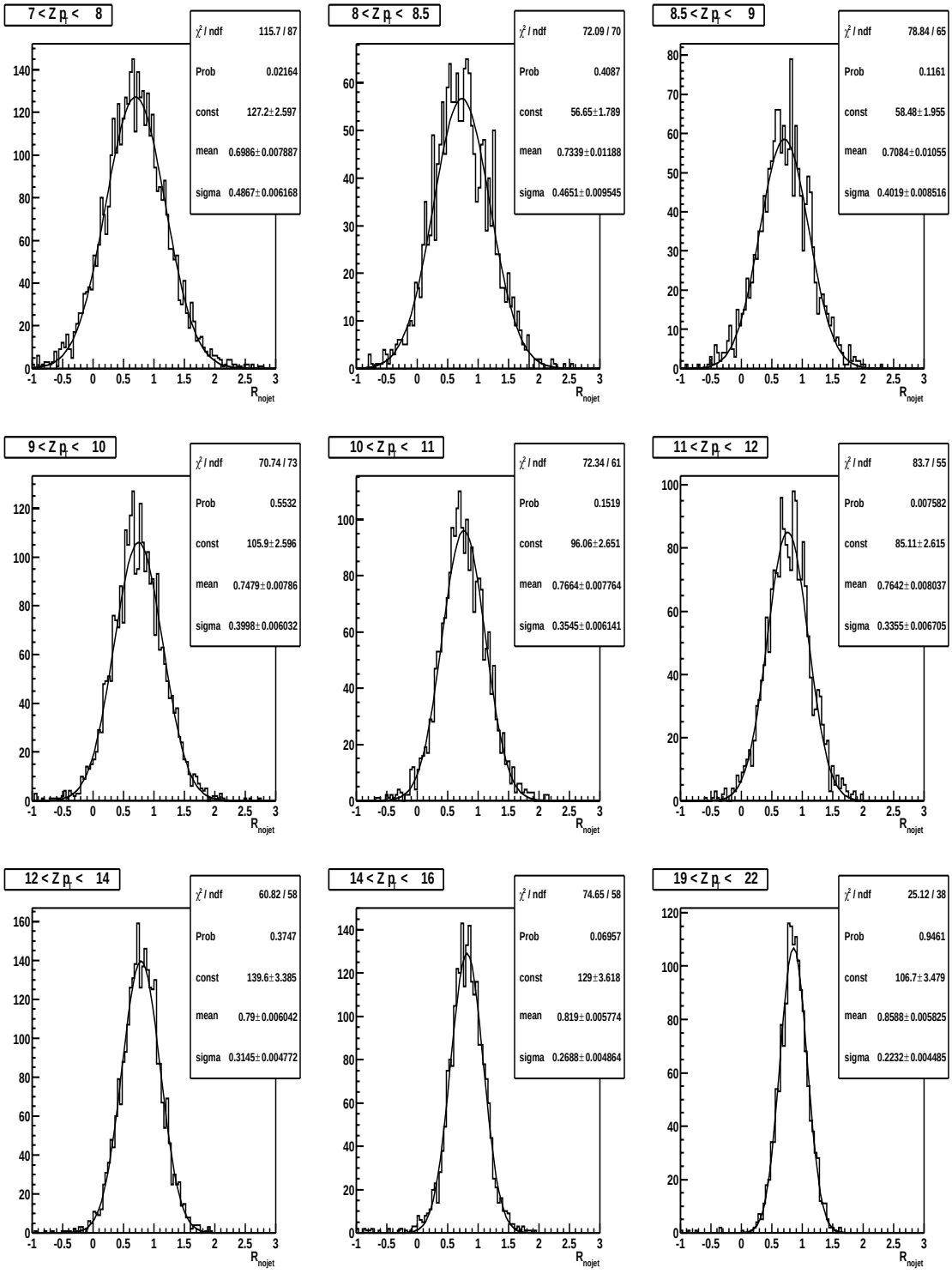

Figure 4.15: Response, R_{jet}, in p_{T_Z} (GeV/c) bins for events with no jet requirement (denoted R_{nojet})

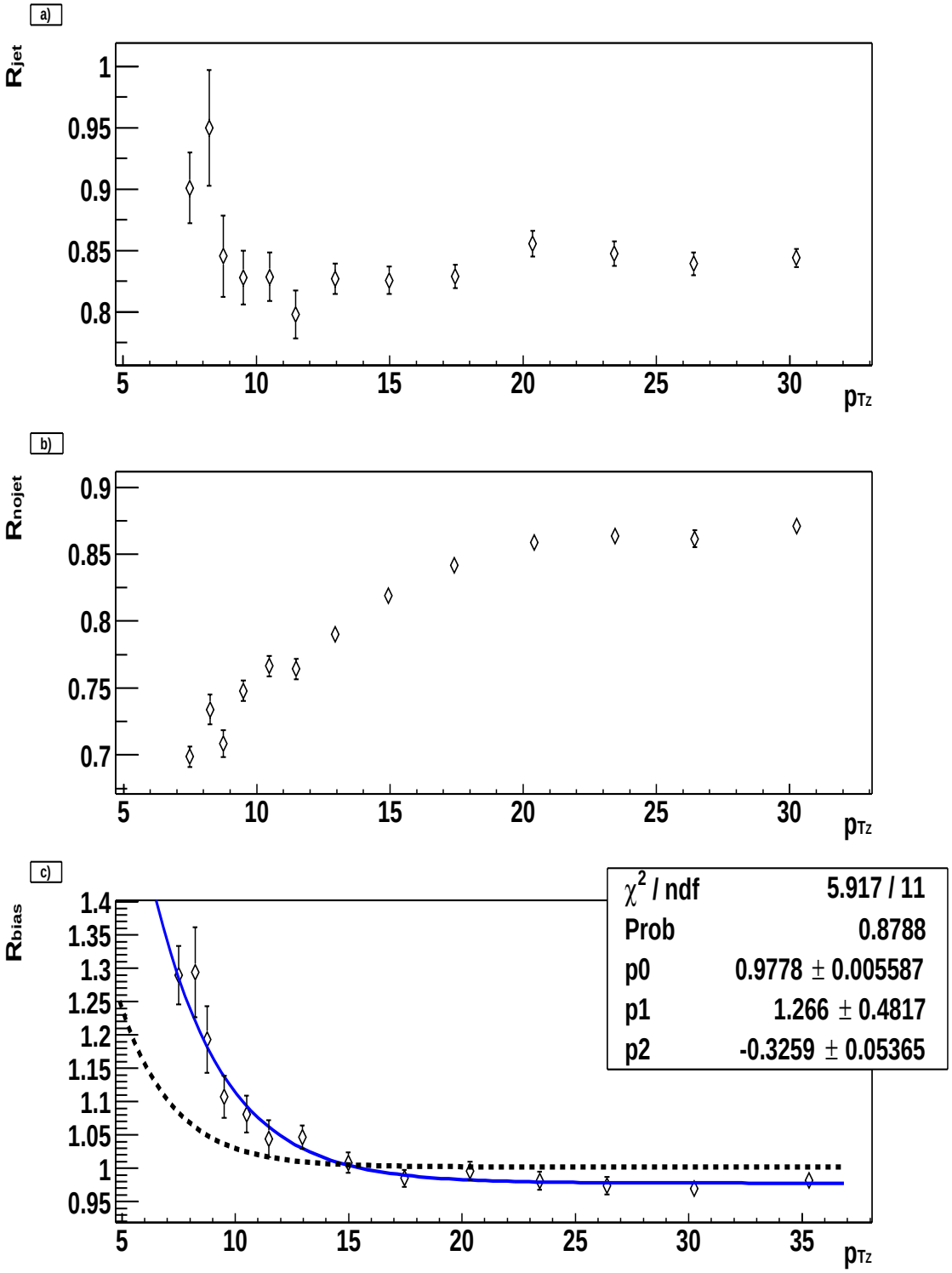

Figure 4.16: Response as a function of p_{T_Z} (GeV/c) a) with a jet requirement, b) with no jet requirement and c) R_{bias} as a function of p_{T_Z}. Dotted line shows R_{bias} as a function of p_{T_γ} from Run I data [44]

The final low E_T bias correction is shown in Fig. 4.17b). The effect of the low E_T bias is limited to jets under an E_T of 17 GeV/c. Again the distribution has a steeper turn on than that in Run I.

The low E_T bias calculated in this way has various short comings. The primary one is that whereas the jet reconstruction and resolution depend on η there is no η information or selection in the denominator of Equation 4.16. As a result the two response figures are not entirely equivalent as one response calculation is limited to a fixed η region, whilst the other is an average response over all regions. For this reason jets in the EC are not corrected using the cryostat factor. The effect of the η difference can be seen by the fact that the ratio does not level off at 1 i.e. there is a residual bias, even at high E_T, from the method.

There is a further problem with applying the bias as a function jet E_T. Due to the resolution bias, when converting Z p_T to jet E_T, the data points where R_{bias} turns on are very close together. As R_{bias} is rapidly increasing in this region any errors in the mapping or R_{bias} can lead to large errors in the fit. Possibly a better solution is to apply the bias directly in terms of p_{T_Z}. This has two advantages: the Z p_T is measured more accurately and hence it avoids any issue of jet resolution which occurs when mapping to jet E_T. Secondly R_{bias} increases more slowly with respect to p_{T_Z} and hence the fit is potentially more stable to errors in the any of the data points.

An alternative method being studied, which would not be susceptible to the aforementioned shortcomings, is to study the change in response as a function of the jet threshold. This can be done as an extension to the method described in Section 4.3 by further binning the response from each E' bin in bins of jet E_T threshold. The jet reconstruction threshold can be arbitrarily increased above 8 GeV/c to give the response per E' bin as a function of jet threshold. The response, in principle, can then be extrapolated to a jet threshold of 0 GeV/c , which would be equivalent to the response for each E' bin with no low E_T bias. This extrapolated response could then be used to derive the response profile as a function of E' and hence jet energy. The main assumption of this method is that the dependence of the response on the jet reconstruction threshold per E' bin below 8 GeV/c is the same as that above.

Generally an accurate and well understood derivation of the low E_T bias is difficult. This is simply because the low E_T region is not well understood at hadron colliders. The low E_T bias depends, among other factors, on exactly the manner in which the missing transverse energy is calculated. Furthermore it is affected by any noise in the calorimeter which is subsequently included in the jet and by the

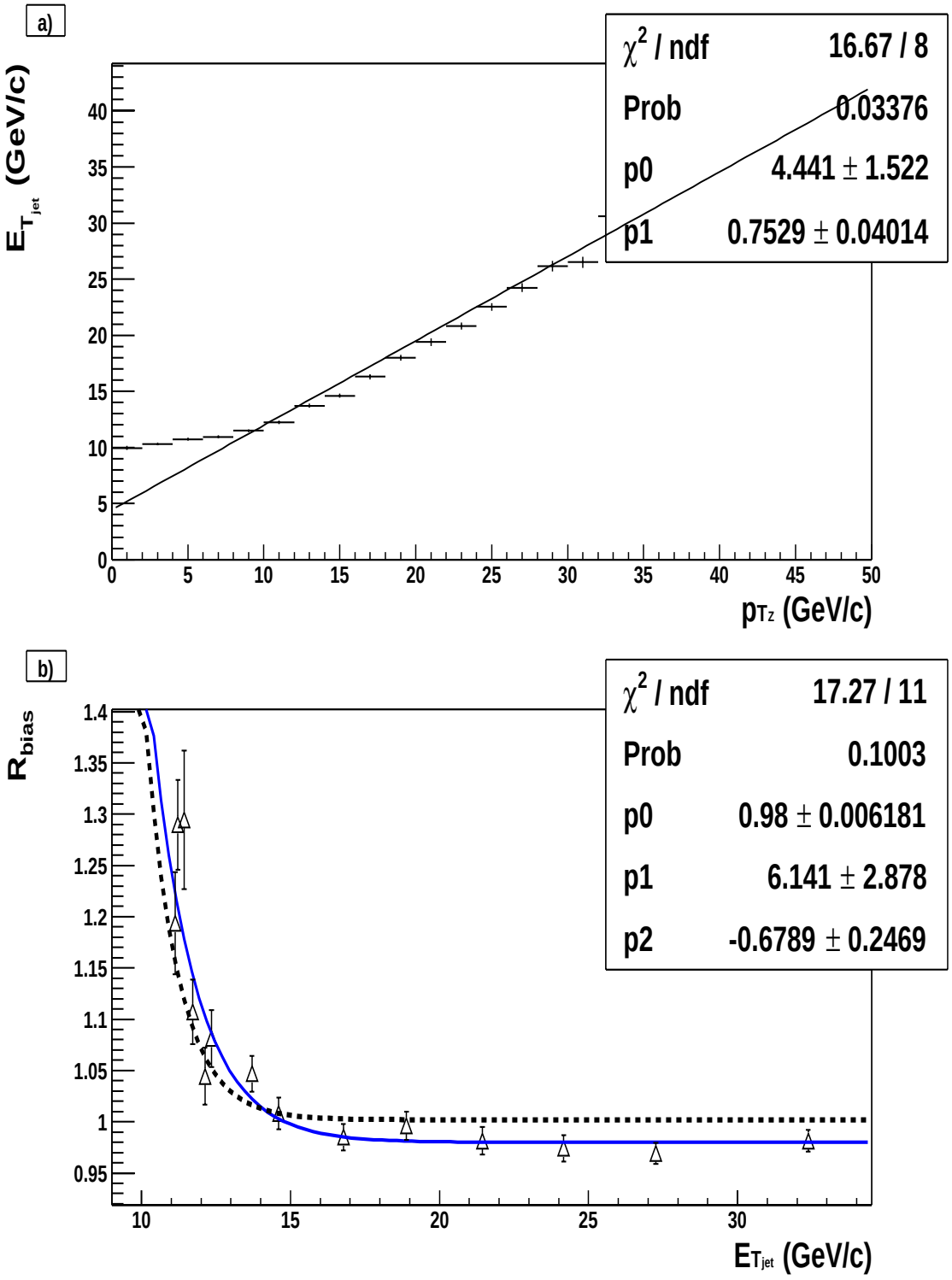

Figure 4.17: a) Mapping between p_{T_Z} and jet E_T b) R_{bias} as a function of jet E_T. Dotted line shows R_{bias} as a function of jet E_T from Run I data [44]

zero suppression threshold of calorimeter cells. Hence in order to really understand the low E_T region one needs to understand these factors in data and one needs an accurate modelling in the Monte Carlo. This can only be done once the calorimeter is fully understood and is running under stable conditions, fixed threshold suppression, etc.

Jet Response After the Low E_T Bias Correction

R_{bias}, having set p0 in Equation 4.17 to 1, is subsequently used to correct the overall jet response. The response is re-calculated as outlined in Section 4.3 with the addition that the E_T of the selected jet, if in the CC, is corrected by a factor $1/R_{bias}(E_T)$ and the missing transverse energy is modified via Equation 4.14 for the change in jet E_T. Only the leading jet in the event is corrected in this way as it is the only jet which is actually required to be present i.e. the only jet for which the implication of a jet reconstruction threshold has an effect on the response.

The response fits per E' bin for the CC, after the low E_T bias correction, are shown in Fig. 4.18. The new response as a function of E' and the new CC E' - E mapping are shown in Fig. 4.19. From 4.19b) one can note the improvement in the mapping at low E' with respect to Fig. 4.9.

Finally Fig. 4.20 displays the jet response as a function of jet energy after all corrections. The functional form fits the points well, although it seems as if the low E_T bias is overestimated.

4.4.2 Discussion

There are various aspects of importance which are highlighted by the derivation of the jet response. First and foremost the method is seen to be a valid cross-check of the γ+jet sample, as shown by Fig. 4.13. Secondly, as highlighted by the difference between Figs. 4.10 and 4.11, the response depends significantly, as expected, on the calorimeter performance and on the way the calorimeter information is used. In the period covered by the p10 reconstruction code the calorimeter information was not used consistently between different analysis groups and indeed between the different reconstruction algorithms. In order to have a jet response which is applicable for all analyses one needs to have a well defined, well understood and coherent use of the calorimeter information. So far this has been limited by the understanding of the calorimeter and the understanding of the effect on the reconstruction algorithms. However recently the emphasis has changed and there have been suggestions for a more coherent use of the calorimeter.

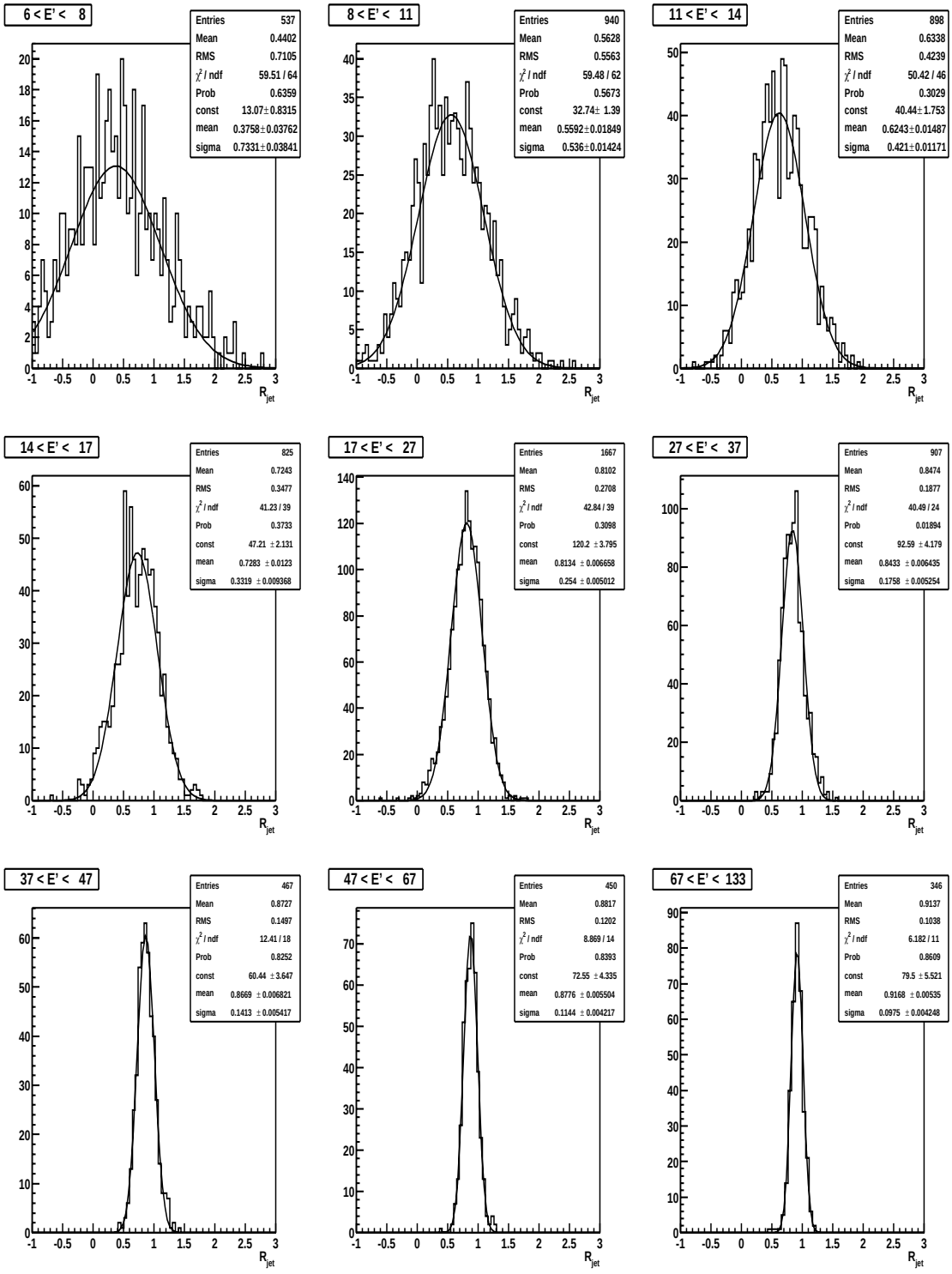

Figure 4.18: Response, R_{jet}, in E' bins for the CC after the low E_T bias correction

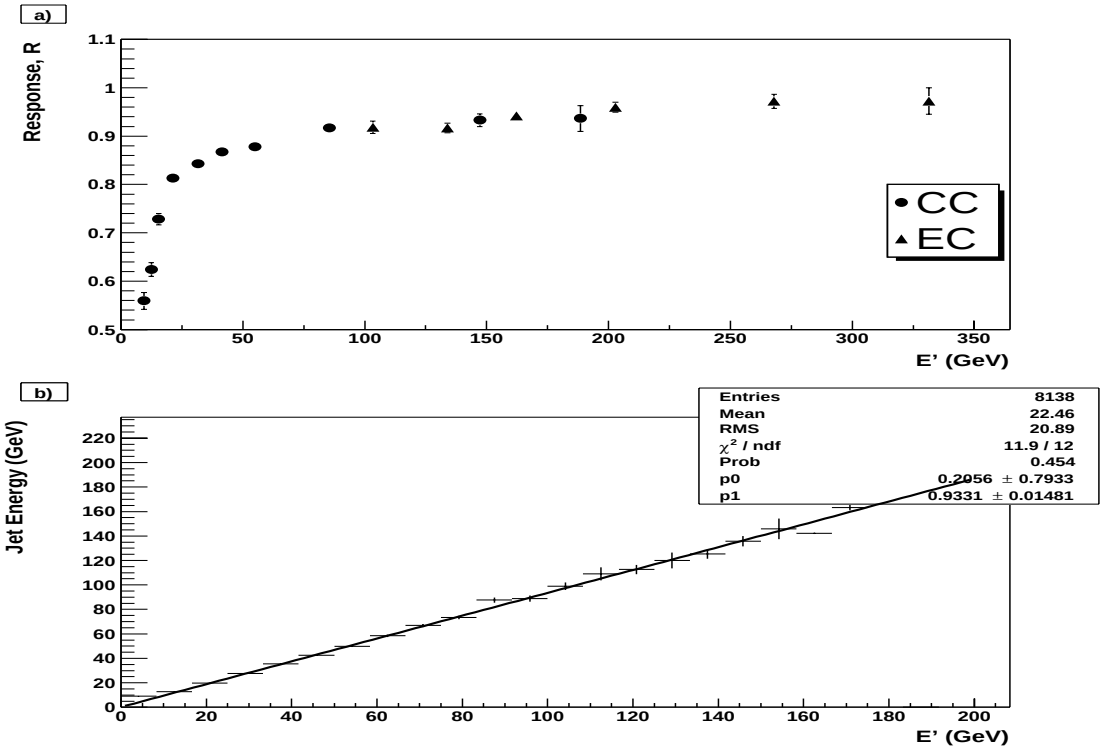

Figure 4.19: a) Response after the low E_T bias correction as a function of E' bins and b) E' - E mapping for the CC after the low E_T bias correction

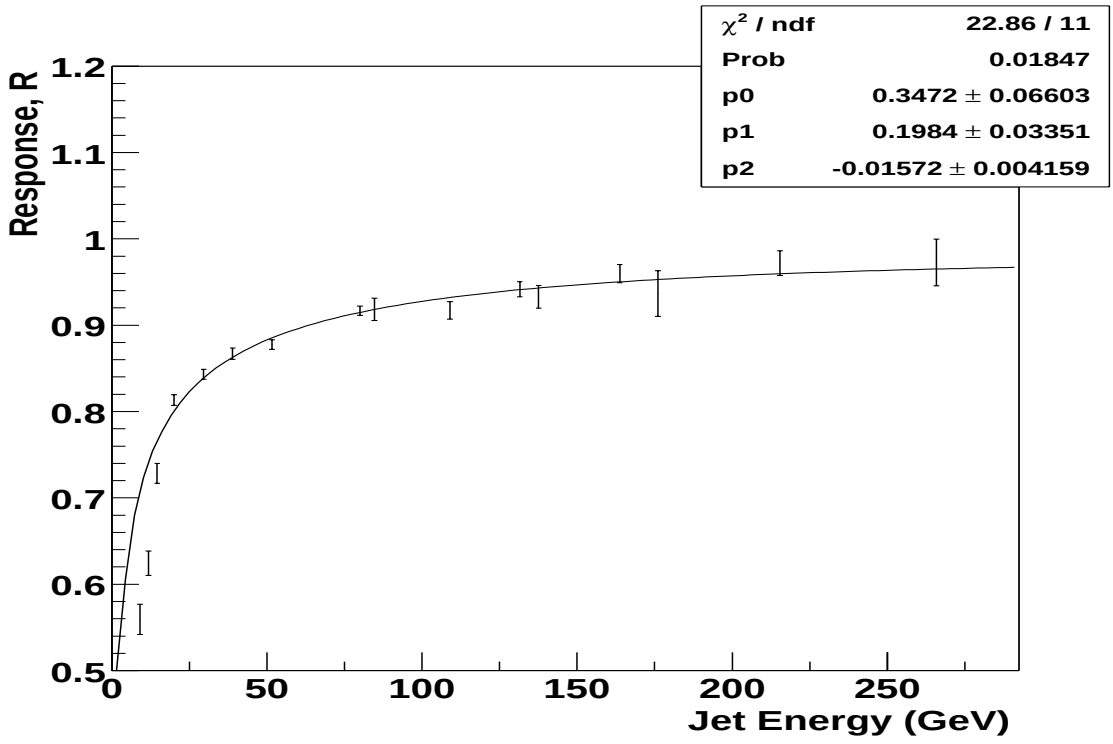

Figure 4.20: Response as a function of jet energy after the low E_T bias correction

What the analysis has really stressed is that the Pythia generator is not suitable to generate events for a response correction using the MPF method. In order to obtain an accurate Z p_T spectrum over the whole response range, an inclusive Z+jets sample has to be generated. This includes also Drell-Yan type processes in which there are no jets recoiling against the Z. As a consequence the event selection efficiency is low and adversely affects the statistics available for the jet response derivation. This is particularly true for the high E' bins due to the falling Z p_T cross-section, as demonstrated in Figs. 4.7 and 4.8. Furthermore the fact that in Pythia one is unable to put a direct cut on the p_T of the Z boson signifies that one is unable to enhance the statistics for the high E' region. This leads to a statistically limited derivation of the cryostat factor due to limited number of points in the overlap region (Fig. 4.12) and a response fit which is unconstrained at high jet energies (Fig. 4.13). Subsequent analyses should investigate the possibility of using generators specifically designed for the production of vector boson and jets in a hadronic environment, which allow for cuts to be placed directly on the Z boson.

4.5 Response from Data

Due to the cross-section of the Z+jet process and the low amount of integrated luminosity accumulated at the Tevatron using the p10 version of the DØ reconstruction code, there are not enough events surviving the cuts to derive a jet response using this process. The γ+jet sample however has a much higher cross-section, 0.0114 mb for $p_{T_\gamma} > 5$GeV/c from Pythia 6.155 compared to 175 pb for Z+multijet production. Hence it is possible to derive a response and an overall energy scale from data [55].

The response as a function of E' for the CC and the EC after the cryostat factor correction is shown in Fig. 4.21. The E' - E mapping is shown in Fig. 4.22; using this mapping and fitting using the functional form given in Equation 4.15 the response in data is determined to be that in Fig. 4.23.

It can be seen that the response in Fig. 4.23 is significantly lower than that for the Monte Carlo. The major reason for the discrepancy is a non-linear effect in the calorimeter read-out chain [59]. The non-linearity occurs when storing the calorimeter signal in an analogue memory pending Level 1 and Level 2 trigger decisions, before the conversion to ADC counts. This non-linearity affects only small input signals, therefore the number of ADC counts to an input signal is linear over the majority of the signal range.

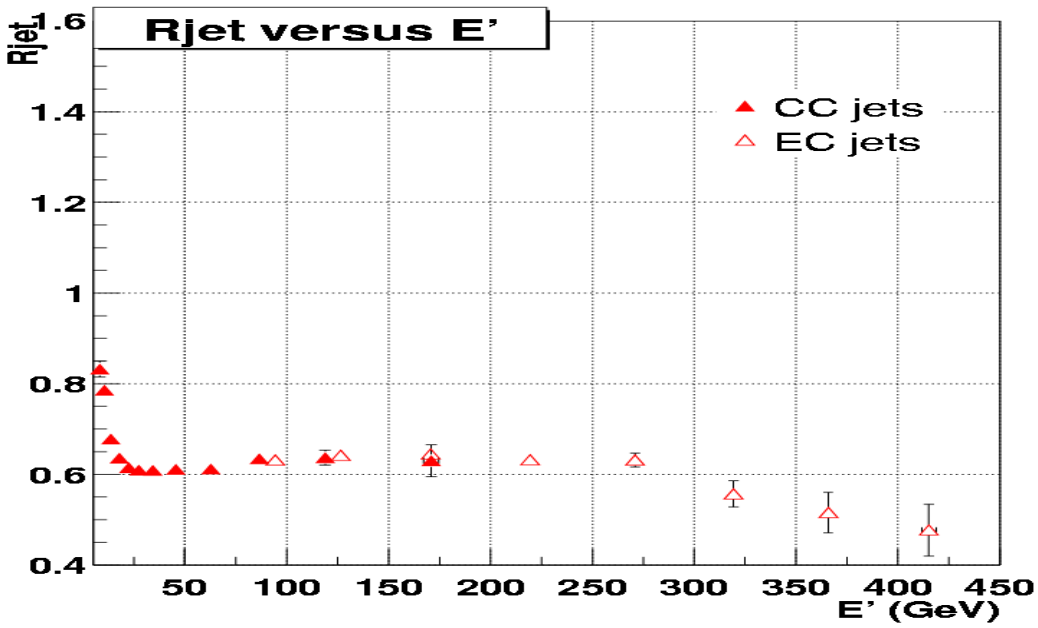

Figure 4.21: Jet response as a function of E' derived from γ+jet data [55]

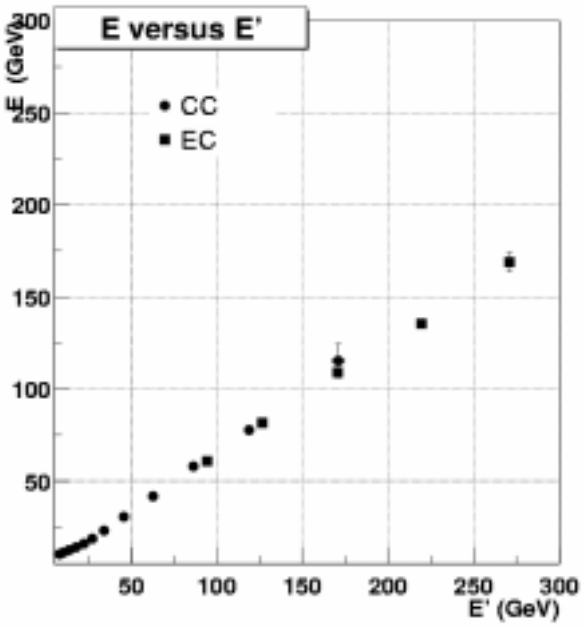

Figure 4.22: E' -E mapping in γ+jet data [55]

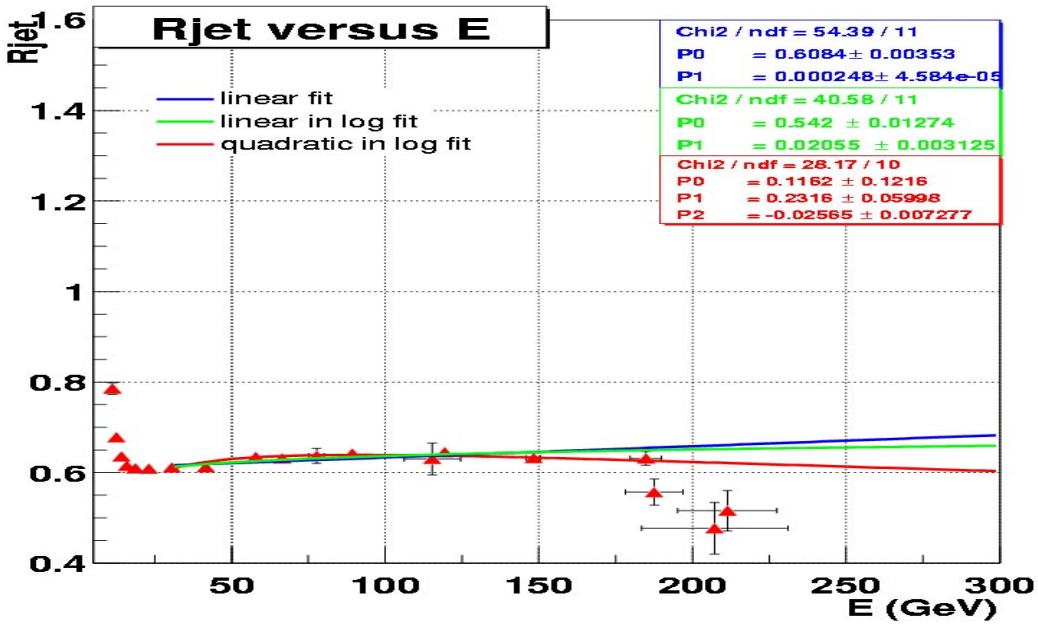

Figure 4.23: Jet response as a function of jet energy derived from γ+jet data [55]

When assuming that the conversion is actually linear over the whole range it seems as if there is a negative offset to the conversion, hence the straight line fit is simply corrected by a positive constant term. As a consequence, the conversion from ADC counts back to energy is lower than it should be; hence the energy of the objects is underestimated if the non-linear effect is not taken into account. This is especially important for jet reconstruction as there is an E_T threshold for the jet seeds. It also has significant implications for the missing energy measurement and jet resolution. A further complication is that calorimeter cells are pedestal-suppressed, so there is a loss of low energy cells if the non-linearity is not taken into account.

It is important to stress that, due to low integrated luminosity accumulated, so far most of the data collected has been used to commission the detector. This coupled with the rapid evolution of the DØ reconstruction software has meant that the Monte Carlo and data reconstruction effort has been continuing for the most part in parallel, without the possibility for the extensive verification using physics objects. The data reconstructed with the p10 version of the DØ reconstruction code was the first major attempt to compare data and Monte Carlo and hence find discrepancies which will be corrected in later versions of the reconstruction code. This is an on-going effort and it will take some amount of time before the Run II environment and the DØ detector are fully understood.

4.6 Conclusions

The analysis presented establishes the validity of using a Z+jet sample to verify the response derived using a γ+jet sample. It also highlights various shortcomings of this verification. The response derived using the Z+jet Monte Carlo sample was found to be consistent with that derived using the γ+jet Monte Carlo sample. The main factor limiting the accuracy of the comparison was the lack of statistics at high jet energy for the Z+jet sample. This led to two main problems: a lack of points in the E' overlap region between the EC and the CC and a weakly constrained jet response fit at high jet energy. The former limited the accuracy of the cryostat factor derivation. The latter limited the extent to which the response fits from the two samples could be compared. Further studies should investigate the use of Monte Carlo generators, other than Pythia, in order to increase the statistics for high energy jets. This lack of statistics will be a greater problem when analysing data as the statistics cannot be artificilly increased at high jet energy.

There is a major discrepancy between the response seen in the γ+jet Monte Carlo and that seen in data. This is mainly due to a non-linearity in the conversion from ADC counts to energy in the calorimeter read-out chain. The effect of the non-linearity (if not taken into account in the subsequent reconstruction) is to lower the energy of each calorimeter cell by as much as a few hundred MeV; thus lowering the overall energy of the reconstructed jets and therefore lowering the jet response. Subsequent versions of the DØ software which take into account the non-linearity show a much better agreement between data and γ+jet Monte Carlo.

The DØ collaboration will use the code developed for this analysis both for Monte Carlo and data. The former mainly as a verification of the response after changes in the reconstruction code and the latter is ongoing as more data is accumulated.

Chapter 5

Search for a Low Mass Higgs in the Channel $ZH \to e^+e^-b\bar{b}$

The search for the Higgs is one of the focal points of the Run II physics programme. The Tevatron is in a unique position to provide evidence for, or even discover, the Higgs as it is currently the only accelerator world-wide which has sensitivity in the predicted mass range. The search for the Higgs at the Tevatron has significant differences both to those performed at LEP2 and to those which will be performed at the LHC. Although the methodology is the same, compared to LEP the $p\overline{p}$ environment is not as clean, limiting the effectiveness of some channels. Though the Tevatron environment is similar to that of the LHC the relevant importance of the production processes is slightly different [60]. The lower number of minimum bias events per collision, due to the lower instantaneous luminosity at the Tevatron, means that some of the "all hadronic channels" which the LHC will not be able to use could be exploited. The estimate of the sensitivity of the Higgs search at DØ using a sequential cuts based analysis is important for a variety of reasons. Up to now the standard estimate of the Tevatron's Higgs reach was derived using a sequential cuts analysis as part of the SUSY Higgs workshop (SHW) [61]. The SHW used a common parametrised Monte Carlo for both DØ and CDF based on an "average" of the expected performance of DØ and CDF. It is important to redo this estimate using full Run II Monte Carlo and reconstruction code so that the SHW result can be compared to a more complete estimate. Besides, a sequential cuts approach provides valuable information on specific areas of the reconstruction code which need to be improved in order to achieve a greater sensitivity e.g. track matching and b-tagging. Indeed such an analysis can be used as a measure of changes to the reconstruction software. This is especially important at a stage in which the reconstruction code

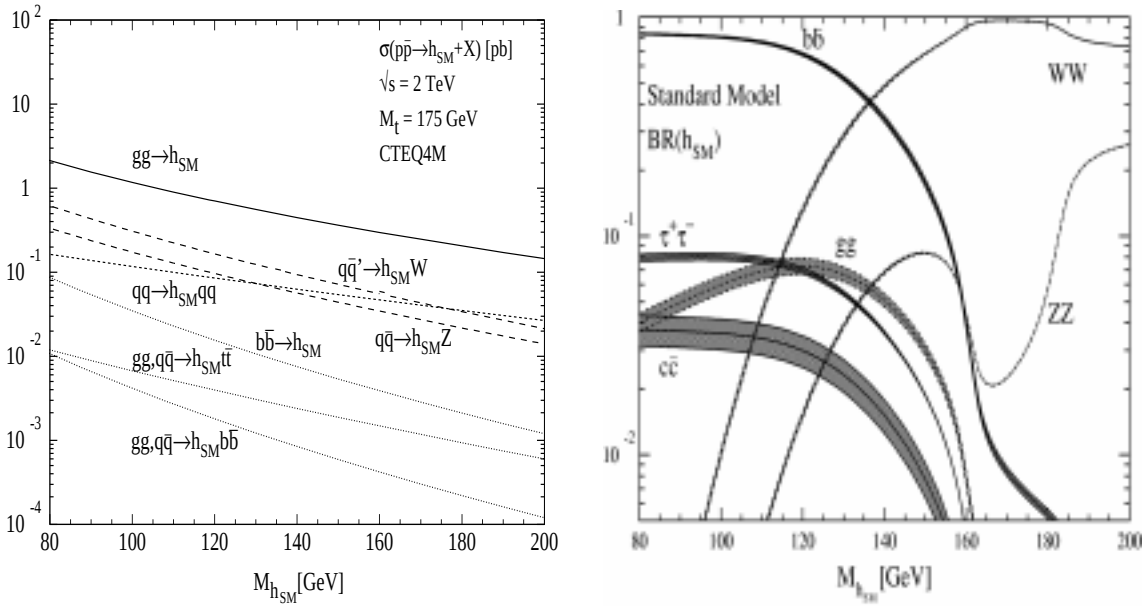

Figure 5.1: Higgs production cross-section at the Tevatron in pb (left) [62] and Higgs branching ratio (right) [62]

is still being extensively developed and tuned. Furthermore a sequential cuts based analysis naturally leads to Monte Carlo and data comparisons.

The other factor of importance for a sequential cuts analysis is that it can be used as a standard scale for more advanced techniques, such as neural networks, in order to test the effectiveness of these techniques and to point to potential pitfalls.

5.1 General Considerations at the Tevatron

The main problems for Higgs searches at the Tevatron are related to the hadronic environment. This creates problems for the triggering of events and dictates which Higgs production mechanisms and which decay channels can be used.

5.1.1 Production Mechanism and Higgs Decay

At the Tevatron there are four primary production modes of interest for the Standard Model Higgs, as shown in Fig. 5.1 [62]. The dominant process is gluon-gluon fusion, in which the Higgs is produced via a top quark loop as shown in Fig. 5.2. Roughly a factor of three lower in cross-section are the two associated processes where the Higgs is produced in association with a W or Z boson, shown in Fig. 5.3. The fourth process is $Hq\overline{q}$; this channel will be difficult to exploit due to the large QCD multi-jet background. However for models in which the Higgs has an augmented

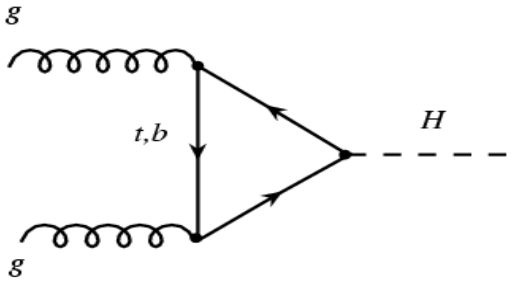

Figure 5.2: Feynman diagram for the Higgs boson gluon-gluon fusion production process

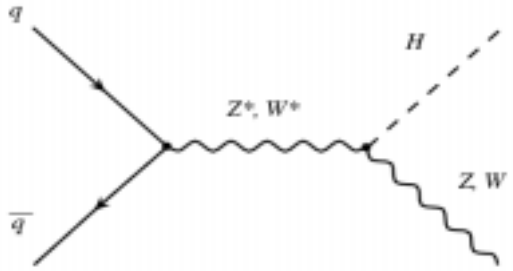

Figure 5.3: Feynman diagram of the associated production of a Higgs and a heavy vector boson

coupling to b quarks (such as Super Symmetry models with large tan β) this channel can be used [63].

The branching ratio for the Higgs is shown in Fig. 5.1 [62]. For a light Higgs (mass less than $\sim$135 GeV/c^2) the decay is predominantly to $b\bar{b}$. For a heavier Higgs the decay is mainly to WW. This divides the search into two scenarios. For the heavier Higgs one can take advantage of the higher gluon-gluon fusion cross-section and reconstruct the Higgs from the decay of the two vector bosons. For a low mass Higgs, the predominant decay to $b\bar{b}$ implies that the gluon-gluon fusion mechanism cannot be exploited due to the large QCD di-jet background. Hence one has to use the vector boson as the trigger, while using the b-jets in order to identify the Higgs. Thus for a low mass Higgs the key issues are b-tagging, di-jet mass reconstruction and vector boson identification.

5.2 General Considerations for $ZH \to e^+e^-b\bar{b}$

5.2.1 Triggering Events

The associated production of the Higgs and Z boson is a relatively straightforward channel to identify and trigger on. For the case in which the Z boson decays to an electron-positron pair the following triggers are a sample of those used to select this type of events.

- Trigger: di-jets and electron candidate "EM_MD_2CJT5":
  - Prescale: 1.
  - L1 term: One electromagnetic calorimeter trigger tower with $E_T > 10$ GeV and two calorimeter towers with $E_T > 5$ GeV. L1 accept rate is 40 Hz.

  - L2 term: One electromagnetic object candidate with $E_T > 10$ GeV and an electromagnetic fraction > 0.85. Two jet candidates with $E_T > 10$ GeV. L2 accept rate is 25 Hz.
  - L3 term : One electron candidate with $E_T > 15$ GeV and with an additional transverse shower shape requirement. Two jet candidates with $E_T > 15$ GeV. 1 event every 160 is marked and passed i.e. the trigger decision is recorded but the event passes the trigger regardless of the outcome of the L3 decision. L3 accept rate is 3.6 Hz.

- Trigger: two high E_T electron candidates "2EM_HI":
  - Prescale: 1.
  - L1 term: Two electromagnetic calorimeter trigger towers with $E_T > 10$ GeV. L1 accept rate is 6.0 Hz.
  - L2 term: No L2 trigger is required. L2 accept rate is 6.0 Hz
  - L3 term : Two electron candidates with $E_T > 10$ GeV. 1 event every 160 is marked and passed. L3 accept rate is 3.0 Hz.

The rates quoted are for an instantaneous luminosity of $2{\times}10^{31}$ cm^{-2}s^{-1} and the trigger rate at this luminosity is $\sim 1.7{\times}10^6$ Hz. All the objects are required to be within the fiducial calorimeter trigger region i.e. $|\eta| < 3.0$.

As the final state particles are produced by the decay of heavy particles, their p_T are expected to be relatively high, which in the case of the b-jets is well above the reconstruction threshold for jets. Hence there are no significant problems from the reconstruction of soft particles. This would be problematic as it is this region of momentum phase space that tends to be populated by most of the minimum bias and background QCD jets. The high transverse momentum in the event, together with the b-tagging and the presence of the electrons from the decay of the Z, implies that beyond the trigger level the contamination from pure QCD background should be negligible. This leaves only the backgrounds with similar signatures to the associated production, i.e. those with two electrons and two heavy flavour jets.

5.2.2 Physics Backgrounds

The main backgrounds to $ZH \to e^+e^-\ b\overline{b}$ associated production are: $ZZ \to e^+e^-\ b\overline{b}$ $(c\overline{c})$, $Z(\to e^+e^-)b\overline{b}$ $(c\overline{c})$ and $t\overline{t}$ production where both top quarks decay via $W(\to e\overline{\nu}_e)b$ to an electron, neutrino and a bottom quark. The $t\overline{t}$ production

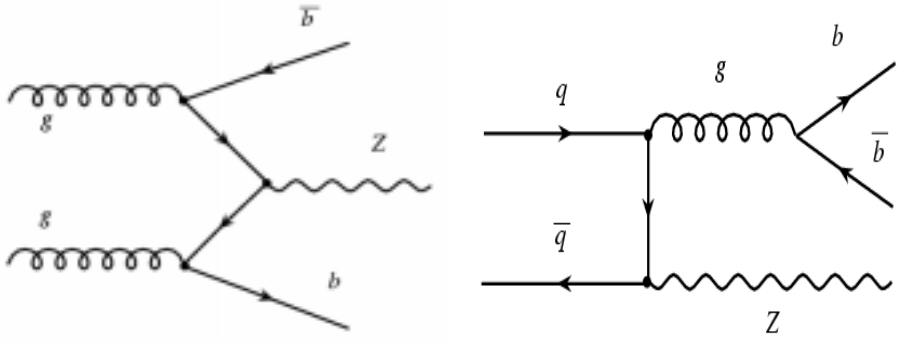

Figure 5.4: Tree level Feynman diagrams for $Zb\overline{b}$ production

is dominated by the s-channel $q\overline{q}$ annihilation. A sample of the tree level Feynman diagrams for $Zb\overline{b}$ are shown in Fig. 5.4. The $c\overline{c}$ decay channels are included as charm can be tagged in the same way as bottom, albeit with a much lower efficiency. Therefore there can be a certain amount of contamination in the b-tagged sample from charm.

5.2.3 Monte Carlo Samples

The Monte Carlo samples used were generated using version p10.15 of the DØ reconstruction code, with an overlay of 0.5 minimum bias events [1]. The samples were generated using Pythia 6.155 [58], except for the $Zb\overline{b}(c\overline{c})$ samples which were generated using Comphep and then passed through Pythia for the fragmentation. Comphep is a complete first order matrix element Monte Carlo generator [64]. CTEQ4L parton distribution functions are used for all the samples. A summary of the samples used can be found in Table 5.1.

The effective cross-section for the signal samples was obtained from extrapolations of next-to-leading order calculations [62], whilst all other numbers were taken directly from the Monte Carlo generators. Recently there have been developments in this field and next-to-next-to-leading order cross-sections have been calculated [65]. At the moment only the inclusive ZH production cross-section at the Tevatron has been calculated. This is approximately 30% greater than the next-to-leading order inclusive cross-section calculation.

The advantage of Comphep is that it not only performs the full calculation in a reliable manner, but also takes into account the non-zero mass of the bottom and charm quarks. Pythia, on the other hand, does not differentiate between the charm

[1] 0.5 is the average number of minimum bias events per event expected at the current instantaneous luminosity.

Process	Generator	$\sigma \times$ Branching Ratio (fb)	Number of Events
$ZH(105) \to e^+e^-b\overline{b}$	Pythia	4.003	16 K
$ZH(115) \to e^+e^-b\overline{b}$	Pythia	2.733	15.5 K
$ZH(125) \to e^+e^-b\overline{b}$	Pythia	1.721	15.75 K
$ZZ \to e^+e^-b\overline{b}$	Pythia	12.76	69.25 K
$ZZ \to e^+e^-c\overline{c}$	Pythia	11.14	38.5 K
$Z(\to e^+e^-)b\overline{b}$	Comphep	150.1	127 K
$Z(\to e^+e^-)c\overline{c}$	Comphep	312.2	124 K
$t\overline{t} \to e^+e^-b\overline{b}$	Pythia	71.09	32.5 K

Table 5.1: Monte Carlo samples used

and the bottom mass. However the effect of the differentiation between charm and bottom is probably not large for the samples under study due to the generally large momentum. Hence the kinematics of the events are to first approximation identical for the $b\overline{b}$ and the $c\overline{c}$ channels whereas for the ZZ sample they should be the same to all orders.

As Comphep uses a full matrix element calculation all the spin correlations of the particles and their subsequent decay products are treated correctly. This differs from Pythia which does not take into account the spin information of the decay products of a two body system (relevant to the $t\overline{t}$ and ZZ channels) i.e. it treats the particles as spin-less for the purpose of their decay. As a result any comparison of distributions involving angular quantities between the final decay products is approximate at best.

There have also been developments in the calculation of higher order corrections for the $Zb\overline{b}$ cross-section using the MCFM Monte Carlo generator [66][67]. This has not yet yielded a firm number when interfaced to the DØ code. Indications from MCFM calculations for the $Wb\overline{b}$ process would suggest that the cross-section is noticeably higher than the tree level value obtained using other generators [68] e.g. Comphep.

The $Zb\overline{b}$ process is problematic for Monte Carlo generators due to soft b-jets in the forward region and as a result is not supported by generators such as Pythia and OneTop [69]. Pythia has discontinued the full calculation for this process in v6.2 due to the slow speed of generation and stability issues. Pythia does allow for the generation of the $Zb\overline{b}$ final state via $b\overline{b} \to Z$ with the two other b quarks generated by $g \to b\overline{b}$ initial state showers [58]. Again there have been recent developments in this field with the development of ALPGEN [70], a Monte Carlo generator specifically designed to generate Z/W + multi-jets in a hadronic environment.

5.2.4 Heavy Flavour Tagging

Heavy flavour tagging is a basic element in the search for the Higgs boson. The use of heavy flavour tagging is needed to separate the signal from the QCD light-jet background. There are various ways to tag heavy flavour; the method used for this analysis is the secondary vertex tag [71][72]. Two other methods which will be used at DØ are the muon tag [73] and the impact parameter tag [74].

Muon Tag

The muon tag takes advantage of the semi-leptonic $b \to c\mu\nu$ decay of the b quark. Due to the high b quark mass the muon from the decay of the b quark can have a high p_T^{rel} i.e. high p_T with respect to the combined jet and muon axis. By cutting on the minimum p_T^{rel} of muons matched to jets it is possible to identify the b quark jets. This method was used successfully in Run I [75].

Impact Parameter Tag

This tagger identifies b quark jets from the fact that tracks from the decay of a long lived particle within a jet (such as the b quark) will have a large impact parameter (or distance of closest approach) with respect to the primary vertex. The significance of the impact parameter, combined with the fact that the projection of the impact parameter on the jet axis is positive, can be used to tag the jet. Tracks originating from the primary vertex have a symmetric impact parameter distribution, centred on 0, with a resolution set by the tracking resolution.

Secondary Vertex Tag

Due to the high momentum with which particles are produced at the Tevatron, long lived particles can travel a measurable distance before they decay. Bottom quarks produced at DØ can travel on the order of a few mm before decaying. This leaves a characteristic signature of a second vertex, well displaced from the primary, which can be reconstructed using tracks from the silicon detector. Currently, at DØ , the secondary vertices are reconstructed using all the available tracks which are not associated to a primary vertex [71][72]. To match a given jet to a given secondary vertex the displacement of the secondary vertex from the selected primary is calculated. From this the ϕ and η_{phys} direction of the secondary vertex with respect to the primary is calculated and the ΔR between this direction and the jet axis is calculated. If the jet axis is within a given ΔR of the direction of the secondary, the jet is considered matched to the secondary vertex. The significance

of the displacement of the secondary vertex with respect to the primary is defined as:

$$s = \frac{\sqrt{(x_{sec} - x_{pri})^2 + (y_{sec} - y_{pri})^2}}{\sigma} \tag{5.1}$$

where σ is the combined resolution of the primary and secondary vertex measurement. The jet is then considered tagged if the significance is greater than a given value. This method to tag jets is intuitive in that the direction between the primary and secondary vertex is simply the direction of flight of the b quark. The subsequent decay and fragmentation of the b quark to form the detected jet preserves this overall direction.

5.2.5 Mass Resolution

The mass resolution of the $b\bar{b}$ system plays a vital part in the search for the Higgs boson. The Higgs boson, if it exists, would appear as an excess of events in the $b\bar{b}$ mass spectrum at the Higgs mass. The location of the mass peak will be offset by the jet energy scale and the width will be broadened by the di-jet mass resolution of the detector. If the mass resolution is too large the mass peak will be washed out and the excess of events will not be apparent. The main factors which determine the mass resolution are the intrinsic detector resolution and the effect of final state radiation of the b quarks. Currently only calorimeter information is used in reconstructing jets and this is what determines the intrinsic resolution. The intrinsic resolution can be improved by combining information from the tracking system and from other sub-detectors. This method has been used successfully in other high energy physics experiments, for example Aleph [76].

The emission of gluons by the b quarks effectively reduces the invariant mass as part of the energy is lost to the gluon. This not only produces a low mass tail but also results in a broadening of the distribution. There are a variety of measures which can be taken to reduce the impact of final state radiation, one of which is to try to add back the gluon radiation. Another solution is to eliminate events which contain more than two jets. This is a much more radical measure. A problem of using this latter method is that in a hadronic environment there can be jets from minimum bias events and from the spectator quarks, hence further limiting the statistics.

5.3 Object Selection

5.3.1 Electromagnetic Object Selection Efficiency

The electromagnetic selection used in this analysis is based on the certified DØ electromagnetic selection code version v2.0 [56] and consists of the following cuts.

- electromagnetic fraction > 0.9.
- isolation < 0.15.
- H-matrix8 < 20.

In order to obtain values for the electron efficiency 4000 events from each sample were used. Events that had at least one reconstructed primary vertex, within ± 50 cm of the centre of the detector and with at least two tracks associated to the vertex were selected. In the case of multiple primary vertices the one with the hardest sum of the p_T of the associated tracks was selected as the primary.

The efficiency for reconstructing an electron can be subdivided into the efficiency for finding a cluster within the electromagnetic calorimeter region ("clustering efficiency") and a subsequent efficiency for the quality cuts outlined above (ID efficiency). All clustering efficiencies are quoted with respect to the two Monte Carlo high p_T electrons in the event, i.e. those from the decay of the top in the case of $t\bar{t}$ and from the Z for all the other processes. Clusters found are considered to be matched to Monte Carlo electrons if they lie within $\Delta R < 0.2$. The ID efficiency is defined as:

$$\epsilon_{ID} = N^{pass}_{emobj}/N_{emobj}, \tag{5.2}$$

i.e. the ratio of the number of electromagnetic objects which pass the selection cuts to the total number of electromagnetic objects.

The difference in the η distributions between the generated Monte Carlo electrons and the reconstructed electromagnetic objects for the $Zb\bar{b}$ sample is shown in Fig. 5.5. The lack of reconstructed objects in the ICR ($0.7 < |\eta| < 1.8$) is evident in Fig. 5.5 and in Table 5.2. Table 5.2 lists the clustering efficiencies in the CC ($|\eta| < 0.7$), ICR ($0.7 < |\eta| < 1.8$) and EC ($|\eta| > 1.8$) for the various samples. The "restricted" efficiency is limited to electrons within $|\eta| < 2.5$. This is the cut which will be used for the analysis in Section 5.4. The main motivation for restricting the η range is to avoid the very forward region where the majority of minimum bias jets are located, this is based on Run I experience and analysis from the SHW. From Fig. 5.5 and

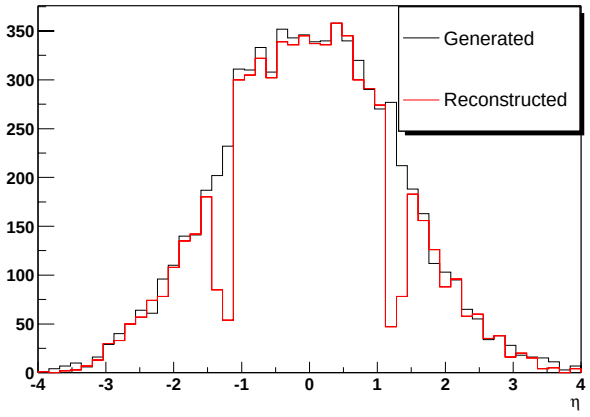

Figure 5.5: η distribution for generated electrons and for matched reconstructed electromagnetic objects

Process	CC (%)	ICR (%)	EC (%)	Restricted (%)
$ZH(105) \to e^+e^-b\bar{b}$	92.66 ± 0.45	70.51 ± 0.82	89.45 ± 0.99	83.41 ± 0.44
$ZH(115) \to e^+e^-b\bar{b}$	92.58 ± 0.45	73.07 ± 0.79	87.66 ± 1.35	83.98 ± 0.43
$ZH(125) \to e^+e^-b\bar{b}$	92.87 ± 0.44	71.84 ± 0.80	89.01 ± 1.10	83.66 ± 0.44
$t\bar{t} \to e^+e^-b\bar{b}$	89.22 ± 0.51	69.49 ± 0.83	87.50 ± 1.37	81.04 ± 0.46
$ZZ \to e^+e^-b\bar{b}$	88.26 ± 0.58	70.24 ± 0.82	82.88 ± 1.08	80.48 ± 0.47
$ZZ \to e^+e^-c\bar{c}$	86.29 ± 0.64	71.74 ± 0.81	85.93 ± 0.96	80.52 ± 0.48
$Z(\to e^+e^-)b\bar{b}$	92.23 ± 0.49	71.71 ± 0.79	86.29 ± 1.00	82.62 ± 0.45
$Z(\to e^+e^-)c\bar{c}$	93.79 ± 0.45	71.84 ± 0.78	88.03 ± 0.91	83.53 ± 0.44

Table 5.2: Electromagnetic clustering efficiency

Table 5.2 it is apparent that the cluster finding efficiency is similar for the CC and the EC, which is to be expected as the electromagnetic calorimeter is similar in these two regions.

The efficiencies in Table 5.2 are similar for all the samples with some slight variations, due to the different topologies and hence different p_T distributions of the electrons. The p_T dependence of the clustering is displayed in Figs. 5.6 and 5.7. The lines in these figures and in subsequent figures are not a fit to the data points but are supplied as a guide. From these figures it can be seen that there is an initial strong dependence between the finding of the cluster and the object p_T. Furthermore as there is only a slight drop in ID efficiency in the ICR, as seen in Figs. 5.6b) and 5.7b), it is clear that most of the inefficiency in the ICR is due to the clustering being unable to locate the objects as seen in Table 5.2, as opposed to clusters found failing the ID cuts. In the forward region the ID efficiency drops noticeably above $|\eta| > 2.5$. It is significant that the clustering does not display this, i.e. the drop in

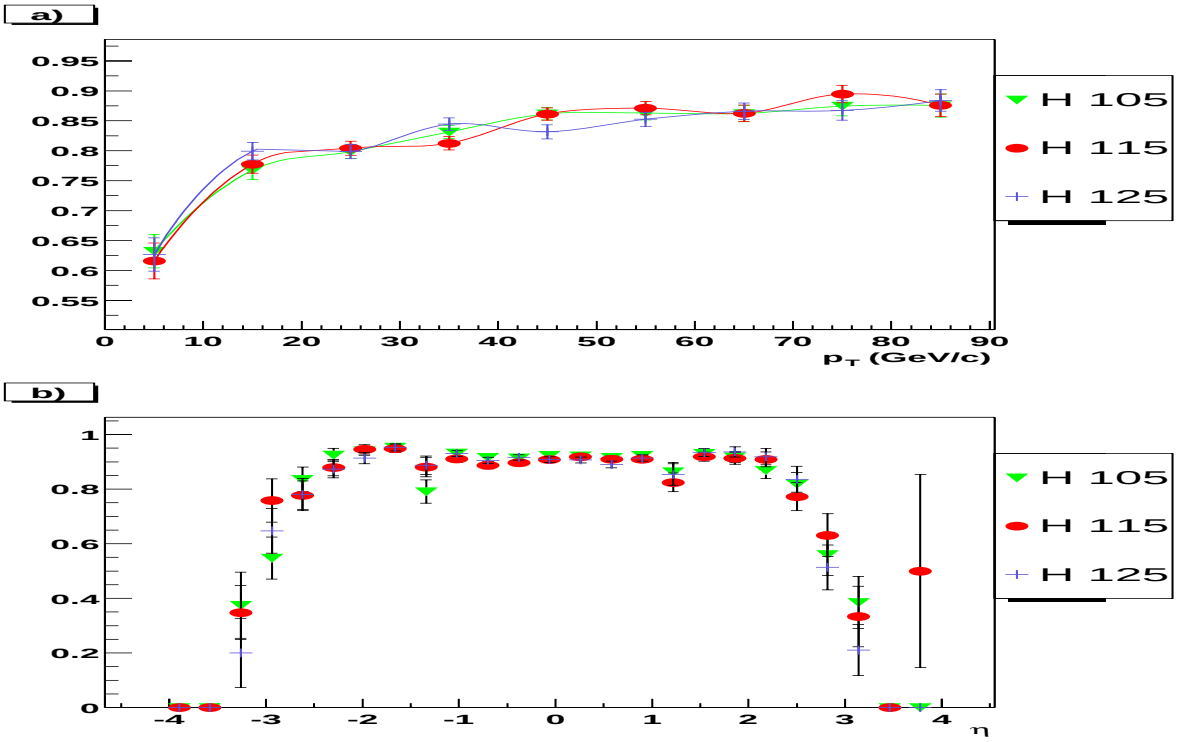

Figure 5.6: Signal samples: a) Electromagnetic clustering efficiency as a function of generated electron p_T. b) ID efficiency as a function of η

efficiency is due to problems in reconstructing "clean" electromagnetic candidates and not in finding the clusters.

Figs. 5.8 and 5.9 show the ID efficiency for, respectively, the signal and background samples, when varying one of the cut values whilst keeping the others constant at the certified value. From these figures it can be seen that the efficiency depends strongly on the isolation and H-matrix values, whereas for the electromagnetic fraction the dependence is flat except at high values. Furthermore there are no major differences in the shapes of the graphs for the different samples, although the $t\bar{t}$ has a slightly higher efficiency for all the distributions. This is linked to the fact that the electrons are generally more isolated which leads to less contamination from other objects in the event, as can be seen in Fig. 5.9a).

Figs. 5.10 and 5.11 show the ID efficiency as a function of p_T for the signal and background samples respectively. The signal samples have virtually identical profiles as the background with the exception of the $t\bar{t}$ sample. The $t\bar{t}$ sample has a higher efficiency than the other backgrounds, as seen in Figs. 5.11a) and 5.11c), with respect to the p_T cut and also for objects which pass the ID cuts and which have a track match. The former can be explained by the fact that the electrons from the top decay have a higher p_T compared to other decays, simply due to the

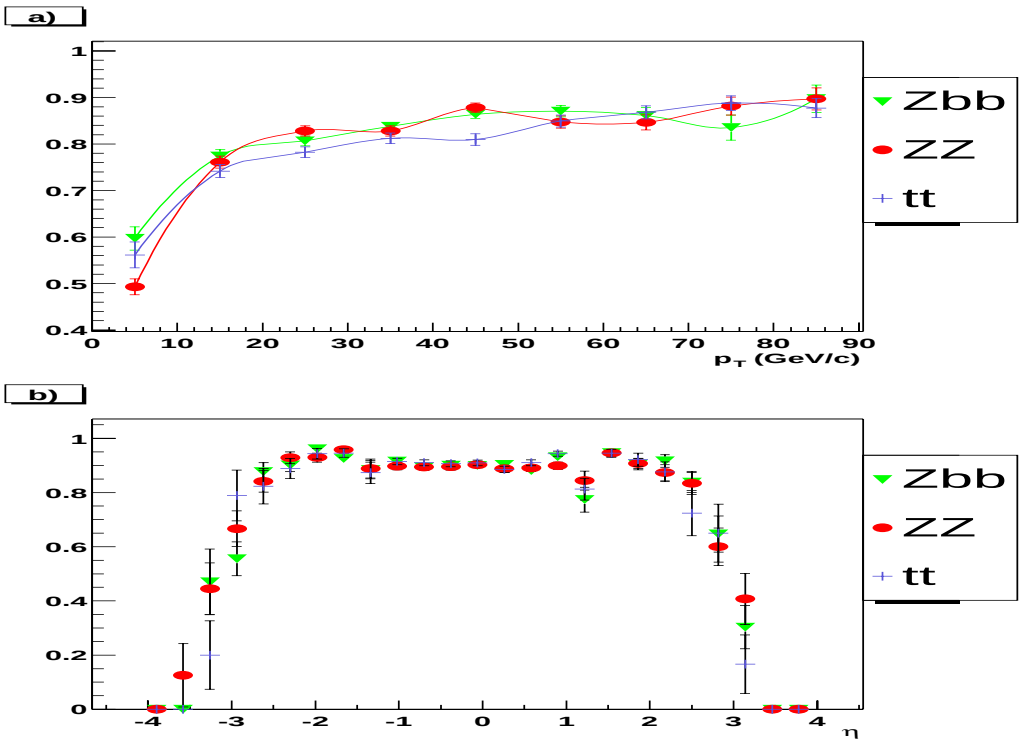

Figure 5.7: Background samples: a) Electromagnetic clustering efficiency as a function of generated electron p_T. b) ID efficiency as a function of η

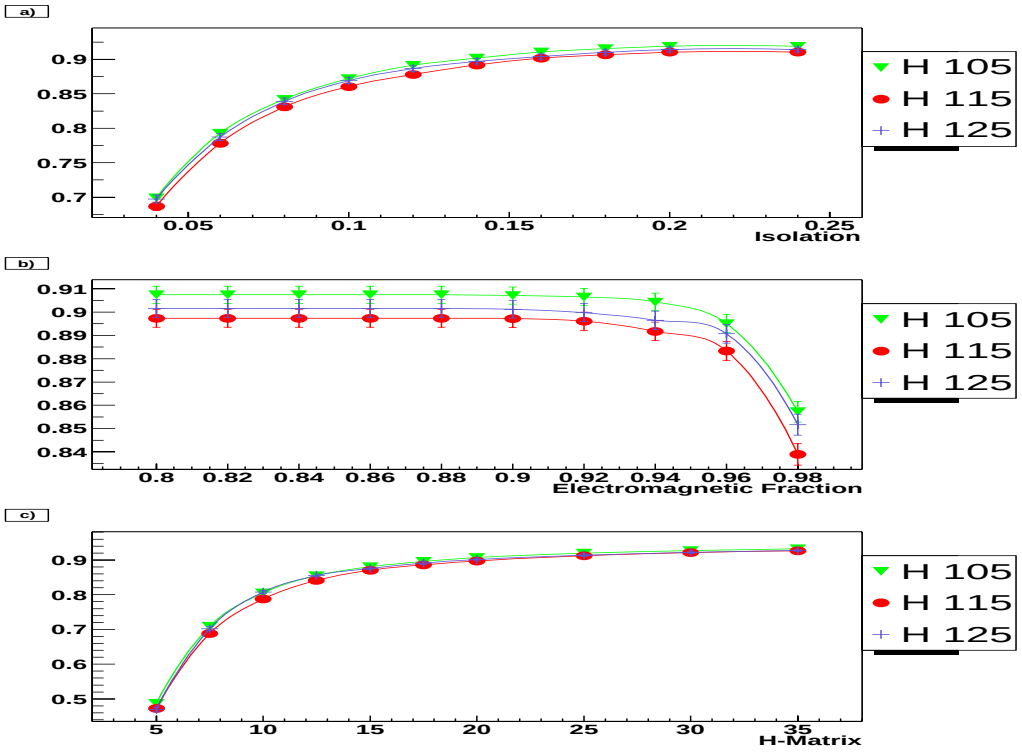

Figure 5.8: Signal samples: electromagnetic ID efficiency as a function of a) isolation, b) electromagnetic fraction, c) H-Matrix

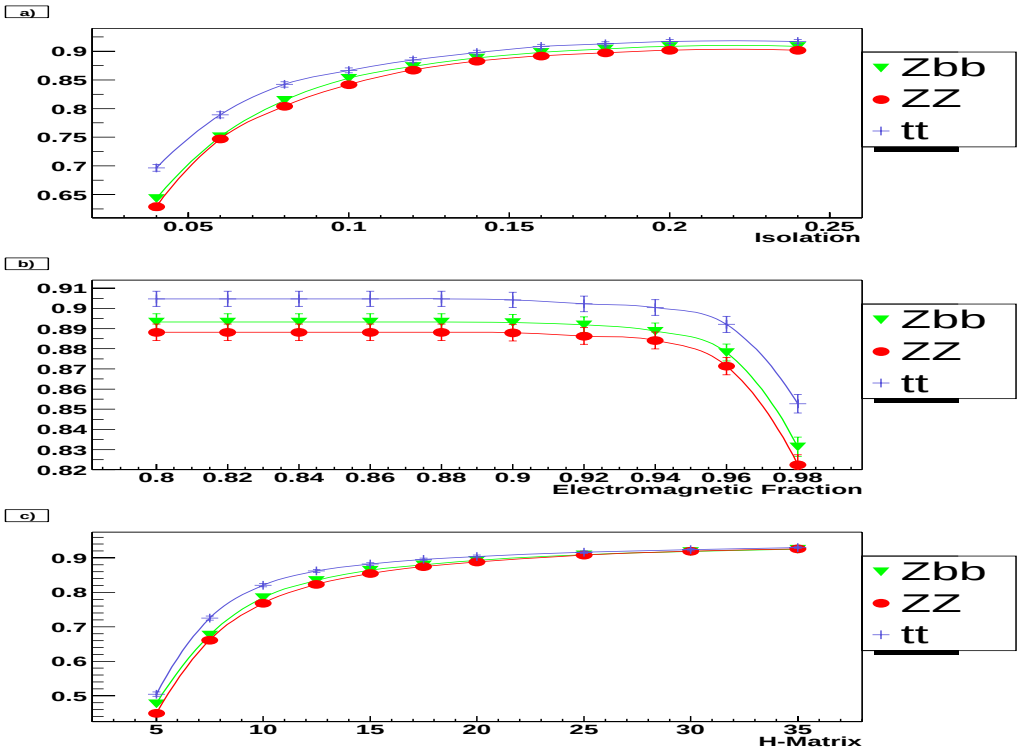

Figure 5.9: Background samples: electromagnetic ID efficiency as a function of a) isolation, b) electromagnetic fraction, c) H-Matrix

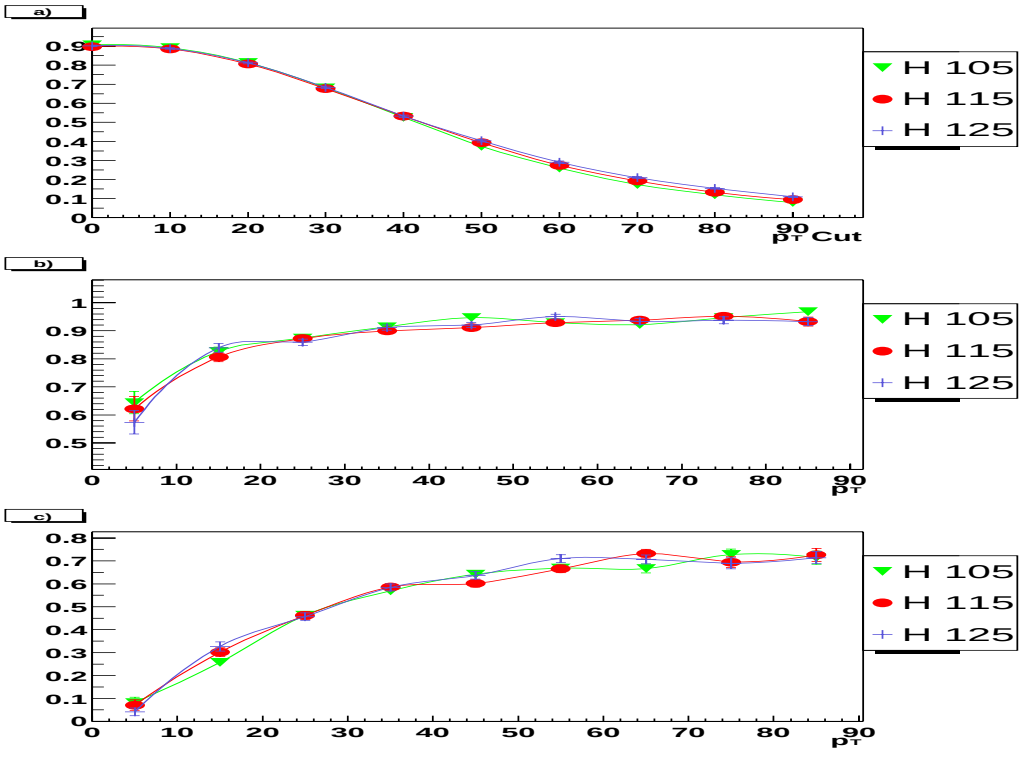

Figure 5.10: Signal samples: Electromagnetic ID efficiency as a function of a) p_T cut, b) p_T, c) p_T with an additional track match. p_T is in units of GeV/c

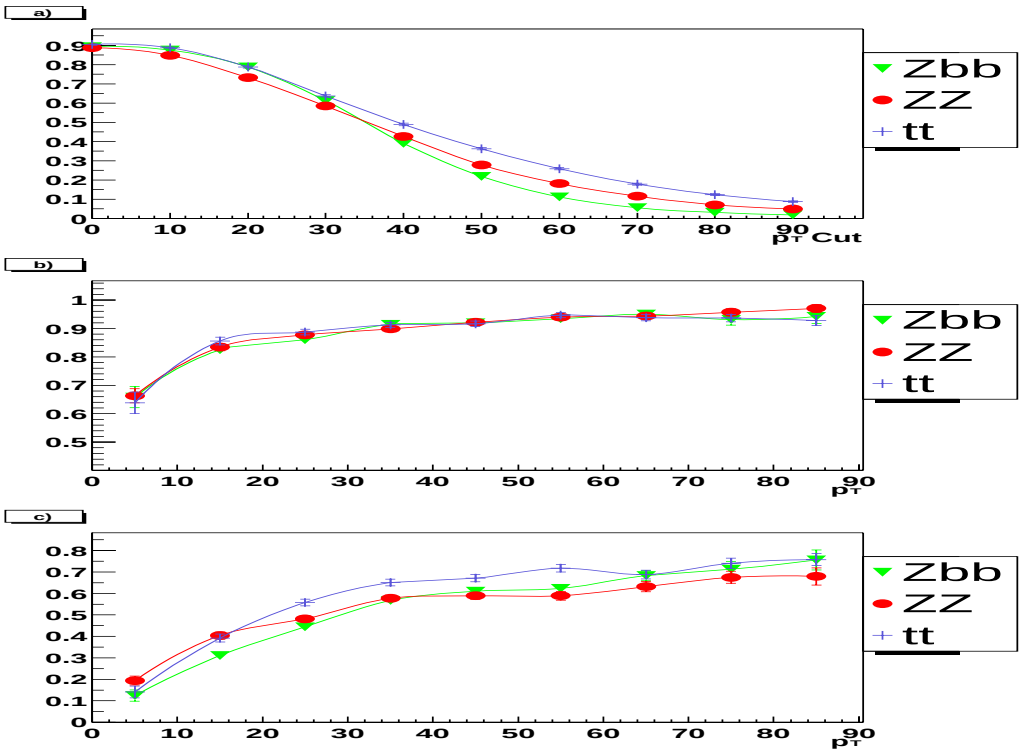

Figure 5.11: Background samples: Electromagnetic ID efficiency as a function of a) p_T cut, b) p_T, c) p_T with an additional track match. p_T is in units of GeV/c

higher top mass (Fig. 5.11a)). The latter can be explained by the kinematics of the top decay; the electrons are more central compared to the other processes. As the tracker, due to its design, is more efficient out to $|\eta| < 1.6$ the $t\bar{t}$ events will have a greater global efficiency for track matches.

It is interesting to note the difference in Fig. 5.11a) between the ZZ and the $Zb\bar{b}$ samples. The ZZ has a very similar shape to the $t\bar{t}$ sample (with a slightly lower efficiency) however the efficiency of the $Zb\bar{b}$ is slightly higher for low p_T cuts but then sharply drops. The difference in initial efficiency can be related to the slightly different ID efficiency distributions (Fig. 5.9), whereas the change in shape indicates that the $Zb\bar{b}$ distribution has a shorter tail in the electron p_T distribution, as seen in Fig. 5.20. Figs. 5.10b) and 5.11b) follow closely the p_T distributions in Figs. 5.6a) and 5.7a). Both sets of figures highlight that at a p_T of $\sim$25 GeV/c the efficiency reaches a plateau. This feature is not present when requiring a track match due to the additional p_T dependence of the tracking.

Table 5.3 lists the ID efficiencies for the various signal and background samples. The efficiencies are split into the three pseudo-rapidity ranges and also quoted is the efficiency for the restricted range. Table 5.4 shows the ID efficiency with an additional track match requirement. The difference between Table 5.3 and Table 5.4

Process	CC (%)	ICR (%)	EC (%)	Restricted (%)
$ZH(105) \to e^+e^-b\bar{b}$	91.96 ± 0.49	92.12 ± 0.58	82.59 ± 1.30	91.93 ± 0.35
$ZH(115) \to e^+e^-b\bar{b}$	90.63 ± 0.53	90.73 ± 0.60	83.07 ± 1.35	90.62 ± 0.38
$ZH(125) \to e^+e^-b\bar{b}$	90.72 ± 0.51	91.79 ± 0.58	82.25 ± 1.42	91.16 ± 0.37
$ZZ \to e^+e^-b\bar{b}$	89.42 ± 0.59	90.88 ± 0.62	82.62 ± 1.19	90.19 ± 0.40
$ZZ \to e^+e^-c\bar{c}$	88.99 ± 0.63	91.01 ± 0.61	79.82 ± 1.19	89.79 ± 0.41
$Z(\to e^+e^-)b\bar{b}$	89.59 ± 0.58	91.64 ± 0.57	83.14 ± 1.17	90.76 ± 0.38
$Z(\to e^+e^-)c\bar{c}$	89.90 ± 0.58	91.06 ± 0.59	82.18 ± 1.15	90.49 ± 0.38
$t\bar{t} \to e^+e^-b\bar{b}$	90.86 ± 0.50	91.39 ± 0.61	83.56 ± 1.64	91.03 ± 0.37

Table 5.3: Electromagnetic ID efficiency

is the tracking efficiency for tracks associated with electrons. This is approximately 85% for the CC. From Table 5.4 it is clear that there is no tracking available for electromagnetic objects in the forward region. The lack of tracking in the forward region is a combination of the absence of the CFT, which only has full coverage up to $|\eta| < 1.6$, and of the current tracking algorithms which depend heavily on the CFT. Improving the tracking efficiency is a high priority for the next release of the DØ reconstruction code, which aims to provide tracking in the forward region using the silicon F and H-disks.

Table 5.5 lists the selection efficiency (clustering efficiency × ID efficiency) for the signal and background samples. Table 5.6 gives the final reconstruction efficiency which is obtained by multiplying the selection efficiency by the geometrical acceptance. The geometrical acceptance is defined as the percentage of generated electrons within the restricted η range. This number does not take into account reconstruction effects which can mean a discrepancy between the η of generated and reconstructed electrons. This effect is relevant for only a small fraction close to the cut value and furthermore, it is symmetrical around the boundary value due to the hermetic nature of the electromagnetic calorimeter at that pseudo-rapidity. Consequently it is assumed that the difference between reconstructed and generated η has a negligible effect.

From Table 5.5 and Table 5.6 the efficiencies for all the processes are again similar. The signal samples have a slightly higher reconstruction efficiency mostly due to the higher selection efficiency in the CC. The slight difference between the ZZ and the $Zb\bar{b}$ selection can be traced back to the difference in "clustering" efficiency. As seen in Fig. 5.7a) this difference is solely at low p_T. The effect of restricting the η range for the electrons adds a $\sim 3\%$ inefficiency for the signal samples.

Process	CC (%)	ICR (%)	EC (%)	Restricted (%)
$ZH(105) \to e^+e^-b\bar{b}$	76.82 ± 0.37	50.71 ± 1.07	0 ± -	56.95 ± 0.63
$ZH(115) \to e^+e^-b\bar{b}$	75.71 ± 0.77	53.15 ± 1.03	0 ± -	57.75 ± 0.63
$ZH(125) \to e^+e^-b\bar{b}$	76.49 ± 0.75	52.41 ± 1.05	0 ± -	58.73 ± 0.63
$ZZ \to e^+e^-b\bar{b}$	75.64 ± 0.82	50.16 ± 1.07	0 ± -	53.35 ± 0.65
$ZZ \to e^+e^-c\bar{c}$	76.18 ± 0.85	50.41 ± 1.06	0 ± -	51.68 ± 0.65
$Z(\to e^+e^-)b\bar{b}$	75.64 ± 0.82	50.41 ± 1.03	0 ± -	53.30 ± 0.64
$Z(\to e^+e^-)c\bar{c}$	76.02 ± 0.82	48.09 ± 1.02	0 ± -	51.66 ± 0.64
$t\bar{t} \to e^+e^-b\bar{b}$	75.06 ± 0.75	55.82 ± 1.07	0 ± -	61.77 ± 0.63

Table 5.4: Electromagnetic ID efficiency with an additional track match

Process	CC (%)	ICR (%)	EC (%)	Global (%)
$ZH(105) \to e^+e^-b\bar{b}$	85.21 ± 0.61	64.95 ± 0.86	73.88 ± 1.42	75.34 ± 0.50
$ZH(115) \to e^+e^-b\bar{b}$	83.91 ± 0.64	66.30 ± 0.84	72.82 ± 1.50	75.00 ± 0.50
$ZH(125) \to e^+e^-b\bar{b}$	84.25 ± 0.62	65.94 ± 0.84	73.21 ± 1.56	75.24 ± 0.50
$ZZ \to e^+e^-b\bar{b}$	78.92 ± 0.73	63.83 ± 0.86	68.48 ± 1.33	70.88 ± 0.53
$ZZ \to e^+e^-c\bar{c}$	76.78 ± 0.78	65.29 ± 0.86	68.59 ± 1.28	70.45 ± 0.53
$Z(\to e^+e^-)b\bar{b}$	82.70 ± 0.69	65.72 ± 0.83	71.74 ± 1.31	73.47 ± 0.51
$Z(\to e^+e^-)c\bar{c}$	84.31 ± 0.68	65.42 ± 0.83	72.34 ± 1.26	73.92 ± 0.51
$t\bar{t} \to e^+e^-b\bar{b}$	81.06 ± 0.64	63.51 ± 0.87	73.12 ± 1.83	73.12 ± 0.52

Table 5.5: Electromagnetic selection efficiency for signal and background

Process	Restricted (%)	Geometrical (%)	Total (%)
$ZH(105) \to e^+e^-b\bar{b}$	76.68 ± 0.50	95.94 ± 0.23	73.56 ± 0.51
$ZH(115) \to e^+e^-b\bar{b}$	76.10 ± 0.50	96.37 ± 0.22	73.34 ± 0.51
$ZH(125) \to e^+e^-b\bar{b}$	76.26 ± 0.50	96.86 ± 0.20	73.87 ± 0.51
$ZZ \to e^+e^-b\bar{b}$	72.59 ± 0.53	94.39 ± 0.27	68.51 ± 0.54
$ZZ \to e^+e^-c\bar{c}$	72.30 ± 0.54	93.86 ± 0.28	67.86 ± 0.55
$Z(\to e^+e^-)b\bar{b}$	74.98 ± 0.52	94.62 ± 0.26	70.95 ± 0.53
$Z(\to e^+e^-)c\bar{c}$	75.59 ± 0.51	94.20 ± 0.27	71.20 ± 0.53
$t\bar{t} \to e^+e^-b\bar{b}$	73.77 ± 0.52	97.98 ± 0.16	72.28 ± 0.52

Table 5.6: Electromagnetic selection efficiency for signal and background

5.3.2 Jet Selection Efficiency

The certified DØ jet selection [77] is based on the following cuts.

- $0.05 <$ electromagnetic fraction < 0.95.
- Coarse hadronic fraction < 0.5.
- Hot fraction < 10.

A cone size of 0.5 is used. It is required that the jets are not matched (within $\Delta R < 0.5$) to a reconstructed electromagnetic object passing the electromagnetic ID cuts. This is to eliminate fake jets from isolated electromagnetic objects. The same event selection and efficiency definitions as in Section 5.3.1 are used. A jet is selected if it is matched to one of the b quarks i.e. if it is within $\Delta R < 0.5$ to one of the two highest p_T generated b quarks (for the $Zb\overline{b}$ and $t\overline{t}$ samples) or to those from the decay of the Higgs or Z.

For the samples with charm quarks the definition of the generated charm quark is problematic as the PDG-id of charm is not stored in the DØ Monte Carlo root-tuples but only those of the fragmentation products of the quark. A way around this is to define the charm quark as being the highest p_T fragmentation product associated with a Z boson (in the case of ZZ) or with the hard scatter (in the case of $Zc\overline{c}$). As the $b\overline{b}$ and $c\overline{c}$ samples are generated in a similar manner one can reasonably assume that the generated charm selection uncertainty is likely to be of the same order or greater than the difference introduced by the different c and b quark mass (which is only relevant for the Comphep samples). Hence it is assumed that the jet efficiencies and errors are equal for the $c\overline{c}$ and $b\overline{b}$ samples.

The clustering efficiencies are listed in Table 5.7. The restricted pseudo-rapidity definition contains jets within $|\eta| < 2.0$. Table 5.7 displays a slight variation in "clustering" efficiency from sample to sample. Whereas the clustering efficiency for most channels is similar, that for $Zb\overline{b}$ is significantly lower by about 10% over the whole η range. The clustering efficiency as a function of p_T is similar for all channels, as expected, as seen in Fig. 5.13a) and 5.12a). However this does not fold in the p_T distribution of the quarks and the fact that there is a jet reconstruction threshold of 8 GeV/c. As the b quark p_T is lower for the $Zb\overline{b}$ channel (Fig. 5.21), most of the difference in efficiency for $Zb\overline{b}$ is due to the b quarks populating the lower efficiency region in Fig. 5.13a). The slight difference between the other channels can also be related to the differences in the p_T spectra of the b quarks.

Process	CC (%)	ICR (%)	EC (%)	Restricted (%)
$ZH(105) \to e^+e^-b\bar{b}$	94.44 ± 0.39	88.49 ± 0.56	61.88 ± 1.69	90.66 ± 0.35
$ZH(115) \to e^+e^-b\bar{b}$	93.58 ± 0.42	90.73 ± 0.52	68.10 ± 1.68	91.51 ± 0.33
$ZH(125) \to e^+e^-b\bar{b}$	94.11 ± 0.40	89.85 ± 0.54	68.94 ± 1.71	92.06 ± 0.33
$ZZ \to e^+e^-b\bar{b}$	91.54 ± 0.51	86.87 ± 0.59	67.92 ± 1.37	88.77 ± 0.39
$Z(\to e^+e^-)b\bar{b}$	80.12 ± 0.76	74.68 ± 0.76	59.26 ± 1.33	76.68 ± 0.53
$t\bar{t} \to e^+e^-b\bar{b}$	92.90 ± 0.42	89.39 ± 0.56	66.84 ± 1.95	91.17 ± 0.34

Table 5.7: Jet clustering efficiency

Process	CC (%)	ICR (%)	EC (%)	Restricted (%)
$ZH(105) \to e^+e^-b\bar{b}$	99.31 ± 0.15	99.22 ± 0.16	99.42 ± 0.34	99.26 ± 0.11
$ZH(115) \to e^+e^-b\bar{b}$	99.69 ± 0.10	99.34 ± 0.15	99.24 ± 0.38	99.52 ± 0.09
$ZH(125) \to e^+e^-b\bar{b}$	99.54 ± 0.12	99.09 ± 0.18	99.41 ± 0.34	99.34 ± 0.10
$ZZ \to e^+e^-b\bar{b}$	99.56 ± 0.13	99.29 ± 0.16	98.86 ± 0.38	99.36 ± 0.10
$Z(\to e^+e^-)b\bar{b}$	99.59 ± 0.14	99.39 ± 0.16	99.14 ± 0.32	99.43 ± 0.11
$t\bar{t} \to e^+e^-b\bar{b}$	99.89 ± 0.06	98.93 ± 0.20	99.74 ± 0.26	99.48 ± 0.09

Table 5.8: Jet ID efficiency

From Table 5.7 the clustering efficiency is notably lower in the forward region. This is probably not due to the event topology as the efficiency for electromagnetic objects does not drop off in a similar way. It is instead likely to be an effect of the different algorithms and the difference in cone sizes used to reconstruct the jets and the electromagnetic objects. Overall the efficiency remains high due to the fact that most jets are central; for the ZZ sample 88% of b-jets are contained within the restricted limit.

From Table 5.8 it is apparent that ID cuts, to all intents and purposes, are 100% efficient. Hence all the inefficiency in reconstructing jets comes from the jet finding algorithm. This is further comfirmed by Fig. 5.14 and 5.15 which show that the cuts are placed at the start of the efficiency plateau, and from Figs. 5.16b) and 5.17b) in which there is no efficiency dependence on the p_T of the reconstructed jet.

The total combined selection efficiency for signal and background is given in Table 5.9 and the total reconstruction efficiency in Table 5.10. The geometrical acceptance efficiency is defined as in Section 5.3.1. The p_T dependence of the reconstruction is highlighted by the lower global selection efficiencies for the $Zb\bar{b}$ and the ZZ samples. The lower total reconstruction efficiency of these two channels reflects the different geometrical acceptance of the samples. The effect of restricting the η

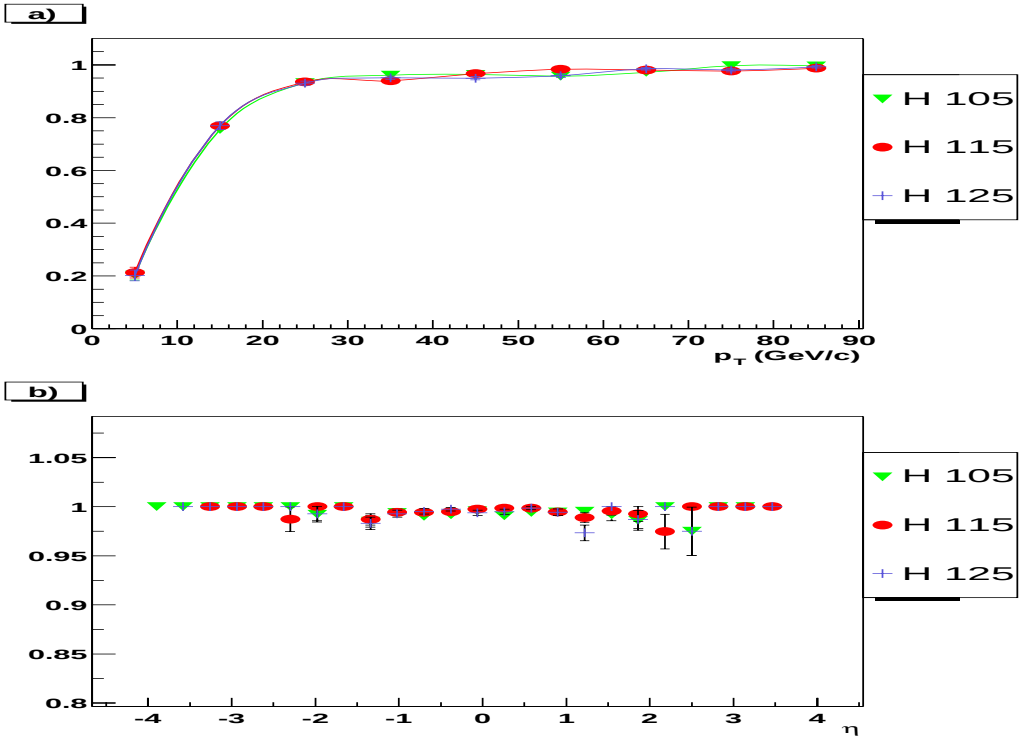

Figure 5.12: Signal samples: a) Jet clustering efficiency as a function of generated quark p_T, b) ID efficiency as a function of η

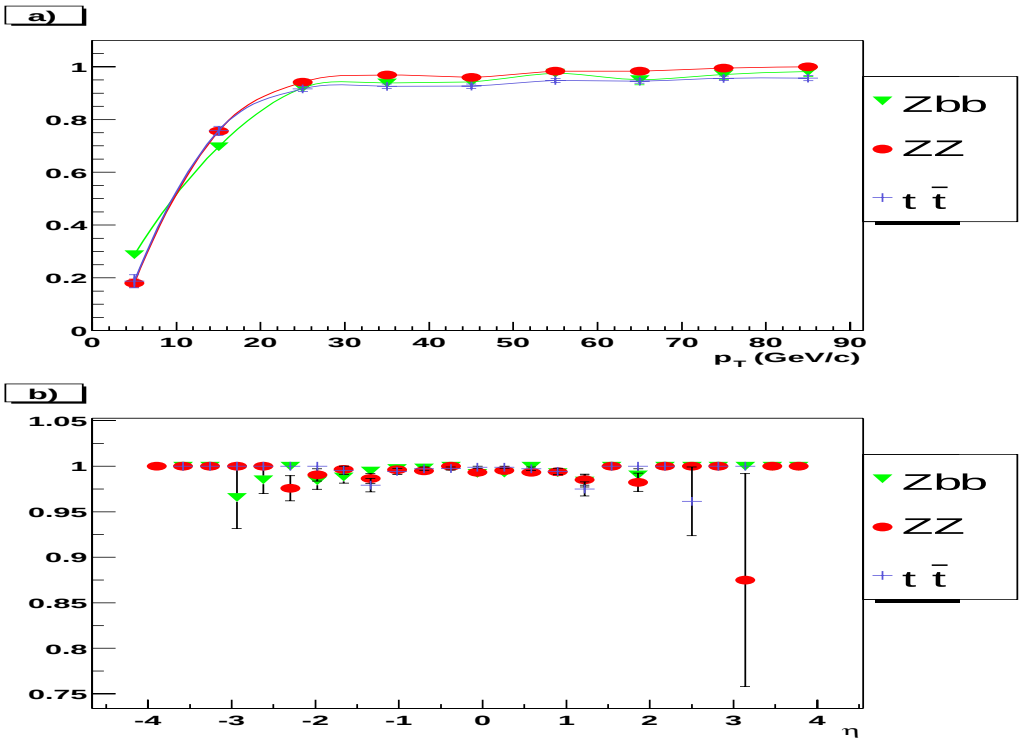

Figure 5.13: Background samples: a) Jet clustering efficiency as a function of generated quark p_T, b) ID efficiency as a function of η

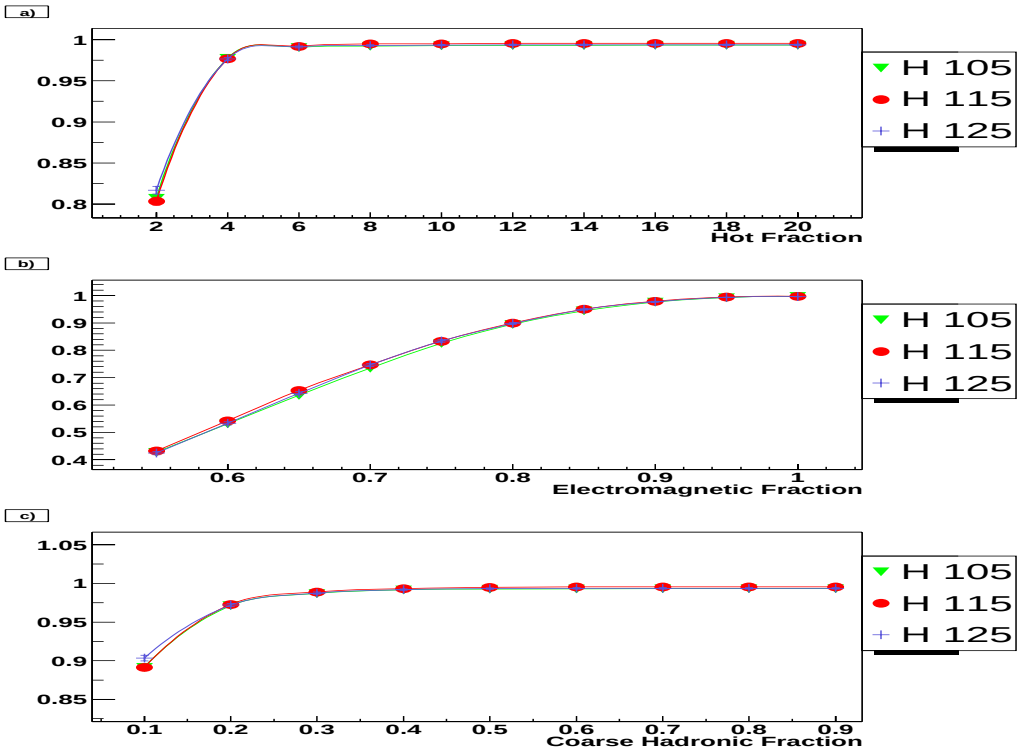

Figure 5.14: Signal samples: Jet ID efficiency as a function of a) hot fraction, b) electromagnetic fraction, c) coarse hadronic fraction

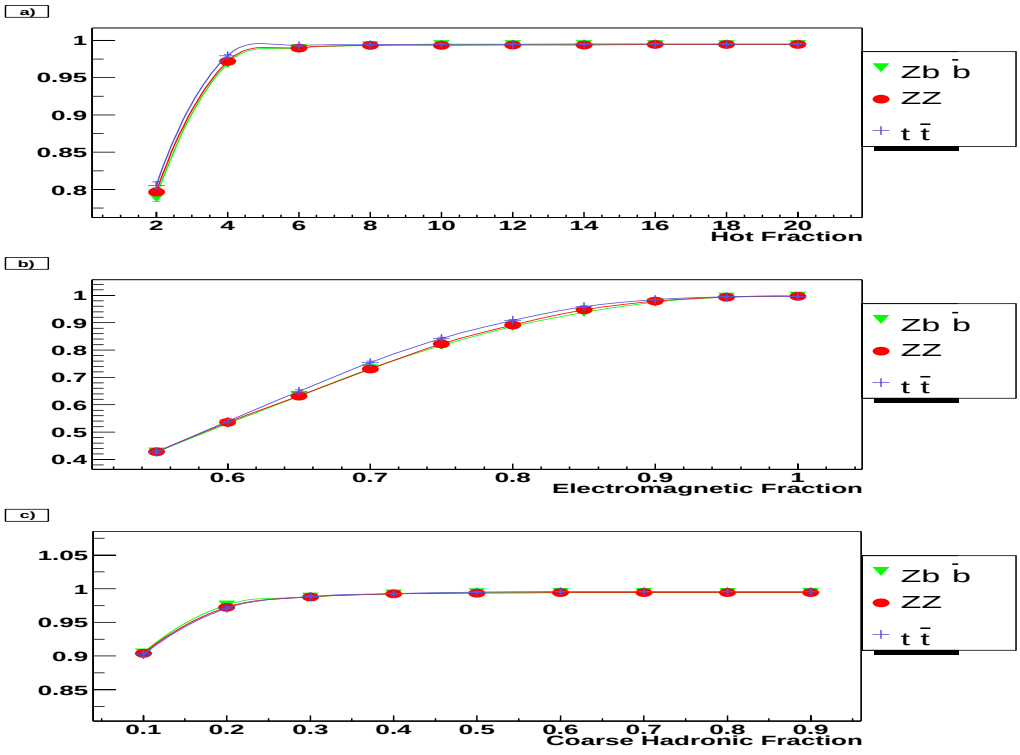

Figure 5.15: Background samples: Jet ID efficiency as a function of a) hot fraction, b) electromagnetic fraction, c) coarse hadronic fraction

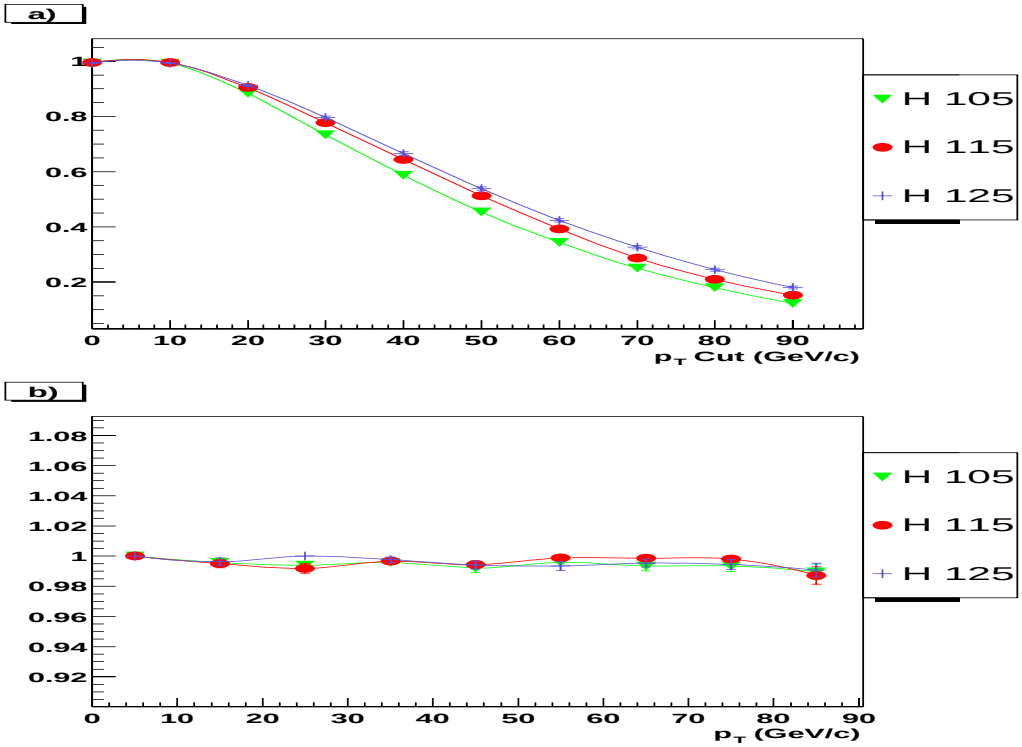

Figure 5.16: Signal samples: Jet ID efficiency as a function of a) p_T cut, b) p_T

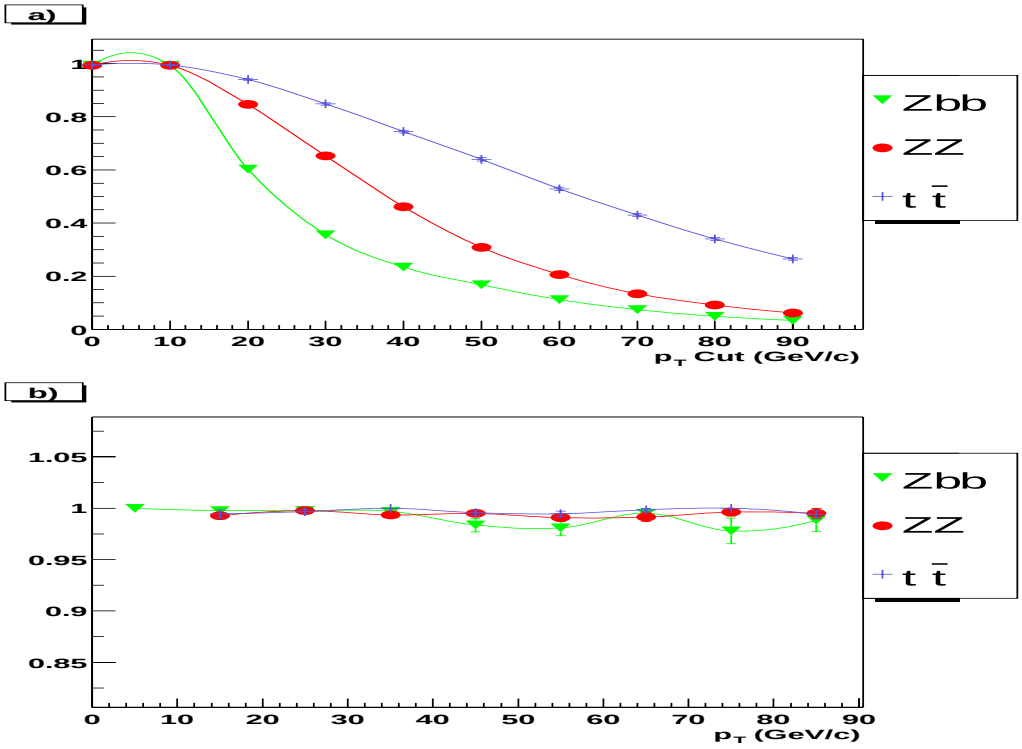

Figure 5.17: Background samples: Jet ID efficiency as a function of a) p_T cut, b) p_T

Process	CC (%)	ICR (%)	EC (%)	Global (%)
$ZH(105) \to e^+e^-b\bar{b}$	93.79 ± 0.41	87.80 ± 0.58	61.52 ± 1.69	87.59 ± 0.38
$ZH(115) \to e^+e^-b\bar{b}$	93.30 ± 0.42	90.13 ± 0.53	67.58 ± 1.69	89.28 ± 0.36
$ZH(125) \to e^+e^-b\bar{b}$	93.69 ± 0.41	89.03 ± 0.55	68.53 ± 1.71	89.20 ± 0.36
$ZZ \to e^+e^-b\bar{b}$	91.14 ± 0.52	86.25 ± 0.61	67.15 ± 1.37	85.22 ± 0.41
$Z(\to e^+e^-)b\bar{b}$	79.79 ± 0.76	74.22 ± 0.76	58.75 ± 1.33	73.44 ± 0.51
$t\bar{t} \to e^+e^-b\bar{b}$	92.79 ± 0.42	88.44 ± 0.58	66.67 ± 1.94	90.70 ± 0.35

Table 5.9: Jet selection efficiency for signal and background

Process	Restricted (%)	Geometrical (%)	Total (%)
$ZH(105) \to e^+e^-b\bar{b}$	89.98 ± 0.38	91.96 ± 0.32	82.75 ± 0.44
$ZH(115) \to e^+e^-b\bar{b}$	91.07 ± 0.34	93.03 ± 0.30	84.72 ± 0.42
$ZH(125) \to e^+e^-b\bar{b}$	91.45 ± 0.30	92.92 ± 0.30	84.97 ± 0.42
$ZZ \to e^+e^-b\bar{b}$	88.20 ± 0.40	88.16 ± 0.38	77.76 ± 0.48
$Z(\to e^+e^-)b\bar{b}$	76.24 ± 0.53	86.61 ± 0.40	66.03 ± 0.55
$t\bar{t} \to e^+e^-b\bar{b}$	90.70 ± 0.35	94.33 ± 0.27	85.56 ± 0.41

Table 5.10: Jet reconstruction efficiency for signal and background

range is a drop of $\sim 4\%$ for the signal samples, whereas it has a much greater effect for ZZ and the $Zb\bar{b}$ channels.

5.3.3 B-Tagging Efficiency

Using the secondary vertex tagging method outlined in Section 5.2.4, with a ΔR cut of 0.3 and a significance cut of 3.0, the heavy-flavour tagging efficiency on 15000 events for the various samples is shown in Table 5.11. The efficiency is defined as:

$$\epsilon_{tag} = N_{tag}^{match}/N^{match} \tag{5.3}$$

where N^{match} is defined as the number of jets which pass the same selection and ID requirements as in Section 5.3.2. N_{tag}^{match} is the subset of these jets which have also been tagged by the secondary vertex tagging algorithm. In the selection of jets matched to the quarks it is assumed that the method used to identify charm is valid.

Table 5.11 highlights the problem of tagging jets in the forward region. The effect of this drop in efficiency is limited as there are relatively few jets reconstructed in the EC compared to the CC and ICR. The decrease in the EC is linked to the decrease in tracking efficiency in jets which is lower in the forward region, as already seen in the case of the tracking efficiency for electromagnetic objects.

The b-tagging p_T dependence is shown in Fig. 5.18: the b-tagging efficiency reaches a maximum above a p_T of ~ 40 GeV/c and then slowly decreases. This

Process	CC (%)	ICR (%)	EC (%)	Global (%)	Restricted (%)
$ZH(105) \to e^+e^-b\bar{b}$	42.68 ± 0.45	42.54 ± 0.48	20.16 ± 0.90	40.81 ± 0.31	42.18 ± 0.33
$ZH(115) \to e^+e^-b\bar{b}$	42.94 ± 0.45	41.10 ± 0.48	19.78 ± 0.90	40.32 ± 0.31	41.59 ± 0.32
$ZH(125) \to e^+e^-b\bar{b}$	43.21 ± 0.44	42.22 ± 0.48	19.94 ± 0.92	41.03 ± 0.31	42.15 ± 0.32
$ZZ \to e^+e^-b\bar{b}$	41.66 ± 0.49	40.32 ± 0.48	19.39 ± 0.71	38.02 ± 0.32	40.33 ± 0.33
$ZZ \to e^+e^-c\bar{c}$	10.56 ± 0.33	10.13 ± 0.31	3.92 ± 0.36	9.45 ± 0.20	10.09 ± 0.22
$Z(\to e^+e^-)b\bar{b}$	32.64 ± 0.51	29.88 ± 0.48	13.68 ± 0.62	28.60 ± 0.32	30.63 ± 0.34
$Z(\to e^+e^-)c\bar{c}$	9.64 ± 0.67	6.59 ± 0.52	3.05 ± 0.63	7.24 ± 0.37	7.85 ± 0.41
$t\bar{t} \to e^+e^-b\bar{b}$	42.93 ± 0.43	44.32 ± 0.49	19.18 ± 0.99	41.99 ± 0.31	43.09 ± 0.32

Table 5.11: Heavy-flavour tagging efficiency

decrease is due to a decrease in the efficiency for finding a secondary vertex associated with a high p_T jet. The lower efficiency around 60 GeV/c for the $Zb\bar{b}$ sample is related to the fact that the two b quarks produced from the tree level process in Fig. 5.4(right) can be close together. This lowers the efficiency for finding secondary vertices as there will be two closely spaced vertices. Instead the lower efficiency in Fig. 5.19 can be associated to the much lower b-jet p_T for this sample.

In theory the "two jet" b-tagging efficiency should just be the efficiency in Table 5.11 squared. This however is not the case for most samples. There seems to be a difference of about 2% between events with two b-tags and the inclusive per jet b-tagging efficiency squared. The difference between the two numbers can be attributed to a higher b-tagging efficiency for the second b-tag. This has been seen in other experiments [78][79].

The light quark tagging rate was estimated with the Z+multijet sample used in Chapter 4. The light quark tagging efficiency is on the order of 1% for a jet p_T of 70 GeV/c and the overall efficiency in the restricted region is of 0.5%.

The performance of this b-tagger is linked to many different factors: the performance of the tracking, the ability to identify both the primary and secondary vertices and the position resolution of the primary and secondary vertices. The vertex identification and resolution depend on the p_T and η of the jet and also on the detector geometry. Therefore if there are any biases or regions of the detector which are not well understood, the performance of the b-tagger will consequently be affected. Due to the new tracking system the vertex reconstruction and the tracking is still in the process of being fully understood and optimised. Hence the status of this b-tagging technique at DØ is currently of a preliminary nature.

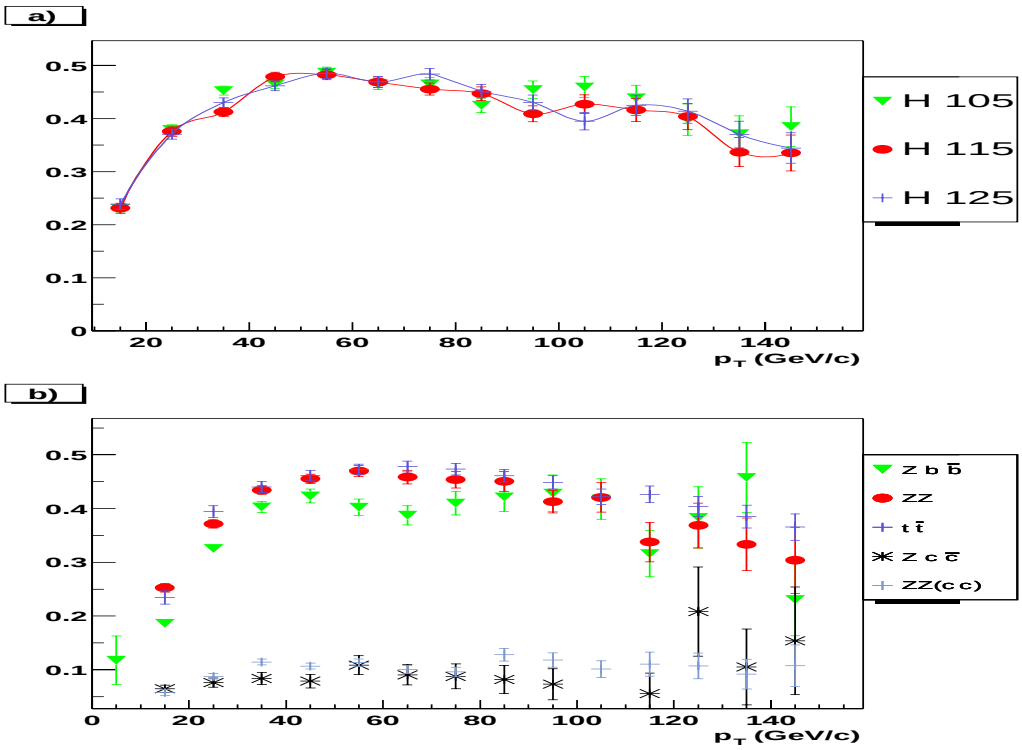

Figure 5.18: B-tagging efficiency as a function of p_T for a) signal b) background

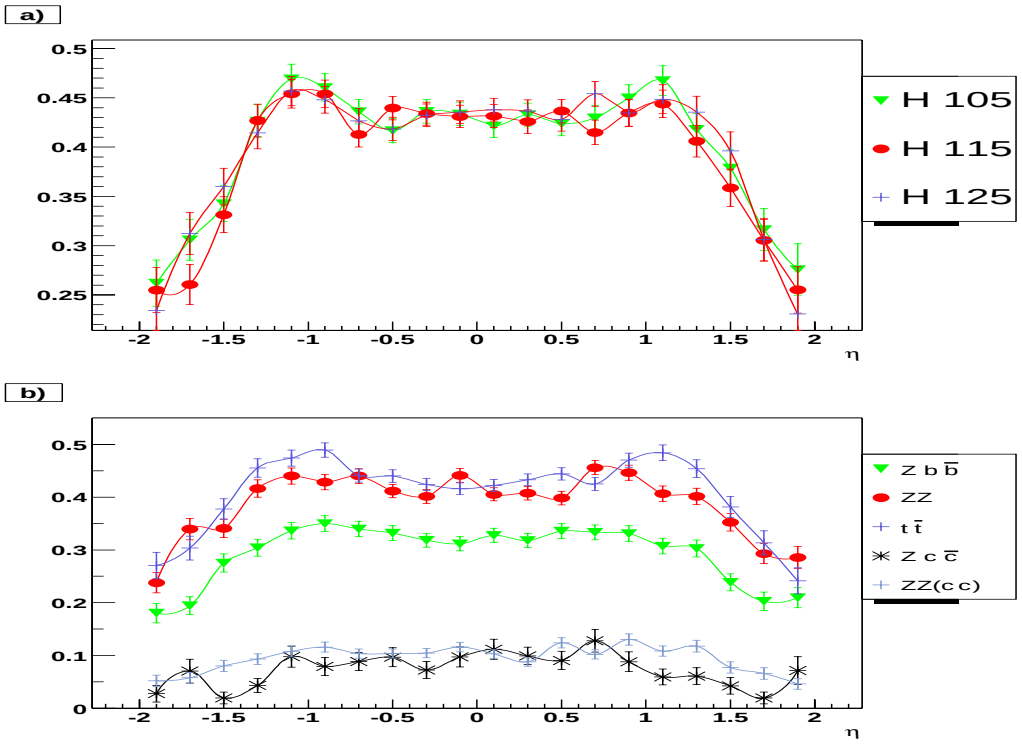

Figure 5.19: B-tagging efficiency as a function of η for a) signal b) background

5.4 Monte Carlo Analysis: Sequential Cuts

5.4.1 Pre-Selection Cuts

The samples used for this analysis are the full samples listed in Table 5.1. There are a series of pre-selection cuts to reject events which do not contain the basic elements present in the signal process. These focus on the basic event selection, electromagnetic object selection and jet selection. The event selection is the same as that used in Section 5.3.1. The other cuts are listed below.

- At least two electromagnetic objects, within $|\eta| < 2.5$, which pass the standard certification cuts given in Section 5.3.1.
- At least two jets, within $|\eta| < 2.0$, which pass the selection cuts outlined in Section 5.3.2. These jets are also required to be well separated ($\Delta R > R_{cone} > 0.5$) from electromagnetic objects which pass the electromagnetic selection cuts. The energy of the jets is corrected using the certified DØ Jet Energy Scale correction v1.5.
- At least two b-tagged jets, as tagged by the secondary vertex tagging algorithm described in Section 5.2.4.

A possible alternative to the above electromagnetic pre-selection of two electromagnetic objects is to require a high p_T, isolated track and an electromagnetic object. This pre-selection has the potential of increasing the acceptance by taking advantage of a looser selection on the electrons and on the theoretically higher tracking efficiency. However this pre-selection, for the current version of the reconstruction code, is not justified as the tracking is mostly limited to the central calorimeter and the efficiency is lower or at best comparable to the total electron efficiency, as seen in Section 5.3.1.

5.4.2 Basic Distributions

After the pre-selection cuts the two leading b-tagged jets are selected and used to construct the Higgs candidate. The basic distributions for the signal and the various backgrounds are shown in Figs. 5.20 - 5.29. These distributions are plotted after the pre-selection cuts, but excluding the electromagnetic requirements for the jets and the jet requirements for the electromagnetic plots. The normalisation is arbitrary for all the plots.

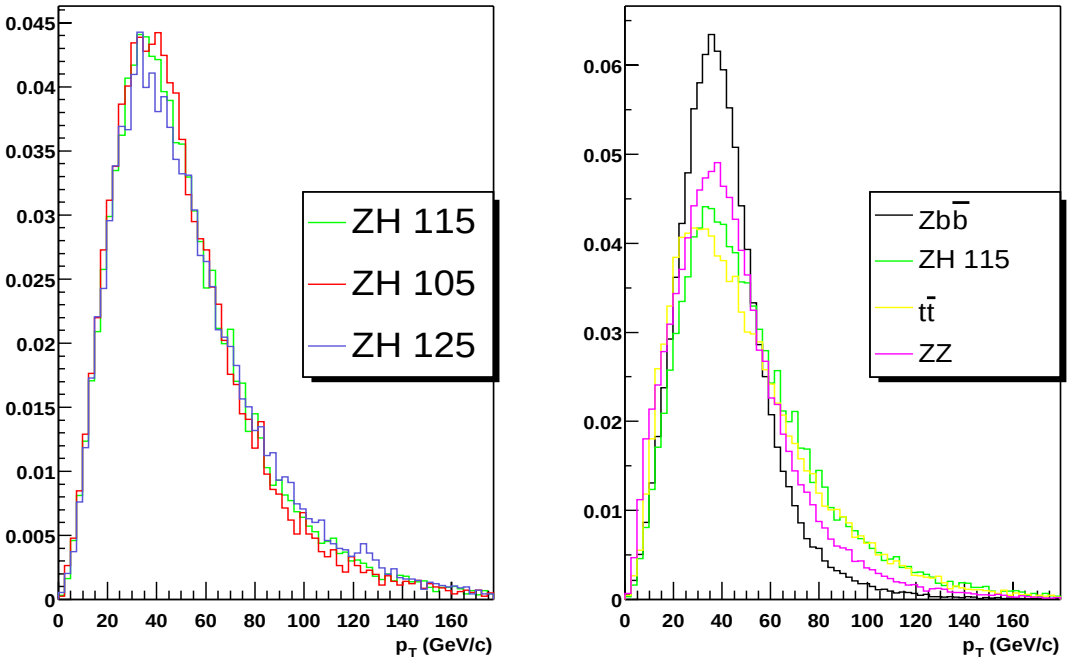

Figure 5.20: p_T of the electromagnetic objects

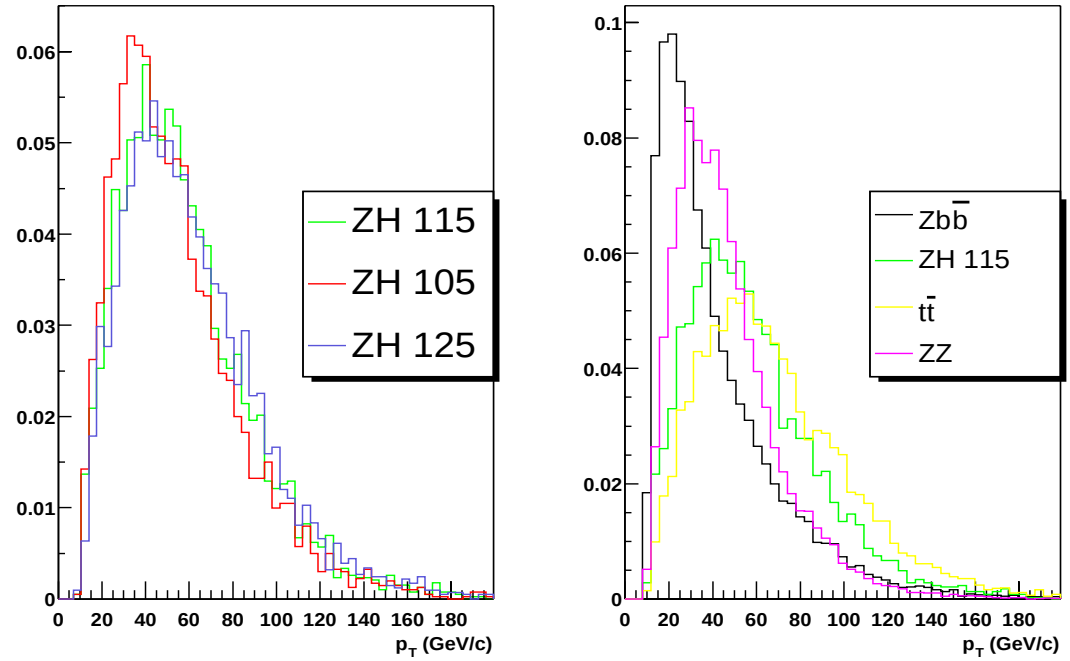

Figure 5.21: p_T of the b-tagged jets

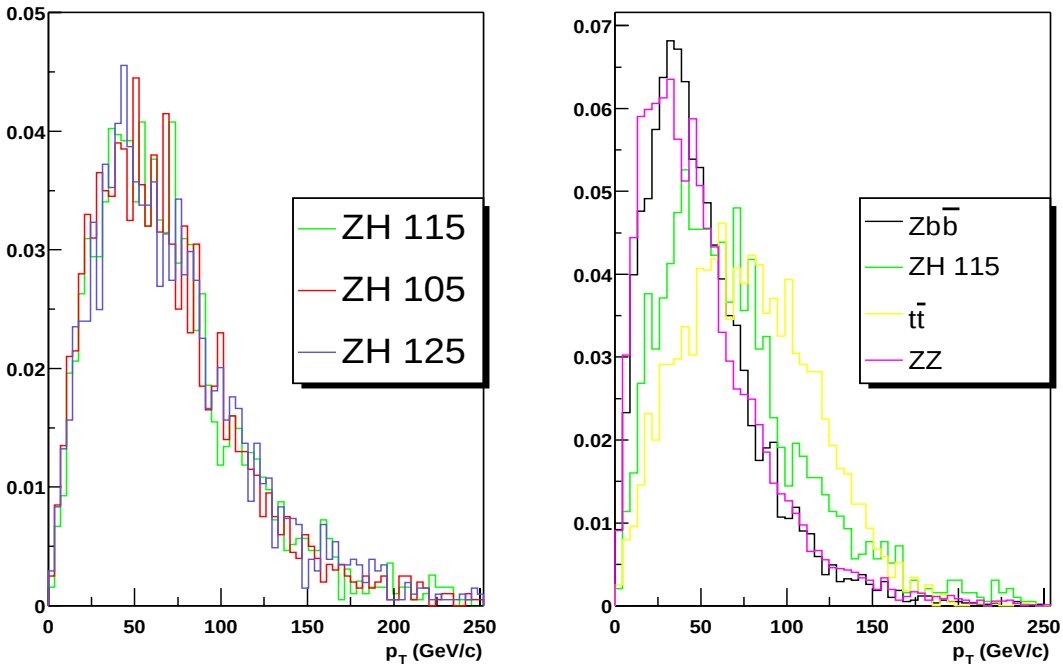

Figure 5.22: Distributions of di b-jet p_T

There are no major differences in the p_T of the selected electromagnetic objects between all the samples, as seen in Fig. 5.20; although the $Zb\bar{b}$ sample has a shorter tail as commented previously. The similarity between the different channels is to be expected as the electromagnetic objects arise from the decay of the Z (with the exception of $t\bar{t}$). What difference there is, is in the other p_T distributions. A difference between the signal and the $Zb\bar{b}$ background which potentially can be exploited is that the spectrum of the b-jets is softer for $Zb\bar{b}$ (Figs. 5.21, 5.25 and 5.26). This is because they are not produced from the decay of a heavy particle but are the result of softer QCD processes. Furthermore, as the Z boson is not recoiling against a heavy mass particle it also has a softer p_T spectrum, shown in Fig. 5.23. The slight difference between the Higgs signal and the ZZ sample in Fig. 5.23 can be related to the slight difference in the invariant mass of the recoiling particle.

The distributions for the leading jet (the jet with the highest p_T) with and without a b-tag are shown in Figs. 5.24 and 5.25. From the two figures the p_T dependence of the heavy flavour tag can be seen via a shift in peak position toward higher p_T. This is consistent with Fig. 5.18.

A seemingly promising variable is H_T, plotted in Fig. 5.27. The H_T is defined as a scalar p_T sum, in this case of the two b-tagged jets and the two electromagnetic

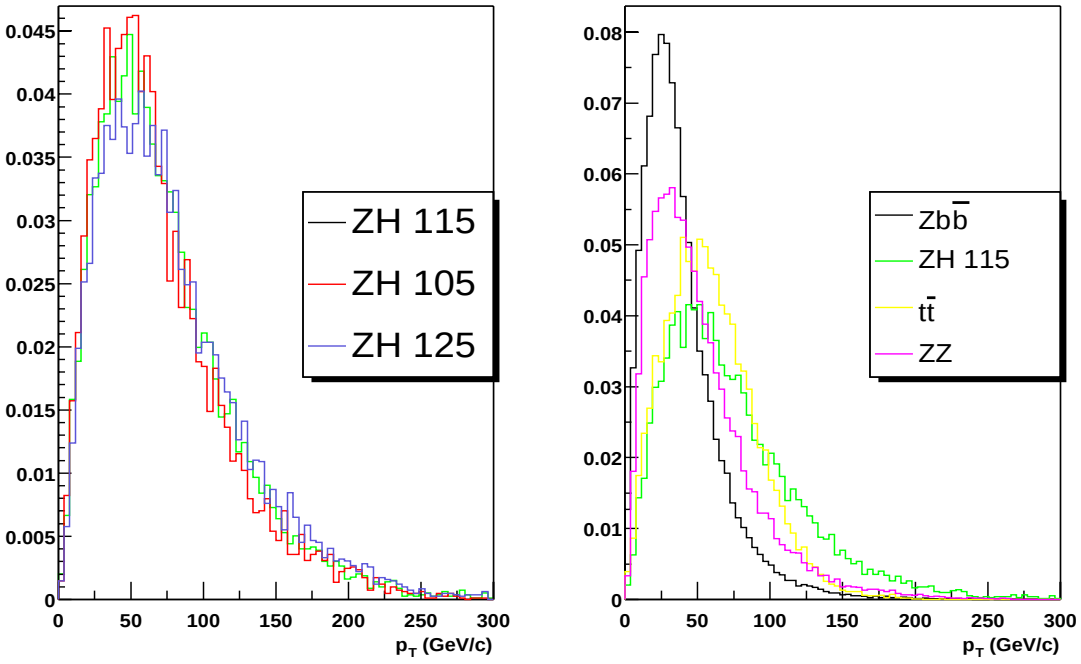

Figure 5.23: Distributions of di-electromagnetic object p_T

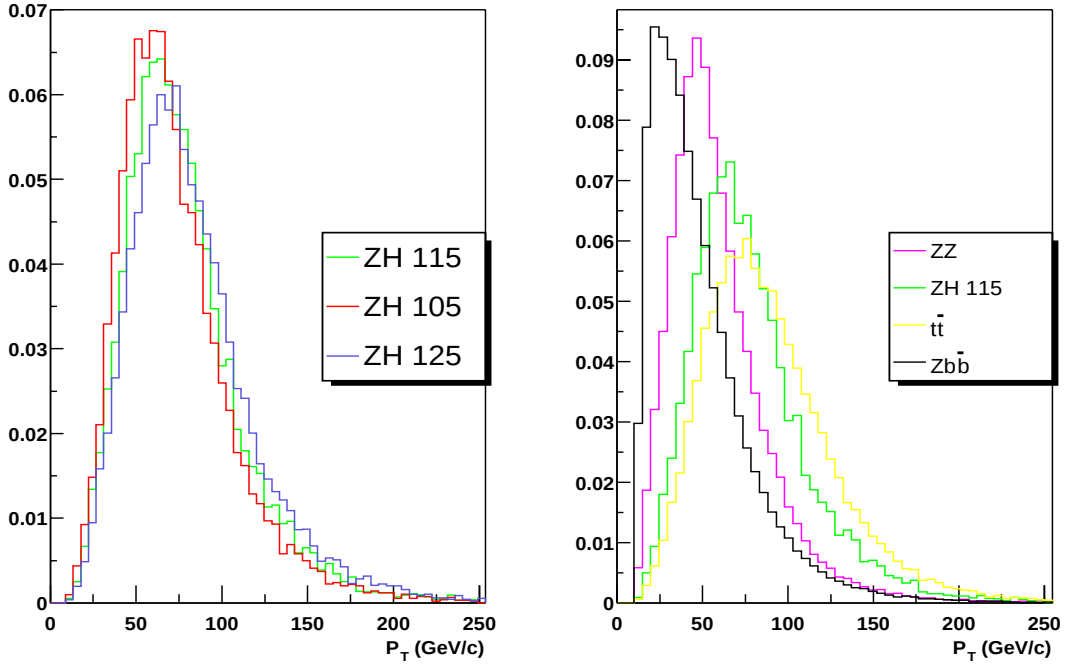

Figure 5.24: p_T distributions of the leading jet

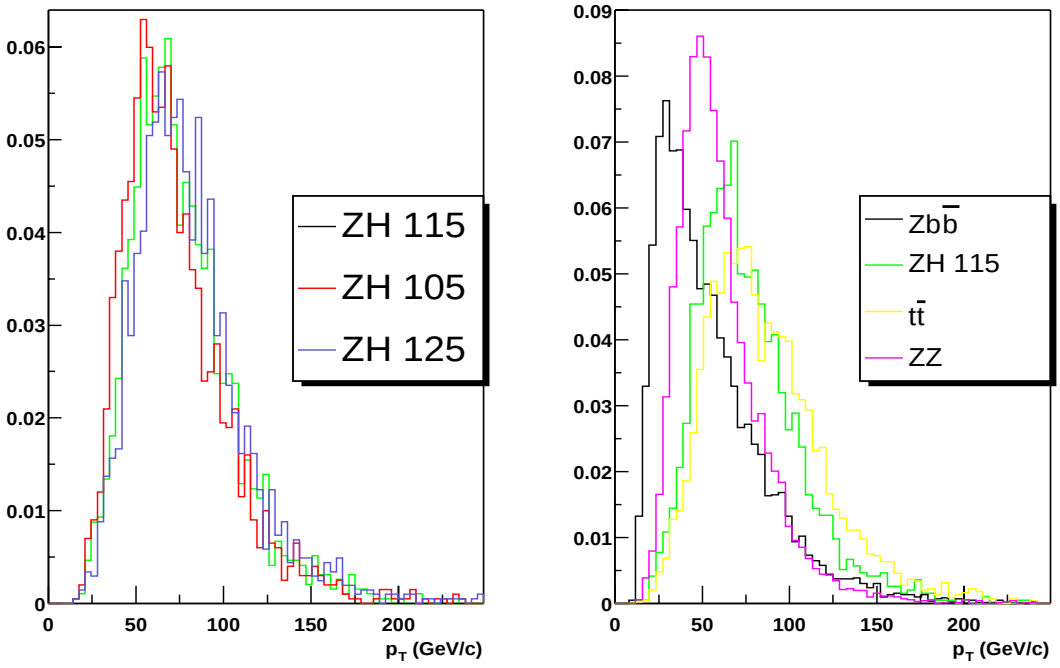

Figure 5.25: p_T distributions of the leading b-tagged jet

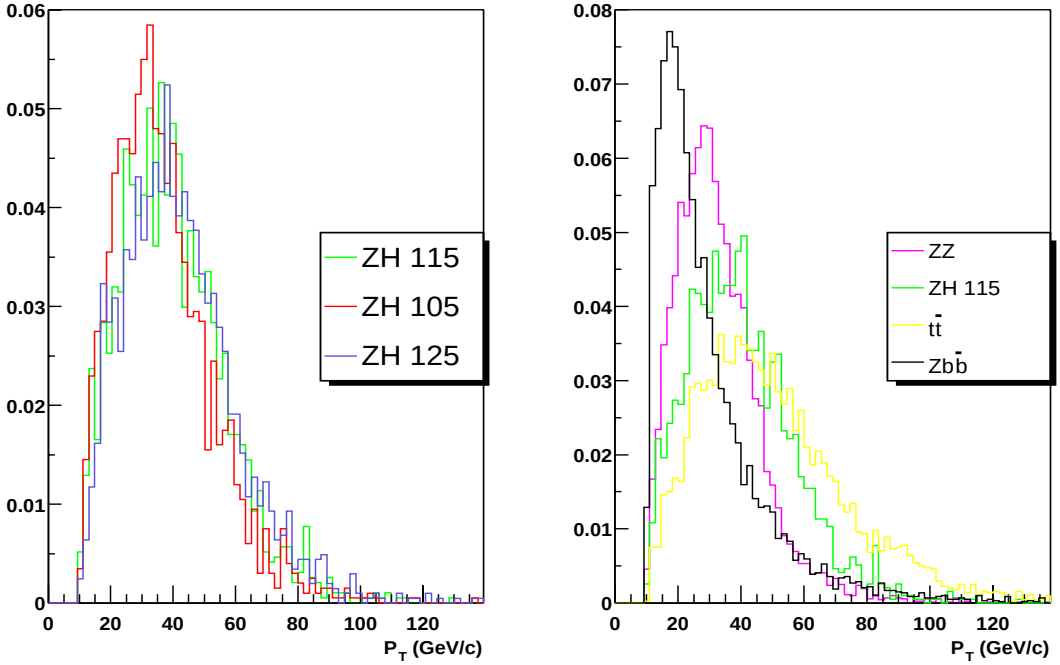

Figure 5.26: p_T distributions of the next to leading b-tagged jet

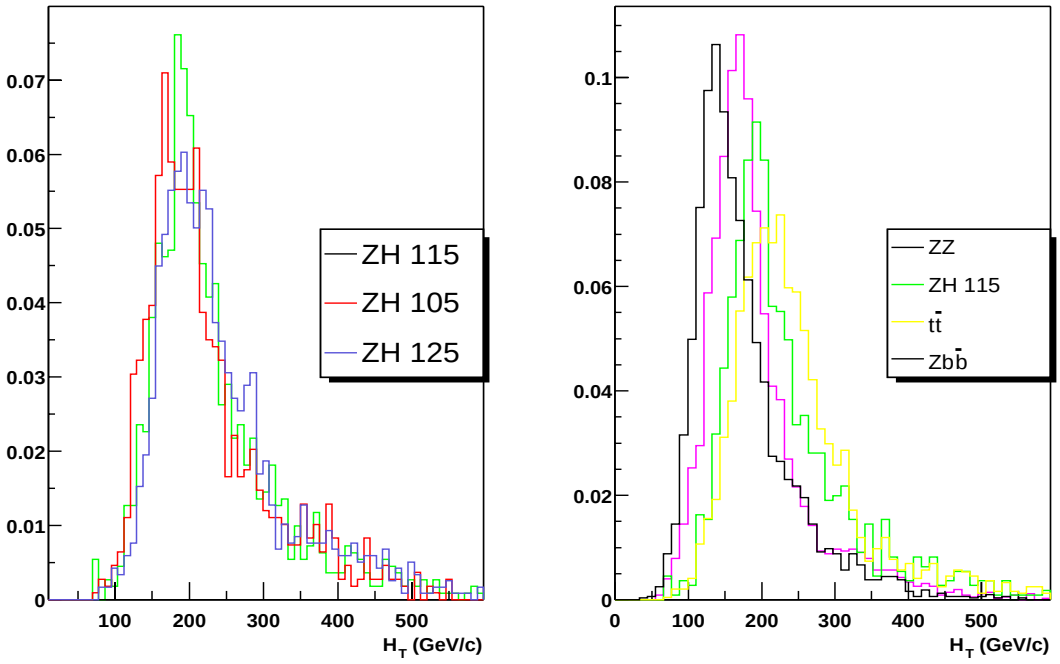

Figure 5.27: H_T distributions

objects. The distributions show different profiles for the various samples; although a clear separation is not present there are distinct differences. However this variable is highly correlated to the p_T of the objects as it is derived from them. Consequently if p_T cuts are applied on the objects themselves the effectiveness of an H_T cut is limited.

The invariant mass distribution for the electromagnetic objects and the b-tagged jets are shown in Figs. 5.28 and 5.29. The $t\bar{t}$ background has the characteristic that the two electrons do not originate from the same decay. Hence their invariant mass reconstructs to a broad distribution and not to a sharp mass peak as seen in Fig. 5.28. Thus by making a tight cut on the di-electron mass the $t\bar{t}$ background can be reduced considerably.

The invariant di b-tagged jet mass distributions shown in Fig. 5.29 stress the importance of mass resolution. The signal and background have distinctly different shapes; although this is not a variable which can be directly cut on, the estimate of the sensitivity for the different Higgs masses depends on the signal mass window. From the distributions shown the only difference between the ZZ and the ZH sample is the different mass of the Z boson and the Higgs. Although it is possible to distinguish the two mass peaks in Fig. 5.29 the normalisation is arbitrary. Hence it is not necessarily true that this distinction will be possible after the final cuts.

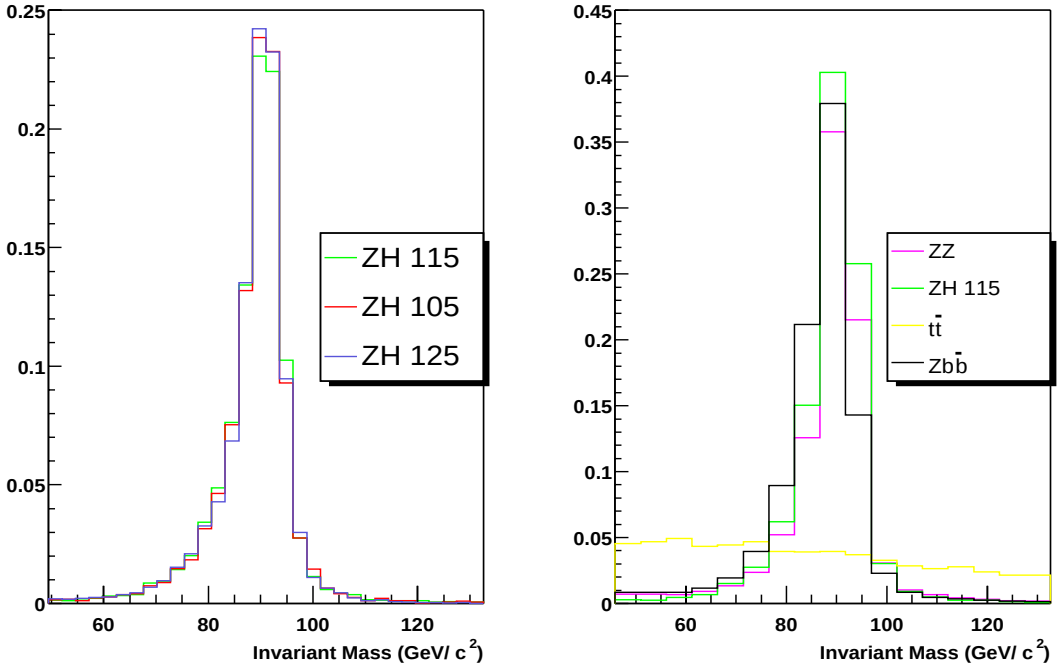

Figure 5.28: Di-electromagnetic object invariant mass

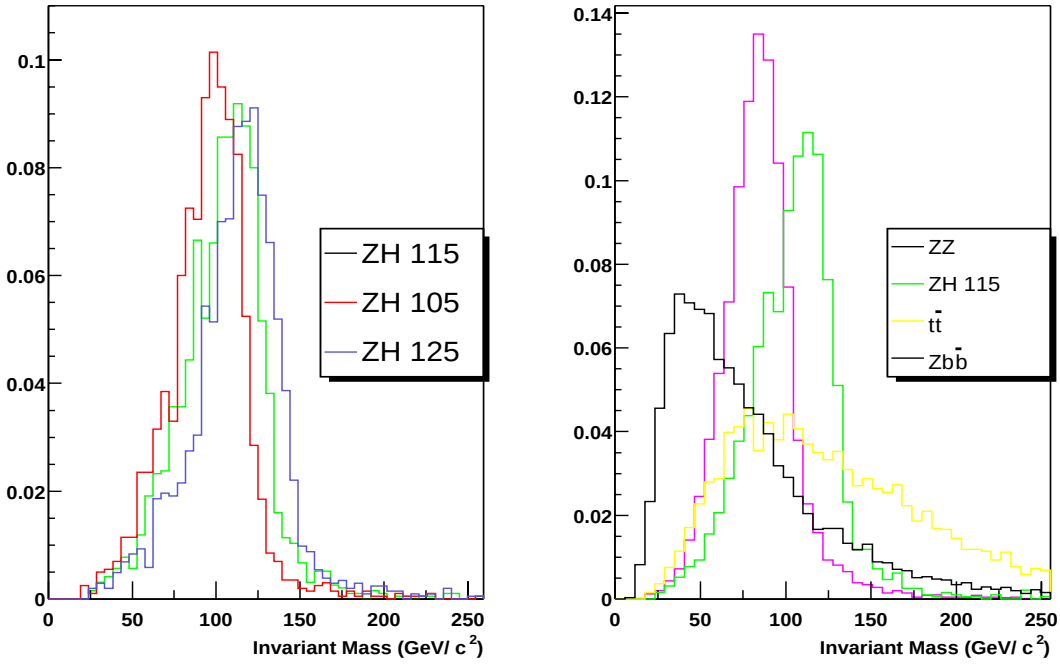

Figure 5.29: Di b-jet invariant mass

Process	$ZH(105)$	$ZH(115)$	$ZH(125)$	$t\bar{t}$	$Zb\bar{b}$	$Zc\bar{c}$	$ZZ(b\bar{b})$	$ZZ(c\bar{c})$
Event	92.7	92.9	92.8	92.5	92.6	92.7	92.6	92.4
EM Pre	54.8	55.3	55.8	55.3	53.2	52.2	48.3	48.1
EM Selection	83.8	84.0	84.5	14.6	77.1	74.0	73.0	73.0
Total EM	46.0	46.4	47.1	8.06	41.0	38.6	35.3	35.0
Jet Pre	89.0	90.5	91.2	89.0	73.6	74.8	83.6	79.8
B-Tag	15.2	14.9	15.3	16.4	6.79	0.627	13.4	1.03
B Selection	95.8	95.8	97.8	98.2	83.5	80.4	94.3	93.8
Total B-jet	12.9	12.9	13.7	14.3	4.17	0.378	10.6	0.772
Total	5.39	5.64	6.11	1.11	1.60	0.144	3.53	0.271

Table 5.12: Selection Efficiencies (%)

5.4.3 Selection Cuts

In order to enable a valid comparison, a similar philosophy to that used in the SHW analysis was adopted; namely trying to retain as much of the signal as possible. The cuts listed below were used.

- Both electromagnetic objects were required to have a $p_T > 10$ GeV/c.
- Leading b-tagged jet $p_T > 20$ GeV/c.
- Next to leading b-tagged jet $p_T > 15$ GeV/c.
- The invariant mass of the selected electromagnetic objects was required to be within ± 10 GeV/c^2 of the Z boson mass, taken to be 90 GeV/c^2.

5.4.4 Selection Efficiency

The signal efficiencies and background fake rates in percent are listed in Table 5.12. The efficiencies listed in Table 5.12 are calculated with respect to the previous cut.

The jet selection and the electromagnetic selection are non-correlated as for each channel the total efficiency can be obtained by multiplication of the relative efficiencies. Theoretically the efficiency numbers in the previous sections (squared) should be equal to the relevant entry in Table 5.12.

The jet pre-selection efficiency is noticeably different from the selection efficiency quoted in Section 5.3.2. This is because the pre-selection requirement is based on any two jets passing the ID cuts, while the numbers in Section 5.3.2 are for the case in which jets matched to the b quarks pass the jet ID cuts. In theory events with only one (or no) b-jet passing the selection requirements should fail the b-tagging selection. This is confirmed by the lower b-tagging efficiency in Table 5.12

Process	Higgs : 105 GeV/c^2	Higgs : 115 GeV/c^2	Higgs : 125 GeV/c^2
Signal, S	0.43	0.31	0.21
$t\bar{t} \to e^+e^-b\bar{b}$	1.58	1.58	1.58
$Z(\to e^+e^-)b\bar{b}$	4.81	4.81	4.81
$Z(\to e^+e^-)c\bar{c}$	0.90	0.90	0.90
$ZZ \to e^+e^-b\bar{b}$	0.90	0.90	0.90
$ZZ \to e^+e^-c\bar{c}$	0.06	0.06	0.06
Background, B	8.25	8.25	8.25
Sensitivity $\frac{S}{\sqrt{S+B}}$	0.15	0.11	0.07

Table 5.13: Expected number of events in 2 fb^{-1} and sensitivity

compared to that in Table 5.11 for most of the channels, except for the charm final state samples. A possibility for the difference in the charm quark samples is that the matching used is not valid or that it adds a large systematic uncertainty. For the SHW the expected heavy flavour tagging efficiency for charm jets was determined to be between 10 and 20%. The efficiency for charm seems to be consistent with that observed here.

Table 5.13 gives the number of expected events for 2 fb^{-1}, using the cross-sections in Table 5.1, when not applying a mass window cut on the di b-jet invariant mass. Also quoted is the sensitivity for the different Higgs masses for the same integrated luminosity. An integrated luminosity of 2 fb^{-1} is used as originally this was the total integrated luminosity to be collected for Run IIa.

From Table 5.13 the largest contribution to the background is $Zb\bar{b}$. This is due to the large cross-section of the process and due to the philosophy of the cuts which are trying to preserve the signal events rather than eliminate background events. If the emphasis was in reducing the number of background events then a tighter cut on the leading b-jet p_T should be applied. The $t\bar{t}$ background is the next highest despite the tight cut on the di-em mass. A further cut which might be envisioned to reduce the $t\bar{t}$ background is to cut on the $\not\!\!E_T$. Due to the presence of the neutrinos in the top quark decay the $t\bar{t}$ process should have a large $\not\!\!E_T$; however a cut on $\not\!\!E_T$ could bias the Higgs mass distribution due to the presence of a neutrino from the possible semi-leptonic decay of the b quarks. This cut should be looked into once there is a well understood jet energy scale correction for b-jets.

The similarity between the expected number of ZZ and $Zc\bar{c}$ events points out the need for a heavy flavour tag which can be used to distinguish between charm jets and b-jets. In principle any light quark jet background should have a negligible contribution, as the events should be rejected by the b-tagging algorithm. However due to the much higher cross-sections the present level of light quark contamination

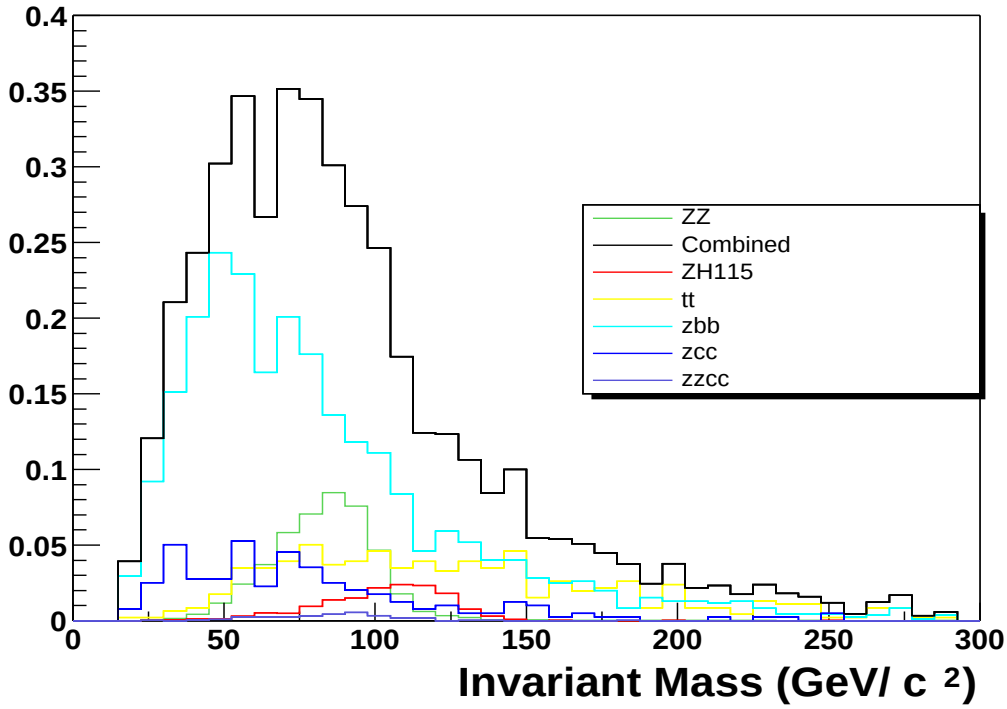

Figure 5.30: Di b-jet mass distributions for a Higgs mass of 115 GeV/c^2 and all background channels

from the b-tagger is potentially too high. By taking the efficiencies for $Zb\bar{b}$ and using the light quark tagging rate quoted in Section 5.3.3, the number of expected Zjj events, assuming a cross-section of 175 pb, is ∼1-2 events. This is simply an estimate of the order of magnitude for one of the light quark backgrounds. One can conclude that if the purity of the b-taggers does not increase the light quark background will be an issue and will have to be taken into account. Even though the SHW light quark tag rate was on the order of 0.5%, the light quark contribution was ignored for most channels.

Fig. 5.30 shows the di b-jet invariant mass for the different backgrounds and for the 115 GeV/c^2 signal sample after all cuts and with the correct weighting. Most notably the two main backgrounds do not peak close to the signal sample. As the $t\bar{t}$ sample has a relatively broad distribution and the $Zb\bar{b}$ distribution is not falling sharply close to the Higgs mass value, an improved mass resolution would not significantly reduce the number of events per mass bin for these two samples. What an improved mass resolution would do is further separate the ZZ and the signal peak. Fig. 5.30 highlights the need for more effective selection cuts to reduce the impact of $Zb\bar{b}$ and $t\bar{t}$, combined with a tight mass window to remove the ZZ background.

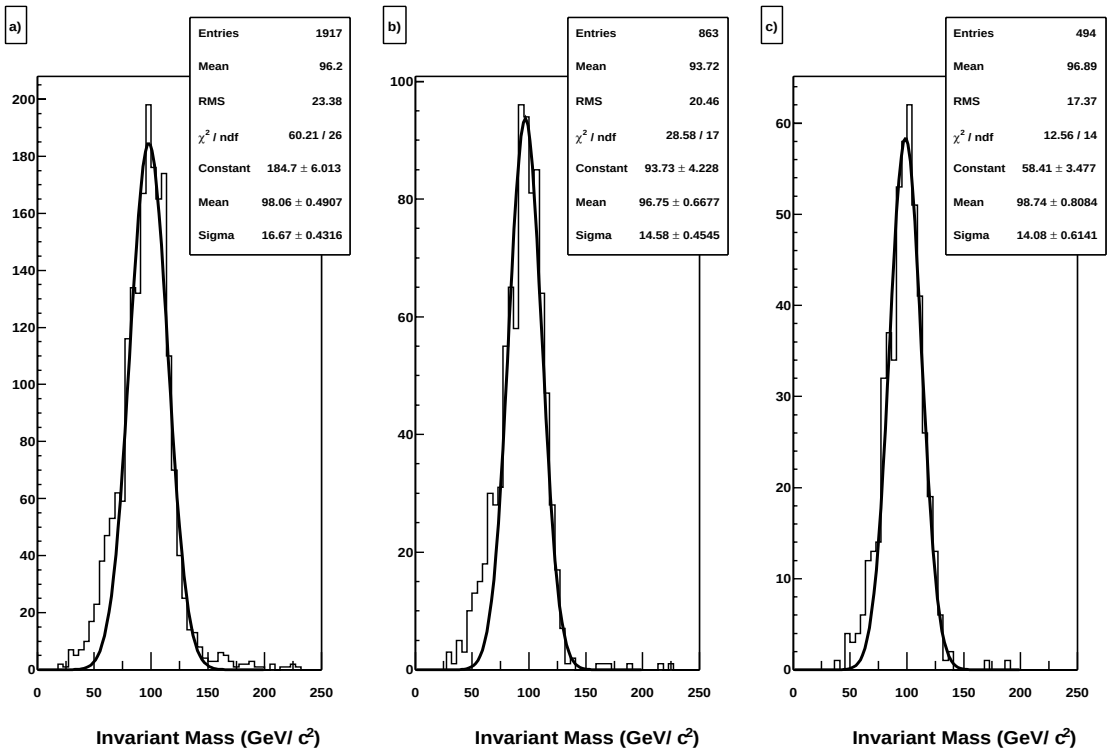

Figure 5.31: Di b-jet mass distributions for a Higgs mass of 105 GeV/c^2

5.4.5 Mass Resolution

The sensitivity quoted in Table 5.13 is the sensitivity when considering the whole $b\overline{b}$ invariant mass parameter space. As the Higgs would be localised in a region of parameter space, a more accurate estimate of the sensitivity would be to apply a $b\overline{b}$ mass window given by the expected di b-jet mass resolution. The SHW report used a mass resolution of 15% in order to estimate the sensitivity. The improvement in sensitivity which could be achieved with a 10% mass resolution was also calculated.

Figs. 5.31a), 5.32a) and 5.33a) show the invariant mass distribution for the different signal samples after final jet selection. A single Gaussian fit is used for comparison purposes; the objective of the fit is to show the central resolution of the distributions and not to try to incorporate any tails. In these figures the effect of final state radiation is apparent in the low side tail. When demanding that, in addition to the jet cuts, two electromagnetic objects satisfy the selection requirements the mass resolution improves to that in Figs. 5.31b)-5.33b). In comparison to the distributions when requiring only two b-jets the presence of the final state radiation tail is not significantly diminished with respect to the peak. However the width of the central peak is significantly narrower. The resolution improves by a couple of

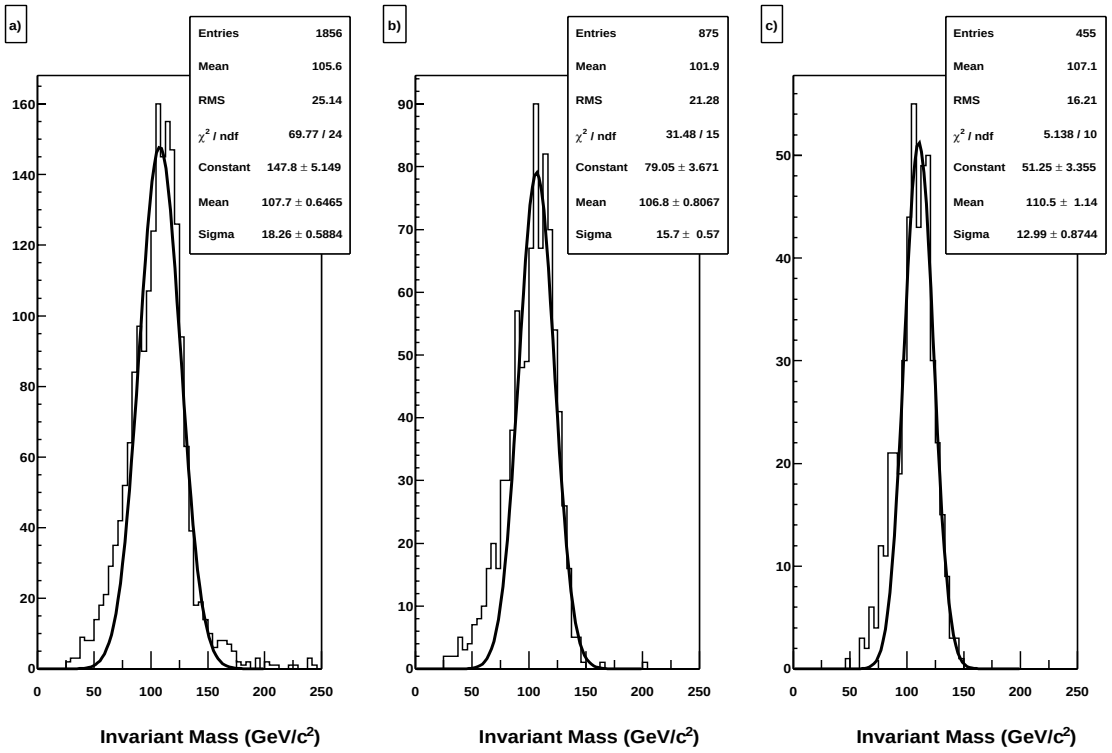

Figure 5.32: Di b-jet mass distributions for a Higgs mass of 115 GeV/c^2

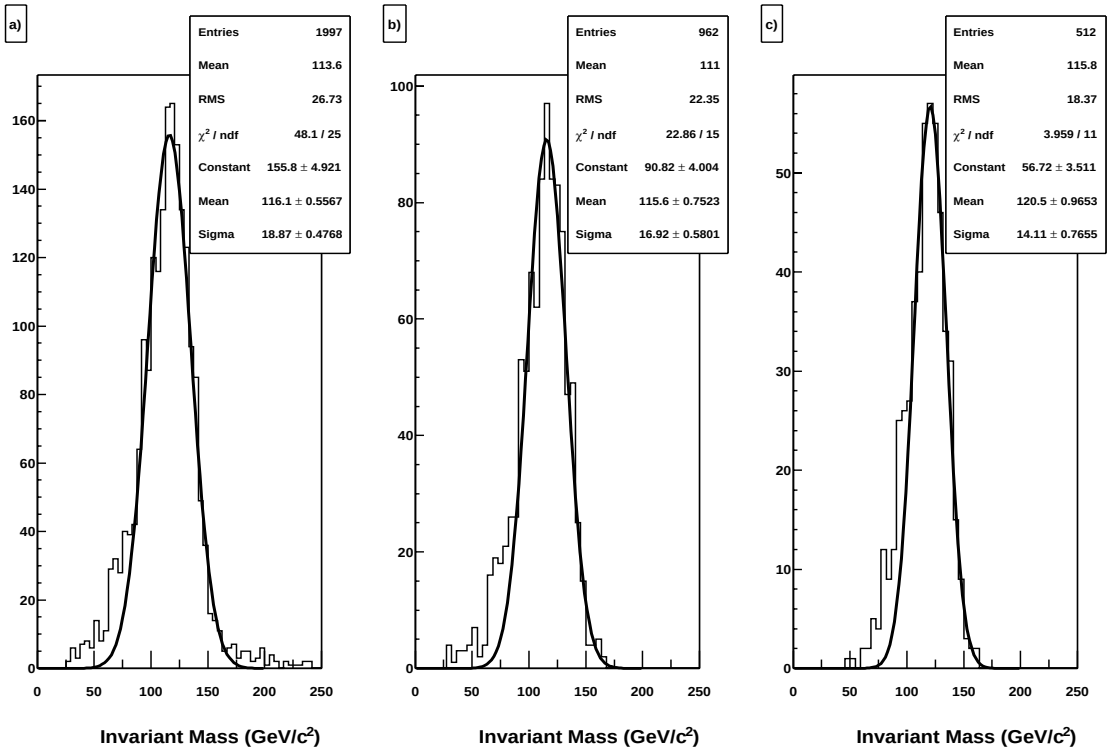

Figure 5.33: Di b-jet mass distributions for a Higgs mass of 125 GeV/c^2

Higgs Mass (GeV/c^2)	Mean (GeV/c^2)	σ (GeV/c^2)	Resolution
105	96.8	14.6	15.1 %
115	106.8	15.7	14.7 %
125	115.6	16.9	14.6 %

Table 5.14: Table of reconstructed mass values and resolutions

percent and the mean is similar. The improvement in resolution is due to the fact that in order to identify both electrons successfully the event has to be relatively clear of significant energy deposits not associated with the electrons themselves. This automatically eliminates events with significant amounts of unclustered energy and events with significant final state radiation.

Figs. 5.31c)-5.33c) show the mass resolution when requiring a veto on a third jet. This eliminates most of the final state radiation however it also reduces the statistics by a factor of approximately half. The improvement in resolution is on the order of 1% for a Higgs mass of 105 GeV/c^2 and of 3% for 115 GeV/c^2 and for 125 GeV/c^2. Whereas the difference when requiring two electrons as well as two b-jets is limited to a narrowing of the central peak, when using a veto on a third jet there is also a noticeable shift in the position of the peak. However the 50% loss in signal efficiency is too great for this option to be used.

Table 5.14 gives the values of the mean and σ for case b). In order to estimate the sensitivity a mass window of $\pm 2\sigma$ around the mean value given in Table 5.14 is applied, as was done in the SHW.

5.4.6 Sensitivity

The sensitivity using the default mass window is given in Table 5.15. Compared to the SHW result this is significantly lower. By extrapolating the numbers from the SHW report, the predicted sensitivity for 1 fb^{-1} is 0.42 for a Higgs mass of 115 GeV for $ZH \to l^+l^-b\bar{b}$. As the tau decays were not explicitly selected one can assume to first approximation that the number relates solely to the muon and electron decay modes. Assuming that the Z and the top decay have an equal branching ratio to electrons and muons and doubling the integrated luminosity, the sensitivity for solely the electron channel is 0.30. This is a factor of 2 higher than the sensitivity quoted in Table 5.15. It is difficult to directly compare the two results due to the lack of specific information from the SHW report in regards to efficiencies for this specific channel.

Process	Higgs : 105 GeV/c^2	Higgs : 115 GeV/c^2	Higgs : 125 GeV/c^2
Signal	0.37	0.27	0.18
$t\bar{t} \to e^+e^-b\bar{b}$	0.63	0.66	0.70
$Z(\to e^+e^-)b\bar{b}$	1.83	1.57	1.42
$Z(\to e^+e^-)c\bar{c}$	0.34	0.27	0.24
$ZZ \to e^+e^-b\bar{b}$	0.73	0.61	0.49
$ZZ \to e^+e^-c\bar{c}$	0.05	0.04	0.04
Background, B	3.58	3.15	2.89
Sensitivity $\frac{S}{\sqrt{S+B}}$	0.19	0.15	0.10

Table 5.15: Expected number of events in 2 fb^{-1} and sensitivity using default mass window

The number of expected signal events is a factor of approximately 3 lower than the SHW result. The background is a factor of 2 lower, although the background estimate for the SHW analysis did not include the charm channels. It is clear that there is a vast difference in the signal acceptance. From Table 5.12 the only two criteria which could be so different are the electromagnetic pre-selection and the b-tagging. It is difficult to imagine vast improvements in the electromagnetic pre-selection though an improvement of the clustering in the ICR to increase the acceptance could be considered. With an increase of 10% in the ICR, the total electromagnetic pre-selection would not increase by more than a factor of 1.3.

An increase in the b-tagging efficiency is more promising. The b-tagging used in the analysis is by no means an optimised b-tag and takes advantage of only one of the possible methods. The SHW used a variety of b-tagging parameterisations, some of which were based on extrapolations of the CDF b-tagging efficiencies from Run I and others on parametrised Monte Carlo simulations of the DØ detector [80]. The double b-tagging efficiency ranged between 30-40% for the different parametrisations which implies that the single b-tagging efficiency is a factor up to $\sim$2 higher than that quoted in Section 5.3.3. Although this is a substantial difference in b-tagging efficiency this does not seem able to fully compensate for the factor of 2 in sensitivity. A large improvement in the b-tagging efficiency, combined with smaller but significant improvements in the clustering of electromagnetic objects and of b-jets is the only possibility to come close to the prediction of the SHW using sequential cuts. It is unlikely that this will yield the required sensitivity without moving to either different cuts and/or more advanced analysis techniques and/or a better mass resolution.

5.4.7 Sensitivity and Mass Resolution

In order to test the effect of an improved mass resolution, the change in sensitivity, for a 115 GeV/c^2 mass Higgs, assuming a 10% resolution with a mean mass value

equal to that in Table 5.14 is investigated. This resolution does not correspond to the physical resolution of the signal sample, hence the mass window cut will not give a reasonable estimate of the number of expected signal events. However it gives an insight into how the expected number of background events changes with the change in resolution. This is a better estimate than for the signal because the di b-jet invariant mass distribution for the two major backgrounds ($Zb\overline{b}$ and $t\overline{t}$) should not change significantly with an improvement in resolution, as the di b-jet system does not correspond to a physical particle. This is not the case for the ZZ background, hence the number of ZZ events will be over estimated.

The expected number of background events in 2 fb^{-1} is given in Table 5.16. In order to estimate the signal, one can assume that the same fraction of events as that using the default mass window will pass the new mass window cut, i.e. 0.27 (from Table 5.15). This would result in a sensitivity of 0.18. This is a factor of 20% greater compared to that with the default mass cut, although still shy of the SHW prediction.

Achieving such a mass resolution will not be trivial; it is likely that tracking information will have to be combined with calorimeter information in order to significantly improve the mass resolution. This is being investigated at DØ [81][82]. A process which will be essential for the understanding of the di b-jet mass resolution and the testing of these algorithms is $Z \rightarrow b\overline{b}$ [83]. This process will also be important for the testing of the b-jet energy scale. Once the mass resolution and the b-jet energy scale are well understood it is feasible that the di b-jet invariant mass could be used in a sliding mass window cut or in a likelihood estimator.

Process	Number of events
$t\overline{t} \rightarrow e^+e^-b\overline{b}$	0.45
$Z(\rightarrow e^+e^-)b\overline{b}$	1.02
$Z(\rightarrow e^+e^-)c\overline{c}$	0.15
$ZZ \rightarrow e^+e^-b\overline{b}$	0.40
$ZZ \rightarrow e^+e^-c\overline{c}$	0.03
Background, B	2.05

Table 5.16: Expected number of background events in 2 fb^{-1} using a 10% mass resolution

5.5 Monte Carlo Analysis: Optimised Cuts

In order to estimate the benefit of different techniques, the change in sensitivity between the sequential cuts analysis and that using optimised cuts was studied using

the 115 GeV/c^2 Higgs mass sample. The same pre-selection cuts were applied including the b-tag requirement. The selection cuts were optimised using a Minuit [84] minimisation. In order to have an exact comparison to the sequential cuts analysis the same set of variables was used with no attempt to find other discriminating variables. The function used by Minuit to perform the minimisation was the sensitivity defined as:

$$f = -\frac{S}{\sqrt{S+B}}. \tag{5.4}$$

A scan of the cut parameters was performed to find sensible starting values for the minimisation and then the cuts were optimised with and without a mass window. The mass window set the range over which the signal and background numbers should be counted. The difference between the Minuit results with and without a mass window was not more than one GeV for all the cuts. The optimised cuts are as follows:

- Both electromagnetic objects were required to have a $p_T > 5$ GeV/c.
- Leading b-tagged jet $p_T > 42$ GeV/c.
- Next to leading b-tagged jet $p_T > 12$ GeV/c.
- The invariant mass of the selected electromagnetic objects was required to be within 90 $\pm$9 GeV/c^2.

The main difference is the much higher cut on the leading b-jet transverse momentum, effectively limiting the $Zb\bar{b}$ background. The results from Minuit also show that the acceptance for the electromagnetic objects should be maximised and hence as low a p_T cut as possible should be applied. For the off-line cuts there is no problem with this, however on-line, as the electrons are used as a trigger for the process, there is momentum threshold and a trigger bias. The significance when performing a parameter scan of the electromagnetic object transverse momentum was approximately flat up to a cut value of $\sim$15 GeV/c. Hence as long as the trigger threshold can be kept to less than the equivalent off-line value there should be no significant effect on the sensitivity.

The number of expected events and the sensitivity with and without the default mass window for the optimised cuts is shown in Table 5.17, alongside are the unoptimised numbers for comparison.

Table 5.17 shows the impact of the Minuit optimisation. The total number of background events is over 30% lower and the total significance, in the case of no

Process	Seq. cuts	Minuit cuts	Seq. cuts (mass win.)	Minuit cuts (mass win.)
$ZH(115) \to e^+e^-b\overline{b}$	0.31	0.30	0.27	0.27
$t\overline{t} \to e^+e^-b\overline{b}$	1.58	1.34	0.67	0.55
$Z(\to e^+e^-)b\overline{b}$	4.81	2.91	1.57	1.29
$Z(\to e^+e^-)c\overline{c}$	0.90	0.54	0.27	0.22
$ZZ \to e^+e^-b\overline{b}$	0.90	0.73	0.61	0.56
$ZZ \to e^+e^-c\overline{c}$	0.06	0.05	0.05	0.04
Background, B	8.25	5.57	3.17	2.66
Sensitivity $\frac{S}{\sqrt{S+B}}$	0.11	0.12	0.15	0.16

Table 5.17: Expected number of events and sensitivity in 2 fb^{-1} for optimised and unoptimised cuts

mass window cut, is ∼10% higher. When applying a mass window the difference in the number of expected background events is reduced as generally high p_T jets tend to populate the higher invariant mass region. There is still a noticeable effect, the background is reduced by 15% and the significance increases by 7%. This is a substantial amount for the optimisation of basically three discriminating variables: leading b-jet p_T and the lower and upper cut on the di-electromagnetic invariant mass. This improvement stresses the importance of using optimised cuts and, more generally, of using advanced techniques.

It is reasonable to assume that the impact of the optimisation would be greater with a set of more discriminating variables; a possibility which is worth investigating, due to the difference in spin between the Higgs and the various backgrounds, is the angular information of the decay products. However this would need all the samples to be generated using exact matrix order Monte Carlo generators. Further methods such as Neural Networks could also be used and could provide an even greater discrimination. A Neural Network was not used as it relies on well understood reconstruction code. In light of the preliminary nature of certain aspects of the p10 reconstruction code, such as the b-tagging and tracking, the output of the Neural Network would not reflect what is its true potential and would result in misleading conclusions.

5.6 Data

Due to the low production cross-sections of the major backgrounds a large amount of data have to be collected before a direct comparison of these backgrounds to the data can be made. The most relevant background which can studied with a data sample on the order of tens of pico barns is the Zjj background with the Z boson

decaying to two electrons. This process is analogous to the $Zb\bar{b}$ and $Zc\bar{c}$ processes but without a flavour requirement on the two jets.

The data sample analysed is reconstructed using the p10 version of the DØ reconstruction code and spans the data taking period from February 2002 to June 2002, effectively comprising the data sample used for ICHEP 2002. The trigger configuration over this period had significant and frequent upgrades. The initial trigger configuration was restricted to solely the output of the Level 1 trigger, which allowed the triggering on objects within the central calorimeter trigger region ($|\eta| < 0.8$). The Level 3 trigger was initially functioning in Mark and Pass mode and hence did not provide rejection. During the course of the data taking period the Level 3 trigger started to provide rejection and, toward the end of this data taking period, the Level 1 calorimeter trigger pseudo-rapidity range was expanded to ± 2.4. There were also significant changes to the trigger list, as more triggers became operational and as the Tevatron luminosity increased so that more rejection was needed.

Two triggers which were relevant to the signal properties and operational throughout the whole data taking period were effectively those described in Section 5.2 with small changes. The differences for the EM_MD_2CJT5 trigger were that the Level 1 E_T thresholds were respectively 10 GeV and 5 GeV for the electromagnetic and hadronic trigger towers. Furthermore there was no Level 2 trigger requirement. For both triggers the Level 3 trigger (when operational) required only one electromagnetic object within $|\eta| < 1.5$ and with a $p_T > 10$ GeV/c. The total luminosity for these two triggers was 7.60 pb^{-1} for the 2EM_HI trigger and 5.89 pb^{-1} for the EM_MD_2CJT5 trigger.

The event selection was similar to that described in Section 5.4 with the exception of no b-tagging requirement, a larger mass window cut on the Z mass (70 - 110 GeV/c^2) and a p_T cut of 15 GeV/c for all four objects. A 15 GeV/c p_T cut is high enough to avoid the trigger turn on [56]. The Monte Carlo sample used was the same as that used for the response derivation in Chapter 4.

As mentioned in Section 4.5 the p10 data sample was the first occasion to compare the expected shapes and efficiencies in data to those from simulation; based not on single objects but on expected signals from physics analysis. Hence it was the first chance to discern whether the response corrections for jets and electromagnetic deposits were correct, whether the overall shape of the distributions looked reasonable, etc.

Basic distributions for the sample taken with the di-em trigger are shown in Figs. 5.34 - 5.38. Those for the sample selected using EM_MD_2CJT5 are shown in Figs. 5.39 - 5.43. The solid line represents the Monte Carlo distributions normalised

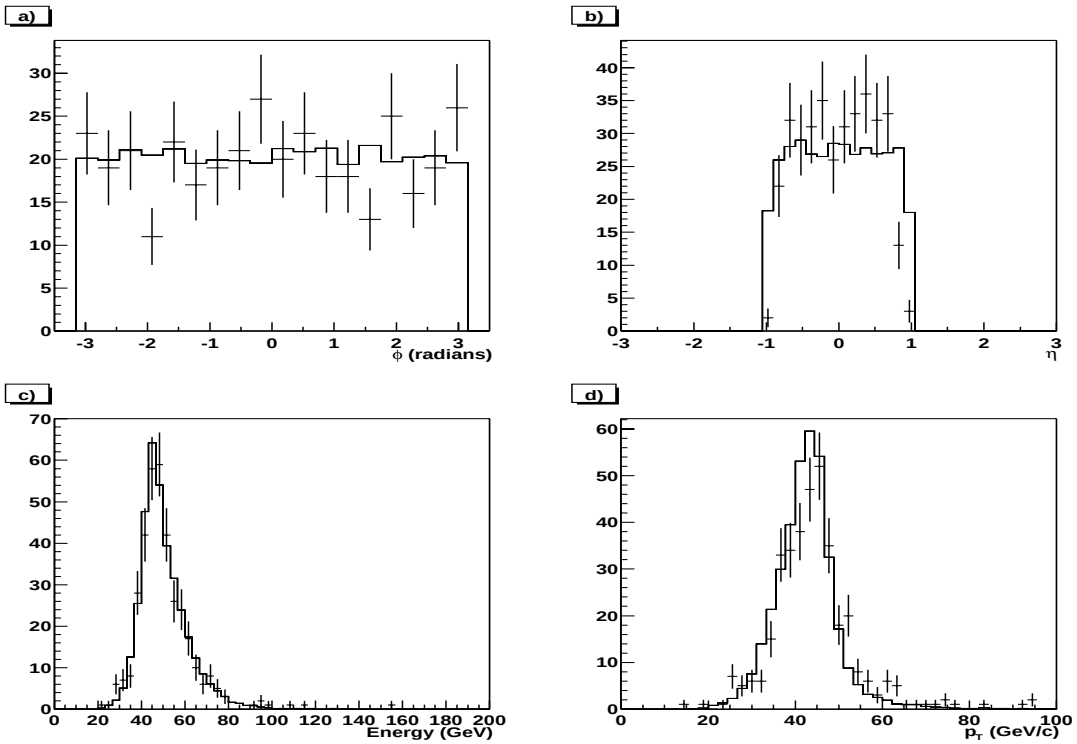

Figure 5.34: Basic distributions for electromagnetic objects in data and Monte Carlo (solid line) a) ϕ, b) η, c) Energy and d) p_T for the sample collected using the 2EM_HI trigger

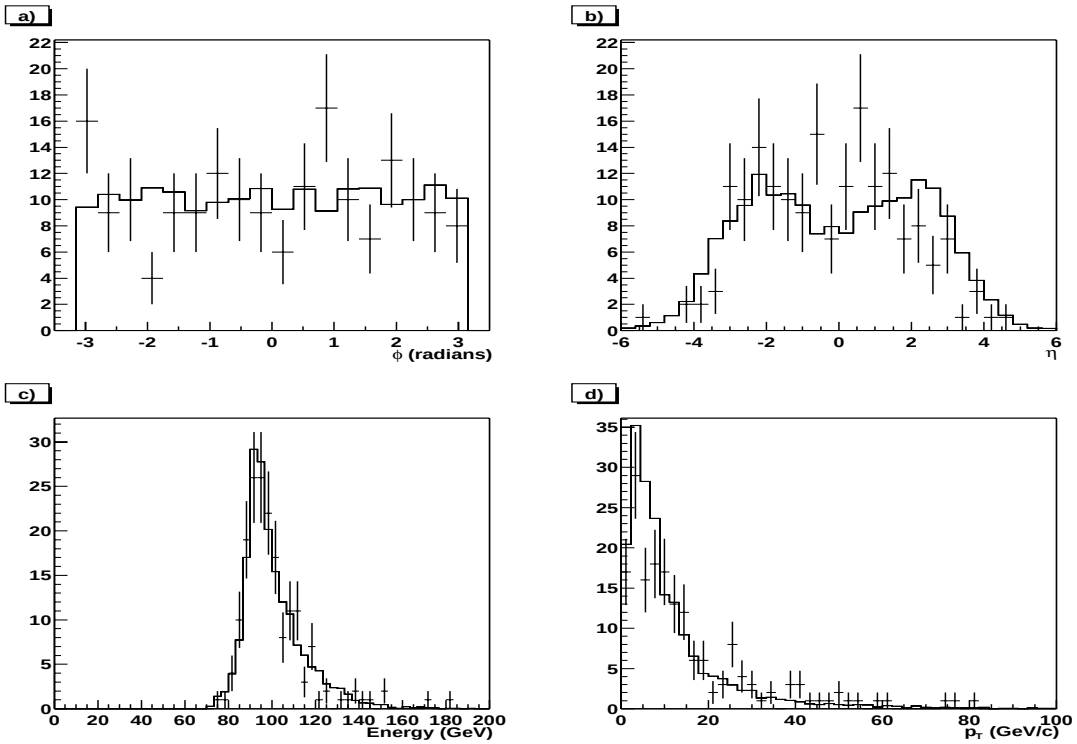

Figure 5.35: Basic distributions for di-electromagnetic objects in data and Monte Carlo (solid line) a) ϕ, b) η, c) Energy and d) p_T for the sample collected using the 2EM_HI trigger

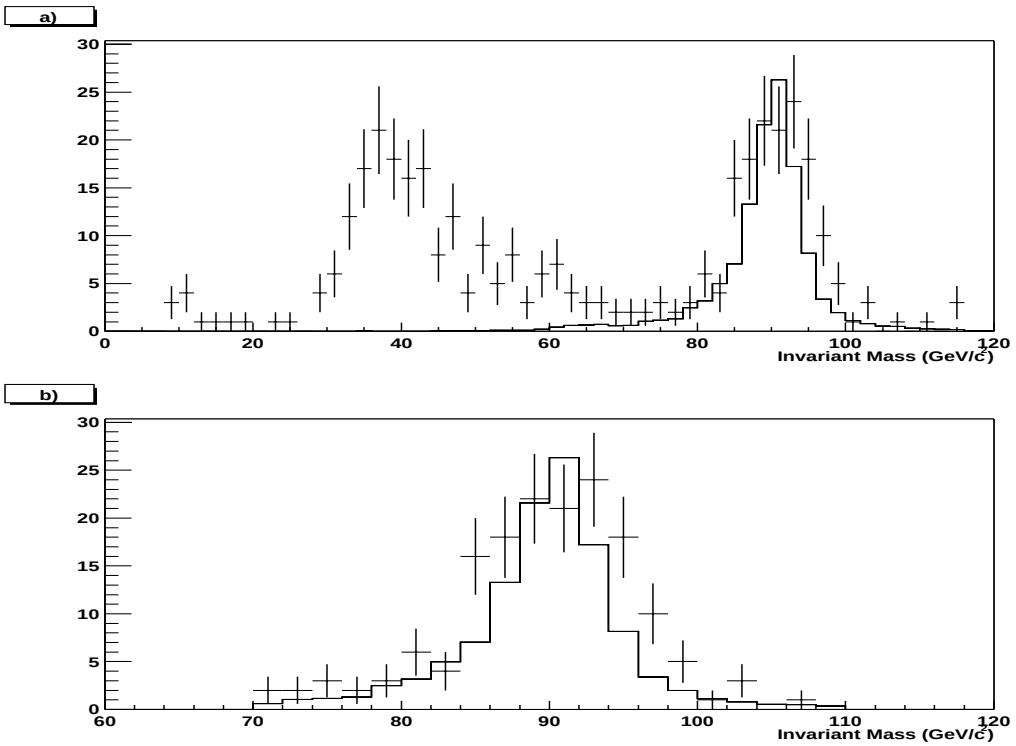

Figure 5.36: Invariant mass for di-electromagnetic objects in data and Monte Carlo (solid line) for the sample collected using the 2EM_HI trigger

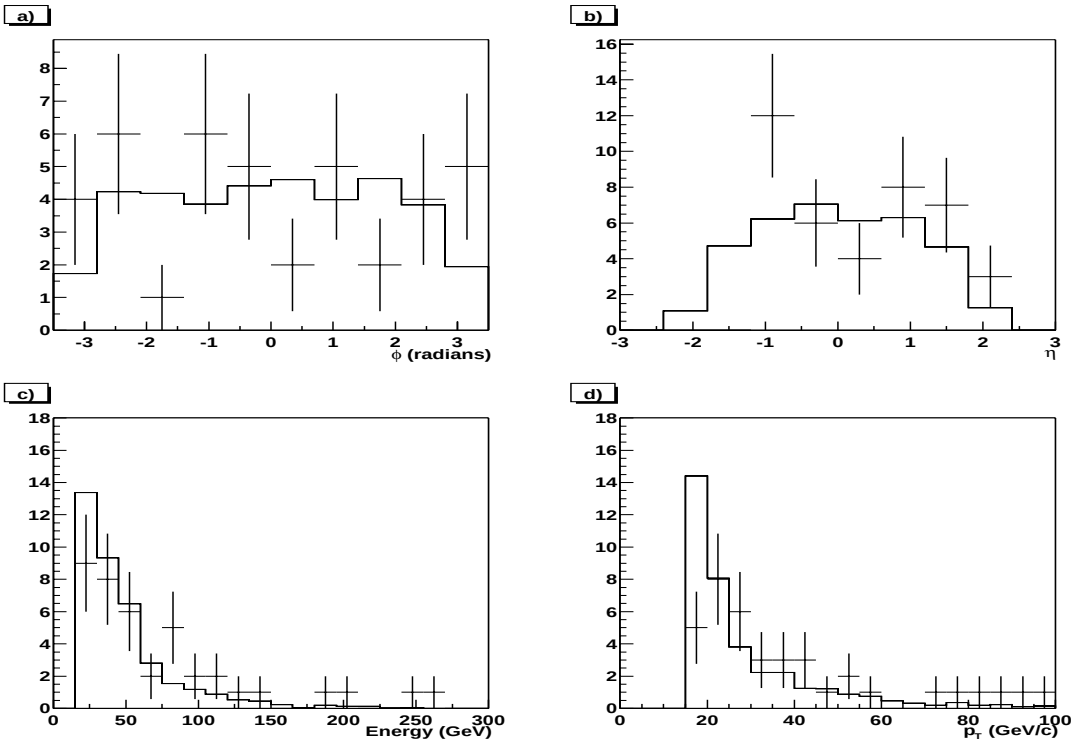

Figure 5.37: Basic distributions for jets in data and Monte Carlo (solid line) a) ϕ, b) η, c) Energy and d) p_T for the sample collected using the 2EM_HI trigger

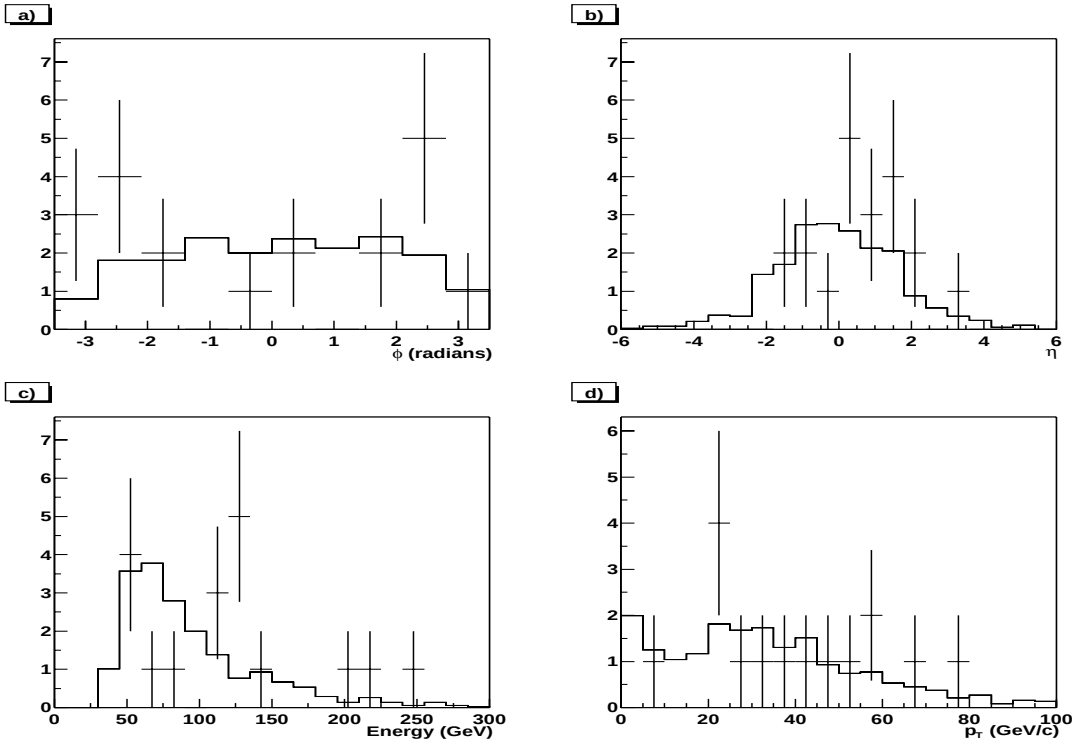

Figure 5.38: Basic distributions for di-jet objects in data and Monte Carlo (solid line) a) ϕ, b) η, c) Energy and d) p_T for the sample collected using the 2EM_HI trigger

to the luminosity of the samples. The electromagnetic distributions displayed are independent of the jet selection, whereas the jet distributions display only events in which the electromagnetic object selection was satisfied. In order to avoid most of the trigger bias, due to the restricted pseudo-rapidity range of the Level 1 calorimeter trigger, only the electromagnetic objects within $|\eta| < 1.0$ are plotted in Figs. 5.34 - 5.36 and Figs. 5.39 - 5.41. It is assumed that there was no trigger bias for the jets in events selected using the di-em trigger; hence no additional requirements were made other than the selection cuts. In Figs. 5.42 and 5.43 either of the two jets was required to be within $|\eta| < 1.0$.

The shapes of the distributions agree reasonably well for all the plots, considering the low statistics for the jet distributions. Also the normalisation of the Monte Carlo to the recorded luminosity seems to be consistent with what is actually observed. These facts, together with the use of two independent triggers, indicate that the overall detector, trigger and reconstruction codes are working well. There seem to be a few specific aspects which do not agree well. There is evidence of a residual trigger bias in the η distribution of the electromagnetic objects in Figs. 5.34b) and 5.39b) from the lower number of events seen at higher η values. In the p_T distribution for the electromagnetic objects (Figs. 5.34d)and 5.39d)) it appears as

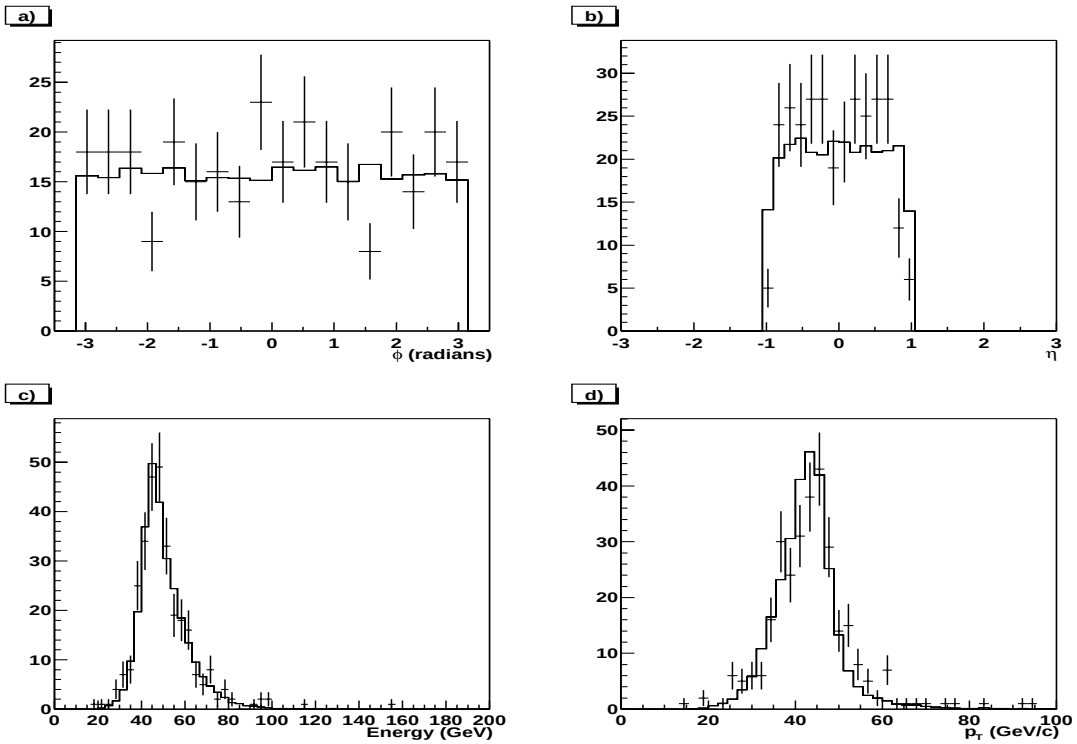

Figure 5.39: Basic distributions for electromagnetic objects in data and Monte Carlo (solid line) a) ϕ, b) η, c) Energy and d) p_T for the sample collected using the EM_MD_2CJT5 trigger

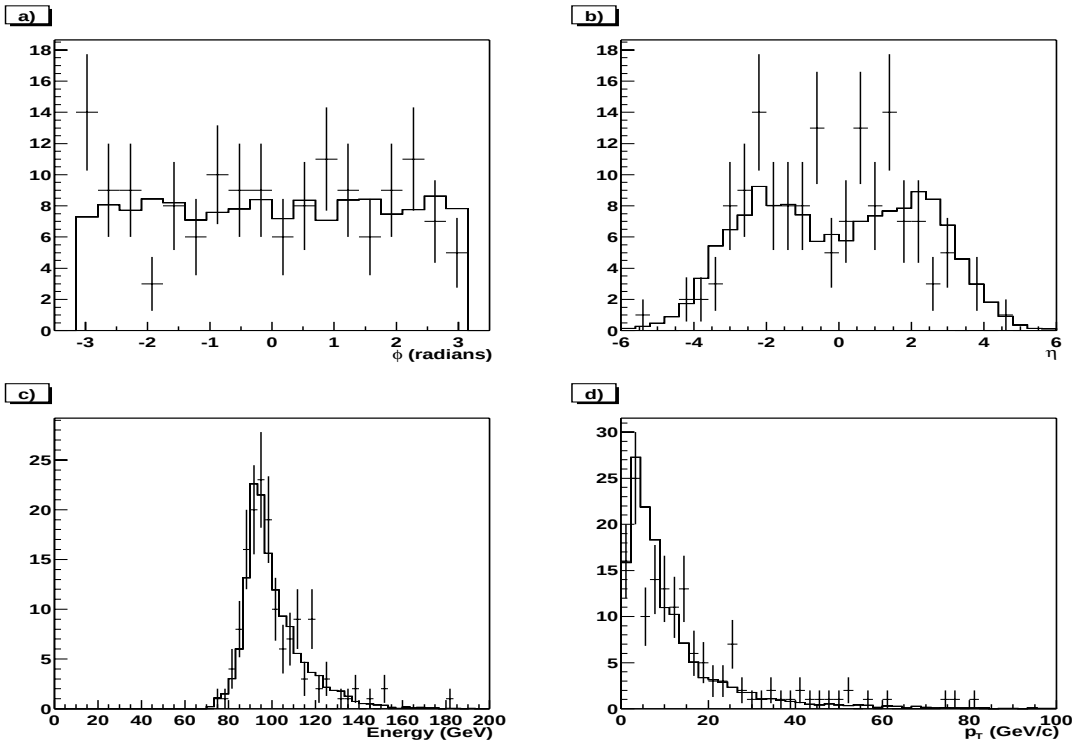

Figure 5.40: Basic distributions for di-electromagnetic objects in data and Monte Carlo (solid line) a) ϕ, b) η, c) Energy and d) p_T for the sample collected using the EM_MD_2CJT5 trigger

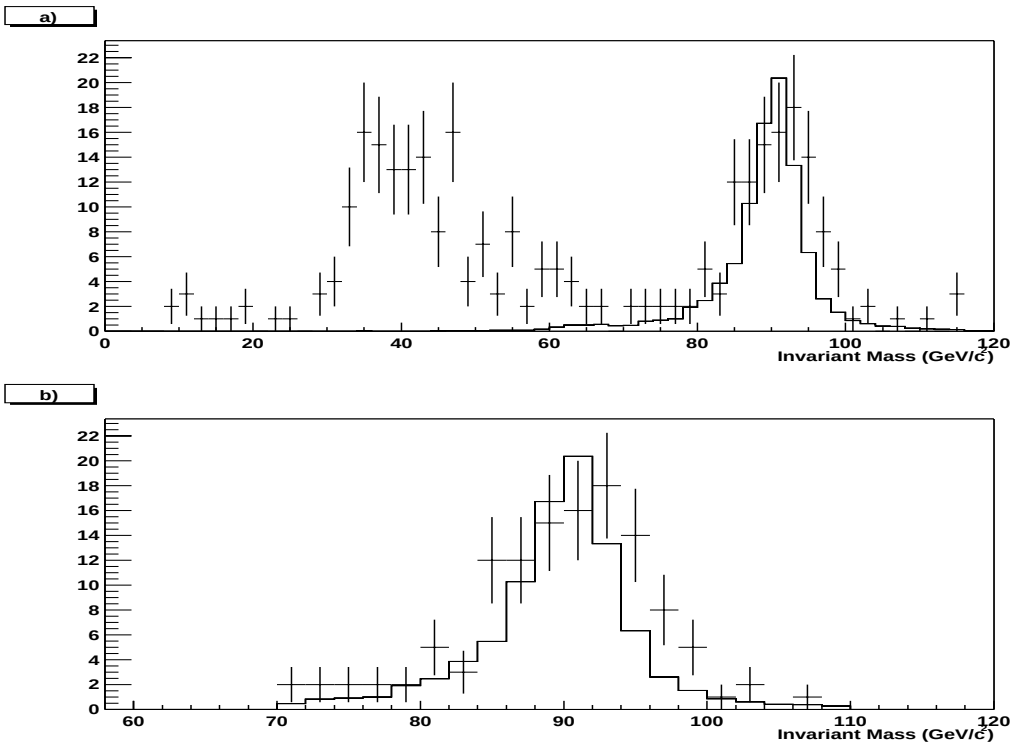

Figure 5.41: Invariant mass for di-electromagnetic objects in data and Monte Carlo (solid line) for the sample collected using the EM_MD_2CJT5 trigger

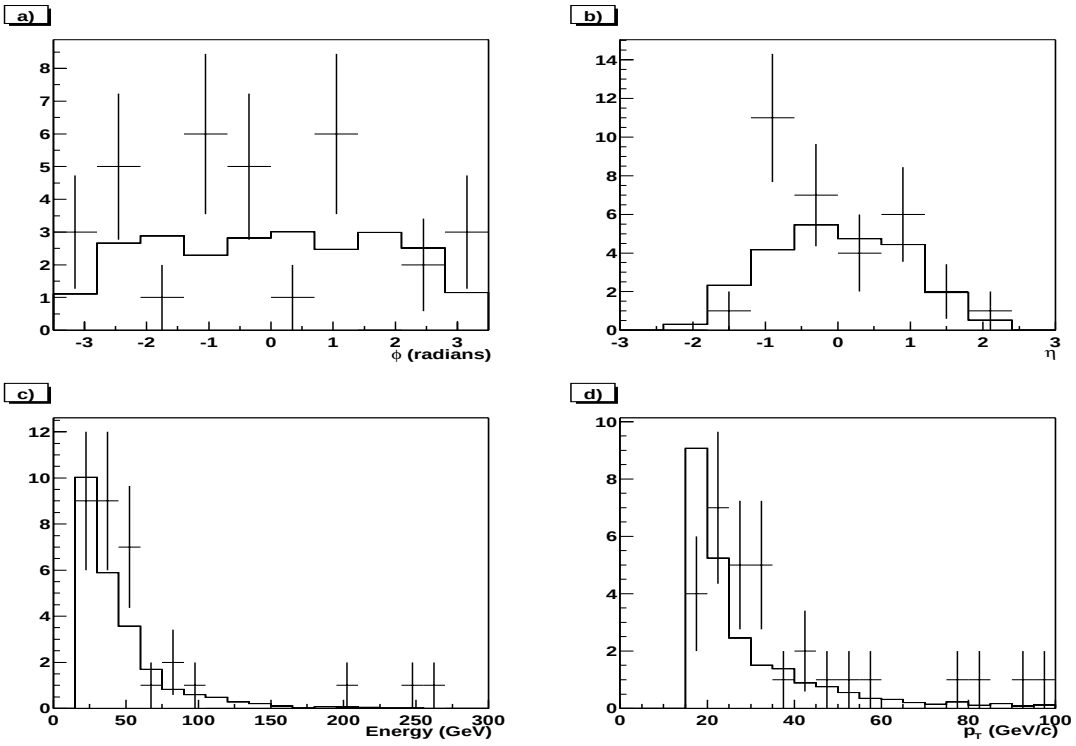

Figure 5.42: Basic distributions for jets in data and Monte Carlo (solid line) a) ϕ, b) η, c) Energy and d) p_T for the sample collected using the EM_MD_2CJT5 trigger

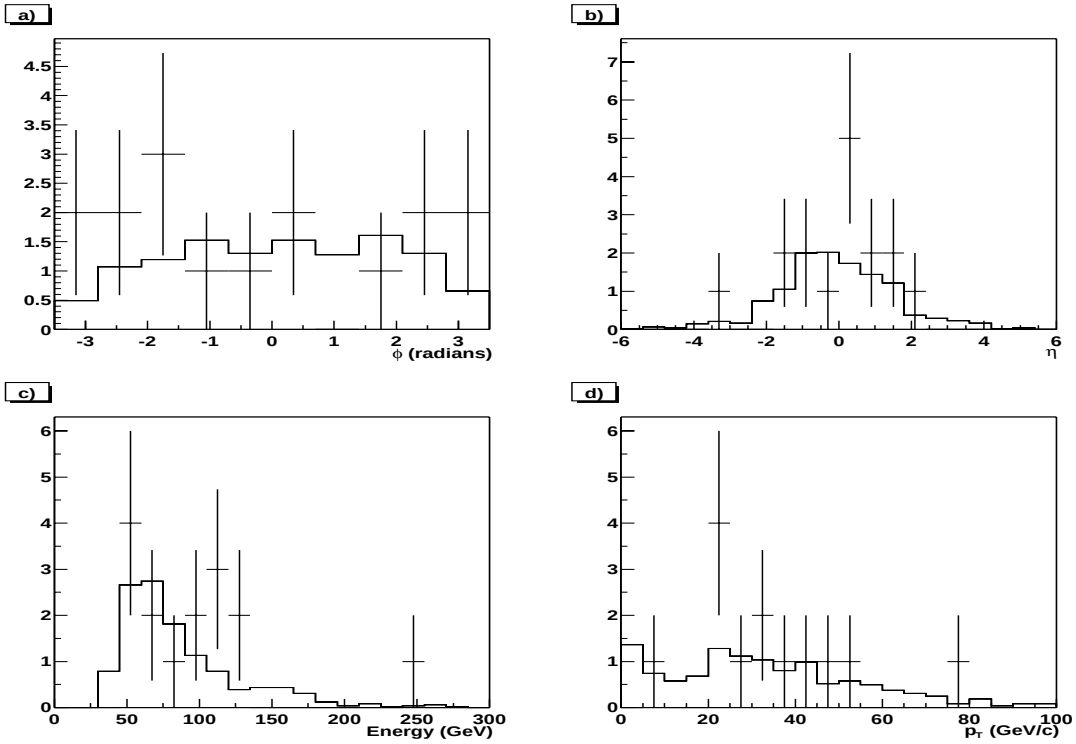

Figure 5.43: Basic distributions for di-jet objects in data and Monte Carlo (solid line) a) ϕ, b) η, c) Energy and d) p_T for the sample collected using the EM_MD_2CJT5 trigger

if the peak value is shifted in the data. The fact that the energy spectrum agrees in Figs. 5.34c) and 5.39d) would indicate that this discrepancy is a feature of the trigger bias. This is supported by the fact that the shift disappears when further restricting the η region.

There does seem to be an overall discrepancy in the electromagnetic object calibration between data and Monte Carlo as the peaks of the di-electromagnetic object invariant mass distributions differ by a few GeV/c^2 as seen in Figs. 5.36 and 5.41. The di-electromagnetic object invariant mass in Figs 5.36a) and 5.41a) shows the contribution of the QCD di-jet background. In the Z mass region it is almost negligible.

At first glance there does seem to be a significant feature in the di-electromagnetic object and jet pseudo-rapidity distributions in Figs. 5.35b) and 5.37b). Whereas the excess of events in Fig. 5.35b) partially disappears when looking at Fig. 5.40b), that for jets is still present in Fig. 5.42b). This excess could be linked with a warm calorimeter cell located at $\eta \sim -0.6$ and $\phi \sim 1.2$. This is further confirmed by Fig. 5.42a) which displays a similar excess in the ϕ bin corresponding to the location of the warm cell. However there is no evidence in Fig. 5.42a) of such an excess in ϕ.

The most likely is that it is a combination of low statistics and the impact of the warm cell.

The non-linearity in the calorimeter read out might be the reason for the comparatively lower number of low energy and low p_T jets in Figs. 5.37c) and 5.37d). As there is a zero suppression of cells with an energy lower than a fixed noise threshold, the non-linearity effect, which biases the measured cell energy to lower values, could result in the loss of cells which would have otherwise contributed to the total energy of the jet. In the case of high p_T jets this effect is not significant, however for jets which already have a relatively low p_T, the loss of cells in this manner could force the jet to fluctuate under the p_T threshold of 8 GeV/c and not be reconstructed or the jet finding algorithm could be unable to find the jet, e.g. due to a lack of seed cells. The lower number of soft p_T jets can also been seen in Fig. 5.42d), whereas in Fig. 5.42c) the lack of jets seems less evident.

It is encouraging that the distributions and the overall normalisation seem to be in fair agreement between data and Monte Carlo, especially in light of the varying trigger configurations, detector effects which have been identified but not yet been corrected for and in light of the preliminary stage of these comparisons.

Chapter 6

Summary and Outlook

The mechanism via which particles can acquire a mass in the Electroweak Lagrangian and the mechanism required for Electroweak symmetry breaking are the least experimentally verified aspects of the Standard Model. The most favoured theoretical solution is that of the Higgs mechanism which solves both aspects and gives rise to an extra particle, the Higgs boson. The search for the Higgs boson has been a central aspect of much of modern particle physics. It has yet to be discovered. Fits to electroweak data constrain the Higgs to have a mass less than 193 GeV/c^2 at 95% confidence level. Direct searches at LEP have excluded the Higgs boson up to a mass of 114.4 GeV/c^2 at 95% confidence level. Currently the two experiments which have the sensitivity to discover the Higgs in the favoured mass window are CDF and DØ at the Tevatron collider at Fermilab.

The Tevatron has been colliding protons and antiprotons since March 2001. Much of the initial data taking period at DØ was devoted to the completion and commissioning of the detector. Since then the physics capability has been limited by the low luminosity of the Tevatron, which has increased noticeably during the latter course of 2002.

The DØ detector has been significantly upgraded to cope with the Run II environment and to meet the goals of the collaboration's Run II physics programme. The detector is working well, as demonstrated by the ability to identify all the basic objects needed for the physics analysis e.g. leptons, jets, b-jets, B-hadrons and vector bosons. Furthermore, first physics results have been presented at the International Conference On High Energy Physics 2002 (ICHEP02).

One of the major efforts of the DØ upgrade was the production and testing of the Silicon Microstrip Tracker (SMT). Although initially behind schedule the SMT was completed and installed on time. In fact it was the first entirely new system to be

fully completed in terms of the hardware and the readout systems. The procedures reported in this thesis follow the work I was directly involved in; initially as part of the testing team and subsequently as coordinator of the F-Disk project. Overall the SMT is functioning well and the remaining problems are currently being addressed. Due to the complexity of the SMT system and to the absence of a silicon tracker in Run I, the SMT project provided much needed experience for the construction and design of the silicon tracker for Run IIb. The experience gained with the construction of the SMT has also contributed significantly to the pool of information needed for the construction and design of the next generation of silicon detectors.

The understanding of the jet energy scale is very important in a hadronic environment. The largest component of the jet energy scale is the calorimeter response to jets. Events in which a jet recoils against a Z boson, which subsequently decays to an electron-positron pair, can be used to measure the jet response by using conservation of momentum in the transverse plane. A full jet response correction for jets using a Monte Carlo Z+jet sample is derived in this thesis. Due to the limited data sample collected with the p10 version of the reconstruction code a direct comparison between data and Monte Carlo using this sample was not possible. The Monte Carlo results have shown that the method is a valid cross-check of the certified jet energy scale derived using a γ+jet sample. Due to the high cross-section of the γ+jet process, the analysis of the data collected with the p10 version of the DØ reconstruction code provided the first jet energy scale from data using this sample. As more luminosity is accumulated it will be possible to use the Z+jet sample to cross-check the response from data. The code used to derive the results presented in this thesis is being updated to interface to the new versions of the reconstruction software and will be the basis of a standard cross-check of the default jet energy scale for Monte Carlo and for data.

One of the main physics topics for Run II is the search for the Higgs boson. At the Tevatron the Higgs boson production cross-section is significantly lower than that of the QCD background. Hence in order to trigger on and reconstruct the signal events, the search is performed in channels in which the Higgs would decay to, or would be produced in association with, massive vector bosons. For a light Higgs (mass < 135 GeV/c^2) the Higgs boson decays predominantly to $b\overline{b}$, therefore the most promising production mechanism is associated production.

The estimate of the discovery sensitivity for a Standard Model Higgs in the channel $ZH \rightarrow e^+e^-b\overline{b}$ using a sequential cuts analysis presented in this thesis highlights various issues. The primary issue is b-tagging; this will need to be greatly improved from the very preliminary b-tagging technique used in the study. Other b-tagging

methods are currently being developed and optimised for the latest versions of the DØ reconstruction code, as are likelihood methods and Neural Network techniques based on the output of the b-taggers. Another issue is that of mass resolution. This will need to be improved and understood in detail in order to increase the sensitivity and understand the di b-jet invariant mass spectrum. Improvement of the b-tagging and the mass resolution is essential if DØ is to achieve the sensitivity outlined in the SUSY Higgs Workshop report. The sequential cuts analysis has been useful in pointing to areas of the reconstruction which need to be addressed e.g. much of the inefficiency of the b-tagging technique used in the analysis can be linked to problems in the tracking. The code developed for this thesis will be re-run on newer versions of the reconstruction software to give updated sensitivity estimates. Furthermore the new b-taggers and more sophisticated optimisation techniques will be incorporated into the code to achieve a better sensitivity.

Much of the initial luminosity collected by DØ was devoted to the process of understanding the detector and the Run II environment via the study of single objects: jets, electrons, etc. DØ entered a new phase using the p10 version of the reconstruction code, in which the emphasis started to shift toward the study of the physics processes, as demonstrated by the talks at ICHEP02 on first physics results [85]. This switch in emphasis is set to continue for the conferences in 2003 which will produce more physics results from the DØ collaboration. The next few years at the Tevatron will certainly produce many new and exciting results and also have the potential to yield new discoveries. The DØ experiment is well placed to contribute significantly to this advancement in the field of particle physics.

References

[1] For example D. Griffiths, "Introduction to Elementary Particles", Wiley, 1987

[2] S. Weinberg, "A Model of Leptons", Phys. Rev. Lett. **19** 1264 (1976)

[3] I. J. R. Aitchison, A. J. G. Hey, "Gauge Theories in Particle Physics (2nd Edition)", Chapter 14, IOP Publishing, 1989

[4] **The SNO Collaboration**, "Direct Evidence for Neutrino Flavor Transformation from Neutral-Current Interactions in the Sudbury Neutrino Observatory", Phys. Rev. Lett. **89** 011301 (2002), nucl-ex/0204008

[5] **The SNO Collaboration**, " Measurement of Day and Night Neutrino Energy Spectra at SNO and Constraints on Neutrino Mixing Parameters", Phys. Rev. Lett. **89** 011302 (2002), nucl-ex/0204009

[6] **The Super-Kamiokande Collaboration**, "Evidence for oscillation of atmospheric neutrinos", Phys. Rev. Lett. **81** 1562 (1998)

[7] P. W. Higgs, "Broken symmetries, massless particles and gauge fields", Phys. Lett. **12** 132 (1964)

[8] P. W. Higgs, "Broken Symmetries and the Masses of Gauge Bosons", Phys. Rev. Lett. **13** 508 (1964)

[9] P. W. Higgs, "Spontaneous Symmetry Breaking without Massless Bosons", Phys. Rev. **145** 1156 (1966)

[10] G. S. Guralnik, C. R. Hagen, T. W. B. Kibble, "Global Conservation Laws and Massless Particles", Phys. Rev. Lett. **13** 585 (1964)

[11] L. H. Ryder, "Quantum Field Theory (2nd Edition)", Chapter 8, Cambridge University Press, 1996

[12] E. Leader, E. Predazzi, "An Introduction to Gauge Theories and Modern Particle Physics Volume 1", pg. 1 - 63, Cambridge University Press, 1996

[13] S. Willenbrock, "Why Top Matters", Advanced Study Institute on Techniques and Concepts of High Energy Physics, 13-24 June 2002, St. Croix US Virgin Islands, `http://www.physics.fsu.edu/ASI/`

[14] L. Scodellaro, "Perspectives for Higgs Boson Search in Full Hadronic Final States at CDF II", PhD thesis, Universita' degli Studi di Padova, 2001

[15] K. Riesselmann, "Limitations of a Standard Model Higgs Boson", hep-ph/9711456

[16] **The LEP Electroweak Working Group**, "A Combination of Preliminary, Electroweak Measurements and Constraints on the Standard Model", hep-ex/0212036, `http://lepewwg.web.cern.ch/LEPEWWG/`

[17] M. Kruse, *et al.*, "Combined Standard Model VH Production Cross Section Limits for Run I CDF", CDF Note 4985

[18] **The LEP Working Group for Higgs Boson Searches**, "Search for the Standard Model Higgs Boson at LEP", Contributed paper for ICHEP02: 31st International Conference On High Energy Physics, Amsterdam 24-31 July 2002, ALEPH 2002-024 CONF 2002-013

[19] **The DØ Collaboration**, "Observation of the Top Quark", Phys. Rev. Lett. **74** 2632 (1995), Fermilab-Pub-95/028-E

[20] **The DØ Collaboration**, "Direct Measurement of Top Quark Mass by the DØ collaboration.", Phys. Rev. D **58** 052001 (1998), Fermilab-Pub-98/031-E, hep-ex/9801025

[21] **The CDF Collaboration**, "Observation of Top Quark Production in $\overline{p}p$ Collisions with the Collider Detector at Fermilab", Phys. Rev. Lett. **74** 2626 (1995), hep-ex/9503002

[22] **The DØ Collaboration**, "The DØ Upgrade: The Detector and its Physics", Fermilab-Pub-96/357-E

[23] "Run II Handbook", Fermilab beams division Run II web-page, `http://www-bd.fnal.gov/runII/index.html`

[24] "Report to the Fermilab Director Concerning 132 Nanosecond Operation During Run 2", Internal Fermilab document, June 6 2002

[25] D. Finley, "Report on 132 Nanosecond Operation During Run 2", Talk at All-DØ Meeting, `http://www-d0.fnal.gov/atwork/adm/d0_private/2002-09-06/DF_132ns.pdf`

[26] **The DØ Collaboration**, "The DØ Detector", Nucl. Instr. and Methods A **338** 185 (1994), Fermilab-Pub-93/179-E

[27] J. Brzezniak, *et al.*, "Conceptual design of a 2-Tesla superconducting solenoid for the Fermilab DØ detector upgrade", Fermilab-tm-1886

[28] The CFT upgrade web-page, `http://d0server1.fnal.gov/projects/SciFi/cft_home.html`

[29] P. Balm, *et al.*, "Magnetic field monitors for the DØ solenoid", DØ Note 3977

[30] A. Gordeev, *et al.*, "Technical Design Report of the Forward Preshower Detector for the DØ Upgrade", DØ Note 3445

[31] **The DØ Collaboration**, "Beam Tests of the DØ Uranium Liquid Argon End Calorimeter", Nucl. Instr. and Methods A **324** 53 (1993), Fermilab-Pub-92/162-E

[32] The muon system upgrade web-page, `http://www-d0.fnal.gov/hardware/upgrade/muon_upgrade/muon_upgrade.html`

[33] J. Blazey, "The DØ Run II Trigger", Talk given at Xth Real Time Conference 1997, Beaune France

[34] The DØ Run II trigger web-page, `http://niuhep.physics.niu.edu/~blazey/upgrade.html`

[35] M. Narain, "DØ Results", talk given at ICHEP02: 31st International Conference On High Energy Physics, Amsterdam 24-31 July 2002, `http://www.ichep02.nl`

[36] L. Babukhadia, "The DØ Detector", talk given at ICHEP02: 31st International Conference On High Energy Physics, Amsterdam 24-31 July 2002, `http://www.ichep02.nl`

[37] D. Glenzinski, "Prospects for RunII EW Physics", talk given at ICHEP02: 31st International Conference On High Energy Physics, Amsterdam 24-31 July 2002, `http://www.ichep02.nl`

[38] The DØ SMT Production Testing Group, "Electrical Production Testing of the DØ Silicon Microstrip Tracker Detector Modules", DØ Note 3841

[39] P. Van Gemmeren, F. Lehner, "Test Results for the F-Disk and 90°-stereo Silicon Microstrip Detectors", DØ Note 3601

[40] I. Kipnis, S. Kleinfelder, *et al.*, "A Beginners Guide to the SVXIIE", Fermilab-TM-1892, `http://d0server1.fnal.gov/projects/silicon/www/svx2e/svxe.html`

[41] F. Lehner, "The phenomenology of the micro discharge effects on DØ silicon modules", DØ Note 3804

[42] R. Demina, A. Khanov, Y. Kulik , A. Nomerotski, L. Shabalina, "Charge distribution in SMT Clusters", DØ Note 3981

[43] S. Hancock, *et al.*, "Energy loss and energy straggling of protons and pions in the momentum range 0.7 to 115 GeV/c", Phys. Rev. A **28** 615 (1983)

[44] **DØ Collaboration**, "Determination of the Absolute Jet Energy Scale in the DØ Calorimeters.", Nucl. Instr. and Methods A **424** 352 (1999), Fermilab-Pub-97/330-E, hep-ex/9805009

[45] B. Abbot, E. Barberis, *et al.*, "Jet Energy Scale at DØ ", DØ Note 3287

[46] F. Hsieh, "Post-CAFIX Jet Corrections for Top Mass Analyses", DØ Note 3055

[47] G. C. Blazey, J. R. Dittman, *et al.*, "Run II Jet Physics", Fermilab-Conf-00-092-E, hep-ex/0005012

[48] S. D. Ellis, D. E. Soper, "Successive Combination Jet Algorithm for Hadron Collisions", Phys. Rev. D **48** 3160 (1993), hep-ph/9305266

[49] S. Catani, Yu. L. Dokshitzer, B. R. Webber, "The $k_\perp$ clustering algorithm for jets in deep inelastic scattering and hadron collisions", Phys. Lett. B **285** 291 (1992)

[50] S. Catani, Yu. L. Dokshitzer, M. H. Seymour, B. R. Webber, "Longitudinally invariant $k_\perp$ clustering algorithms for hadron-hadron collisions", Nucl. Phys. B **406** 187 (1993)

[51] D. Sopper, *et al.*, Recommendations from Les Houches 1999 Jet Definition Group, letter to J. Blazey, `http://niuhep.physics.niu.edu/~blazey/jet_alg/les_houches.ps`

[52] P. Grannis, "Search for an Improved Estimate of B Hadron Energy in Semileptonic Decays", OPAL Technical Note 232 (1994)

[53] B. Abbott, V. D. Elvira, *et al.*, "Kt Jet Momentum Scale at DØ ", DØ Note 3585

[54] **DØ Collaboration**, "Subjet Multiplicity of Gluon and Quark Jets Reconstructed with the $k_\perp$ Algorithm in $p\bar{p}$ Collisions", Phys. Rev. D **65** 052008 (2002), hep-ex/0108054

[55] F. Canelli, *et al.*, "Jet Energy Scale at DØ in Run II", `http://www-d0.fnal.gov/phys_id/jes/d0_private/v2.2/note.ps`, DØ Note 4011

[56] DØ EM-ID Group, "EM ID Certification Results Version 2.1", `http://www-d0.fnal.gov/phys_id/emid/d0_private/certification/main_v2_0.html`

[57] T. S. Virdee, "Experimental Techniques", lectures at European School of HEP, St. Andrews Scotland 23^{rd} Aug. - 5^{th} Sept. 1998.

[58] T. Sjostrand, L. Lonnblad, S. Mrenna, "Pythia 6.2, Physics and Manual", hep-ph/0108264

[59] R. Zitoun, "Study of the non linearity of the DØ calorimeter readout chain", DØ Note 3997

[60] D. Zeppenfeld, R. Kinnunen, A. Nikitenko, E. Richter-Was, "Measuring Higgs boson couplings at the LHC", Phys. Rev. D **62** 013009 (2000), hep-ph/0002036

[61] M. Carena, *et al.*, "Report of the Tevatron Higgs Working Group", hep-ph/0010338

[62] M. Spira, "Higgs boson production and decay at the Tevatron", hep-ph/9810289

[63] M. Carena, S. Mrenna, C. E. M. Wagner, "MSSM Higgs Boson Phenomenology at the Tevatron Collider", Phys. Rev. D **60** 075010 (1999), hep-ph/9808312

[64] A. Pukhov, *et al.*, "CompHEP: A package for evaluation of Feynman diagrams and integration over multi-particle phase space", hep-ph/9908288

[65] R. V. Harlander, W. B. Kilgore, "Soft and virtual corrections to pp $\rightarrow$ H + X at next-to-next-to-leading order", Phys. Rev. D **64** 013015 (2001)

[66] J. Campbell, R. K. Ellis, "An update on vector boson pair production at hadron colliders", Phys. Rev. D **60** 113006 (1999), hep-ph/9905386

[67] J. Campbell, R. K. Ellis, "Radiative corrections to $Zb\overline{b}$ production", Fermilab-Pub-00/145-T

[68] J. Campbell, R. K. Ellis, "Next-to-leading order corrections to W+2 jet and Z+2 jet production at hadron colliders", hep-ph/0202176

[69] D. O. Carlson, "Physics of Single-Top Quark Production at Hadron Colliders", hep-ph/9508278

[70] M. L. Mangano, *et al.*, "ALPGEN, a generator for hard multiparton processes in hadronic collisions", hep-ph/0206293

[71] A. Schwartzman, M. Narain, "Secondary Vertex Reconstruction using the Kalman Filter", DØ Note 3908

[72] A. Schwartzman, M. Narain, "Secondary Vertex b-tagging using the Kalman Filter Algorithm", DØ Note 3909

[73] R. Van Kooten, A. Kryemadhi, "b-ID Muon+Jet tagger Certification Results (v2.0)", `http://www-d0.fnal.gov/phys_id/bid/d0_private/certification/p13/muonjet/muonjet_v1.html`

[74] R. Demina, A. Khanov, F. Rizatdinova, "Counting Signed Impact Parameter Tagging Method", `http://www-d0.fnal.gov/phys_id/bid/d0_private/certification/p13/CSIP/CSIP_v1.html`

[75] **The DØ Collaboration**, "The $b\overline{b}$ Production Cross Section and Angular Correlations in $p\overline{p}$ Collisions at $\sqrt{s} = 1.8$ TeV", Phys. Lett. B **487** 264 (2000), hep-ex/9905024

[76] **ALEPH Collaboration**, "Performance of the ALEPH detector at LEP", Nucl. Instr. and Methods A **360** 481 (1995)

[77] DØ Jet/ME_T ID Group, "Jets in Run II", DØ Note 3985

[78] M. Caccia, "Measurements of R_b and R_c at LEP", Nucl. Phys. B (Proc. Suppl.) **75B** 246 (1999)

[79] **ALEPH Collaboration**, "A measurement of R_b using a lifetime-mass tag", Phys. Lett. B **401** 150 (1997)

[80] P. Avery, *et al.*, "MCFAST: A Fast Simulation Package for Detector Design Studies", Fermilab-Conf-97-151

[81] L. Duflot, M. Ridel, "An Energy Flow Algorithm for DØ ", DØ Note 3927

[82] L. Duflot, M. Ridel, "The CellNN Algorithm: Cell Level Clustering in the DØ Calorimeter", DØ Note 3923

[83] M. Narain, U. Heintz, "Observability of the Decay $Z \to b\overline{b}$ in Run II", DØ Note 3604

[84] F. James, "Minuit Reference Manual (Version 94.1)", CERN Program Library D506

[85] Talks at ICHEP02: 31st International Conference On High Energy Physics, Amsterdam 24/07/2002- 31/07/2002, `http://www.ichep02.nl`